OPTICAL CHARACTERIZATION OF COMPOUND SEMICONDUCTOR MATERIALS USING SPECTROSCOPIC ELLIPSOMETRY

BY

NUWANJULA SAMARASINGHA, B.S., M.S.

A dissertation submitted to the Graduate School

in partial fulfillment of the requirements

for the degree

Doctor of Philosophy

Major Subject: Physics

New Mexico State University

Las Cruces New Mexico

December 2021

Nuwanjula Samarasingha

Candidate

Physics

Major

This dissertation is approved on behalf of the faculty of New Mexico State University, and it is acceptable in quality and form for publication:

Approved by the Dissertation Committee

Dr. Stefan Zollner

Chairperson

Dr. Michael Engelhardt

Committee Member

Dr. Heinz Nakotte

Committee Member

Dr. David Voelz

Committee Member

DEDICATION

This work is dedicated to my beloved mother Anoma Nandani and my husband Menaka Herath who encouraged me to pursue my dreams and supported me throughout this process.

ACKNOWLEDGMENTS

I would like to extend my sincere gratitude to my research advisor Dr. Stefan Zollner for his invaluable guidance, throughout my research work. I would also like to thank Dr. Michael Engelhardt, Dr. Heinrich Nakotte, and Dr. David Voelz for accepting to be a member of my Ph.D. dissertation committee. I am also grateful to our ellipsometry group members Zach Yoder, Farzin Abadizaman, and Carola Emminger for their support. In addition, a thank you to Rosa Urioste, our Physics department senior fiscal assistant, and our administrative assistant Marisela Chavez. I would also like to mention here about the NMSU research cores program. Through this program I was able to get access to the X-ray diffractometer (XRD) and the Atomic force microscope (AFM). I am thankful to Dr. Peter Cooke and Dr. Huiyao Wang for giving me training to use the AFM located at Skeen Hall. I am also grateful to our collaborator Dr. Sudeshna Chattopadhyay for providing us samples. I am also grateful to Adam Dubroka, Daniel Franta at Masaryk University (Brno, Czech Republic), Oliver Herrfurth (Universität Leipzig, Germany), Professor David J. Lockwood (National Research Council of Canada), and Professor Sotirios Ves (Aristotle University of Thessaloniki, Greece) for their advice and helpful discussions on my research.

This work was supported by the National Science Foundation (NSF, No. DMR-1505172) and the US Army (No. W911NF-16-1-0492).

VITA

2008-2013	B.S. in Physics, University of Peradeniya, Peradeniya, Kandy, Sri Lanka
2015-2018	M.S in Physics, New Mexico State University, NM, USA
2021	Ph.D. in Physics, New Mexico State University, NM, USA

PROFESSIONAL AND HONORARY SOCIETIES

American Vacuum Society (AVS)

American Physical Society (APS)

AWARDS

- 2nd place in oral presentation - Research and Creativity Week presentation, New Mexico State University, November 2020.
- Winner, Research and Creativity Week presentation, New Mexico State University, November 2019.
- Outstanding Graduate Assistant Award from the New Mexico State University Graduate School 2018.
- Best student presentation in Ellipsometry focus topic session -AVS 63rd International Symposium and Exhibition, Nashville, TN, 2016.

- 3rd place in oral presentation - AVS New Mexico Symposium, Albuquerque, NM, May 16th, 2017.

PUBLICATIONS

- **Nuwanjula Samarasingha** and Stefan Zollner, Temperature dependence of optical phonon reflection bands in GaP, J. Vac. Sci. Technol. B **39**, 052201 (2021).
- **Nuwanjula S. Samarasingha**, Stefan Zollner, Dipayan Pal, Rinki Singh, and Sudeshna Chattopadhyay, Thickness dependence of infrared lattice absorption and excitonic absorption in ZnO layers on Si and SiO_2 grown by atomic layer deposition, J. Vac. Sci. Technol. B **38**, 042201 (2020).
- Carola Emminger, **Nuwanjula S. Samarasingha**, Melissa Rivero Arias, Farzin Abadizaman, José Menéndez, and Stefan Zollner, Excitonic effects of the temperature-dependent direct band gap of Ge (in progress).
- Carola Emminger, Farzin Abadizaman, **Nuwanjula S. Samarasingha**, Thomas E. Tiwald, and Stefan Zollner, Temperature dependent dielectric function and direct bandgap of Ge, J. Vac. Sci. Technol. B **38**, 012202 (2020).
- I. S. A. Abeysiriwardana-Arachchige, **N. Samarasingha**, R. Rosalez, S. Munasinghe-Arachchige, H. Dilanke-Pedige, C. E. Brewer and N. Nirmalakhan-

dan, Maximizing phosphorus recovery as biofertilizer in an algal wastewater treatment system, Resources, Conservation and Recycling **170**, 105552 (2021).

- Stefan Zollner, Pablo P. Paradis, Farzin Abadizaman, and **Nuwanjula S. Samarasingha**, Drude and Kukharskii mobility of doped semiconductors extracted from Fourier transform infrared ellipsometry spectra, J. Vac. Sci. Technol. B **37**, 012904 (2019).

- T.N. Nunley, N.S. Fernando, **N. Samarasingha**, J.M. Moya, C.M. Nelson, A.A. Medina, and S. Zollner, Optical constants of germanium and thermally grown germanium dioxide from 0.5 to 6.6 eV via a multi-sample ellipsometry investigation, J. Vac. Sci. Technol. B **34**, 061205 (2016).

- T.N. Nunley, N. Fernando, J.M. Moya, **N.S. Arachchige**, C.M. Nelson, A.A. Medina, and S. Zollner, Precise Optical Constants of Ge and GeO_2 from 0.5 to 6.6 eV, IEEE Summer Topicals Conference on Emerging Technology for Integrated Photonics, 11-13 July 2016, Newport Beach, CA.

CONFERENCE PRESENTATIONS AND POSTERS

- **Nuwanjula Samarasingha** and Stefan Zollner, Temperature Dependence of Optical Phonon Bands in GaP, 63rd Electronic Materials Conference (Virtual), June 23-25, 2021.

- **Nuwanjula Samarasingha** and Stefan Zollner, Temperature dependence of optical phonon bands in GaP, APS March Meeting (Virtual), 16 March 2021.

- **Nuwanjula Samarasingha** and Stefan Zollner, Temperature dependence of optical phonon bands in GaP, APS Four Corners Section Meeting (Virtual), 23 October 2020.

- **Nuwanjula Samarasingha**, Stefan Zollner, Dipayan Pal, Aakash Mathur, Ajaib Singh, Rinki Singh, Sudeshna Chattopadhyay, Thickness-dependent Optical Properties of ZnO Films from the Mid-infrared to the Vacuum-ultraviolet, 8th International Conference on Spectroscopic Ellipsometry, Barcelona, Spain, May 26- May 31, 2019.

- **Nuwanjula Samarasingha**, Stefan Zollner, Dipayan Pal, Aakash Mathur, Ajaib Singh, Rinki Singh, and Sudeshna Chattopadhyay, Phonon confinement and excitonic absorption in the optical properties of ZnO films, AVS 65th International Symposium and Exhibition, Long Beach, CA, 21-26 October 2018.

- **Nuwanjula Samarasingha**, Stefan Zollner, Dipayan Pal, Aakash Mathur, Ajaib Singh, Rinki Singh, and Sudeshna Chattopadhyay, Phonon and exciton absorption in the optical properties of ZnO films, 2018 NMAVS Symposium and Exhibition, Albuquerque, NM, 22 May 2018.

- **Nuwanjula Samarasingha**, Zachary Yoder, Stefan Zollner, Dipayan Pal, Aakash Mathur, Ajaib Singh, Rinki Singh, Sudeshna Chattopadhyay, Excitonic absorption and optical properties of ZnO films, APS March Meeting, Los Angeles, California, March 5 – March 9, 2018.

- **Nuwanjula Samarasingha**, Zachary Yoder, Stefan Zollner, Dipayan Pal, Aakash Mathur, Ajaib Singh, Rinki Singh, Sudeshna Chattopadhyay, Excitonic effects on the optical properties of thin ZnO films on different substrates, AVS 64th International Symposium & Exhibition, Tampa, Florida, October 30 – November 3, 2017.

- **Nuwanjula Samarasingha**, Cesar Rodriguez, Jaime Moya, Nalin Fernando, Stefan Zollner, Patrick Ponath, Kristy J. Kormondy, Alex Demkov, Dipayan Pal, Aakash Mathur, Ajaib Singh, Surjendu Dutta, Jaya Singhal, Sudeshna Chattopadhyay, Excitonic effect at interfaces in thin oxide films, AVS New Mexico Symposium, Albuquerque, NM, May 16th, 2017.

- **Nuwanjula Samarasingha**, Cesar Rodriguez, Jaime Moya, Nalin Fernando, Stefan Zollner, Patrick Ponath, Kristy J. Kormondy, Alex Demkov, Dipayan Pal, Aakash Mathur, Ajaib Singh, Surjendu Dutta, Jaya Singhal, Sudeshna Chattopadhyay, Excitons at interfaces in ellipsometric spectra, AVS 63rd International Symposium & Exhibition, Nashville, TN,

6-11, November 2016.

- **Nuwanjula Samarasingha**, Cesar Rodriguez, Jaime Moya, Nalin Fernando, Stefan Zollner, Patrick Ponath, Kristy J. Kormondy, Alex Demkov, Dipayan Pal, Aakash Mathur, Ajaib Singh, Surjendu Dutta, Jaya Singhal, Sudeshna Chattopadhyay, Excitons at interfaces in thin oxide films, APS Four Corners Section Meeting, Las Cruces, NM, 21-22 October 2016.

- **N. Samarasingha**, C. Rodriguez, J. Moya, S. Zollner, N. Fernando, S. Chattopadhyay, P. Ponath, and A.A. Demkov, Structural and optical properties of $SrTiO_3$ thin films on different substrates, Lawrence Symposium on Epitaxy, Scottsdale, AZ, 21-24 February 2016.

- **N. Samarasingha**, C. Rodriguez, J. Moya, S. Zollner, N. Fernando, S. Chattopadhyay, P. Ponath, and A.A. Demkov, Structural and optical properties of $SrTiO_3$ thin films on semiconductors, The 43rd Conference on the Physics and Chemistry of Surfaces and Interfaces, Palm Springs, CA, 17-21 January 2016.

- **N. Samarasingha**, J. Moya, S. Zollner, S. Chattopadhyay, P. Ponath, and A. Demkov, Structural properties of $SrTiO_3$ thin films on semiconductors, APS Four Corners Section Meeting, Tempe, AZ, 16 October 2015.

- Carola Emminger, Shirly Espinoza, Steffen Richter, Mateusz Rebarz, Oliver Herrfurth, Martin Zahradník, Rüdiger Schmidt-Grund, Jakob Andreasson, Farzin Abadizaman, **Nuwanjula S. Samarasingha**, José Menéndez, and Stefan Zollner, Computational Analysis of Critical Points in Temperature Dependent and Time Resolved Ellipsometry Spectra of Ge Using Digital Filtering, Virtual MRS Spring Meeting, April 17-23, 2021.

- Carola Emminger, Farzin Abadizaman, **Nuwanjula S. Samarasingha**, José Menéndez, Shirly Espinoza, Steffen Richter, Mateusz Rebarz, Oliver Herrfurth, Martin Zahradník, Rüdiger Schmidt-Grund, Jakob Andreasson, and Stefan Zollner, Analysis of critical points in temperature dependent and time resolved ellipsometry spectra using digital filtering, APS March Meeting (Virtual), March 15-19, 2021.

- Carola Emminger, Farzin Abadizaman, **Nuwanjula S. Samarasingha**, Shirly Espinoza, Steffen Richter, Mateusz Rebarz, Oliver Herrfurth, Rüdiger Schmidt-Grund, Jakob Andreasson, and Stefan Zollner, Analysis of Critical Points in Ellipsometry Spectra Using Digital Filtering, ELI Beamlines User Conference, Prague, Czech Republic, October 2020.

- Shirly Espinoza, Steffen Richter, Mateusz Rebarz, Oliver Herrfurth, **Nuwanjula Samarasingha**, Rüdiger Schmidt-Grund, Jakob Andreasson, Stefan Zollner, Time-resolved spectroscopic ellipsometry on Ge and InP,

8th International Conference on Spectroscopic Ellipsometry, Barcelona, Spain, May 26- May 31, 2019.

- Carola Emminger, **Nuwanjula Samarasingha**, Farzin Abadizaman, Stefan Zollner, Temperature Dependence of the Critical Point Parameters of the Direct Band Gap of Germanium, 8th International Conference on Spectroscopic Ellipsometry, Barcelona, Spain, May 26- May 31, 2019.

- C. Emminger, **N. Samarasingha**, F. Abadizaman, S. Zollner, Investigation of the Temperature Dependence of the Critical Points E_0 and $E_0+\Delta_0$ of Bulk Ge, DPG Spring Meeting, Regensburg, Germany, March 31 – April 5, 2019.

- C. Emminger, **N. Samarasingha**, F. Abadizaman, S. Zollner, Analysis of the Critical Point Parameters of E_0 and $E_0+\Delta_0$ of Bulk Ge, APS March Meeting, Boston, Massachusetts, March 4-8, 2019.

- Cesy M. Zamarripa, **Nuwanjula Samarasingha**, Farzin Abadizaman, Rigo A. Carrasco, and Stefan Zollner, Temperature-dependent ellipsometry and thermal stability of $Ge_2Sb_2Te_5$:C phase change memory alloys, AVS 65th International Symposium and Exhibition, Long Beach, CA, 21-26 October 2018.

- Rigo A. Carrasco, Carola Emminger, **Nuwanjula Samarasingha**, Farzin

Abadizaman, and Stefan Zollner, Temperature dependent dielectric function and critical point comparison of bulk Ge and α-Sn on InSb, AVS 65th International Symposium and Exhibition, Long Beach, CA, 21-26 October 2018.

- C. Emminger, R. Carrasco, **N. Samarasingha**, F. Abadizaman, and S. Zollner, Temperature dependent dielectric function and critical points of bulk Ge compared to α-Sn on InSb, IEEE Photonics Society 2018 Summer Topicals Meeting Series, Waikoloa, HI, July 9-11, 2018.

- Carola Emminger, **Nuwanjula Samarasingha**, Farzin Abadizaman, and Stefan Zollner, Analysis of Critical Points in the Dielectric Function of Ge between 10 and 738 K, 2018 NM AVS Symposium and Exhibition, Albuquerque, NM, 22 May 2018.

- Cesy M. Zamarripa,**Nuwanjula Samarasingha**, Farzin Abadizaman, Rigo A. Carrasco, and Stefan Zollner, Temperature-dependent ellipsometry and thermal stability of $Ge_2Sb_2Te_5$:C phase change memory alloys, 2018 NM AVS Symposium and Exhibition, Albuquerque, NM, 22 May 2018.

- Stefan Zollner, **Nuwanjula Samarasingha**, Zachary Yoder, Dipayan Pal, Aakash Mathur, Ajaib Singh, Rinki Singh, and Sudeshna Chattopadhyay, Excitonic absorption and optical properties of ZnO films, DPG Frühjahrstagung, Berlin, 11-16 March 2018.

- Rigo A. Carrasco, **Nuwanjula Samarasingha**, Bich-Yen Nguyen, Stefan Zollner, Ellipsometry Analysis of Germanium-on-Insulator Wafers, APS March Meeting, Los Angeles, California, March 5 – March 9, 2018.

- Carola Emminger, **Nuwanjula Samarasingha**, Farzin Abadizaman, Nalin Fernando, Stefan Zollner, Temperature dependence of the dielectric function and analysis of critical point parameters of bulk Ge, APS March Meeting, Los Angeles, California, March 5 – March 9, 2018.

- R. Carrasco, **N. Samarasingha Arachchige**, C. Zamarripa, S. Zollner, S. Chastang, G. Grzybowski, J. Duan, B. Claflin, and A. Kiefer, Dayton, Spectroscopic Ellipsometry and Band Structure of α-tin on InSb, OH, 10 January 2018.

- Carola Emminger, **Nuwanjula Samarasingha**, Farzin Abadizaman, Nalin Fernando, Stefan Zollner, Temperature dependence of the dielectric function and interband critical points of bulk Ge, AVS 64th International Symposium & Exhibition, Tampa, Florida, October 30 – November 3, 2017.

- Rigo Carrasco,**Nuwanjula Samarasingha**, Bich-Yen Nguyen, Stefan Zollner, Ellipsometry analysis of a germanium-on-insulator wafer, AVS 64th International Symposium & Exhibition, Tampa, Florida, October 30 – November 3, 2017.

- Carola Emminger, **Nuwanjula Samarasingha**, Farzin Abadizaman, Nalin Fernando, Stefan Zollner, Temperature Dependence of the Dielectric Function of Bulk Ge, AVS New Mexico Symposium, Albuquerque, NM, May 16th, 2017.

- T.N. Nunley, N.S. Fernando, **N. Samarasingha**, J.M. Moya, C.M. Nelson, A.A. Medina, S. Zollner, Precise optical constants of Ge and GeO_2 from 0.5 to 6.6 eV, IEEE Summer Topicals Conference on Emerging Technology for Integrated Photonics, Newport Beach, CA, 11-13 July 2016.

- Jaime M. Moya, T Nathaniel Nunley, **Nuwanjula Samarasingha**, and Stefan Zollner, FTIR Ellipsometry Studies of Thermally Grown GeO_2 on Ge, AVS 63rd International Symposium & Exhibition, Nashville, TN, 6-11 November 2016.

- C. Rodriguez, **N. Samarasingha**, J. Moya, S. Zollner, P. Ponath, and A. Demkov, Comparison of the dielectric function of $SrTiO_3$ on $SrTiO_3$, Si, and Ge substrates, APS Four Corners Section Meeting, Tempe, AZ, 16 October 2015.

- J. Moya, **N. Samarasingha**, and S. Zollner, Comparison of LiF and NiO crystallographic structure using XRD, APS Four Corners Section Meeting, Tempe, AZ, 16 October 2015.

- J. Moya, **N. Samarasingha**, and S. Zollner, Comparison of LiF and NiO crystallographic structure using XRD, The National Mentoring Community (NMC) Conference, Miami, FL, October 2015.

ABSTRACT

OPTICAL CHARACTERIZATION OF COMPOUND SEMICONDUCTOR MATERIALS
USING SPECTROSCOPIC ELLIPSOMETRY

BY

NUWANJULA SAMARASINGHA, B.S., M.S.

Doctor of Philosophy

New Mexico State University

Las Cruces, New Mexico, 2021

Dr. Stefan Zollner, Chair

In this thesis, I present the thickness dependent optical properties of Zinc Oxide (ZnO) thin layers on Si and quartz (SiO_2) substrates and the temperature dependence of the optical phonon reflection band in bulk Gallium Phosphide (GaP) using J. A. Woollam FTIR-VASE and UV-VASE instruments. The FTIR-VASE instrument was used to measure in the mid-and near-infrared spectral regions from 0.03 to 0.60 eV and the UV-VASE instrument provides data from 0.5 to 6.5 eV (near-infrared to deep ultraviolet). All ZnO measurements were performed

in air at 300 K at three angles of incidence (60°, 65°, and 70°). My main focus has been on the thickness dependence of the infrared lattice absorption and the excitonic absorption (near the bandgap) in ZnO thin films. Also, I focused on the effect of temperature on the frequency and linewidth of zone-center transverse (TO) and longitudinal (LO) optical phonons in bulk GaP from 80 to 720 K. The GaP temperature dependence measurements were performed inside the Janis ST-400 ultrahigh vacuum (UHV) cryostat at 70° angle of incidence. Powder X-ray diffraction (XRD), X-ray reflectivity (XRR), and atomic force microscopy (AFM) were used to characterize the structural and surface properties of thin films.

The conventional approach to describe the dielectric function (ϵ) as a sum of oscillators (Drude, phonons, interband transitions) sometimes fails because each term only has a single broadening parameter. Instead, we find it more convenient to describe ϵ over a broad range from the mid-infrared to the vacuum ultraviolet as a product of Drude, TO/LO phonon, and electronic interband transitions. This comprehensive factorized description of ϵ was applied to a few doped and undoped semiconductors and insulators. These results are reported in chapter 3.

ϵ of bulk and ZnO thin films was defined over a broad range from the mid-infrared to the vacuum ultraviolet as a product of TO/LO phonon and oscillator functions for the infrared lattice response and electronic interband transitions respectively. Both real (ϵ_1) and imaginary (ϵ_2) parts of ϵ in thin ZnO films on Si are much smaller than in bulk ZnO and show significant variations with thickness over

the complete spectral range. The excitonic enhancement decreases monotonically with decreasing ZnO film thickness on Si. Due to quantum confinement, a small blueshift of the bandgap was observed with decreasing thickness. A similar behavior was observed for ZnO films on SiO_2 as a function of thickness.

To determine the energy and linewidth of GaP optical phonons, the ellipsometric angles (Ψ and Δ) were fitted with the Lowndes–Gervais model. We found a significant variation of the optical phonon energy and the broadening with temperature. These temperature-dependent phonon features were explicitly described in chapter 5.

CONTENTS

LIST OF TABLES xxviii

LIST OF FIGURES xli

1 INTRODUCTION 1

2 Experimental and theoretical methods 3

2.1 Variable Angle Spectroscopic Ellipsometry (VASE) 3

2.1.1 How spectroscopic ellipsometry (SE) works 3

2.1.2 Pseudodielectric function 6

2.1.3 SE and thin films 7

2.1.4 Data acquisition and basic optical components used in UV and IR spectroscopic ellipsometry: UVVASE & FTIR . . . 9

2.1.5 Temperature dependent ellipsometry 16

2.1.6 SE data modeling 17

2.1.7 Excitons 22

2.1.8 Quantum Confinement 24

2.1.9 Optical phonons 25

2.2 X-ray powder diffraction (XRD) 27

2.3 X-ray reflectance (XRR) 30

2.4 Atomic force microscopy (AFM) 36

3 DRUDE AND KUKHARSKII MOBILITY OF DOPED SEMICONDUCTORS EXTRACTED FROM FOURIER-TRANSFORM INFRARED ELLIPSOMETRY SPECTRA 39
3.1 Abstract 39
3.2 Introduction 40
3.3 Model dielectric functions 41
3.3.1 Drude-Lorentz model (sum) 41
3.3.2 Kukharskii model (product) 46
3.4 Experimental procedure 52
3.5 Results and Discussion 52
3.5.1 Intrinsic and n-type GaAs, doped GaSb, InAs 52
3.5.2 Bulk undoped ZnO 56
3.6 Summary 60
3.7 Supplementary Materials 61
3.7.1 Definition of the Pseudo-dielectric Function 61
3.7.2 Results for GaSb 63
3.7.3 Results for InAs 71
3.7.4 Results for spinel 75
4 THICKNESS DEPENDENCE OF INFRARED LATTICE ABSORPTION AND EXCITONIC ABSORPTION IN ZNO LAYERS ON SI AND SIO_2 GROWN BY ATOMIC LAYER DEPOSITION . . 78

4.1 Abstract 78
4.2 Introduction 79
4.3 Experimental Methods and Results 83
4.4 Dielectric function models 84
4.5 Ellipsometry Analysis 92
4.6 Discussion 100
4.6.1 Quantum confinement 100
4.6.2 High-frequency dielectric constant 100
4.6.3 Decreased absorption 103
4.6.4 Phonon energies and Born effective charge 105
4.6.5 Static dielectric constant 108
4.7 Summary 109
4.8 Supplementary Material 110
4.8.1 Surface roughness 110
4.8.2 Crystal structure 111
4.8.3 X-Ray Reflectivity (XRR) 116
4.8.4 Optical properties of bulk ZnO 121
4.8.5 Dielectric function of quartz substrate 123
4.8.6 Comparison of oscillator and point-by-point fits 130
4.8.7 Band gap determination using Tauc plot 132
4.8.8 Comparison of ellipsometry and transmission results 133

4.8.9 Lattice vibration versus total infrared optical response . . 135
4.8.10 Impact of Si substrate optical constants 137
4.8.11 Accuracy of thicknesses determined from ellipsometry . . . 146
5 TEMPERATURE DEPENDENCE OF THE OPTICAL PHONON REFLECTION BAND IN GAP 150
5.1 Abstract 150
5.2 Introduction 151
5.3 Experimental methods and models 155
5.4 Results and discussion 159
5.4.1 Optical phonon parameters at 300 K 159
5.4.2 Two-phonon absorption 165
5.4.3 Temperature dependence of optical phonon parameters . . 166
5.5 Summary 178
5.6 Supplementary Material 180
5.6.1 Lorentz model for a single phonon 180
5.6.2 Frequency-dependent broadening 183
5.6.3 Accurate determination of the broadening parameter . . . 188
5.6.4 Relationship between Phonon Lifetimes and Broadenings . 192
5.6.5 Origin of the TO and LO Phonon Broadenings 194
5.6.6 GaP born effective charge 199
5.6.7 Variation of the apparent GaP surface layer thickness . . . 202

6 CONCLUSION 206

7 FUTURE WORK 207

REFERENCES 208

LIST OF TABLES

3.1 Screened plasma frequency $E_P = \hbar\omega_P$, Drude broadening $\Gamma_D = \hbar\gamma_D$, high-frequency dielectric constant ϵ_∞, carrier density n, mobility μ, TO and LO phonon energies $E_{\mathrm{TO}} = \hbar\omega_{\mathrm{TO}}$ and $E_{\mathrm{LO}} = \hbar\omega_{\mathrm{LO}}$ and broadening $\Gamma_{\mathrm{TO}} = \hbar\gamma_{\mathrm{TO}}$, Kukharskii broadening $\Gamma_K = \hbar\gamma_K$, and lower and upper plasmon-polariton frequencies $E_{\mathrm{LP}} = \hbar\omega_{\mathrm{LP}}$ and $E_{\mathrm{UP}} = \hbar\omega_{\mathrm{UP}}$ and their broadenings $\Gamma_{\mathrm{LP}} = \hbar\gamma_{\mathrm{LP}}$ and $\Gamma_{\mathrm{UP}} = \hbar\gamma_{\mathrm{UP}}$ for undoped and n-type GaAs as well as n-type and p-type GaSb and InAs. For uniaxial undoped ZnO, values for the ordinary (o) and extraordinary (eo) parameters are listed separately. Quantities marked (f) were fixed during the fit, those marked with an asterisk were taken from the literature. For each material, the top row (model DL) shows a fit with Eq. (64), where E_P, Γ_D, E_{TO}, Γ_{TO}, and ϵ_∞ are experimental values from ellipsometry data, whereas n, μ, and E_{LO} were calculated using Eqs. (65), (72). and (68); the bottom row (model KK) shows experimental values ϵ_∞, E_{TO}, Γ_{TO}, Γ_K, E_{LP}, E_{UP}, Γ_{LP}, and Γ_{UP} determined from a fit to the ellipsometry data with Eq. (74), whereas E_P, E_{LO}, n, and μ were calculated using Eqs. (77), (78), (65), and (85), respectively. Calculated quantities are shown in bold. The broadenings shown in italics show strong parameter correlations and therefore are not reliable. 54

4.1 Longitudinal (LO) and transverse optical (TO) phonon energies E and broadenings Γ (errors in parentheses) of ZnO films on Si compared to the bulk for the ordinary (o) and extraordinary (eo) beam. Some films required additional Gaussian (G) oscillators with dimensionless amplitude A, energy E, and broadening Γ (both in cm^{-1}). Parameters marked (f) were adjusted to the infrared portion of the data and then fixed during the fit over the whole range. . . 94

4.2 As Table 4.1, but for ZnO films on SiO_2. The fit is not sensitive to the values shown in italics, which were chosen arbitrarily. 95

4.3 List of samples used in this study with nominal thickness t and results from XRR analysis, including thickness t_{XRR}, interfacial SiO_2 layer thickness $t_{\mathrm{SiO_2}}$ (for ZnO on Si), surface roughness R from XRR, and average electron density ρ_e. For comparison, the bulk ZnO electron density is 1.51 $e/\mathrm{\AA}^3$. The layer thickness t_{SE} determined from ellipsometry is also given. The last two columns list the grain size d and the vertical strain $\epsilon_\perp$ measured with XRD. . . 113

5.1 Phonon parameters at 300 K determined with different models:(1) TO phonon parameters obtained from the Lorentz model by fitting the ellipsometric angles with the experimental errors. ω_{LO} was calculated from Eq. (121). (2) Same, but from fitting only $\langle\epsilon_2\rangle$. (3) LO phonon parameters from a Lorentzian fit to the pseudo-loss function. (4) Results from the Lowndes-Gervais model, Eq. (105). Data from the literature is also shown. Probable errors are listed in parentheses. 162

5.2 Anharmonic decay parameters for Eq. (106) for the temperature dependence of TO and LO phonon broadenings. Errors are shown in parentheses. Energies marked (f) were fixed during the fit, compare Table 5.3. 172

5.3 Anharmonic decay parameters for the temperature dependence of TO and LO phonon energies. Errors are shown in parentheses. . . 176

LIST OF FIGURES

2.1 The working principle of spectroscopic ellipsometry [3]. 4

2.2 Ellipsometric angle Ψ [4]. 6

2.3 Schematic of light reflection and transmission for a thin film on a substrate [5]. 8

2.4 (a) A picture of J.A Woollam UV variable angle spectroscopic ellipsometer (UVVASE), (b) Schematic diagram of the UVVASE. . 10

2.5 A picture of a Xe lamp. 11

2.6 A picture of the HS-190 monochromator. 12

2.7 (a) A picture of the J.A Woollam IR-VASE Mark II ellipsometer (FTIR), (b) Schematic diagram of the FTIR [2]. 14

2.8 Janis ST-400 ultrahigh vacuum (UHV) cryostat mounted on the J. A Woollam IR-VASE Mark II ellipsometer. 18

2.9 Comparison of the dielectric functions of the Lorentzian and the Gaussian oscillators [6]. 20

2.10 Schematic diagram of interband optical absorption and formation of an exciton [122]. 23

2.11 Imaginary (ϵ_2: right axis) part of the complex dielectric function and pseudo-loss function (right axis) of bulk GaP at 300 K versus photon energy. 26
2.12 Schematic illustration of the Bragg condition [7]. 27
2.13 Schematic representation of the in-plane ($\epsilon_{\|}$) and out-of-plane ($\epsilon_{\perp}$) strain in a thin film due to lattice mismatch with the substrate. . 30
2.14 Schematic of total external reflection of the X-ray beam at a planar surface 31
2.15 Scattering vector Q 33
2.16 The basic principle of AFM [12]. 37
3.1 (Color online) Real and imaginary parts of the pseudo-dielectric function for silicon-doped (top) and undoped (bottom) GaAs covered with native oxide. Data from two different instruments were merged. The insets show expanded views of the regions of lattice absorption. Symbols show experimental data, lines the best fit to Eq. (74) with parameters given in Table 3.1. 50

3.2 (Color online) Ellipsometric angle ψ at five angles of incidence for silicon-doped (top) and undoped (bottom) GaAs covered with native oxide in the region of plasmon-polariton absorption (grey). Symbols show experimental data, lines the best fit to Eq. (74) with parameters shown in Table 3.1. The reststrahlen bands are shaded in grey. 51

3.3 (Color online) Real and imaginary parts of the pseudo-dielectric function for undoped c-axis oriented bulk ZnO with 21 Å surface roughness. Data from two different instruments were merged. Points show experimental data, lines the best fit to Eq. (74) with parameters in Table 3.1. 58

3.4 (Color online) Ellipsometric angles ψ and Δ for undoped c-axis oriented bulk ZnO with 21 Å surface roughness in the region of infrared lattice absorption. Points show experimental data, lines the best fit to Eq. (74) with parameters in Table 3.1. 59

3.5 Same data as in Fig. 3.2 for n-type GaAs (top) and undoped GaAs (bottom), but displayed as the loss function $-\mathrm{Im}\,(1/\epsilon)$. The line shows the model, the symbols the data. The LP and UP polariton modes are shown as peaks, shifting and broadening dependent on carrier concentration. 64

3.6 As Fig. 3.1, but for n-type compensated bulk GaSb with an electron density of 4–6×10^{16} cm^{-3}. 65

3.7 As Fig. 3.2, but for n-type compensated bulk GaSb with an electron density of 4–6×10^{16} cm^{-3}. 66

3.8 As Fig. 3.1, but for p-type bulk GaSb with 6 nm native oxide and a hole density greater than 10^{18} cm^{-3}. The lines show the best fit with a single Drude term and fixed TO lattice absorption. 69

3.9 As Fig. 3.2, but for p-type bulk GaSb with a hole density greater than 10^{18} cm^{-3}. The lines show the best fit with a single Drude term and fixed TO lattice absorption. 70

3.10 As Fig. 3.1, but for nominally undoped InAs. Experimental data are shown by symbols (green-$\langle\epsilon_1\rangle$, blue-$\langle\epsilon_2\rangle$). Data from two instruments were merged. The lines show the best fit with Eq. (74), including one plasmon-phonon polariton and a parametric oscillator model to account for interband electronic transitions. The native oxide thickness is 6 nm. 71

3.11 As Fig. 3.2, but for nominally undoped InAs. The lines show the best fit with a single plasmon-phonon polariton to account for free carrier and lattice absorption. 72

3.12 Pseudodielectric function for spinel ($MgAl_2O_4$) with 16.4 Å surface roughness from the mid-IR to the vacuum-UV. Data are shown in green ($\langle\epsilon_1\rangle$) and blue ($\langle\epsilon_2\rangle$), the model fit using Eq. (74) in red. Two Tauc-Lorentz oscillators and a pole define the dispersion in this energy range. 74

3.13 As Fig. 3.12, but for the mid-infrared spectral range of spinel ($MgAl_2O_4$). Seven TO/LO phonon pairs as in Eq. (76) define the dispersion in this energy range. 76

3.14 As Fig. 3.13, but data are displayed as ellipsometric angles ψ (green) and Δ (blue) for four angles of incidence from 60° to 75°. 77

4.1 Ellipsometric angles ψ and Δ for 9 nm ZnO on Si. Symbols: experimental data; solid: best fit with an isotropic model based on Eq. (88). The inset shows a magnified view of the infrared spectral region from 0 to 0.25 eV. 85

4.2 As Fig. 4.1, but for 51 nm ZnO on Si. 86

4.3 As Fig. 4.1, but for 9 nm ZnO on SiO_2. ZnO vibrational features affect the spectra mostly within the ovals. 87

4.4 As Fig. 4.3, but for 50 nm ZnO on SiO_2 with a partially anisotropic model for ZnO. Effects of ZnO anisotropy appear within the rectangular boxes. 88

4.5 Real and imaginary parts of the complex dielectric function for ZnO films on Si versus photon energy. The inset shows a magnified view of the infrared spectral region from 30 to 70 meV. The dotted lines are explained in Sec. 4.8.11. 90

4.6 As Fig. 4.5, but for ZnO on SiO_2 (quartz). 93

4.7 Tauc band gap of ZnO on Si (a) and SiO_2 (b) as a function of layer thickness from ellipsometry (•) and transmission measurements (∘). The dotted line shows the best fit with Eq. 90. 97

4.8 (a) Static dielectric constant ϵ_s calculated from Eq. (88) by setting ω=0 (•, ∘) and calculated from the TO and LO energies using the Lyddane-Sachs-Teller (LST) relation (119) (✦). (b) Thickness dependence of the high-frequency dielectric constant ϵ_∞, determined from the second factor in Eq. (88) by setting ω=0. (c) Born effective charge of the E_1 (•) and A_1 (∘) optical phonon calculated from Eq. (91) for ZnO on Si (blue) and on SiO_2 (red). The lines are drawn to guide the eye. 99

4.9 Transverse optical (E_1 TO) phonon energies versus layer thickness for ZnO on Si and SiO_2 in comparison with bulk ZnO. 105

4.10 Surface roughness of ZnO films on (a) Si and (b) quartz as a function of ZnO thickness. + and ■: unflattened root mean square (RMS) roughness determined from AFM and XRR, respectively; ○: half of the roughness layer thickness obtained from an ellipsometry (SE) model with roughness. (c) Projection of the 3D AFM image for the 51 nm thick ZnO/Si film onto a plane perpendicular to the surface. The white frame shows the EMA surface roughness layer used to model SE data. (d) Same as (c), but for a 5 nm ZnO/Si layer. 112

4.11 X-Ray diffraction pattern for (a) ZnO/Si and (b) ZnO/SiO_2 with different film thickness. 115

4.12 X-ray reflectivity for (a) ZnO/Si with film thickness 5 nm, 9 nm, 19 nm, 37 nm, 51 nm, and 66 nm (b) ZnO/SiO_2 with film thickness 5 nm, 9 nm, 19 nm, 38 nm, 50 nm, and 65 nm. The solid line shows the model data and circles represent the experimental data. The curves were shifted vertically for clarity. The inset shows the electron density versus depth from the x-ray reflectivity fit for one thickness (38 nm). 119

4.13 Ellipsometric angles (a) ψ and (b) Δ for bulk ZnO with 21 Å surface roughness, similar to Ref. 21. Symbols: experimental data; solid: fit using Eq. (99). 120

4.14 (a) Real and (b) imaginary parts of the complex dielectric function for bulk ZnO versus photon energy, determined from the ellipsometric angles in Fig. 4.13 with a partially anisotropic model. Here ϵ_o and ϵ_e are the ordinary and extraordinary dielectric function, respectively 124

4.15 Ellipsometric angles ψ and Δ for a bare single-side polished fused quartz substrate for angles of incidence from 50° to 80° (symbols). The lines show the best fit to a model which describes the quartz optical constants with a sum of Gaussians and poles and which includes a thin surface layer, which has a slightly larger ϵ than the substrate. 125

4.16 Dielectric function of fused (amorphous) quartz, obtained by fitting the ellipsometric angles shown in Fig. 4.15. The insets show the infrared spectra region. 126

4.17 Results from point-by-point fits to determine the optical constants of ZnO on Si for various thicknesses (dashed), in comparison to oscillator fits (solid). The mid-infrared spectral region is not shown, because the data are quite noisy in that range. 128

4.18 As Fig. 4.17, but for ZnO on SiO_2. 129

4.19 Tauc plot extrapolation for bulk ZnO and (a) ZnO on Si (b) ZnO on SiO_2 with different film thickness 131

4.20 Absorption coefficient of ZnO layers with different thicknesses on SiO_2 quartz substrates determined from ellipsometry measurements (solid) and transmission measurements of the same layers with the bare single-side polished quartz substrate as a reference (dotted). 136

4.21 Total dielectric function in the infrared region (solid) in comparison with the contribution from the E_1 phonon given by Eq. (103) (dotted). 138

4.22 Comparison of several sets of optical constants for the Si substrate referenced in the text. 139

4.23 Dielectric functions for ZnO layers on Si with different thicknesses as shown in Fig. 4.17, but with different reference constants for the Si substrate. 141

4.24 As Fig. 4.23, but for the 5 nm ZnO on Si layer. 143

4.25 As Fig. 4.23, but for the 9 nm ZnO on Si layer. 145

4.26 Uniqueness fit (mean standard error versus thickness in Å) for a ZnO layer on Si with a nominal thickness of 5 nm. 147

4.27 Same data as in Fig. 4.26, but shown in a narrower range of thicknesses. 148

4.28 Transient dielectric function of Ge versus photon energy. 149

5.1 Ellipsometric angles (a) ψ and (b) Δ at 300 K in air at 70° angle of incidence (AOI) for bulk GaP with a surface layer. The symbols show experimental data. Solid and dashed lines show the result of a fit using Eq. (105). 158

5.2 (a) Real and (b) imaginary parts of the complex dielectric function of bulk GaP at three different temperatures versus photon energy (dashed), determined from a "point-by-point" fit, in comparison with room temperature results as described in [47] (solid). 160

5.3 (a) Imaginary part of the complex dielectric function for GaP versus photon energy in the region of two-phonon absorption. (b) Absorption coefficient from a high-resolution transmission measurement [59]. Reprinted with permission from [B. Ulrici and E. Jahne, phys. stat. sol. (b) **86**, 517 (1978)]. Copyright [2021], [John Wiley and Sons]. 167

5.4 Temperature dependence of the TO and LO phonon broadenings (symbols). Solid lines show the best fit to our data using Eq. (106) with parameters in Table 5.2. Raman linewidths from Refs. 33, 34 are shown by dashed and dotted lines, respectively. The dashed-dotted lines show results from density-functional perturbation theory [22, 23] 171

5.5 Temperature dependence of the (a) transverse (ω_{TO}) and (b) longitudinal (ω_{LO}) optical phonon energies of GaP (symbols). The dashed line shows the contribution of thermal expansion. Fits using Eqs. (111) and (112) with parameters in Table 5.3 are shown by dashed-dotted lines. 175

5.6 Temperature dependence of the (a) high-frequency (ϵ_∞) and (b) static (ϵ_s) dielectric constants. ϵ_∞ was found by fitting the experimental data with Eq. (105). ϵ_s was calculated from the Lyddane-Sachs-Teller relation (119). Data from the literature [20, 48, 50] are also shown. 179

5.7 Pseudo-loss function for GaP in the reststrahlen region at room temperature (in air) fitted with a Lorentzian as in Eq. (123). . . . 184

5.8 Frequency-dependent scattering rate of GaP at (a) 80 K, (b) 300 K, and (c) 720 K calculated from the Lowndes lineshape in Eq. (105) (solid) and from our experimental (point-by-point fit) data (dashed) in Fig. 5.2. 186

5.9 Ellipsometric angles (a) ψ and (b) Δ, (c) imaginary part $\langle\epsilon_2\rangle$ of the pseudo-dielectric function, and (d) pseudo-loss function $-\langle\eta_2\rangle$ versus photon energy for GaP at 80 K (symbols) fitted with two different Lorentz models (blue, green) with different broadening parameters. A Lowndes fit (red) is also shown. The pseudo-loss function is also fitted with a Lorentzian, compare Eq. (123), shown by the brown line. 189

5.10 Same as Fig. 5.9, but at 300 K (inside the cryostat). The parameters are slightly different from Fig. 5.7. 190

5.11 Same as Fig. 5.9, but at 720 K. 190

5.12 Optical penetration depth for GaP in the reststrahlen region as a function of photon energy. 195

5.13 Phonon dispersion curves for GaP, calculated using a ten-parameter shell model [28] 196

5.14 Doping dependence of the ellipsometric angle ψ for bulk GaP at room temperature and 70° angle of incidence. 199

5.15 Intrinsic carrier concentration of GaP as a function of temperature calculated from Eq. (136). 200

5.16 Temperature dependence of the Born effective charge calculated from Eq. (138) for bulk GaP. 201

5.17 Variation of the apparent GaP surface layer thickness with temperature. 205

1 INTRODUCTION

ZnO is a direct wide band gap ($E_g \approx 3.37$ eV at room temperature) [116] II-VI compound semiconductor material. It crystallizes in the wurtzite structure. This is the most stable crystalline state of ZnO under ambient conditions [1]. Due to its unique properties, this thermally and chemically stable material has a large number of applications in optoelectronics and photonics industry. Owing to its large excitonic binding energy (60 meV) ZnO has been identified as a potential candidate for short-wavelength optoelectronic devices, such as UV light-emitting diodes and laser diodes [106]. ZnO has also been seen as an ideal semiconductor material for thin film transistors, solar cells, gas sensors, high power, high temperature electronics [106]. Therefore, it is very important to have a universal description and better understanding of the optical properties of this semiconductor. In this thesis, I have explicitly described how the optical properties of bulk and ZnO thin films change with the film thickness and the substrate material.

In this work, I also investigated the temperature dependence optical phonon bands in GaP. This is another fascinating III-V indirect bandgap ($E_g \approx 2.25$ eV at room temperature) [26, 27] semiconductor material which crystallizes in the zinc blende structure. Like ZnO, this thermally stable wide bandgap material is an excellent semiconductor material for optoelectronics and photonics applications, especially in light-emitting diodes (LEDs) [31], detectors, solar cells, and high-

temperature transistors [27]. Therefore, studying the temperature dependence of optical phonon energies and linewidths of GaP is valuable for its application in optoelectronic and photonic devices to achieve their best performance.

2 Experimental and theoretical methods

2.1 Variable Angle Spectroscopic Ellipsometry (VASE)

Spectroscopic Ellipsometry or simply "SE" is the most commonly used inline process control tool in the semiconductor industry. SE is a fast and accurate optical technique for studying the dielectric properties of materials, specially for thin film and multi layered materials. This technique is mainly used to measure optical constants (refractive index (n), extinction coefficient (k), or complex dielectric constants ϵ_1, ϵ_2) and film thickness. It is also used to describe surface roughness, doping concentration, electrical conductivity, material composition [2], etc. It is a very flexible optical tool and can be used to determine the optical properties of all types of materials, such as semiconductors, dielectrics, metals, polymers, etc.

2.1.1 How spectroscopic ellipsometry (SE) works

The basic principle of SE is to measure the change of the polarization state of the light beam as it reflects or transmits from a sample surface. As shown in Figure 2.1, the polarization state of the incoming beam is linear with both s and p components (s component: electric field of the light waves oscillates perpendicular to the plane of incidence and p component: electric field of the light waves oscillates parallel to the plane of incidence). This linearly polarized light beam interacts with the sample surface and then it will reflect. The reflected light beam

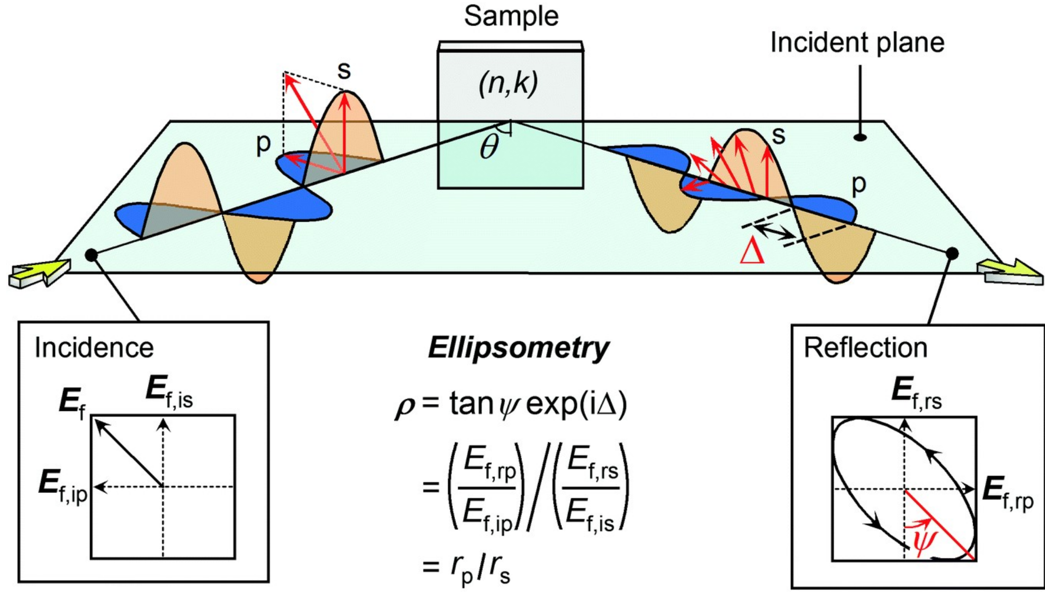

Figure 2.1: The working principle of spectroscopic ellipsometry [3].

is elliptically polarized.

This interaction between the material surface and the light beam induces a phase difference and an amplitude difference between the p and s polarized light. SE measures this amplitude ratio and phase difference between the p and s polarized light waves as ellipsometric angles Ψ and Δ, respectively. The amplitude of the reflected p and s components are represented as r_p and r_s. The Fresnel's equations describe the r_p and r_s (Fresnel reflection coefficients) [46],

$$r_p = \frac{E_{rp}}{E_{ip}} = \frac{n_t cos\theta_i - n_i cos\theta_t}{n_t cos\theta_i + n_i cos\theta_t}, \tag{1}$$

$$r_s = \frac{E_{rs}}{E_{is}} = \frac{n_i cos\theta_i - n_t cos\theta_t}{n_i cos\theta_i + n_t cos\theta_t}. \tag{2}$$

The subscripts i, r, and t denote incident, reflected, and transmitted light respectively. E_p is the amplitude of the electric field which is vibrating parallel to the plane of incidence and E_s is the amplitude of the electric field which is vibrating perpendicular to the plane of incidence. n is the refractive index. θ_i and θ_t represent the angle of incidence and angle of transmission respectively. The ellipsometric angles Ψ and Δ are related to the Fresnel reflection coefficients as,

$$\rho = tan\Psi * e^{i\Delta} = \frac{r_p}{r_s} \tag{3}$$

Ellipsometric angle Δ

The ellipsometric angle Δ is the change of the phase difference between the p and s polarized light waves. If we define the phase difference between the p and s polarized light waves before the reflection as δI and after the reflection as δF. Then we can define Δ as,

$$\Delta = \delta F - \delta I \tag{4}$$

Ellipsometric angles Ψ

Figure 2.2 shows how the ellipsometric angle Ψ is related to the Fresnel reflection coefficients r_p and r_s. The amplitude ratio tanΨ of r_p and r_s is a real number and the ellipsometric angle Ψ can change from 0 to 90°.

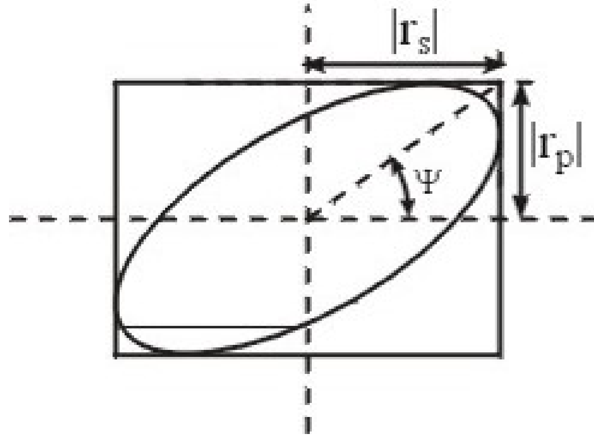

Figure 2.2: Ellipsometric angle Ψ [4].

2.1.2 Pseudodielectric function

In the case of bulk isotropic materials with no surface layer (ex: surface roughness, a native oxide layer, etc.) we can directly convert the measured ellipsometric angles Ψ and Δ into the pseudodielectric function ($\langle\epsilon_1\rangle$) as [45],

$$\langle\epsilon_1\rangle = \langle N^2\rangle = sin^2\theta_i\left[1 + tan^2\theta_i\left(\frac{1-\rho}{1+\rho}\right)\right], \quad (5)$$

where θ_i is the angle of incidence. In general, material surfaces are not perfectly flat. Sometimes these surfaces are rough or sometimes there is a surface oxide layer. To obtain the thickness and the actual optical constants, we must construct a model to describe the sample. Here we mainly study the dielectric constants (ϵ_1, ϵ_2) of materials. These real (ϵ_1) and imaginary (ϵ_2) parts of the complex dielectric function ($\epsilon\ (\omega)$) are related to energy stored and lost (absorption) in the material.

$$\epsilon(\omega) = \epsilon_1(\omega) + i\epsilon_2(\omega) \tag{6}$$

This complex dielectric function is related to the refractive index N (this is also a complex function) as [122],

$$N = \sqrt{\epsilon} \tag{7}$$

where N=n+ik [122]

From Eqs. (6) and (7),

$$\epsilon_1 = n^2 - k^2, \tag{8}$$

$$\epsilon_2 = 2nk, \tag{9}$$

where k is the extinction coefficient which is related to the absorption coefficient through [122],

$$\alpha = \frac{4\pi k}{\lambda}, \tag{10}$$

where λ is the wavelength of the light.

2.1.3 SE and thin films

Eqs. (1) and (2) describe the amount of light reflected at an interface between materials. In the case of a thin film (Figure 2.3) and multi-layered materials (more

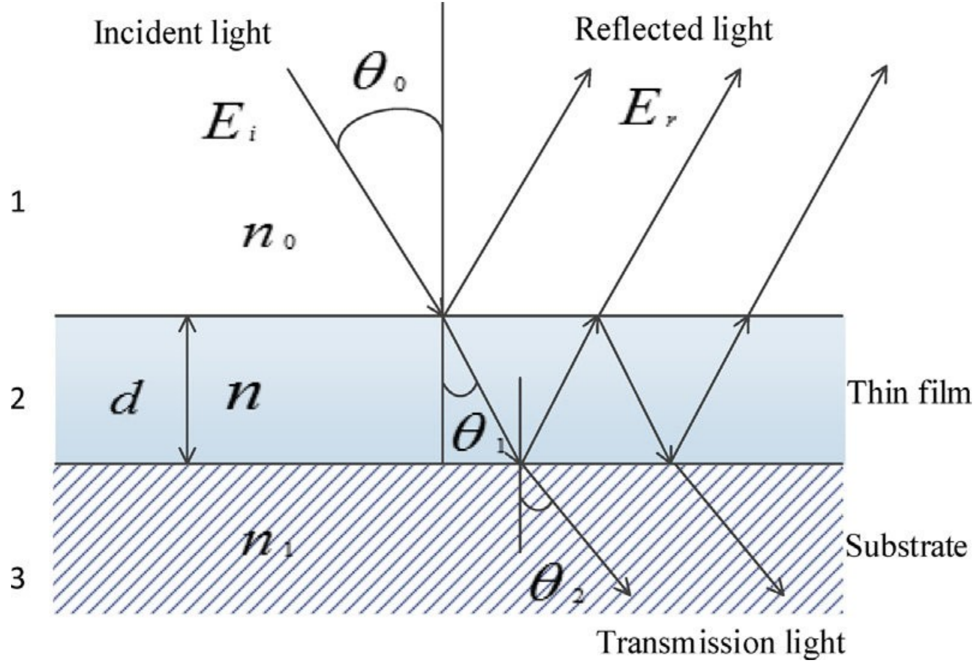

Figure 2.3: Schematic of light reflection and transmission for a thin film on a substrate [5].

than one reflection), the p and s Fresnel reflection coefficients should be modified as below [45],

$$r_p = \frac{r_{p,12} + r_{p,23}e^{-i2\beta}}{1 + r_{p,12}r_{p,23}e^{-i2\beta}}, \tag{11}$$

$$r_s = \frac{r_{s,12} + r_{s,23}e^{-i2\beta}}{1 + r_{s,12}r_{s,23}e^{-i2\beta}}, \tag{12}$$

$$\beta = 2\pi\frac{d}{\lambda}ncos\theta_0, \tag{13}$$

where d and n are the thickness and refractive index of the thin film respectively.

2.1.4 Data acquisition and basic optical components used in UV and IR spectroscopic ellipsometry: UVVASE & FTIR

A) UVVASE Figure 2.4 shows the J.A. Woollam variable angle spectroscopic ellipsometer. This allows to measure the ellipsometric angles Ψ and Δ from 0.5 to 6.5 eV (near-infrared to deep ultraviolet) at different angles of incidence. The choice of the angle of incidence is very important. In order to get more accurate results with the least errors, the angle of incidence is chosen around an angle called Brewster angle which depends on the refractive index of the two media. At this Brewster angle, the reflected light is completely s polarized and the p polarized component of the reflected light is equal to zero (r_p=0). This difference between r_p and r_s increases the sensitivity of the results. So the variation of the ellipsometic angles is larger near the Brewster angle [45].

A.1) Light source: A Xenon (Xe) lamp is used in our ellipsometer. It covers the wavelength ranging from the near infrared to the deep ultraviolet (0.5 to 6.5 eV). Unlike conventional lamps with a filament, Xe lamps are more stable and long lasting.

A.2) Monochromator: A Monochromator is a high precision wavelength selection optical device. For the VASE we use a HS-190 high throughput monochromator (Figure 2.6) which is placed before the sample. This black box contains

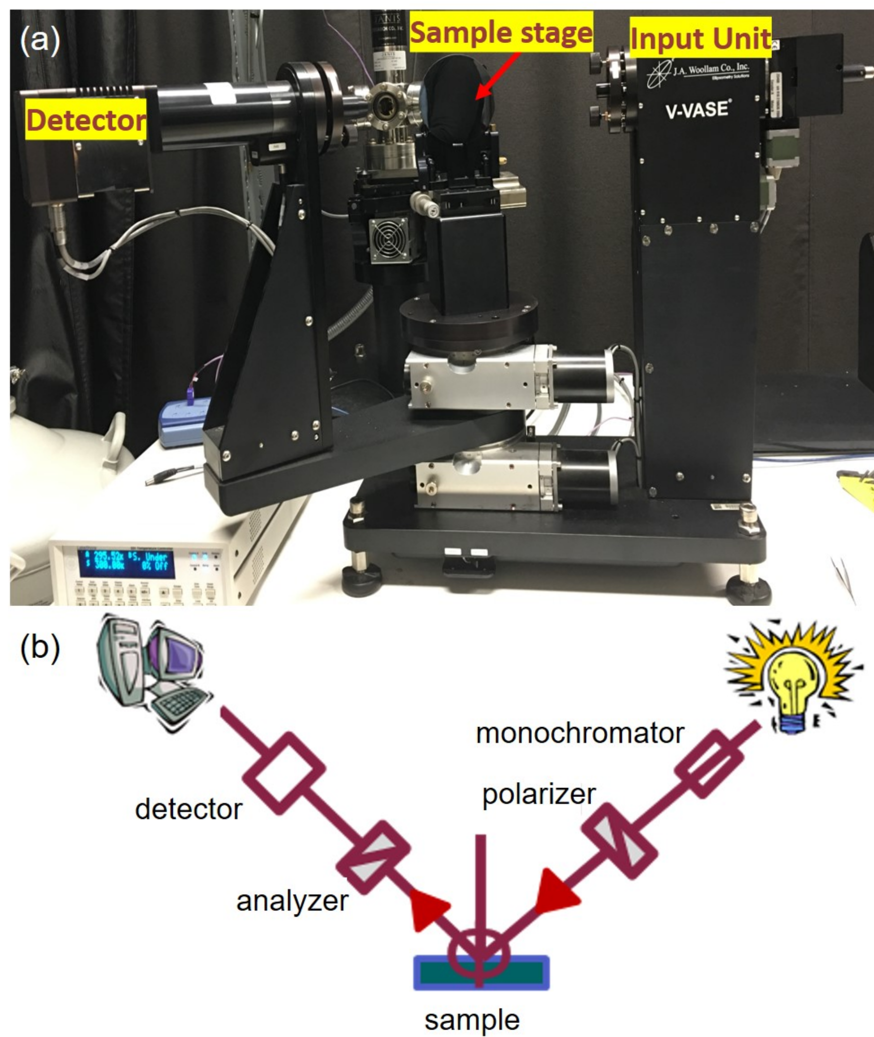

Figure 2.4: (a) A picture of J.A Woollam UV variable angle spectroscopic ellipsometer (UVVASE), (b) Schematic diagram of the UVVASE.

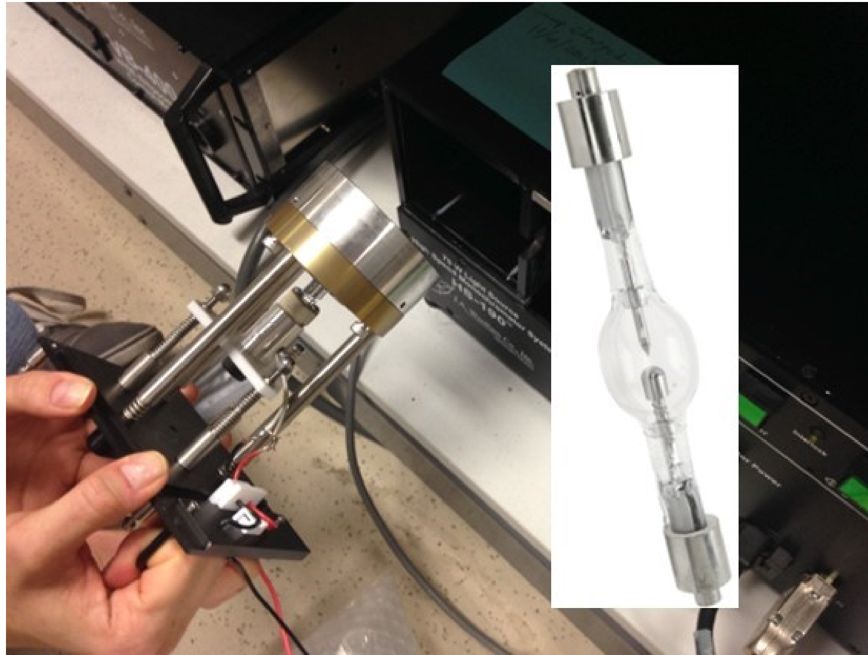

Figure 2.5: A picture of a Xe lamp.

turrets with gratings, slits, choppers, filter wheels, etc. This optical device is placed with the Xe light source and it optimizes the accuracy of the wavelength.

A.3) Optical Fiber: The unpolarized light coming from the Xe lamp first passes through the optical elements of the monochromator. Then this modulated beam couples with the input unit of the ellipsometer via a fiber optic cable.

A.4) Polarizer: The light beam entering the input unit of the ellipsometer through the fiber optic cable is randomly polarized (unpolarized). This unpolarized light beam passes through the polarizer and is converted into linearly polarized light.

Figure 2.6: A picture of the HS-190 monochromator.

A.5) Alignment detector: An alignment detector is a four-quadrant silicon detector that is used to align the sample to the beam. This detector is removable and placed after the polarizer. If the sample is perfectly aligned (perpendicular to the beam), the signal from each of the four quadrant displayed in the alignment screen should be equal.

A.6) Sample stage: The J.A. Woollam Vase is designed with a vertical sample stage which has small vacuum holes in it. These vacuum holes hold the sample during data acquisition. This design allows a variety of data acquisition geometries such as transmission, reflection, etc.

A.7) Analyzer: The analyzer is another important optic used in the VASE. This is similar to the polarizer in the input unit. Both the polarizer and the

analyzer change the polarization state of the light beam. However, the polarizer is fixed, and the analyzer rotates during the data acquisition. This design enhances the sensitivity and accuracy of the data.

A.8) Detector: Our ellipsometer has two types of photodiode detectors. One is a Si photodiode detector, and the other detector is made from InGaAs. Depending on the wavelength range, these two detectors are switched. The Si detector is sensitive in the visible and ultraviolet wavelength range (1.1-6.5 eV) and the InGaAs detector is used at low energies.

B) Fourier Transform Infrared Spectroscopic Ellipsometer (FTIR SE) Figure 2.7 shows the J. A Woollam IR-VASE Mark II ellipsometer. Similar to the UVVASE, the IR-VASE also has a wide range of optical characterization capabilities. In this work, we used the FTIR ellipsometer to study phonon absorption. The FTIR measures the ellipsometric angles Ψ and Δ from 0.03 to 0.8 eV at different angles of incidence.

As shown in Figure 2.7, the FTIR ellipsometer includes a light source, moving and fixed mirrors, a beam splitter, polarizers, a sample stage, a rotating compensator, and a detector.

B.1) Source: A hot piece of Silicon carbide (SiC), simply known as a globar, is used in the J.A Woollam IR-VASE Mark II ellipsometer as the IR light source.

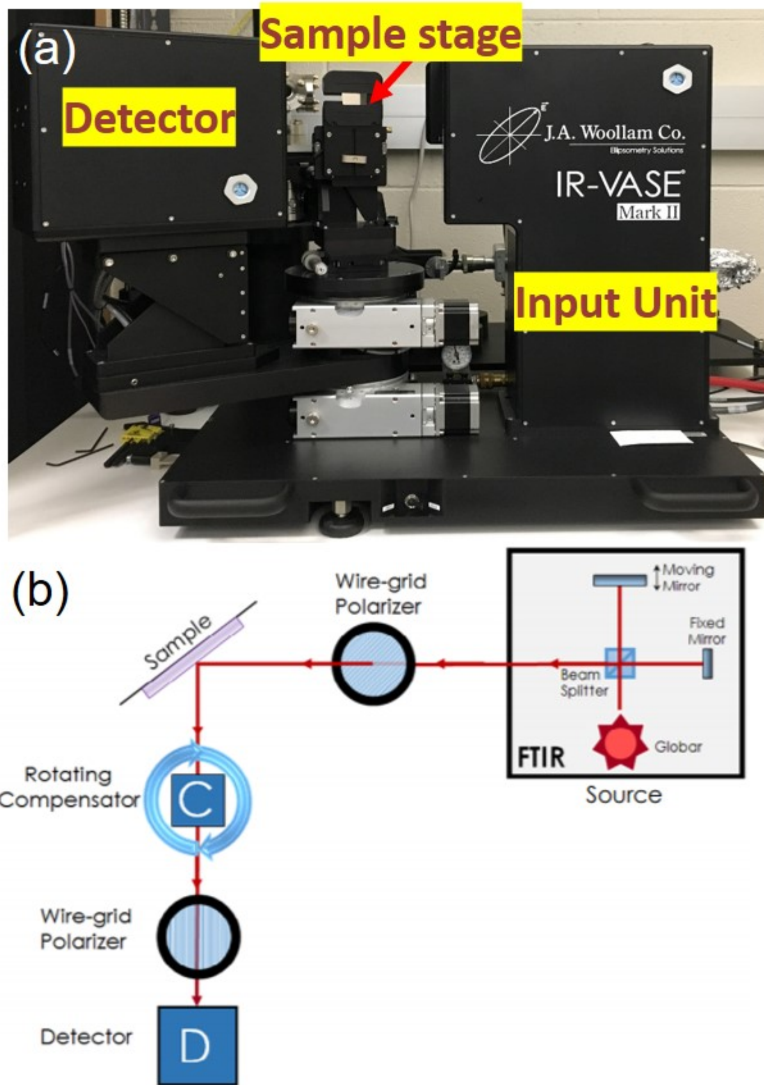

Figure 2.7: (a) A picture of the J.A Woollam IR-VASE Mark II ellipsometer (FTIR), (b) Schematic diagram of the FTIR [2].

This is a U-shaped rod and produces IR radiation when it is hot. This globar is normally operated at 1300 K and is expected to last about a year.

B.2) Beam splitter and mirrors: The IR radiation coming from the glorbar strikes the beam splitter and then it is divided into two beams. These two beams reach the fixed and moving mirrors which are made of highly reflective materials and then reflect back to the beam splitter. This produces an interference pattern.

B.3) Wide-grid polarizer As mentioned earlier the polarizer changes the polarization state of the light beam.

B.4) Rotating compensator A compensator is another optical element used in the FTIR ellipsometer. During the data acquisition, the compensator is rotated overa $360°$ range to provide accurate results of the ellipsometric angles Ψ and Δ.

B.5) Detector A deuterated triglycine sulfate (DTGS) thermal detector is used in the IR-VASE Mark II ellipsometer. This is a low sensitivity room temperature detector.

2.1.5 Temperature dependent ellipsometry

The temperature dependent measurements were performed inside a Janis ST-400 ultrahigh vacuum (UHV) cryostat at 70° angle of incidence. In order to achieve a sufficiently low base pressure of 10^{-9} to 10^{-8} Torr for the temperature scans, an Agilent dry scroll roughing pump and a turbo pump were used. A second roughing pump was attached to the cryogen space for high temperature measurements (above room temperature) to protect the cryogen space from corrosion. Based on the experimental requirement we use two types of windows. Diamond windows are used for the low energy range measurements (transparent range: 0.01-5.4 eV). The other type of window we use is ZnSe (transparent range: 0.06-1.7 eV). Figure 2.8 shows the FTIR ellipsometer with the ST-400 cryostat installed at the position of the sample stage. The ST-400 UHV cryostat is designed for low and high temperature measurements. This system allows us to measure samples from 4 K (liquid helium) to 800 K. A Lakeshore 335 temperature controller was used to control the temperature. The temperature was measured with two type-E (nickel-chromium/constantan) thermocouples. One thermocouple located near the cryogen reservoir was used to control the temperature with the Lakeshore temperature controller. The second thermocouple was directly attached to the surface of the sample and measured the temperature of the sample surface. The difference between both thermocouple readings depends on the sample and increases

with increasing temperature. A detailed explanation of the data acquisition steps and the experimental procedure are explained in the experimental methods and models section (section II) in chapter 5.

2.1.6 SE data modeling

We use WVASE32 software for the ellipsometric data analysis. This is a very fast, accurate, and powerful software package.

Oscillator Models The oscillator model is the most common ellipsometry data modeling method for bulk materials or simple multilayered systems. There are different types of oscillator functions that can describe the frequency dependent complex dielectric function. The selection of the oscillator type depends on the material (metal, insulator, etc) and the type of charges present in the materials. The key point of this oscillator model is the direct connection between the real and imaginary parts of the complex dielectric function which is known as Kramers-Kronig consistent (KK consistent).

A) Gaussian Oscillator: This oscillator describes the imaginary part of the complex dielectric function (ϵ_2: Im[G(ω)]) with three main parameters [6],

$$Im[G(\omega)] = Ae^{-\left(\frac{\omega-E}{\sigma}\right)^2} - Ae^{-\left(\frac{\omega+E}{\sigma}\right)^2} \tag{14}$$

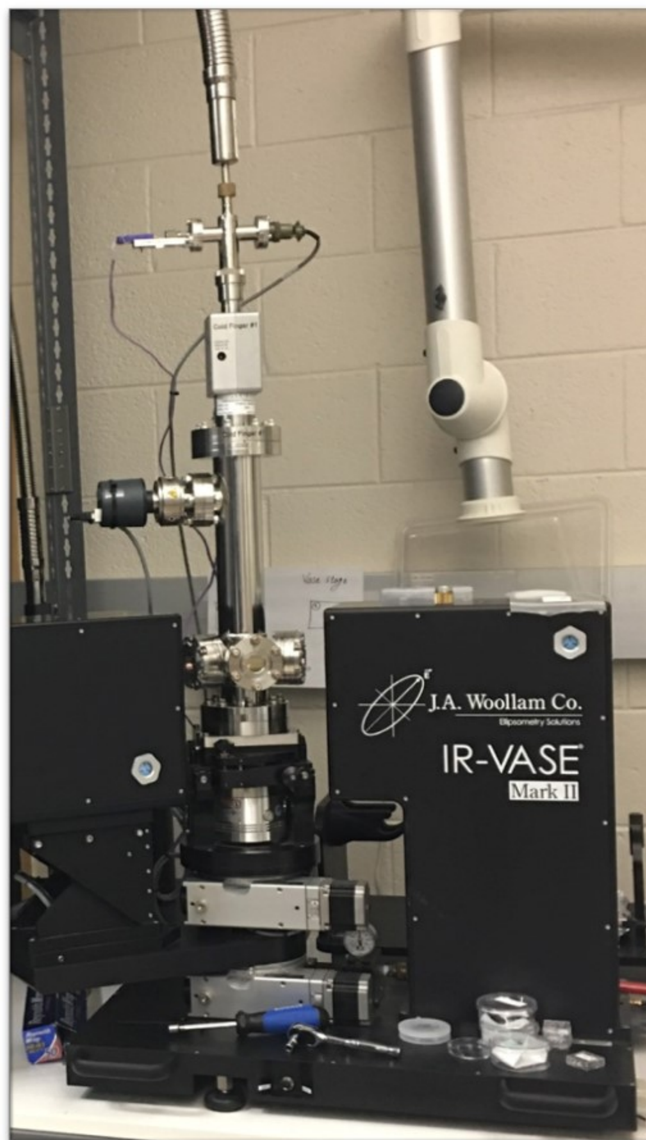

Figure 2.8: Janis ST-400 ultrahigh vacuum (UHV) cryostat mounted on the J. A Woollam IR-VASE Mark II ellipsometer.

where A is the dimensionless amplitude, E the center energy (resonance frequency), and the full width at half maximum (FWHM broadening) Γ is defined as

$$\Gamma = 2\sigma\sqrt{(ln2)}, \tag{15}$$

where σ is the standard deviation.

The real part is calculated from the KK relation. Mostly this oscillator function is used to define the UV and IR absorptions in amorphous materials.

B) Lorentz model [46] The dispersion due to damped vibrations of molecules in a solid under the influence of an electromagnetic wave can be described by a Lorentz oscillator. The shape of the Lorentz oscillator is similar to the Gaussian oscillator. However, the Gaussian oscillator reaches zero faster than the Lorentz oscillator. Figure 2.9 compares the ϵ_1 and ϵ_2 of the Lorentzian and the Gaussian oscillators.

This Lorentz model is a pure classical model. If we consider a bound electron with charge q in an electric field ($E(t)=E_0e^{-i\omega t}$), the equation of motion of can be written as,

$$qE - kx - bv = ma, \tag{16}$$

where E_0 is the amplitude of the electric field, m is the mass of the charge, b is

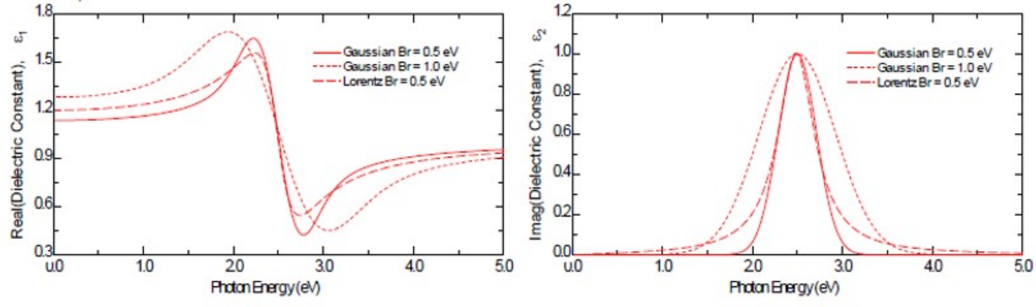

Figure 2.9: Comparison of the dielectric functions of the Lorentzian and the Gaussian oscillators [6].

the damping constant (b=γm), and k is the strength of the restoring force. We can define k as,

$$k = m\omega_0^2, \tag{17}$$

where ω_0 is the resonance frequency (natural angular frequency) of the charge. By substituting x(t) = $x_0e^{-i\omega t}$ we can rewrite the Eq.(16) as

$$qE_0 - kx_0 + ib\omega x_0 = -m\omega^2 x_0. \tag{18}$$

We can define the polarization

$$P(t) = qnx(t) = \epsilon_0\chi(\omega)E(t), \tag{19}$$

where n is the charge density per unit volume which is related to the plasma frequency ω_p as

$$\omega_p = \sqrt{\frac{nq^2}{m\epsilon_0}}. \tag{20}$$

From Eqs. 18 and 19, the dielectric susceptibility can be interpreted as,

$$\chi(\omega) = \frac{-q^2 n}{\epsilon_0(m\omega^2 + ib\omega - k)} \tag{21}$$

Finally, the Lorentz model defines the complex dielectric function as

$$\epsilon(\omega) = 1 + \chi(\omega) = 1 + \frac{\omega_p^2}{\omega_0^2 - \omega^2 + i\gamma\omega} \tag{22}$$

C) Drude model The Drude model is used to describe free carrier absorptions in metals, conductive dielectrics, and doped semiconductors. For free carriers, there is no restoring force. Therefore, we can get the Drude model by substituting k=0 (ω_0=0) into the Lorentz dielectric function,

$$\epsilon(\omega) = 1 - \frac{\omega_p^2}{\omega^2 - i\gamma\omega}. \tag{23}$$

D) Tauc–Lorentz oscillator As we discuss in this section, different oscillators are used for different types of absorption. The Tauc-Lorentz oscillator is one of the common oscillators used to describe the electronic transitions of semiconductor materials. This oscillator is primarily used for amorphous semiconductor materials. Unlike the Gaussian and Lorentz oscillators which are symmetric

around the resonance frequency, the Tauc-Lorentz oscillator is capable to define the asymmetric shapes in ϵ_2 with an additional band gap (E_g) parameter.

If ($E>E_g$) [106]

$$\epsilon_2(\omega) = \frac{AE_0C(E-E_g)^2}{(E^2-E_0^2)^2+C^2E^2}.\frac{1}{E} \tag{24}$$

$\epsilon_2(\omega)=0$, if ($E \leq E_g$).

The real part of the complex dielectric function (ϵ_1) can be extracted from the KK relation [106].

$$\epsilon_1(\omega) = \epsilon_\infty + \frac{2P}{\pi}\oint \frac{\zeta\epsilon_2(\zeta)}{\zeta^2-E^2}d\zeta \tag{25}$$

A is the amplitude of the oscillator, C is the broadening and E_0 is the energy of the peak.

2.1.7 Excitons

As shown in Figure 2.10 the absorption of a photon with energy $\hbar\omega$ can excite an electron from the valence band into the conduction band. This transition creates a hole in the valence band and an electron in the conduction band. This positively charged hole and the negatively charged electron attract each other through the Coulomb interaction and create an electron-hole pair. The bound state of the electron-hole pair is known as an exciton.

Among the two main types of excitons (Wannier-Mott and Frenkel excitons) I studied the absorption of Wannier-Mott excitons also called free excitons from

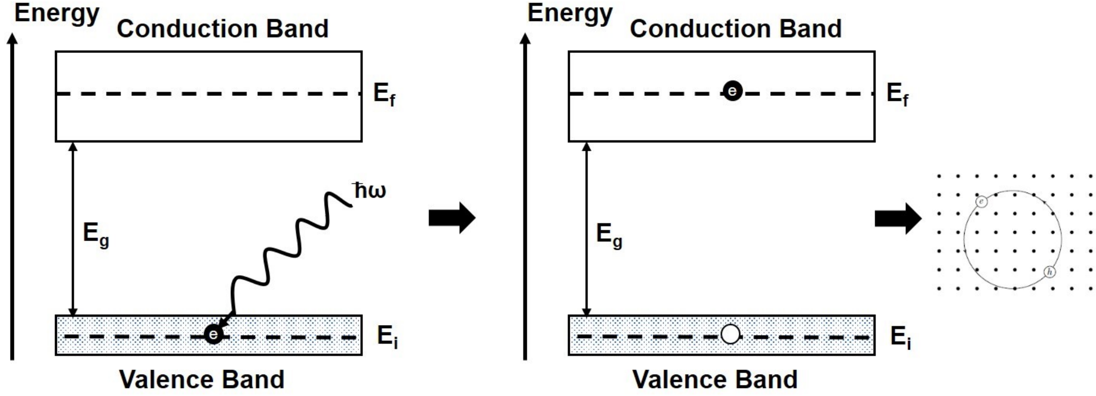

Figure 2.10: Schematic diagram of interband optical absorption and formation of an exciton [122].

the dielectric function as explained in chapter 4.

If the excitonic binding energy (Eq. 26) [122] is greater than k$_B$T (average energy of a thermally excited phonon at temperature T), free excitonic absorption is visible in the dielectric function which is obtained through the spectroscopic ellipsometer. We observe a series of bound states with energies

$$E_n = E_g - \frac{R_X}{n^2}, \tag{26}$$

where the excitonic binding energy R_X is given by [122]

$$R_X = \left(\frac{\mu}{m_0 \epsilon_r^2}\right) R_H, \tag{27}$$

where E$_g$ is the band gap, R$_H$ is the Rydberg energy of the hydrogen atom (13.6 eV), μ is the excitonic reduced mass of the electron and hole, m$_0$ is the free electron

mass and ϵ_r is the relative dielectric constant.

2.1.8 Quantum Confinement

The change of electronic and optical properties of a material with size is a consequence of quantum confinement. This effect is observed only in very small crystals (the size of the particle is very small). According to the Heisenberg uncertainty principle, the uncertainly in the position Δx (confine a particle in Δx) introduces an uncertainly in the momentum Δp [122]

$$\Delta p_x \approx \frac{\hbar}{\Delta x}. \tag{28}$$

This momentum uncertainty leads to an additional kinetic energy (confinement energy) as expressed in Eq. 29 [122].

$$E_{confinement} \approx \frac{\hbar^2}{2m(\Delta x)^2} \tag{29}$$

This phenomenon is briefly described in the chapter 4 for thin films. As we change the thickness of the thin films the band gap changes. The confinement model for thin films can be expressed as [122]

$$E_g(t) = E_{g,\infty} + \frac{F}{t^2} - \Delta E, \tag{30}$$

where E_g is the band gap of the bulk material, t is the layer thickness, F is

the confinement factor (equal to $\hbar^2\pi^2/2\mu_{eh}$ for infinitely high barriers, where μ_{eh} is the electron-hole reduced effective mass), and ΔE is a thickness-independent difference between the bulk and layer band gap.

According to the Eq. 30, the band gap can be controlled by the thickness of the thin film. This concept is very important for practical applications.

2.1.9 Optical phonons

Phonons are vibrations of the atoms in a solid about the equilibrium position. If we consider a unit cell which contains more than one atom, then the crystal contains two types of phonons. One is the low energy vibrations (translation) or simply known as acoustic phonons and the other type is the higher energy vibrations or simply optical phonons. In this thesis, I mainly focus on phonon modes that interact directly with light which are known as infrared active optical phonons. These phonons absorb light at their resonance frequency which occurs in the infrared spectral region. Depending on the direction of the displacement, these optical phonon modes are divided into transverse optical (TO-displacement perpendicular to the direction of propagation) and longitudinal optical (LO-displacement parallel to the direction of propagation) phonon modes. As shown in Figure 2.11 a TO phonon appears as a strong peak in the imaginary part of the complex dielectric function (ϵ_2) and an LO phonon appears as a strong peak in the loss function.

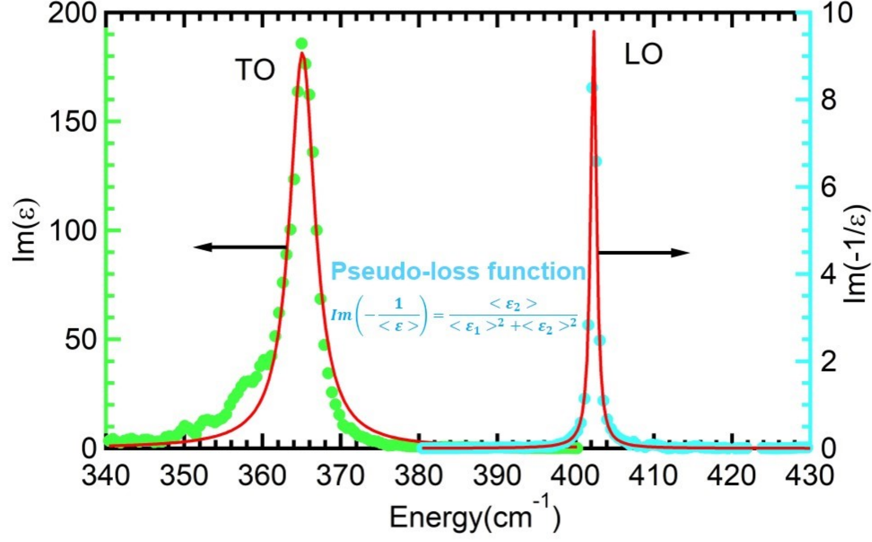

Figure 2.11: Imaginary (ϵ_2: right axis) part of the complex dielectric function and pseudo-loss function (right axis) of bulk GaP at 300 K versus photon energy.

Lowndes–Gervais model The Lorentzian (section 2.1.6) or Lowndes–Gervais models can be used to extract the optical phonon parameters (amplitude A, TO and LO phonon energies ω_{TO} and ω_{LO}, and corresponding broadenings γ_{TO} and γ_{LO}) and the static and high-frequency dielectric constants ϵ_s and ϵ_∞. As explained, the Lorentz model has only one broadening parameter, while the Lowndes-Gervais model assigns two different broadening parameters γ_{TO} and γ_{LO} to the two phonons. the Lowndes–Gervais model describes the complex dielectric function as [14, 18]

$$\epsilon(\omega) = \epsilon_\infty \frac{\omega_{LO}^2 - \omega^2 - i\gamma_{LO}\omega}{\omega_{TO}^2 - \omega^2 - i\gamma_{TO}\omega}. \tag{31}$$

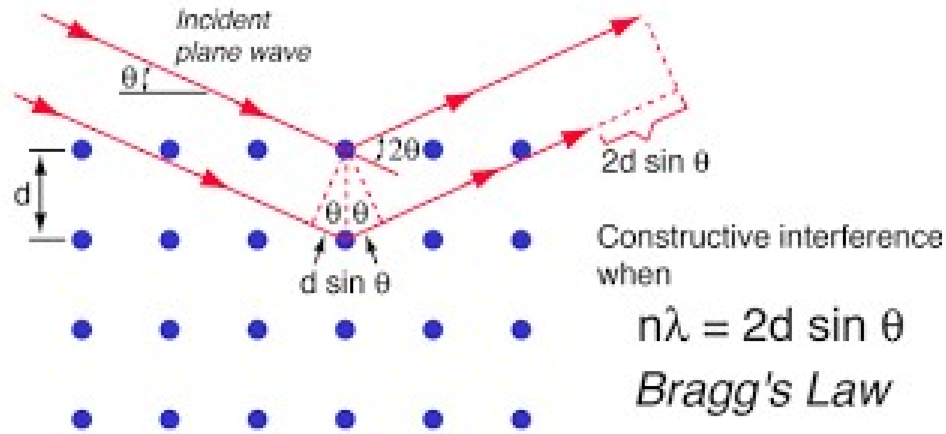

Figure 2.12: Schematic illustration of the Bragg condition [7].

The static dielectric constant can be obtained from the Lyddane–Sachs–Teller (LST) relation [17]

$$\epsilon_s = \epsilon_\infty \frac{\omega_{LO}^2}{\omega_{TO}^2}. \tag{32}$$

2.2 X-ray powder diffraction (XRD)

X-ray powder diffraction (XRD) is the most commonly used rapid powerful non-destructive structural characterization technique. This method has been used extensively to characterize the crystal structure, lattice constant, preferred orientation, grain size, and out-of-plane strain.

The basic principle of this technique is the monochromatic X-ray beam directed toward the sample. Since the wavelength of this incoming x-ray beam and the atomic spacing of the crystal have the same order of magnitude, these X-rays get diffracted. For a crystalline material (long-range order of atoms) these

diffracted beams undergo constructive or destructive interference. When Bragg's Law is satisfied, they interfere constructively and produce a diffraction pattern. Since every crystalline material produces its own diffraction pattern, X-ray powder diffraction is considered a fingerprint of materials.

Bragg's law states that

$$2dsin\theta = n\lambda, \tag{33}$$

where d is the spacing between atomic planes, θ is the angle of incidence, λ is the wavelength of the X-ray beam, and n is an integer that represents the order of reflection. The lattice spacing d=a/$\sqrt{h^2 + k^2 + l^2}$ for a cubic lattice. Where a is the out-of-plane lattice constant, and h, k, l are Miller indices of the Bragg planes.

The PANalytical Empyrean diffractometer operated in line focus mode with 45 kV anode voltage and a 40 mA beam current producing Cu Kα radiation with wavelength 1.5419 Å, was used for the powder X-ray diffraction of thin films explained in chapter 4. Symmetric 2θ-ω scans were performed with a Bragg-Brentano HD (BBHD) optical module and a PIXcel1D Medipix3 array detector to investigate the grain height of polycrystalline thin films, preferred orientation, and vertical lattice strain ($\epsilon_{\perp}$).

Scherrer Formula From the full width at half maximum (FWHM) of the powder diffraction pattern, the grain height of polycrystalline thin films can be determined [8].

$$t = \frac{K\lambda}{\beta cos\theta}. \tag{34}$$

This is known as the Scherrer formula. Where K is the dimensionless shape factor. This is a function of the shape of the crystallite and normally K is 0.9 (0.89 and 0.94 for spherical and cubic crystallites respectively [9]). λ is the X-ray wavelength. θ is the Bragg angle. β is the FWHM of the Bragg peak (plotted as a function of 2θ, after subtracting the instrumental broadening) in radians.

Strain The vertical lattice strain ($\epsilon_\perp$: Figure 2.13) can be calculated from the out-of-plane lattice constant of the layer and the bulk lattice constant as below

$$\epsilon_\perp = \frac{a_\perp}{a_{bulk}} - 1. \tag{35}$$

The out-of-plane lattice constant ($a_\perp$) can be calculated from the position of the Bragg peak in symmetric 2θ-ω scan and Bragg's law.

$$a_\perp = \frac{n\lambda\sqrt{h^2 + k^2 + l^2}}{2sin\theta} \tag{36}$$

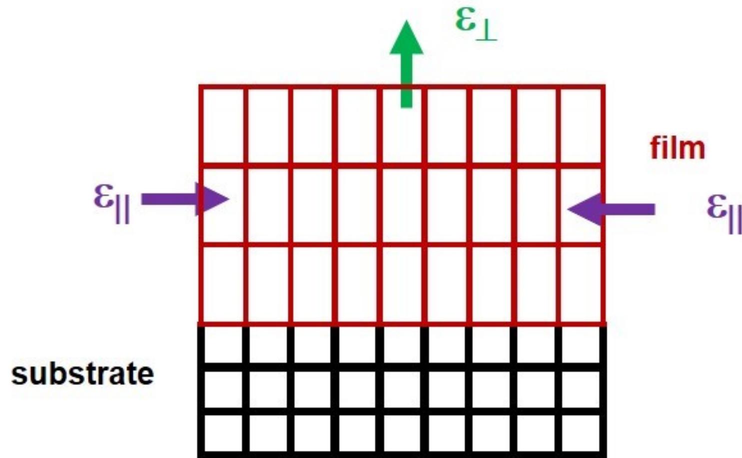

Figure 2.13: Schematic representation of the in-plane ($\epsilon_{||}$) and out-of-plane ($\epsilon_{\perp}$) strain in a thin film due to lattice mismatch with the substrate.

2.3 X-ray reflectance (XRR)

Thin films have been used in many optoelectronic and photonic devices, such as thin film transistors, solar cells, light emitting diodes, etc. Film thickness is one of the key parameters in these applications. This is because most properties of thin films vary with the film thickness. Hence determination of film thickness is very important for these applications. Among many surface characterization techniques, X-ray reflectivity or simply XRR is a more accurate non-destructive method for thin film characterization. Detailed surface properties of thin films such as thickness, surface, and interface roughness, and electron density profile can be obtained using the XRR technique. XRR is more accurate than electron microscopy.

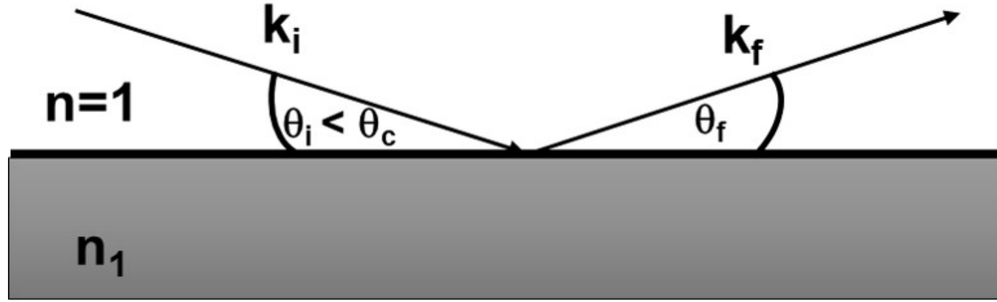

Figure 2.14: Schematic of total external reflection of the X-ray beam at a planar surface

In the case of X-ray reflection, we define the incident angle as the angle between the sample surface and the incoming X-ray beam. This is known as the grazing angle. When this grazing angle is smaller than the critical angle (θ_c) (Eq. 40) the X-ray beam undergoes total external reflection (Figure 2.14). This is because the refractive index of a material is slightly less than 1 at X-ray wavelengths (Eq. 37) [10].

$$n_1 = 1 - \delta + i\beta, \tag{37}$$

$n > n_1$

where δ and β explain the wavelength dependent scattering and absorption respectively.

$$\delta = \frac{\lambda^2 r_e}{2\pi}\rho_e, \tag{38}$$

$$\beta = \frac{\lambda}{4\pi}\mu, \tag{39}$$

where r_e is the classical electron radius. $r_e=\frac{1}{4\pi\epsilon_0}\frac{e^2}{m_e C^2}=2.8*10^{-15}$ m, λ is the X-ray wavelength, ρ_e is electron density and μ is the linear absorption coefficient.

The critical angle for total external reflection can be explained as below,

$$\theta_c = \sqrt{2\delta} \tag{40}$$

If the angle of incidence is greater than θ_c, X-rays transmit into the material. When the X-rays penetrate a layering system with different electron densities (ρ_e) a part of the X-rays is reflected at every interface. These reflected beams interfere constructively or destructively. XRR technique involves measuring the intensity of these reflected X-rays from a sample R(Q) as a function of X-ray incident angle (θ_i). Here R(Q) (Eq. 41) in the reflectivity curve and Q is the scattering vector (Figure 2.15).

The wave vector [11] $k=\frac{2\pi}{\lambda}$, $Q=k_s+k_i$, $Q=2k_i\sin(\theta)$

$$Q = \frac{4\pi sin\theta}{\lambda} \tag{41}$$

How does the scattering length density (SLD) β function relate to R(Q) : The Fourier transform of the SLD function is an elastic differential cross section $(\frac{d\sigma}{d\Omega})_{el}$ [11].

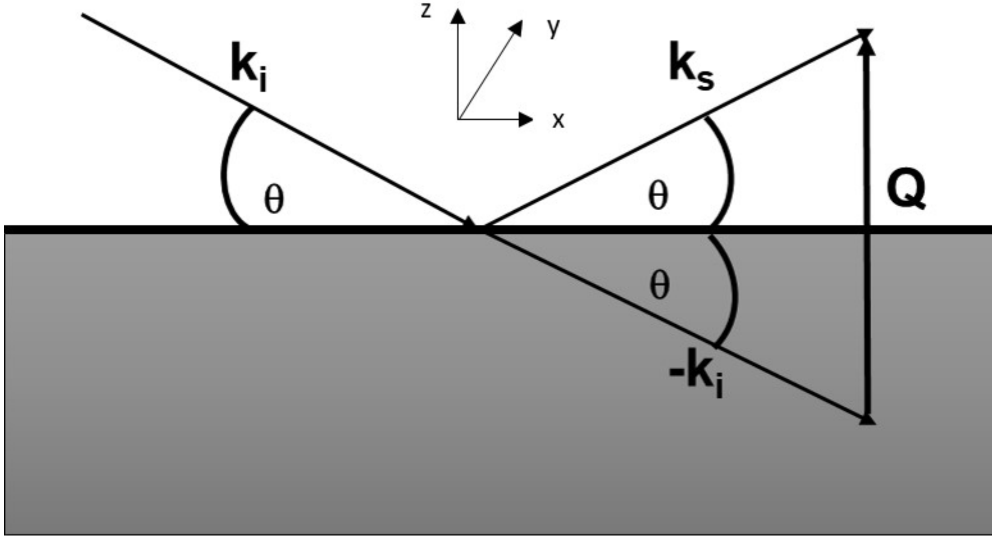

Figure 2.15: Scattering vector Q

$$\left(\frac{d\sigma}{d\Omega}\right)_{el} \propto \left| \iiint_V \beta(r) e^{iQ.r} d^3r \right|^2, \tag{42}$$

where V is the total scattering volume. The reflectivity curve R(Q) is related to the elastic differential cross section through [11],

$$R(Q) = \frac{1}{4L_x L_y sin\theta} \iint_{\Delta\Omega} \left(\frac{d\sigma}{d\Omega}\right)_{el} d\Omega, \tag{43}$$

where $4L_xL_y\sin(\theta)$ represents the area of the sample illuminated perpendicular to the incoming beam [11].

$$\left(\frac{d\sigma}{d\Omega}\right)_{el} \propto 16L_x^2L_y^2 \left| \int_{-\infty}^{\infty} \beta(z) e^{-iQ.z} dz \right|^2 \tag{44}$$

$$\Delta\Omega \approx \frac{16\pi^2 sin\theta}{L_x L_y Q^2} \tag{45}$$

Hence,

$$R(Q) \approx \frac{16\pi^2}{Q^2}\left| \int_{-\infty}^{\infty} \beta(z) e^{-iQ.z} dz \right|^2 \tag{46}$$

Integration by parts [11],

$$R(Q) \approx \frac{16\pi^2}{Q^4}\left| \int_{-\infty}^{\infty} \frac{d\beta}{dz} e^{-iQ.z} dz \right|^2 \tag{47}$$

For an ideal surface of a bare substrate (SLD β_s), the depth profile is, β_s for z<0 and 0 for z>0. The derivative of the SLD function is a δ function [11].

$$\frac{d\beta}{dz} = -\beta_s \delta(z) \tag{48}$$

From Eq. 47 the reflectivity curve R(Q) for a bare substrate is given by [11],

$$R(Q) \approx \frac{16\pi^2 \beta_s^2}{Q^4} \tag{49}$$

However, surfaces are not ideal. Generally, we should consider the surface and interface roughness. Therefore, a rough bare substrate is modeled by a Gaussian function. Hence the derivative of β function [11],

$$\frac{d\beta}{dz} = -\frac{\beta_i}{\sigma\sqrt{2\pi}} exp\left(-\frac{z^2}{2\sigma^2} \right) \tag{50}$$

Finally, the reflectivity curve R(Q) for a bare rough substrate can be defined as,

$$R(Q) \approx \frac{16\pi^2\beta_s^2}{Q^4} exp(-\sigma^2 Q^2) \tag{51}$$

Another simple situation is one uniform layer of film thickness L and SLD β_L on a substrate with SLD β_S. Without considering any surface or interface roughness the depth profile is, β_S for z<-L, β_L for -L<z<0, and 0 for z>0. Similar to the previous case the derivative of the SLD function is a δ function.

$$\frac{d\beta}{dz} = (\beta_L - \beta_s)\delta(z + L) - \beta_L\delta(z) \tag{52}$$

From Eq. 47 the reflectivity curve R(Q) for one uniform layer on a substrate is given by,

$$R(Q) \approx \frac{16\pi^2}{Q^4}\left[\beta_L^2 + (\beta_L - \beta_s)^2 - 2\beta_L(\beta_L - \beta_s)cos(LQ)\right] \tag{53}$$

For a rough surface and interface the Eq. 53 can be modified as,

$$R(Q) \approx \frac{16\pi^2\beta_i^2}{Q^4}\left[\frac{5}{4} - cos(LQ)\right]\beta_i exp\left(\frac{-Q^2\sigma^2}{2}\right) \tag{54}$$

According to the Eqs. 49 and 54, the reflectivity R(Q) decreases with increasing Q. The film thickness is related to the ΔQ as [11],

$$\Delta Q = \frac{2\pi}{L} \tag{55}$$

ΔQ is the period of the oscillation of the XRR fringe pattern.

XRR results shown in chapter 4 were taken on a PANalytical Empyrean instrument (the same instrument that we used for XRD) with a Ge (220) two-bounce hybrid monochromator. In order to limit the divergence of the X-ray beam, we used a fixed $1/32°$ divergence slit, and a 4 mm beam mask as the incident beam optics. Because of the low incidence angle of radiation large samples are more preferable for X-ray reflectance. Due to this effect of the sample size, the XRR profile needs to be corrected by a geometrical factor which is known as foot-print correction.

The reflected beam path consisted of a $0.27°$ parallel-plate collimator (refocusing the X-ray beam into a parallel path) with a 0.1 mm XRR slit, a 0.04 rad soller slit, and a Xe proportional detector. A programable Ni 0.125 mm beam attenuator was activated when the Xe detector count rate exceeded a preset threshold. More details about the sample alignment and the data analysis part are explained in chapter 4.

2.4 Atomic force microscopy (AFM)

Atomic force microscopy (AFM) is one of the primary forms of scanning probe microscopy (SPM) [12]. This is a high-resolution three-dimensional surface characterization tool used in a wide range of fields, including solid-state physics, surface chemistry, molecular biology, medicine, etc. Since this requires minimal sample

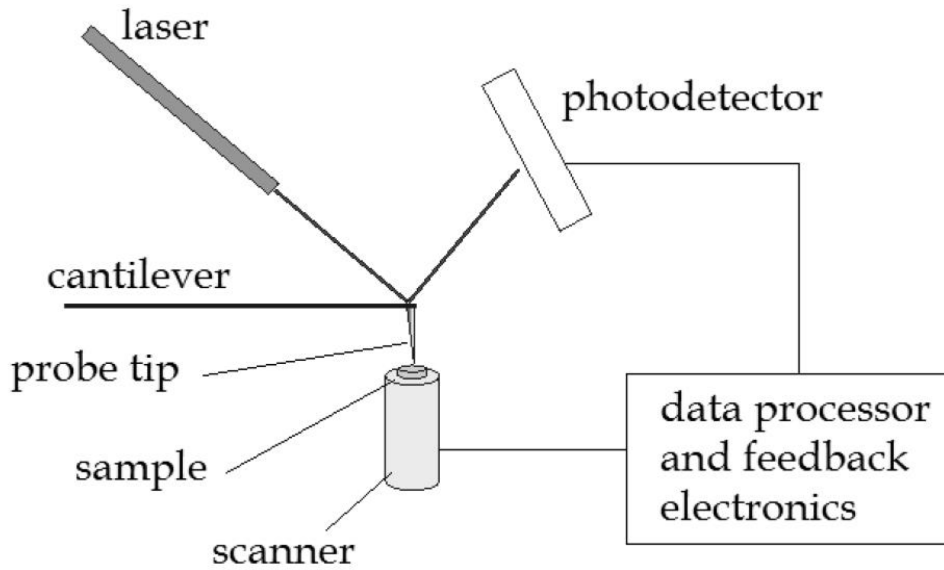

Figure 2.16: The basic principle of AFM [12].

preparation [13], it is easier to use.

As shown in Figure 2.16 the AFM tip (probe tip) is attached near the free end of a cantilever. When the distance between this tip and the sample surface is very small, according to the Hooke's law (Eq. 56) the probe tip experiences a repulsive force as below [12],

$$F = -k.x, \tag{56}$$

where F is the force between the sample surface and the probe tip, k is the spring constant, and x is the cantilever deflection. This force between the tip and the sample surface results in a deflection of the cantilever. Depending on the height between the tip and the surface, the deflection of the cantilever changes.

This deflection is monitored by a laser beam and directed into a photodetector as shown in Figure 2.16. According to the motion of this cantilever tip on the surface of the sample, the AFM operation is categorized into three modes. Those are imaging mode, contact mode, and non-contact tapping mode. A widely applied non-contact tapping mode was used for all the AFM measurements in this work.

AFM results shown in chapter 4 were performed on a Bruker Dimension FastScan instrument with a TESPA etched Si probe. To get the high-resolution AFM data with minimum sample damage here we used non-contact tapping mode across $10 \times 10\ \mu\text{m}^2$ area of the sample and several different positions of the same sample were imaged in order to diminish the inhomogeneity of the sample surface. Then we quantitatively analyzed this data and mainly obtained the root mean square (rms) surface roughness (R_q) using NanoScope analysis software.

3 DRUDE AND KUKHARSKII MOBILITY OF DOPED SEMICONDUCTORS EXTRACTED FROM FOURIER-TRANSFORM INFRARED ELLIPSOMETRY SPECTRA

This article was published in the Journal of Vacuum Science and Technology B, volume **37**, 012904 (2019).

Stefan Zollner, Pablo P. Paradis, Farzin Abadizaman, and Nuwanjula S. Samarasingha

Department of Physics, New Mexico State University, P.O. Box 30001, Las Cruces, NM 88003, USA

3.1 Abstract

The factorized plasmon-phonon polariton description of the infrared dielectric function is generalized to include an additional factor to account for the effects of interband electronic transitions. This new formalism is superior to the usual Drude-Lorentz summation of independent oscillators, especially in materials with large transverse-longitudinal optical phonon splittings, multiple infrared-active phonon modes, or high concentrations of free carriers, if a broad-band description of the dielectric function from the far-infrared to the vacuum-ultraviolet spectral region is desired. After a careful comparison of both approaches, the factorized description is applied to the dielectric function of undoped and doped semicon-

ductors (GaAs, GaSb, InAs) and metal oxides from 0.03 to 9.0 eV. Specifically, we find that both descriptions of the far-infrared dielectric function yield the same carrier density and mobility, at least for a single species of carriers. To achieve valid results for moderately high doping concentrations, measurements to lower energies would be helpful.

3.2 Introduction

The infrared optical spectra of semiconductors obtained from Fourier-transform infrared (FTIR) ellipsometry measurements contain rich information about their free carrier and lattice vibrational properties, such as the plasma frequency, carrier density, mobility, and energies and broadenings of transverse and longitudinal optical phonons [15]. There have been many discussions in the literature, if the dielectric function $\epsilon(\omega)$ should be written as a Drude-Lorentz sum of the contributions of various elementary excitations (such as plasmons, phonons, polaritons, excitons, etc) or as a Berreman-Unterwald product of the various terms. In this manuscript, we introduce a broadband factorized description of the dielectric function, which can be used from the far-infrared to the vacuum-ultraviolet spectral region, and apply it to undoped bulk cubic GaAs, wurtzite ZnO, and other materials. We also show that the factorized (Kukharskii) description of the infrared dielectric function for doped GaAs yields a similar electron concentration and mobility as the more commonly applied Drude-Lorentz model, if experimental er-

rors and our limited experimental range (0.031 to 6.5 eV) are properly taken into account.

3.3 Model dielectric functions

3.3.1 Drude-Lorentz model (sum)

Following Helmholtz [143], Kettler [144], and Drude [145–147], one can write the dielectric function $\epsilon(\omega)$ versus angular frequency ω as a sum

$$\epsilon(\omega) = 1 + \chi_{\text{Drude}}(\omega) + \chi_{\text{TO}}(\omega) + \chi_{\text{electronic}}(\omega), \tag{57}$$

where the constant 1 is the contribution of the vacuum, the first term

$$\chi_{\text{Drude}}(\omega) = -\sum_i \frac{\omega_{u,i}^2}{\omega^2 + i\gamma_{D,i}\omega} \tag{58}$$

the susceptibility of free carriers, the second term

$$\chi_{\text{TO}}(\omega) = \sum_i \frac{A_i \omega_{\text{TO},i}^2}{\omega_{\text{TO},i}^2 - \omega^2 - i\gamma_{\text{TO},i}\omega} \tag{59}$$

the susceptibility of transverse optical (TO) phonons, and the last term

$$\chi_{\text{electronic}}(\omega) = \sum_i \frac{B_i \omega_{0,i}^2}{\omega_{0,i}^2 - \omega^2 - i\gamma_{0,i}\omega} \tag{60}$$

the susceptibility of bound carriers due to interband optical transitions.

The justification for this summation (57) is the electromagnetic superposition principle: We assume that the polarization fields of the various charges under the

influence of the external electric field of the light source can be added, because they are independent of each other, ignoring interactions between charges.

As suggested by Drude [145, 147], we allow more than one species i of free carriers with an unscreened (angular) plasma frequency [148]

$$\omega_{u,i}^2 = \frac{n_i e^2}{\epsilon_0 m_i^* m_0}, \tag{61}$$

Drude scattering rate $\gamma_{D,i}$, carrier density n_i, and effective mass m_i^* to contribute to the dielectric function. e is the electronic charge, ϵ_0 the vacuum permeability, and m_0 the free electron mass. Usually, just a small number of free carrier species (often one or two) are sufficient to describe $\epsilon(\omega)$, such as electrons and holes, light and heavy holes, electrons in different conduction band valleys, s- and d-electrons, or bulk and surface electrons. For n-type semiconductors with a single occupied conduction band valley or for metals with a simple spherical Fermi surface, only one term should be sufficient, while more terms might be needed for more complex Fermi surfaces of metals.

In the lattice absorption term (59), $\omega_{\mathrm{TO},i}$ is the (angular) TO phonon frequency with scattering rate $\gamma_{\mathrm{TO},i}$ and dimensionless oscillator strength A_i. Since electromagnetic waves are transverse, only TO phonons (not LO phonons) lead to a pole in the lattice susceptibility (59).

Similarly, in the interband absorption term (117) due to bound carriers, $\omega_{0,i}$ is the (angular) frequency of the transition, $\gamma_{0,i}$ its scattering rate [149], and B_i

its dimensionless oscillator strength. The summation in Eq. (59) runs over all infrared-active phonon modes in the crystal (usually a small number, much less than three times the number of atoms in the primitive unit cell), but additional modes may be required due to higher-order phonon absorption or impurity-related vibrational modes [15].

The summation in Eq. (117) in principle runs over all $\vec{k}$-vectors in the Brillouin zone and all possible combinations of interband transitions. Therefore, the interband contribution is usually replaced by a summation

$$\chi_{\text{electronic}}\left(\omega\right)=\sum_{i}g_{i}\left(\omega\right) \tag{62}$$

over a much smaller number of Kramers-Kronig-consistent general oscillator functions $g_i\left(\omega\right)$, which might include Lorentzians with complex (or even negative) amplitudes, Gaussians, Tauc-Lorentz or Cody-Lorentz lineshapes, or the Herzinger-Johs parametric oscillator model [150].

Writing the dielectric function as a sum of Lorentzians or other lineshapes as in Eq. (57) implies that the various contributions are independent and that there is no cross-talk (interaction) between different transitions. Therefore, these models only use one broadening parameter for each term, in each denominator.

If we are only interested in the infrared portion of the dielectric function spectrum, we can define the high-frequency dielectric constant

$$\epsilon_{\infty}=1+\lim_{\omega\rightarrow0}\sum_{i}g_{i}\left(\omega\right). \tag{63}$$

This quantity describes the contribution of the vacuum and the electronic interband transitions to the static dielectric constant $\epsilon_s = \epsilon(\omega = 0)$. Experimentally, one obtains ϵ_∞ for insulators by measurements at frequencies above the region of lattice absorption (thus the subscript ∞), but far below the band gap. The infrared dielectric function then becomes

$$\begin{aligned} \epsilon_{\mathrm{IR}}(\omega) &= \epsilon_\infty - \sum_i \tfrac{\omega_{u,i}^2}{\omega^2 + i\gamma_{D,i}\omega} + \sum_i \tfrac{A_i \omega_{\mathrm{TO},i}^2}{\omega_{\mathrm{TO},i}^2 - \omega^2 - i\gamma_{\mathrm{TO},i}\omega} \\ &= \epsilon_\infty \left(1 - \sum_i \tfrac{\omega_{P,i}^2}{\omega^2 + i\gamma_{D,i}\omega}\right) + \sum_i \tfrac{A_i \omega_{\mathrm{TO},i}^2}{\omega_{\mathrm{TO},i}^2 - \omega^2 - i\gamma_{\mathrm{TO},i}\omega}, \end{aligned} \tag{64}$$

where we have introduced the screened (angular) plasma frequency

$$\omega_{P,i}^2 = \frac{n_i e^2}{\epsilon_0 \epsilon_\infty m_i^* m_0} = \frac{\omega_{u,i}^2}{\epsilon_\infty}. \tag{65}$$

We will use Eq. (64) to fit the infrared dielectric function of undoped and doped GaAs [151, 152].

For ω=0, Eq. (64) shows that in the absence of free carriers the amplitudes A_i describe the contribution of lattice absorption to the static dielectric constant, since [19]

$$\epsilon_s = \epsilon_\infty + \sum_i A_i. \tag{66}$$

For a single phonon absorption band, we can use the Lyddane-Sachs-Teller (LST) relation [153]

$$\epsilon_s = \epsilon_\infty \frac{\omega_{\mathrm{LO}}^2}{\omega_{\mathrm{TO}}^2} \tag{67}$$

to calculate the longitudinal optical (LO) phonon frequency

$$\omega_{\mathrm{LO}} = \omega_{\mathrm{TO}} \sqrt{1 + \frac{A}{\epsilon_\infty}}. \tag{68}$$

(Kurosawa [154] and Barker [19] generalized the LST relation for cubic materials with multiple phonons and Schubert [155] for anisotropic crystals.)

In the presence of free carriers, the dielectric function (57) diverges at low frequencies. It is convenient to introduce the complex optical conductivity

$$\sigma\left(\omega\right) = -i\epsilon_0\omega\left[\epsilon\left(\omega\right) - 1\right], \tag{69}$$

which cancels the divergence of the Drude term and therefore remains finite at low frequencies. We can then identify the quantity

$$\sigma_{\mathrm{DC}} = \lim_{\omega\to 0} \sigma\left(\omega\right) \tag{70}$$

with the electrical low-frequency conductivity. For the specific case of the Drude-Lorentz model (64), we find

$$\sigma_{\mathrm{DC}} = \epsilon_0\epsilon_\infty \sum_i \frac{\omega_{P,i}^2}{\gamma_{D,i}} = \frac{e^2}{m_0} \sum_i \frac{n_i}{m_i^* \gamma_{D,i}} = \sum_i n_i e \mu_i. \tag{71}$$

A similar expression was already given by Drude [145]. The mobility of the carrier species i is given by [148]

$$\mu_i = \frac{e}{m_i^* m_0 \gamma_{D,i}} = \frac{e\tau_{D,i}}{m_i^* m_0}, \tag{72}$$

where $\tau_{D,i} = \gamma_{D,i}^{-1}$ is the Drude collision time.

3.3.2 Kukharskii model (product)

Berreman and Unterwald [16] take a completely different approach in their description of the dielectric function. Without making physical assumptions about the line shape of oscillators, they start with the mathematical fact that the dielectric function, like any analytic function in the complex plane, is completely determined by its zeroes and poles and therefore can be written as a quotient of two polynomials. Since $\epsilon(\omega)$ approaches unity as the angular frequency goes to infinity, the number of poles must be equal to the number of zeroes and the highest-order polynomial coefficients in the numerator and denominator must be equal. Considering also the symmetry $\epsilon(-\omega) = \epsilon^*(\omega)$ to ensure that the time-dependent dielectric displacement remains real, poles and zeroes come in pairs and those not located on the imaginary axis must be symmetric relative to the imaginary axis. This results in the functional form [14]

$$\epsilon(\omega) = \prod_i \frac{\omega_{\mathrm{L},i}^2 - \omega^2 - i\gamma_{\mathrm{L},i}\omega}{\omega_{\mathrm{T},i}^2 - \omega^2 - i\gamma_{\mathrm{T},i}\omega}, \qquad (73)$$

which was frequently applied to model the infrared reflectance of insulators [18]. For insulators with many phonon modes or for large TO/LO splittings, it often gives a better description than the Drude-Lorentz model of independent oscillators [156, 157].

Since the dielectric function $\epsilon(\omega)$ and its inverse $\epsilon^{-1}(\omega)$ (called the loss function) obey causality (i.e., the polarization response follows the applied electric

field), both zeroes and poles must be located below the real axis in the complex plane, which is equivalent to the condition that all scattering rates $\gamma_{T,i}$ and $\gamma_{L,i}$ must be positive. (We assume a time-dependence $\exp(-i\omega t)$ for the electromagnetic wave. The other choice for the time-dependence $\exp(i\omega t)$ leads to complex conjugate equations with poles and zeroes above the real axis, see Barker [19]).

To understand the physical significance of the zeroes and poles in Eq. (105), it is instructive to place the various factors into three groups

$$\epsilon(\omega) = \epsilon(\omega)_{\mathrm{Drude}}\, \epsilon(\omega)_{\mathrm{TO}}\, \epsilon(\omega)_{\mathrm{electronic}}. \tag{74}$$

Berreman and Unterwald [16] already recognized that the Drude response of free carriers can be described by

$$\epsilon(\omega)_{\mathrm{Drude}} = \prod_i \frac{\omega_{\mathrm{LP},i}^2 - \omega^2 - i\gamma_{\mathrm{LP},i}\omega}{-\omega^2 - i\gamma_{K,i}\omega}, \tag{75}$$

which corresponds to one pole at the origin and another one at $-i\gamma_{K,i}$. We chose the subscript K after Kukharskii, who first applied Eq. (75) to describe the reflectance of doped GaAs [158,159]. The zeroes in Eq. (75) are related to the lower longitudinal plasmon-phonon polaritons (LP) [15,160,161]. In the absence of free carriers, the LP angular frequency vanishes and the Drude factor (75) becomes unity.

The second factor

$$\epsilon(\omega)_{\mathrm{TO}} = \prod_i \frac{\omega_{\mathrm{UP},i}^2 - \omega^2 - i\gamma_{\mathrm{UP},i}\omega}{\omega_{\mathrm{TO},i}^2 - \omega^2 - i\gamma_{\mathrm{TO},i}\omega}, \tag{76}$$

describes the dielectric response of infrared lattice absorption. The poles are related to TO phonons, while the zeroes are the upper longitudinal plasmon-phonon polaritons (UP). In the absence of free carriers, the UP modes are the LO phonons. They are pushed towards higher energy by the interaction with longitudinal plasmon oscillations of free carriers [160, 161]. (Since the plasmon oscillations are longitudinal, they interact only with the LO, but not with the TO phonons.) Additional factors may be attached to describe higher-order phonon absorption or impurity-related absorption.

For a single plasmon-phonon polariton mode, the lower and upper polariton frequencies are related to the screened plasma frequency and the LO frequency by [159, 160]

$$\omega_P = \frac{\omega_{\mathrm{LP}}\omega_{\mathrm{UP}}}{\omega_{\mathrm{TO}}} \quad \text{and} \tag{77}$$

$$\omega_{\mathrm{LO}}^2 = \omega_{\mathrm{LP}}^2 + \omega_{\mathrm{UP}}^2 - \omega_P^2. \tag{78}$$

The third factor

$$\epsilon(\omega)_{\mathrm{electronic}} = \prod_i \frac{\omega_{\mathrm{L},i}^2 - \omega^2 - i\gamma_{\mathrm{L},i}\omega}{\omega_{0,i}^2 - \omega^2 - i\gamma_{0,i}\omega}, \tag{79}$$

can be expressed as a sum similar to Eq. (117)

$$\epsilon(\omega)_{\mathrm{electronic}} \approx 1 + \sum_i \frac{B_i\omega_{0,i}^2 + i\omega\left(\gamma_{0,i} - \gamma_{L,i}\right)}{\omega_{0,i}^2 - \omega^2 - i\gamma_{0,i}\omega} \tag{80}$$

with the oscillator strength

$$B_i = \frac{\omega_{L,i}^2}{\omega_{0,i}^2} - 1, \tag{81}$$

if we pretend that all broadenings are small and thus neglect the coupling between different interband transitions. (The presence of broadenings justifies complex Lorentzian amplitudes.) More conveniently, we write this factor (80) as a sum of general oscillators

$$\epsilon\left(\omega\right)_{\text{electronic}} = 1 + \sum_i g_i\left(\omega\right), \tag{82}$$

just like in the Drude-Lorentz case (62). We use the same definition (63) for ϵ_∞. If we are only interested in the dielectric function of doped insulators well below the band gap, this allows us to write

$$\epsilon_{\text{IR}}\left(\omega\right) = \epsilon_\infty \prod_i \frac{\omega_{\text{LP},i}^2 - \omega^2 - i\gamma_{\text{LP},i}\omega}{-\omega\left(\omega + i\gamma_{K,i}\right)} \prod_j \frac{\omega_{\text{UP},j}^2 - \omega^2 - i\gamma_{\text{UP},j}\omega}{\omega_{\text{TO},j}^2 - \omega^2 - i\gamma_{\text{TO},j}\omega}, \tag{83}$$

which is known as Kukharskii's equation [158, 159].

From the Kukharskii model (83), we can calculate the DC conductivy defined by Eq. (70) as

$$\sigma_{\text{DC}} = \epsilon_0\epsilon_\infty \prod_i \frac{\omega_{\text{LP},i}^2}{\gamma_{K,i}} \prod_j \frac{\omega_{\text{UP},j}^2}{\omega_{\text{TO},j}^2}. \tag{84}$$

It is not straightforward to break up this product into a sum of contributions of different species of carriers to the DC conductivity, but for a single carrier species we can write using Eq. (77)

$$\mu = \frac{\sigma_{\text{DC}}}{ne} = \frac{\epsilon_0\epsilon_\infty}{ne}\frac{\omega_{\text{LP}}^2\omega_{\text{UP}}^2}{\gamma_K\omega_{\text{TO}}^2} = \frac{e}{m_0 m^* \gamma_K}, \tag{85}$$

which is exactly the same expression as in the Drude-Lorentz case (72). The Drude and Kukharskii scattering rates are therefore the same and we can omit this distinction.

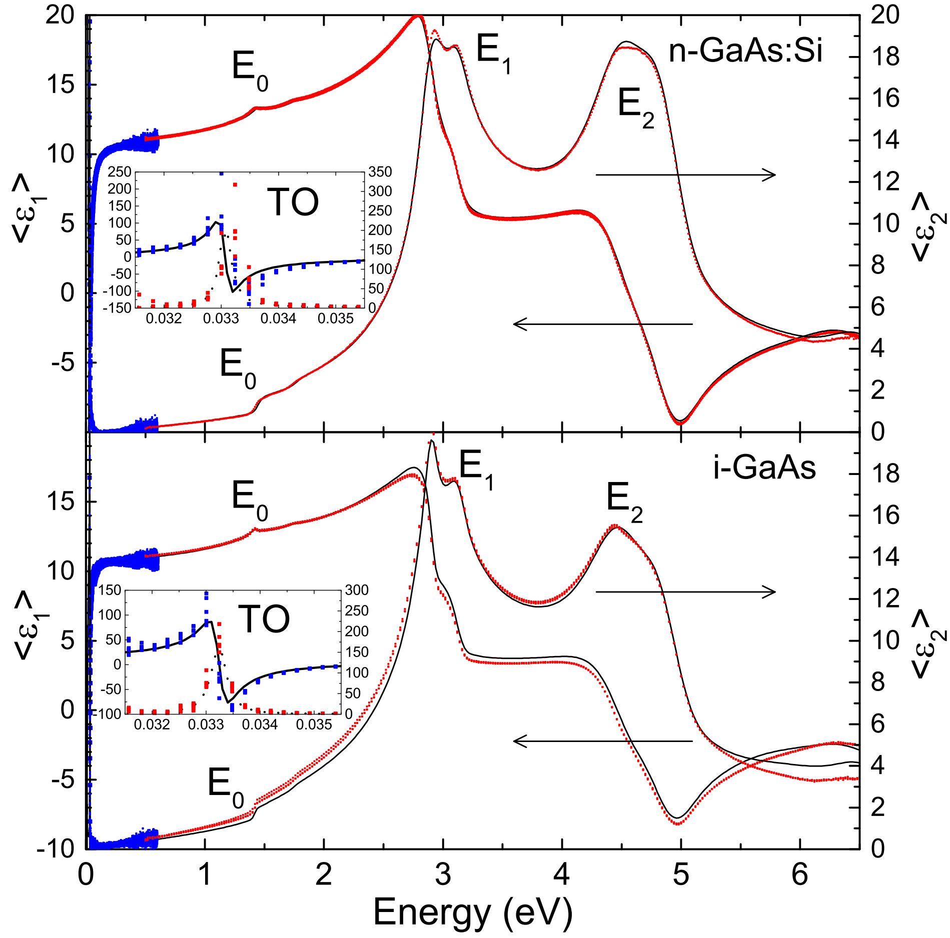

Figure 3.1: (Color online) Real and imaginary parts of the pseudo-dielectric function for silicon-doped (top) and undoped (bottom) GaAs covered with native oxide. Data from two different instruments were merged. The insets show expanded views of the regions of lattice absorption. Symbols show experimental data, lines the best fit to Eq. (74) with parameters given in Table 3.1.

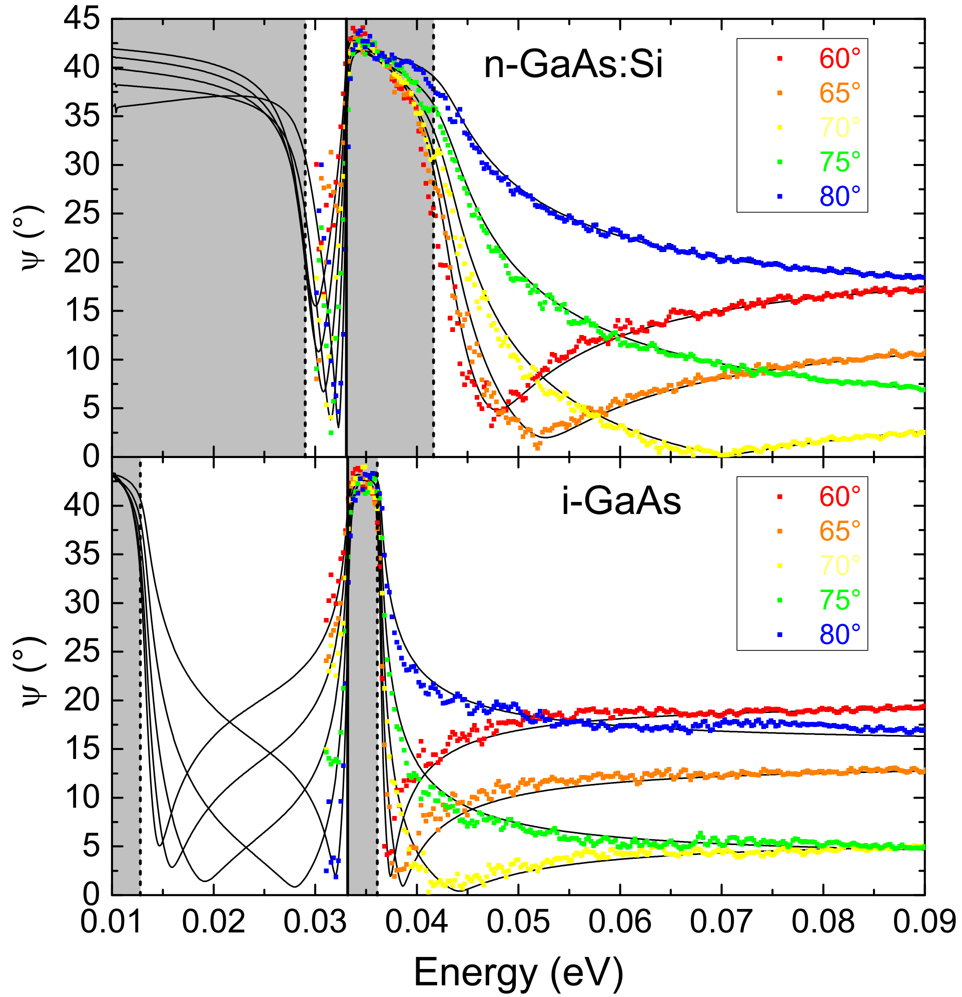

Figure 3.2: (Color online) Ellipsometric angle ψ at five angles of incidence for silicon-doped (top) and undoped (bottom) GaAs covered with native oxide in the region of plasmon-polariton absorption (grey). Symbols show experimental data, lines the best fit to Eq. (74) with parameters shown in Table 3.1. The reststrahlen bands are shaded in grey.

3.4 Experimental procedure

In the infrared spectral region, we acquired the ellipsometric angles ψ and Δ as a function of angular frequency ω on a J. A. Woollam FTIR variable angle of incidence spectroscopic ellipsometer (FTIR-VASE) from 0.031 to 0.600 eV with a resolution of 4 cm^{-1}, usually at five equally spaced angles of incidence from 60° to 80°. We performed two-zone measurements with two polarizer angles (±45°) and two analyzer angles (0°, 180°) and a rotating compensator (15 spectra per revolution, 20 FTIR scans per spectrum). We also acquired ψ and Δ from 0.50 to 6.60 eV with 0.01 eV steps at the same angles of incidence on a J.A. Woollam VASE ellipsometer equipped with a computer-controlled Berek wave plate compensator.

Since data from two these instruments were merged, small discrepancies can be noticed in the region of overlap, possibly due to slight misalignment. Most noticeably, the data taken with the FTIR ellipsometer is noisy above 0.5 eV.

3.5 Results and Discussion

3.5.1 Intrinsic and n-type GaAs, doped GaSb, InAs

In Figure 3.1, we show the pseudodielectric functions for a nominally undoped (intrinsic) and a Si-doped (n-type) GaAs substrate from 0.031 to 6.5 eV. Above 1 eV, we used tabulated optical constants for undoped and n-type GaAs and its native oxide taken from the literature [162–164]. This allowed us to determine the

native oxide thickness (40 and 26 Å, respectively). This fit is generally quite good, although some discrepancies were found, most likely due to polishing damage near the surface and uncertainties in the optical constants of the native oxide [164].

Using the tabulated optical constants for the electronic part of the dielectric function $\epsilon_{\text{electronic}}(\omega)$, we then fitted the remaining parameters (TO phonon and polariton energies and broadenings) in Eqs. (74) and (83), with results shown in Table 3.1. ϵ_∞ was taken as the zero-energy limit of the tabulated dielectric functions.

Since the effects of plasmon-phonon polaritons on the optical constants can only be seen at the lowest photon energies, we also show the ellipsometric angle ψ below 0.09 eV for both substrates in Fig. 3.2. For each sample, there are two regions called *reststrahlen* bands (shown in grey), where ψ is close to 45° (and the normal-incidence reflectance is high). One of these bands extends from zero to E_{LP}, while the other one extends from E_{TO} to E_{UP}. Our FTIR ellipsometer has good sensitivity to E_{UP} (which appears as a strong peak in the loss function shown in Fig. 3.5) and its broadening. E_{TO} is right at the edge of our experimental range, but clearly visible in ϵ, see the insets in Fig. 3.1. The energy range of the lower plasmon-phonon polariton band, on the other hand, is too low to be measurable using our instrument. Nevertheless, we obtain reasonable values for all relevant parameters, see Table 3.1. The only exceptions are the Kukharskii and LP broadenings, which are strongly correlated.

Table 3.1: Screened plasma frequency $E_P = \hbar\omega_P$, Drude broadening $\Gamma_D = \hbar\gamma_D$, high-frequency dielectric constant ϵ_∞, carrier density n, mobility μ, TO and LO phonon energies $E_{\text{TO}} = \hbar\omega_{\text{TO}}$ and $E_{\text{LO}} = \hbar\omega_{\text{LO}}$ and broadening $\Gamma_{\text{TO}} = \hbar\gamma_{\text{TO}}$, Kukharskii broadening $\Gamma_K = \hbar\gamma_K$, and lower and upper plasmon-polariton frequencies $E_{\text{LP}} = \hbar\omega_{\text{LP}}$ and $E_{\text{UP}} = \hbar\omega_{\text{UP}}$ and their broadenings $\Gamma_{\text{LP}} = \hbar\gamma_{\text{LP}}$ and $\Gamma_{\text{UP}} = \hbar\gamma_{\text{UP}}$ for undoped and n-type GaAs as well as n-type and p-type GaSb and InAs. For uniaxial undoped ZnO, values for the ordinary (o) and extraordinary (eo) parameters are listed separately. Quantities marked (f) were fixed during the fit, those marked with an asterisk were taken from the literature. For each material, the top row (model DL) shows a fit with Eq. (64), where E_P, Γ_D, E_{TO}, Γ_{TO}, and ϵ_∞ are experimental values from ellipsometry data, whereas n, μ, and E_{LO} were calculated using Eqs. (65), (72). and (68); the bottom row (model KK) shows experimental values ϵ_∞, E_{TO}, Γ_{TO}, Γ_K, E_{LP}, E_{UP}, Γ_{LP}, and Γ_{UP} determined from a fit to the ellipsometry data with Eq. (74), whereas E_P, E_{LO}, n, and μ were calculated using Eqs. (77), (78), (65), and (85), respectively. Calculated quantities are shown in bold. The broadenings shown in italics show strong parameter correlations and therefore are not reliable.

Sample	Model	E_P	Γ_D	ϵ_∞	n	μ	E_{TO}	E_{LO}	Γ_{TO}	Γ_K	E_{LP}	E_{UP}	Γ_{LP}	Γ_{UP}
		(meV)	(meV)	(1)	(cm^{-3})	(cm/Vs)	(meV)	(meV)	(meV)	(meV)	(meV)	(meV)	(meV)	(meV)
u-GaAs	DL	12.4	4.2	10.8	**7.5×10^{16}**	**4400**	33.3	**35.9**	0.3					
u-GaAs	KK	**13.0**		10.8	**8.5×10^{16}**	**45000**	33.2	**35.8**	0.3	*0.4*	11.9	36.2	*0.6*	0.3
n-GaAs	DL	35.6	5.4	11.0	**6.4×10^{17}**	**3400**	33.3	**35.6**	0.3					
n-GaAs	KK	**36.7**		11.0	**6.8×10^{17}**	**1600**	33.0	**35.0**	0.2	*11.3*	29.2	41.5	*4.9*	4.3
n-GaSb	DL	17	2 (f)	14.6	**1.8×10^{18}**	1000 (f)	27.78*	28.89*	0.3 (f)					
n-GaSb	KK	**10.9**		14.6	**7.2×10^{17}**	**1000**	27.78*	**28.3**	0.3 (f)	*2*	10.7	28.4	*1*	1 (f)
p-GaSb	DL	33.3	32.8	14.0	**3.4×10^{18}**	**120**	27.78*	28.89*	0.3 (f)					
p-GaSb	KK	**28.9**		14.0	**2.5×10^{18}**	**600**	27.78*	**28.6**	0.3 (f)	*6.4*	25.1	32.0	1 (f)	*11.7*
InAs	KK	**17**		12.2	**5.9×10^{16}**	**50000**	27*	**30**	0.3 (f)	1 (f)	15	31	1 (f)	1 (f)
ZnO (o)	KK			3.73			50.7		1.2			73.2		1.1
ZnO (eo)	KK			3.81*			46.8		1 (f)			71.1		0.9

Using Eqs. (77) and (78) we calculated the plasma and LO phonon frequencies. From E_P=13.0 meV for undoped GaAs, we obtain a carrier density of 8.5×10^{16} cm^{-3}, which should be considered an upper limit. For n-type GaAs, E_P=36.7 meV implies a carrier density of 6.8×10^{17} cm^{-3}, which is within the range of doping densities specified by the supplier (5.5 to 14×10^{17} cm^{-3}). An effective electron mass of m_0=0.063 was used.

For comparison, we also fitted the same data shown in Fig. 3.2 with the Drude-Lorentz model (64). The Drude and TO phonon energies and broadenings are also shown in Table 3.1. The LO energy, carrier density, and mobility were calculated from Eqs. (68), (65), and (72). The carrier densities and LO frequencies agree quite well between both models. Also, the optical mobility for undoped and doped GaAs obtained from the Drude-Lorentz fit agrees with the electrical mobility expected for the given carrier concentration [165].

Unfortunately, the Kukharskii scattering rate γ_K disagrees with the Drude scattering rate γ_D, compare Eqs. (72) and (85), and therefore the Kukharskii mobilities are not reliable, see Table 3.1. As mentioned earlier, this is due to our limited spectral range and the correlations in the fit between γ_K and γ_{LP} because of the larger number of broadening parameters in the Kukharskii model.

Results for n-type and p-type GaSb and for InAs are also listed in Table 3.1 and discussed in the supplementary materials.

3.5.2 Bulk undoped ZnO

According to Kukharskii [159], the factorized dielectric function (74) can also be applied to each diagonal component of the dielectric tensor of anisotropic materials with at least orthorhombic symmetry, where the dielectric properties can be described by a diagonal tensor in a coordinate system that is invariant with photon energy.

To illustrate this point, we analyze the ellipsometric angles and the pseudo-dielectric function of a bulk c-axis oriented ZnO substrate obtained commercially, see Fig. 3.3. To model these data, we use a uniaxial model for a bulk substrate with an ordinary and an extraordinary dielectric function, each described independently with the form given by Eq. (74). Since no free carrier effects are visible for this substrate, the Drude factor was set to unity. A surface roughness layer thickness (described with a 50/50 mixture of ZnO and voids using the Bruggeman effective medium approximation) of 21 Å was found from the magnitude of the pseudo-absorption below the band gap of about 3.1 eV. The electronic part of the ordinary dielectric function was described using two Tauc-Lorentz oscillators to account for the absorption of the main exciton triplet [115, 120, 166] (not resolved) and the exciton-phonon complexes [119–121]. At higher energies, we added two simplified Herzinger-Johs parametric oscillators and a pole at 11 eV. For our c-axis oriented ZnO substrate, the extraordinary dielectric function does not have a significant

impact on the pseudo-dielectric function above the region of lattice absorption. We therefore assume that the electronic part of the extraordinary dielectric function is equal to that of the ordinary dielectric function, except for a rigid shift upward by 0.08, see Ref. 114. Our data are not sensitive to the complications described by Shokovets *et al.* [113] The infrared lattice absorption of ZnO is dominated by the E_1 (A_1) phonons in the ordinary (extraordinary) dielectric function, each of which is split into a TO/LO pair by the Fröhlich interaction [114].

Our experimental ellipsometry data for bulk ZnO along with the best fit using Eq. (74) in the low and high photon energy regions are shown in Figs. 3.3 and 3.4, respectively. The physical significance of the various structures in the spectra has been explained elsewhere [114]. Our main point here is to show that Eq. (74) gives an excellent description over the complete spectral range from 0.03 to 6.5 eV. Our fit only has one problem: We are unable to describe the exact energy where the pseudo-Brewster angle of the sample changes from 0 to π. This energy depends on the precise value of the high-frequency dielectric constant ϵ_∞. In our approach, ϵ_∞ is not a free parameter, but determined by the electronic part of the spectrum shown in Fig. 3.3. A slight mismatch of the data from the two instruments causes a small error in ϵ_∞ (on the order of 0.05), which is responsible for the error seen near 0.14 eV in Fig. 3.4.

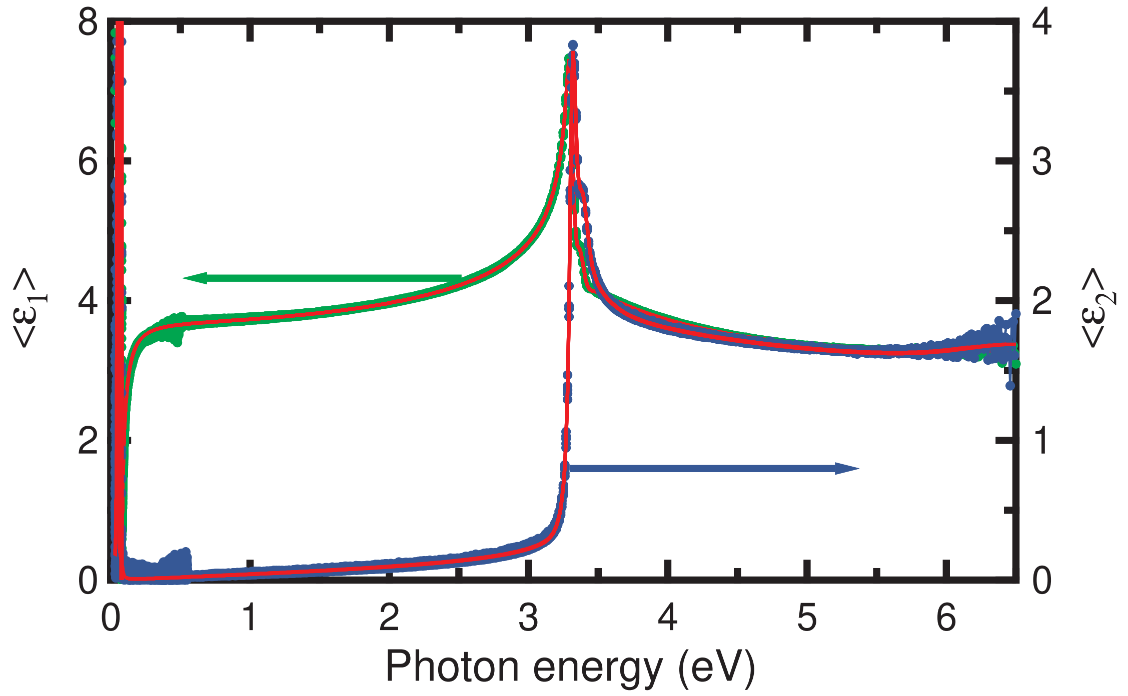

Figure 3.3: (Color online) Real and imaginary parts of the pseudo-dielectric function for undoped c-axis oriented bulk ZnO with 21 Å surface roughness. Data from two different instruments were merged. Points show experimental data, lines the best fit to Eq. (74) with parameters in Table 3.1.

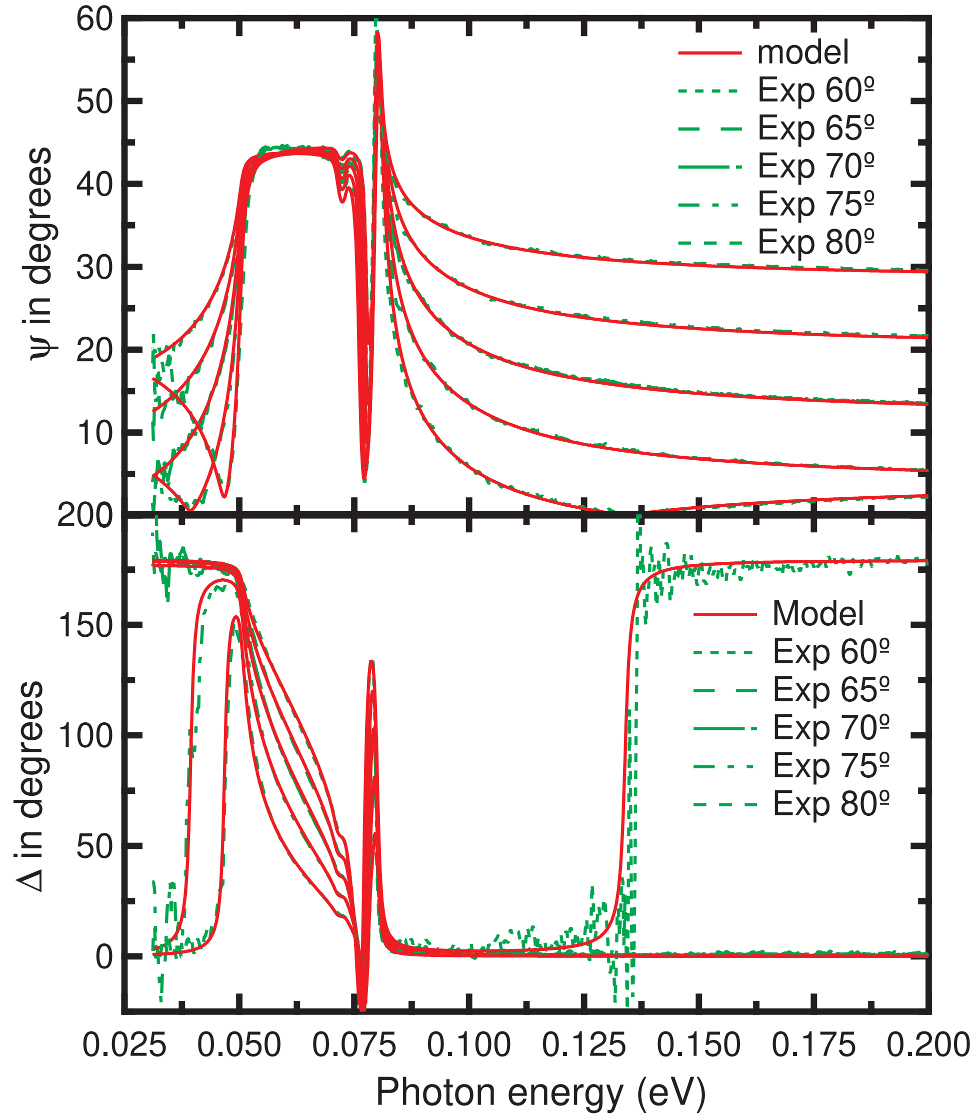

Figure 3.4: (Color online) Ellipsometric angles ψ and Δ for undoped c-axis oriented bulk ZnO with 21 Å surface roughness in the region of infrared lattice absorption. Points show experimental data, lines the best fit to Eq. (74) with parameters in Table 3.1.

3.6 Summary

Fifty years ago, modulation spectroscopy [167] (to study the electronic band structure of materials) and vibrational spectroscopy [15,168] (Raman and FTIR, especially) were distinctly different fields, with different approaches to describe experiments. The availability of modern commercial ellipsometry instruments covering the range from 0.03 to 9.0 eV requires a consistent broadband approach suitable for insulators, semiconductors, and metals. The Drude-Lorentz summation (57) meets the broadband requirement, but it is not suitable for interacting excitations, such as insulators with multiple phonons [156,157] or doped semiconductors with coupled longitudinal phonon-plasmon polaritons [158,159]. We therefore introduced a factorized formalism (105), a generalization of Kukharskii's equation (83), which is appropriate to describe insulators, semiconductors, and metals over the complete spectral range from the mid-IR to the vacuum-UV. This product (105) is easily implemented in commercial software. Several examples were given in the main text and in the supplementary materials.

Specifically, we also presented an approach to calculate the carrier mobility of doped semiconductors from Kukharskii's equation, if the effective mass of the carriers is known. We applied this approach to doped GaAs, InAs, and GaSb. Our results are reasonable, but the study of doped semiconductors could be more reliable if the lower spectral range of commercial FTIR ellipsometers could be

extended to 0.01 eV.

Supplementary Material

See supplementary material for additional experimental data and discussion of n- and p-type GaSb, InAs, and spinel ($MgAl_2O_4$).

Acknowledgements

This material is based, in part, on research sponsored by Air Force Research Laboratory (AFRL) under agreement number FA9453-18-2-0046. The work at NMSU was supported by the National Science Foundation (DMR-1505172). The U.S. Government is authorized to reproduce and distribute reprints for Governmental purposes notwithstanding any copyright notation thereon. The views and conclusions contained herein are those of the authors and should not be interpreted as necessarily representing the official policies or endorsements, either expressed or implied, of Air Force Research Laboratory (AFRL) and or the US Government.

3.7 Supplementary Materials

3.7.1 Definition of the Pseudo-dielectric Function

As described in the main manuscript, each isotropic pure material is characterized by a frequency-dependent dielectric function $\epsilon(\omega)$. A sample in an ellipsometry experiment consists of more than one material (even a bulk material will have

a surface region with optical constants different from the bulk) and therefore is described by ellipsometric angles ψ and Δ and a Fresnel reflectance ratio

$$\rho = \tan \psi \exp(i\Delta), \tag{86}$$

which depend on the optical constants of all materials and the thicknesses of all layers (Fujiwara 2006).

The pseudo-dielectric function of a bulk material with a very thin surface overlayer defined by

$$\langle \epsilon(\omega) \rangle = \sin^2 \phi \left[1 + \tan^2 \phi \left(\frac{1-\rho}{1+\rho} \right)^2 \right], \tag{87}$$

where ϕ is the angle of incidence, is a zero-order approximation of the dielectric function $\epsilon(\omega)$ of the bulk material where the effects of the surface overlayer are ignored (Fujiwara 2006, Yu and Cardona 2010). If overlayers are thin, the pseudo-dielectric function does not usually depend on the angle of incidence and therefore is a good representation of experimental data. For thick layers on a substrate, it is better to display ellipsometric angles, since there is little resemblance of the pseudo-dielectric function to the dielectric functions of the constituent materials (Kormondy 2014). We also display the ellipsometric angles in the infrared spectral region, where the pseudo-dielectric function is dominated by a few sharp peaks that obliterate smaller features in the data.

3.7.2 Results for GaSb

We measured the ellipsometric angles for two commercial GaSb substrates. The first one was Te doped, to compensate the p-type nature of nominally undoped GaSb, where Ga vacancies and Sb antisite defects result in a hole concentration of about 10^{17} cm^{-3} (Kulala 2014). This Te doping resulted in an electron concentration of $4-6\times10^{16}$ cm^{-3}, as specified by the supplier. Since the L-valleys in the conduction band of GaSb are just 70 meV about the Γ conduction band minimum, most electrons are expected to be in the L-valley at room temperature (Rode 1975), which has a density of states effective mass of 0.57. The effective mass in the Γ-valley is much smaller, only 0.041.

The other GaSb substrate was a zinc-doped p-type sample with a hole density greater than 10^{18} cm^{-3} specified by the supplier. Hole transport in GaSb is complicated because of k-linear terms due to the lack of inversion symmetry and the warped non-parabolic heavy and light hole bands (Heller 1985). To model this transport at room temperature with one band, an effective mass of 0.3 was chosen. The mobility expected for this sample is $200-450$ cm^2/Vs.

A. n-type GaSb with low doping

Studying GaSb was more challenging than GaAs, because no high-accuracy optical constants for bulk GaSb were available over the complete spectral range from 0.5 to 6.6 eV. We therefore acquired the pseudo-dielectric function, determined

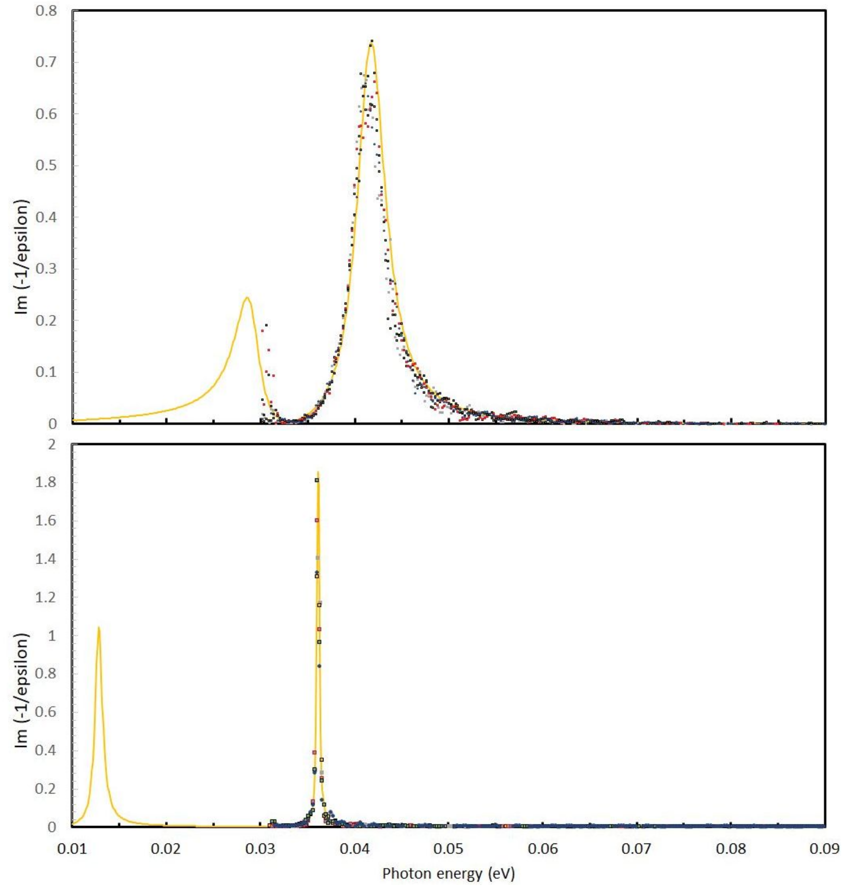

Figure 3.5: Same data as in Fig. 3.2 for n-type GaAs (top) and undoped GaAs (bottom), but displayed as the loss function $-\mathrm{Im}\,(1/\epsilon)$. The line shows the model, the symbols the data. The LP and UP polariton modes are shown as peaks, shifting and broadening dependent on carrier concentration.

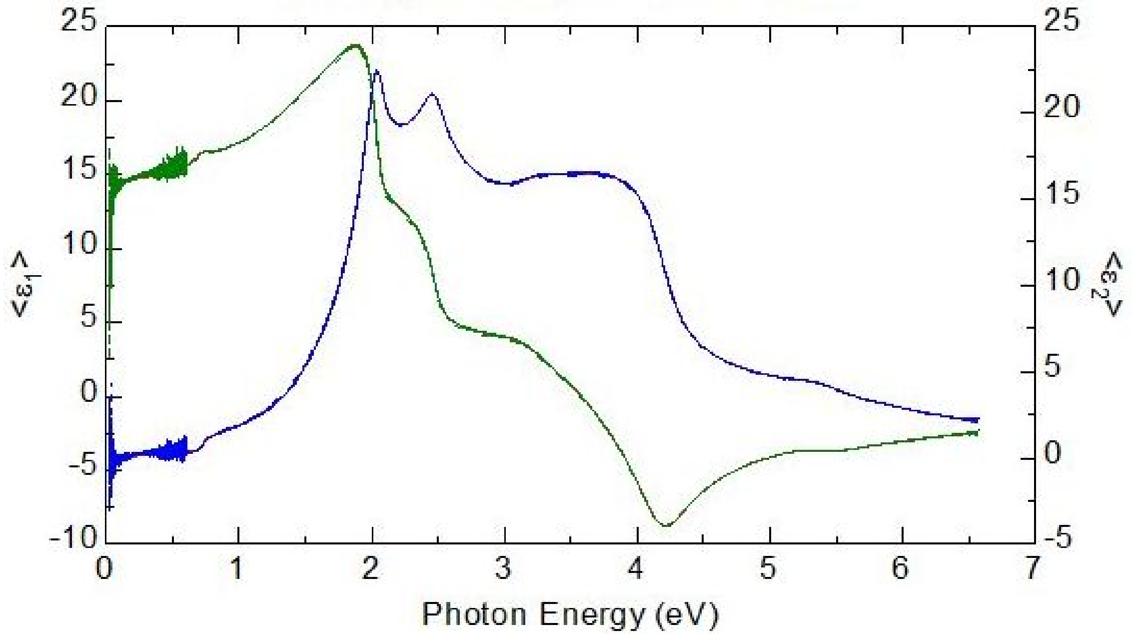

Figure 3.6: As Fig. 3.1, but for n-type compensated bulk GaSb with an electron density of $4{-}6{\times}10^{16}$ cm^{-3}.

the oxide thickness (15 Å) from the pseudo-absorption below the band gap [150], and then fitted GaSb optical constants using a parametric oscillator model. The results are shown in Fig. 3.6. Unfortunately, our results for ϵ of GaSb are quite different from the literature, presumably due to surface polishing damage of our commercial GaSb wafer. A high-frequency dielectric constant ϵ_∞=14.6 was found from these data, consistent with the literature.

The ellipsometric angle ψ in the mid-infrared is shown in Fig. 3.7. Despite the noise, it is clear that ψ is not flat, but shows some curvature. For angles of incidence ϕ between 60° and 70°, ψ bends down towards lower energies, while it bends up for ϕ=75°. For ϕ=75°, Δ also shows a phase change by π as the Brewster

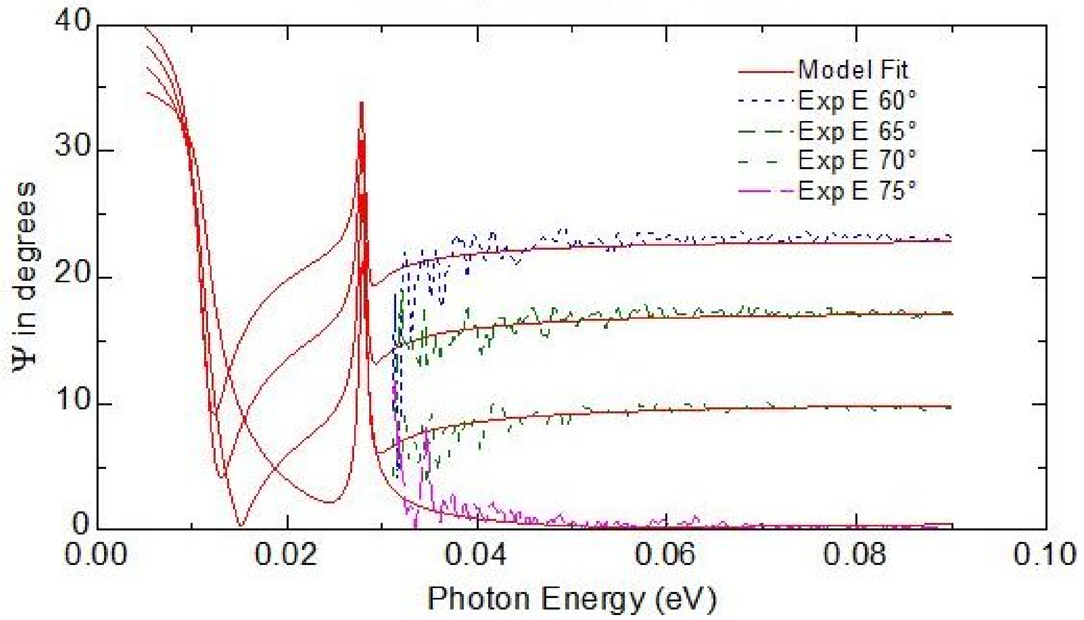

Figure 3.7: As Fig. 3.2, but for n-type compensated bulk GaSb with an electron density of 4−6×10^{16} cm^{-3}.

angle crosses the angle of incidence (not shown). To describe this curvature, we fix the TO phonon energy and its broadening as well as the UP broadening and fit the other parameters of the Kukharski model. The model fits the data well and the parameters are quite reasonable, see Table 3.1. We find a plasma frequency of 10.9 meV from Eq. (77), which corresponds to a carrier density of 7.2×10^{17} cm^{-3} (an order of magnitude larger than the electron concentration specified by the supplier) for the L-valley effective mass of 0.57. This should be considered an upper limit. The upper limit of the electron concentration measurable with our FTIR-VASE instrument is an order of magnitude larger for n-type GaSb than for n-type GaAs, because the effective (L-valley) electron mass in GaSb is an order

of magnitude larger than the effective (Γ-valley) mass in GaAs. The Kukharski broadening of Γ_K=2 meV has a large error bar, but it corresponds to a mobility of 1000 cm^2/Vs, which is quite reasonable for n-type GaSb at room temperature. (The manufacturer specifies mobilities in the range of 2000−3500 cm^2/Vs.) We also calculate an LO phonon energy of 28.3 meV from Eq. (78), which is just slightly lower than the accepted value of 28.9 meV.

We stress that the carrier density and mobility listed above used the L-valley effective mass of 0.57. If we instead used the Γ-valley effective mass of 0.041, this would result in a carrier concentration n=5.1×10^{16} cm^{-3} (within specifications) and a mobility of 14,000 cm^2/Vs (which is much too high).

To fit the data for n-type GaSb with the Drude-Lorentz model, we fix the TO energy at 27.78 meV and its broadening at 0.3 meV (instrumental resolution). We also calculate the amplitude A=1.19 from Eq. (68) using the value of 28.89 meV for the LO phonon energy. This leaves the plasma frequency and Drude broadenings as the only parameters, assuming an L-valley electron mass of 0.57. Since the Drude broadening trends to very small values in the fit (leading to unphysically high mobilities), we fix γ_D at 2 meV, which corresponds to a mobility of 1000 cm^2/Vs, just like for the Kukharskii model. The screened plasma frequency is the only remaining parameter. We find E_P=17 meV (independent of our choice of γ_D), which corresponds to an electron concentration of 1.8×10^{18} cm^{-3}, clearly much higher than expected.

We note that the curvature of ψ at the lowest photon energies has two contribution, due to TO phonon absorption and due to free carriers. The TO phonon contribution to ψ is known (since the TO and LO phonon energies are known and the broadening can be set to the instrumental resolution) and therefore the Drude contribution can be fitted with a single parameter (the electron contribution). Nevertheless, the sensitivity to the Drude contribution is small and therefore an actual determination of the carrier contribution would require measurements at longer wavelengths, beyond the TO energy of 27.78 meV. Perhaps the extrapolation of our data to longer wavelengths and the subtraction of the lattice absorption effect is the reason for our poor values for carrier concentration and mobility of n-type GaSb.

B. p-type GaSb with high doping

The effects of free carrier absorption are much more pronounced for the p-type sample with very high doping, see Fig. 3.8 (data above 0.8 eV are not available for this sample). We clearly see an increase of $\langle\epsilon_2\rangle$ and a decrease of $\langle\epsilon_1\rangle$ at the lowest energies, which is much larger than the expected phonon response. To fit these data with the Drude-Lorentz model, we fix the phonon parameters as stated above for the n-type sample. Figures 3.8 and 3.9 show the best fit with a single Drude term, leading to a hole concentration of 3.4×10^{18} cm^{-3} (with an effective hole mass of 0.3) and a mobility of 117 cm^2/Vs, which is quite reasonable.

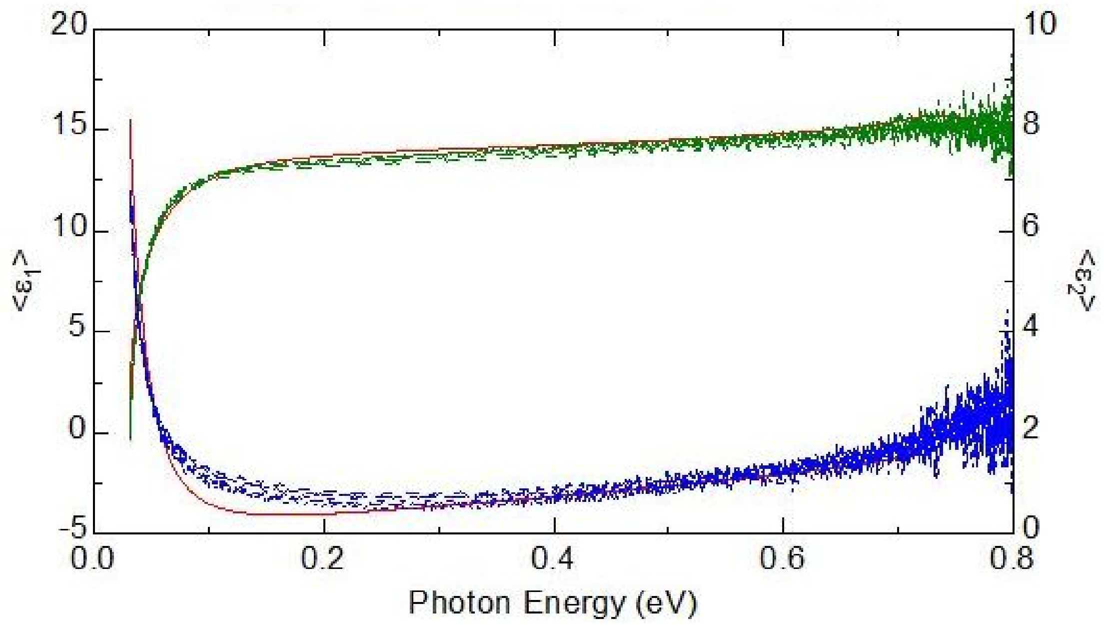

Figure 3.8: As Fig. 3.1, but for p-type bulk GaSb with 6 nm native oxide and a hole density greater than 10^{18} cm^{-3}. The lines show the best fit with a single Drude term and fixed TO lattice absorption.

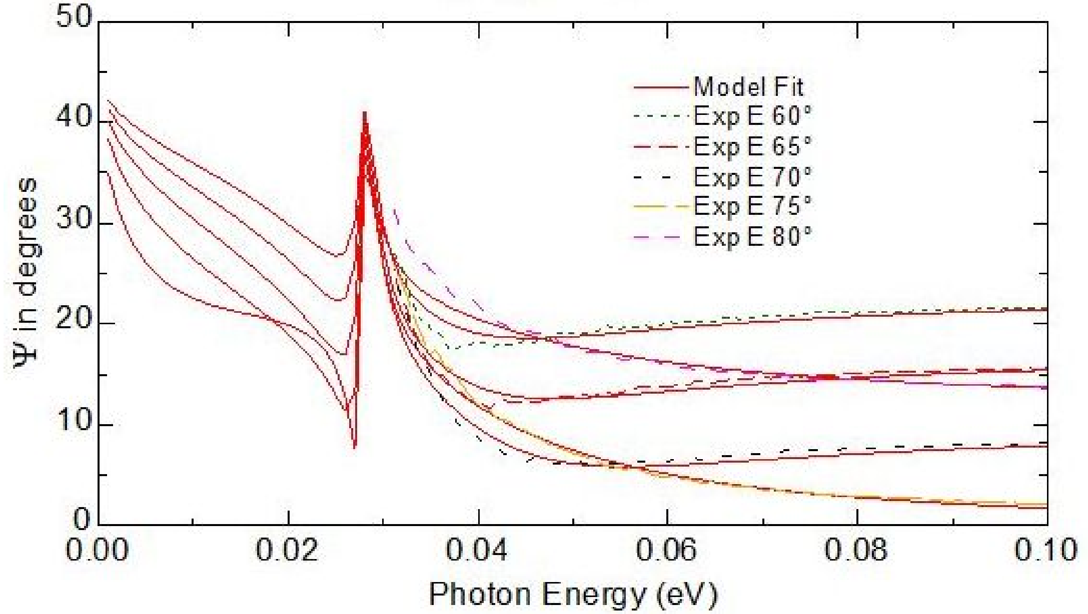

Figure 3.9: As Fig. 3.2, but for p-type bulk GaSb with a hole density greater than 10^{18} cm^{-3}. The lines show the best fit with a single Drude term and fixed TO lattice absorption.

However, this fit is not very good. A much better fit can be obtained with two carrier species, a large term with a (screened) plasma frequency of 49.3 meV and Γ_D=318 meV (unreasonably large), and a smaller term with ω_P=26.5 meV and Γ_D=9.2 meV.

A Kukharskii fit using Eq. (83) with a single plasmon-phonon polariton (single hole species plus TO/LO phonon) yields a better fit than the Drude-Lorentz fit with a single type of holes. The parameters are shown in Table 3.1. We find E_{LP}=25.1 meV and E_{UP}=32.0 meV, which yields a plasma frequency of E_P=28.9 meV and a carrier density of 2.5×10^{18} cm^{-3}, which is reasonable. The

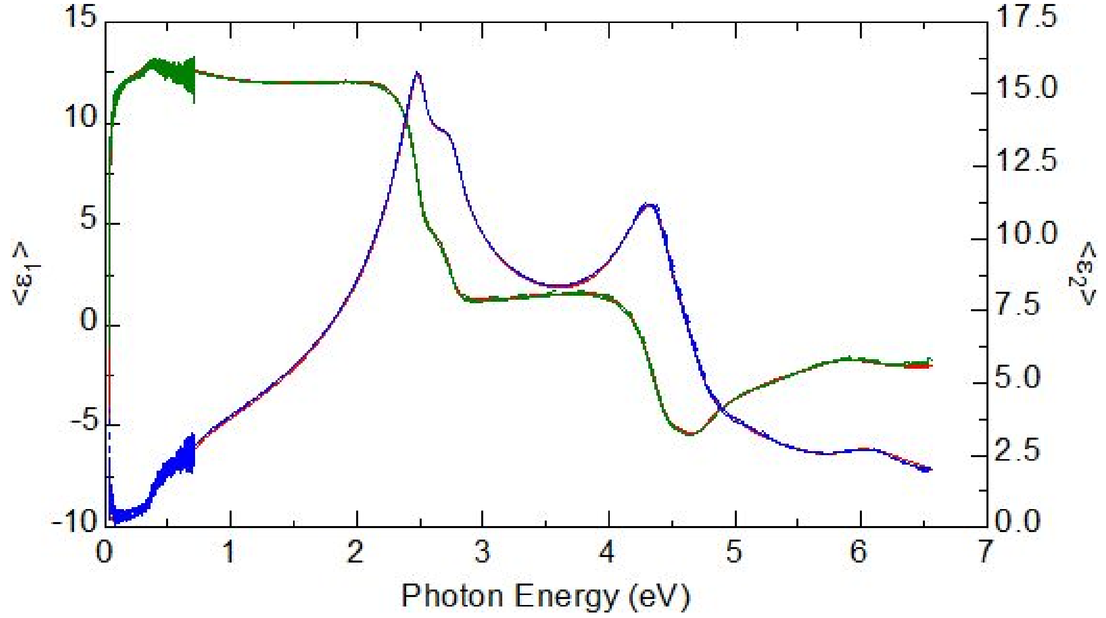

Figure 3.10: As Fig. 3.1, but for nominally undoped InAs. Experimental data are shown by symbols (green-$\langle\epsilon_1\rangle$, blue-$\langle\epsilon_2\rangle$). Data from two instruments were merged. The lines show the best fit with Eq. (74), including one plasmon-phonon polariton and a parametric oscillator model to account for interband electronic transitions. The native oxide thickness is 6 nm.

Kukharskii broadening is Γ_K=6.4 meV, which seems a bit small, yielding a high mobility of 600 cm^2/Vs. We were unable to find a better fit by adding a second plasmon to Eq. (83).

3.7.3 Results for InAs

Figure 3.10 shows the pseudo-dielectric function of nominally undoped InAs from 0.03 to 6.5 eV. The model for this wafer consists of a bulk InAs substrate and a

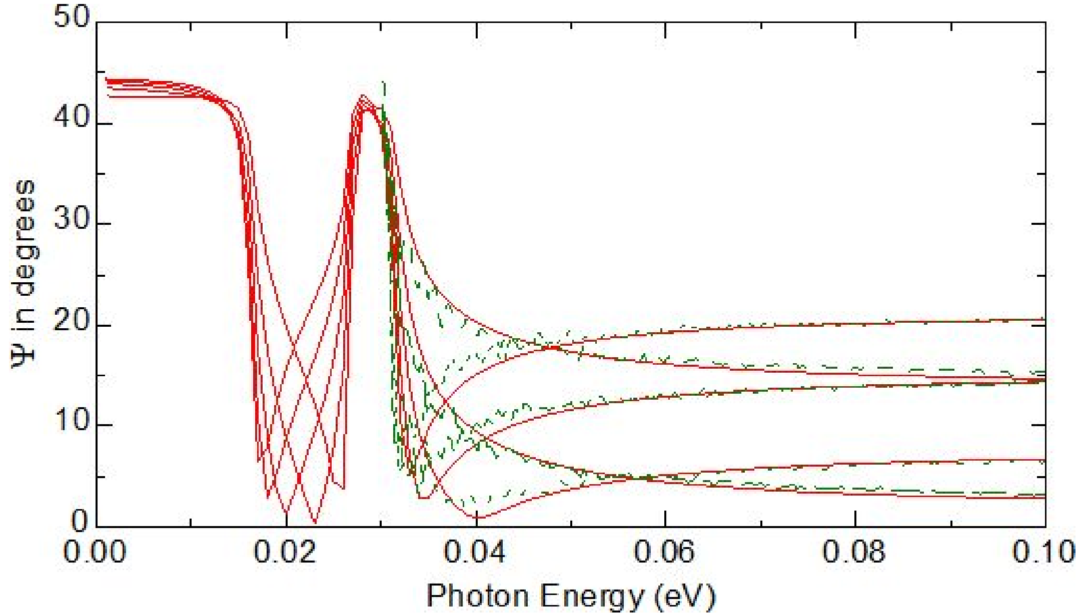

Figure 3.11: As Fig. 3.2, but for nominally undoped InAs. The lines show the best fit with a single plasmon-phonon polariton to account for free carrier and lattice absorption.

6 nm thick native oxide [164] (quite thick, no surface cleaning was attempted). The interband electronic transitions in the substrate are described using a semiconductor parametric oscillator model. Since prior experimental data for InAs are sparse below 1.5 and above 6 eV, we made small adjustments to the published model parameters, especially in the region near the direct band gap E_0, which can be seen clearly as an absorption threshold and a peak in $\langle\epsilon_1\rangle$ near 0.37 eV. Below E_0, $\langle\epsilon_2\rangle$ is about zero (except for the native oxide contribution to the pseudo-absorption), but $\langle\epsilon_1\rangle$ shows a clear drop below E_0. The high-frequency dielectric constant from our parametric model is ϵ_∞=12.2, close to its accepted value.

The FTIR-VASE data (below 0.7 eV) are noisier than in the near-IR, visible, and UV. Despite these noise issues, it is clear that there is a slow drop below 0.35 eV (due to the contribution of E_0 to the dielectric function) and then a sharp drop below 0.08 eV (due to plasmon-phonon polaritons).

We show a magnified graph of the far-IR data in Fig. 3.11. ψ is rather flat near 0.1 eV and drops slowly towards smaller energies, until reaching a minimum between 0.33 and 0.38 eV (depending on the angle of incidence). There is a very steep egde near 0.03 eV, where ψ reaches almost 45°. This is the upper edge of the second restrahlen band and indicates the upper phonon-plasmon polariton energy. Our model places the TO phonon of bulk InAs at 27 meV, since it is not affected by free carrier effects. We also fix its broadening at 0.3 meV (the instrumental resolution). The UP polariton is at 31 meV, significantly higher than the LO phonon energy of 29 meV. This is due to the polariton effects pushing the UP energy above the LO phonon energy because of free carrier effects (doping). We fix its broadening at 1 meV to get good agreement with the data. Finally, the LP polariton energy is 15 meV, well below our experimental range, also with a fixed broadening of 1 meV. We also fix the Kukharskii (mobility) broadening at 1 meV, since our data are not sensitive to this parameter.

The plasma frequency calculated from Eq. (77) is 17 meV, and the LO frequency calculated from Eq. (78) is 30 meV, only slightly higher than the accepted value of 29 meV. From the plasma frequency, we calculate an electron density of

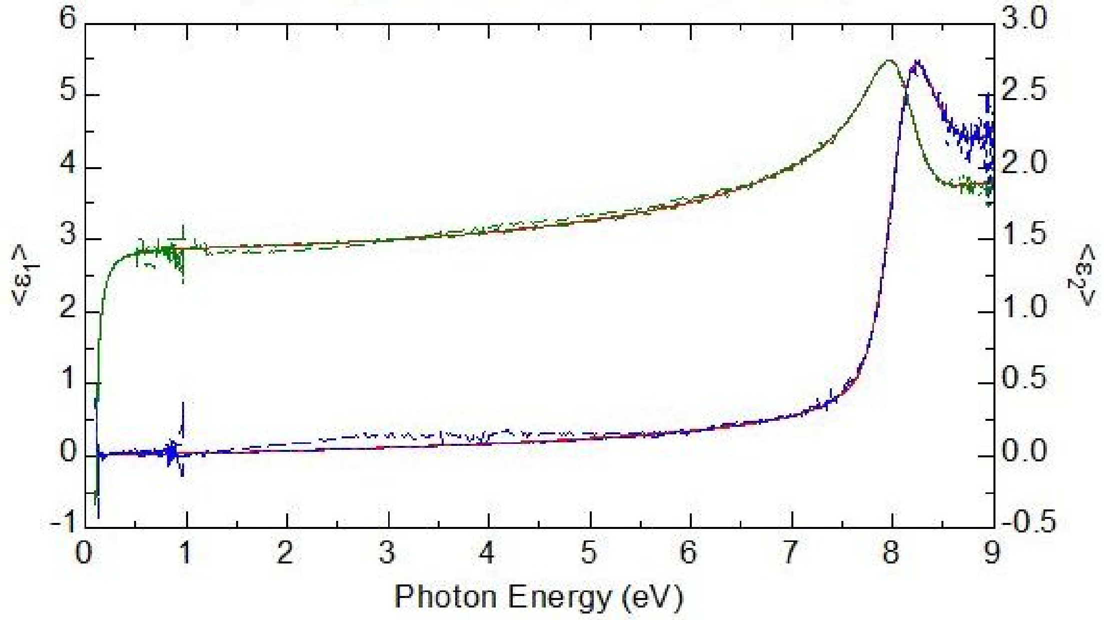

Figure 3.12: Pseudodielectric function for spinel ($MgAl_2O_4$) with 16.4 Å surface roughness from the mid-IR to the vacuum-UV. Data are shown in green ($\langle\epsilon_1\rangle$) and blue ($\langle\epsilon_2\rangle$), the model fit using Eq. (74) in red. Two Tauc-Lorentz oscillators and a pole define the dispersion in this energy range.

5.9×10^{16} cm^{-3} for this nominally undoped sample, assuming an effective electron mass of 0.023 for InAs. Our Kukharskii broadening of 1 meV results in a mobility of 50000 cm^2/Vs, which is a little (but not much) too high (Karataev 1977), since we are not sensitive to the broadenings parameters in our InAs data. (Basic parameters for bulk InAs were taken from the Ioffe Institute web site.)

3.7.4 Results for spinel

To demonstrate that Eq. (74) can be applied over the complete spectral range from 0.03 to 9.0 eV, we present a new fit to data previously [157] published for spinel ($MgAl_2O_4$). In our previous work [157], we used five TO/LO oscillators as in Eq. (76) to describe the infrared spectral region and two Tauc-Lorentz oscillators and a pole for the near-IR to vacuum-UV region. Both regions were fitted separately. The problem with this approach was that ϵ_∞ entered as a separate parameter in both fits and we had to make sure that it was consistent in both parts.

Our new Eq. (74) allows us to fit the entire dataset from 0.03 to 9.0 eV in one step. All parameters were adjusted simultaneously, including the surface roughness. To reduce the differences between data and fit, we increased the number of TO/LO phonon pairs from five to seven, but it is not clear if the two additional phonon modes are uniquely defined by the data. Results are shown in Figs. 3.12, 3.13, and 3.14. The Drude factor was set to unity for this insulator. Our revised parameters are very similar to those published previously [157] and therefore not listed again.

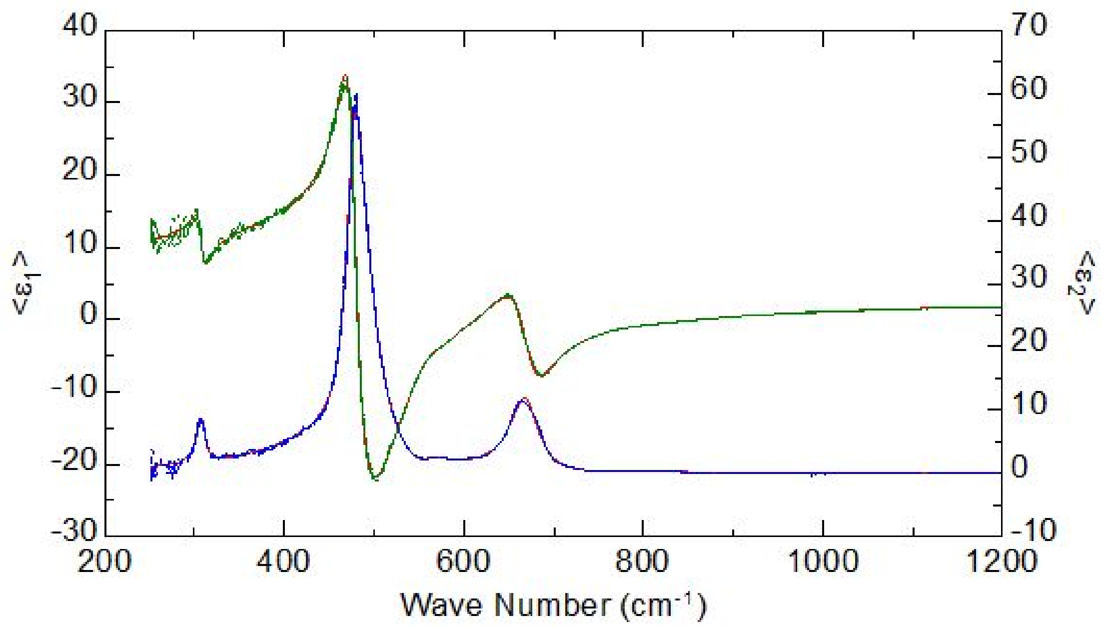

Figure 3.13: As Fig. 3.12, but for the mid-infrared spectral range of spinel ($MgAl_2O_4$). Seven TO/LO phonon pairs as in Eq. (76) define the dispersion in this energy range.

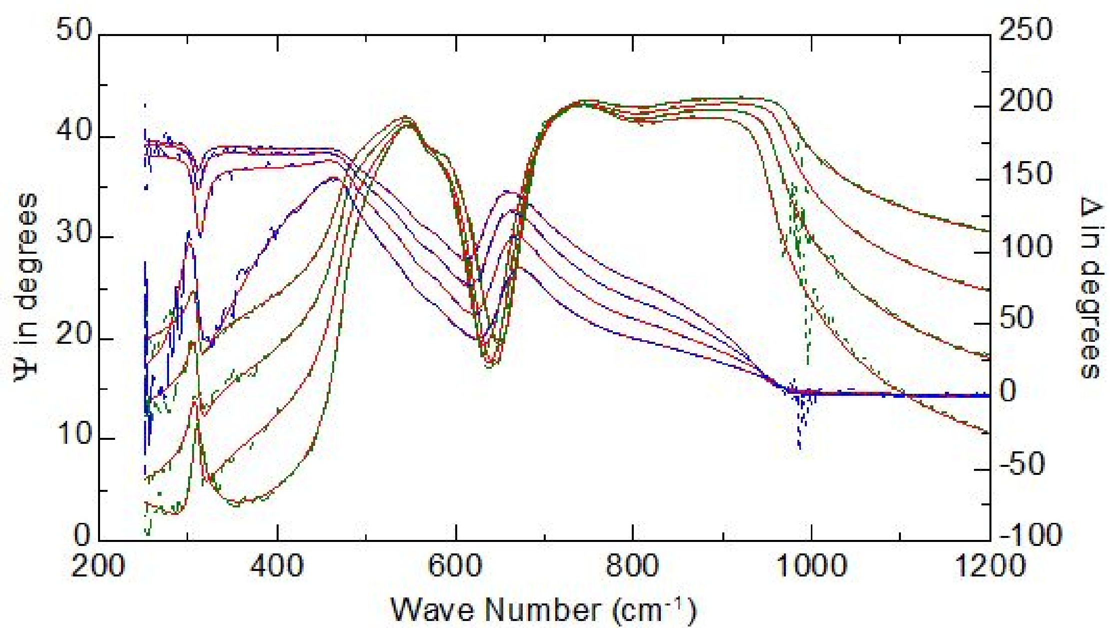

Figure 3.14: As Fig. 3.13, but data are displayed as ellipsometric angles ψ (green) and Δ (blue) for four angles of incidence from 60° to 75°.

4 THICKNESS DEPENDENCE OF INFRARED LATTICE ABSORPTION AND EXCITONIC ABSORPTION IN ZNO LAYERS ON SI AND SIO_2 GROWN BY ATOMIC LAYER DEPOSITION

This article was published in the Journal of Vacuum Science and Technology B, volume **38**, 042201 (2020).

Nuwanjula S. Samarasingha[1], Stefan Zollner[1], Dipayan Pal[2], Rinki Singh[3], Sudeshna Chattopadhyay[2,3,4]

1.Department of Physics, New Mexico State University, MSC 3D, P.O. Box 30001, Las Cruces, New Mexico 88003, USA

2.Discipline of Physics, Indian Institute of Technology Indore, Indore 453552, India

3.Discipline of Biosciences and Biomedical Engineering, Indian Institute of Technology Indore, Indore 453552, India

4.Discipline of Metallurgy Engineering and Materials Science, Indian Institute of Technology Indore, Indore 453552, India

4.1 Abstract

Using spectroscopic ellipsometry from the mid-infrared (0.03 eV) to the deep ultraviolet (6.5 eV), the authors determined the thickness dependence of the dielectric function for ZnO thin layers (5 to 50 nm) on Si and quartz in comparison

to bulk ZnO. They observed a small blueshift of the band gap (about 80 meV) in thin ZnO layers due to quantum confinement, which is consistent with a simple effective mass theory in an infinite potential well. There is a drastic reduction of the excitonic effects near the band gap, especially for thin ZnO on Si, which affects not only the excitonic absorption peak, but also lowers the high-frequency dielectric constant by up to 40%. No significant change of the phonon parameters (except an increased broadening) in thin ZnO layers was found.

4.2 Introduction

The dielectric function (DF) of crystalline group-IV and III/V semiconductors does not vary significantly with growth conditions, substrate, or layer thickness. For example, the DF of bulk silicon [74] is very similar to that of thick polycrystalline Si [75] or silicon-on-insulator [76, 77]. The DF of bulk GaN [78, 79] is nearly the same as for layers grown on sapphire [80,81], SiC, or GaAs [82]. Differences, if any, appear primarily near the infrared-active phonon peaks or interband critical points due to strain (small shifts), disorder, or finite-size effects (shifts, broadenings), but the high-frequency dielectric constant ϵ_∞ is nearly constant [77].

On the other hand, the DF of complex metal oxides is highly variable. Bulk [83] $SrTiO_3$ (STO), for example, has a much higher DF than thick polycrystalline STO on Si [84] or thin polycrystalline layers of STO on Pt [83]. The high-frequency dielectric constant ϵ_∞ of epitaxial STO on Si decreases monotonically with thickness,

accompanied by a Kramers-Kronig-consistent decrease in the UV absorption [85]. This was attributed to an interfacial SiO_2 layer, which becomes more important for thinner STO layers [85]. Strain-induced effects in metal oxides [86–88], such as $BaTiO_3$ or $PbTiO_3$, are also much larger than elasto-optic effects in semiconductors [89, 90].

Without thickness and roughness measurements by x-ray reflectance (XRR, which is more accurate than electron microscopy) and atomic force microscopy (AFM), such ellipsometry results are often problematic to analyze due to parameter correlations: ellipsometry cannot determine both the optical constants and the thickness of ultrathin layers or may not be able to detect thin interfacial layers, surface roughness, or density variations [45, 46, 91].

Similar thickness-dependent DFs were also found for several metals [92, 93]. This might be due to variations in density caused by voids in the layers, island growth for ultrathin layers, or variations of the Drude parameters with grain size [94].

To avoid the well-known defectivity and variability of complex metal oxides [95], such as perovskites, the present study focuses on ZnO layers. ZnO is an attractive material for applications [96], especially for photovoltaics [97], as a transparent conductor made of abundant elements (alternative to indium tin oxide), and high-temperature electronics. Unique properties include a high excitonic binding energy [96] of 60 meV, good chemical and mechanical stability [96, 98],

and the ability of doping [99] as an n-type conductor [100, 101].

Several studies on the variability of the optical constants of ZnO layers have already appeared [98, 102–107]. Using spectroscopic ellipsometry, Logothetidis *et al.* [98] found a dependence of the optical constants of sputtered ZnO on Si on partial pressure and thickness, but the thickness dependence was not monotonic. Nie *et al.* [102] found a quantum confinement shift of the band gap of ZnO produced on sapphire by pulsed laser deposition. Their measured shift was 250 meV in the thinnest layers (5 nm), but this study has three flaws: The thickness was determined from XRD using the Scherrer formula [101] (which is not very accurate and does not determine density or roughness) and the absorption coefficient was determined from transmission measurements (which might be affected by varying reflection losses due to changes in refractive index). The absorption coefficient did not depend monotonically on thickness. Using photoluminescence of annealed ZnO layers on glass produced by DC magnetron sputtering, Mosquera *et al.* [103] found a much larger confinement shift of up to 650 meV in layers of only 10 nm. They determined thickness using a DECTAC profilometer and found the band gap by photoluminescence, which might be related to defects rather than band edges. Li *et al.* [104] found a monotonic decrease of the DF in thinner ZnO on Si (sputtered on a 30 nm thermal SiO_2 oxide) with ellipsometry and a confinement shift of up to 140 meV in their thinnest (10 nm) layers with a grain size of 6 nm determined using the Scherrer formula and scanning electron microscopy. No in-

dependent method to determine thickness or density was used. The decrease in the DF was attributed to reductions of single-particle interband absorption and exciton-continuum absorption, while the discrete exciton absorption was affected less [104]. Their theoretical model was rather incomplete, because it did not address the reasons for these changes, especially the relative weight of the discrete and continuum exciton absorption. To rule out layer density as a factor influencing the dependence of the ZnO DF on thickness, Pal *et al.* [105, 106] determined thickness, density, grain size, and roughness of ZnO on Si grown by atomic layer deposition [99] (ALD) using XRR, XRD, and AFM [101]. They found a monotonic dependence of the DF on thickness and a confinement shift of no more than 100 meV.

Given the considerable variability in the literature regarding the optical constants of ZnO thin layers, we deposited a new set of ZnO layers by ALD, with thicknesses from 5 to 69 nm. To reduce the influence of interfacial layers, we studied ZnO layers on Si as well as on SiO_2, compare Ref. 108. We carefully determined crystallinity, surface roughness, density, and layer thickness with x-ray diffraction (XRD), AFM, and XRR. To understand the physics of the variability of the DF and the influence of electronic and vibrational structure changes, we combined data over a broad spectral range, from the mid-infrared (0.03 eV) to the deep ultraviolet (6.6 eV).

We find significant variations of the optical constants of ZnO as a function of

thickness. The role of the substrate (Si or quartz) is also very important. The excitonic direct-gap peak is strongly broadened and weakened in thinner layers. The infrared-active E_1 phonons are also broadened due to finite-size effects. The blueshift of the band gap due to quantum confinement is smaller than reported before, but in excellent theory with a simple theoretical model. Our most striking result is a 40% reduction of the high-frequency dielectric constant in thin layers on Si, which we explain with a shift of oscillator strength to higher photon energies due to the weakening of the excitonic electron-hole attraction.

4.3 Experimental Methods and Results

Wurtzite-type ZnO films with preferred c-axis orientation were grown at 200°C on single-side polished Si (001) and SiO_2 (fused amorphous quartz) substrates using atomic layer deposition (ALD) with diethylzinc and water as precursors and nitrogen as a carrier and purge gas, as described elsewhere [105, 106]. Large-area uniform layers for shallow-angle ellipsometry and XRR measurements were produced by growth on 20 by 20 mm^2 substrates. By varying the number of ALD growth cycles from 30 to 410, layer thicknesses between 5 and 70 nm could be achieved, as measured using XRR. The growth rate of ZnO was about 1.7 Å per cycle. Table 4.3 gives an overview of the samples with XRR characterization results. Layers on Si had an interfacial oxide with a thickness of about 1 nm. The surface roughness was also about 1 nm, much less than for sputtered ZnO

layers [98, 103, 109, 110], and agreed well between AFM and XRR, see Fig. 4.10. Most layers had an electron density just below that of bulk ZnO, except for the thinnest layers on SiO_2, for which it was about 10% lower. See supplemental material for more information regarding characterization of the layers with AFM, XRD, and XRR.

The ellipsometric angles [45, 46] ψ and Δ of the as-received layers (without cleaning) were acquired from 0.03 to 6.5 eV at three angles of incidence (60°, 65°, and 70°) on two different instruments. A J. A. Woollam FTIR-VASE instrument was used to measure in the mid- and near-infrared spectral regions from 0.03 to 0.6 eV. A J. A. Woollam VASE instrument provided data from 0.5 to 6.5 eV (near-infrared to deep ultraviolet). The overlap in the region between 0.5 and 0.6 eV (where data were taken on both instruments) is good, but not perfect. All measurements were performed in air at 300 K. Typical spectra for thin and thick ZnO on Si and SiO_2 are shown in Figs. 4.1, 4.2, 4.3, and 4.4. Strong anisotropy effects [111] were seen in thick ZnO layers on quartz.

4.4 Dielectric function models

We extract the dielectric functions for the ZnO layers on Si [74] by fitting the ellipsometric angles versus angular frequency ω with an isotropic model for ZnO [21]

$$\epsilon(\omega) = \frac{\omega_{\mathrm{LO}}^2 - \omega^2 - i\gamma_{\mathrm{LO}}\omega}{\omega_{\mathrm{TO}}^2 - \omega^2 - i\gamma_{\mathrm{TO}}\omega} \left[1 + \sum_i g_i(\omega)\right] \times \prod_i \left[1 + G_i(\omega)\right], \quad (88)$$

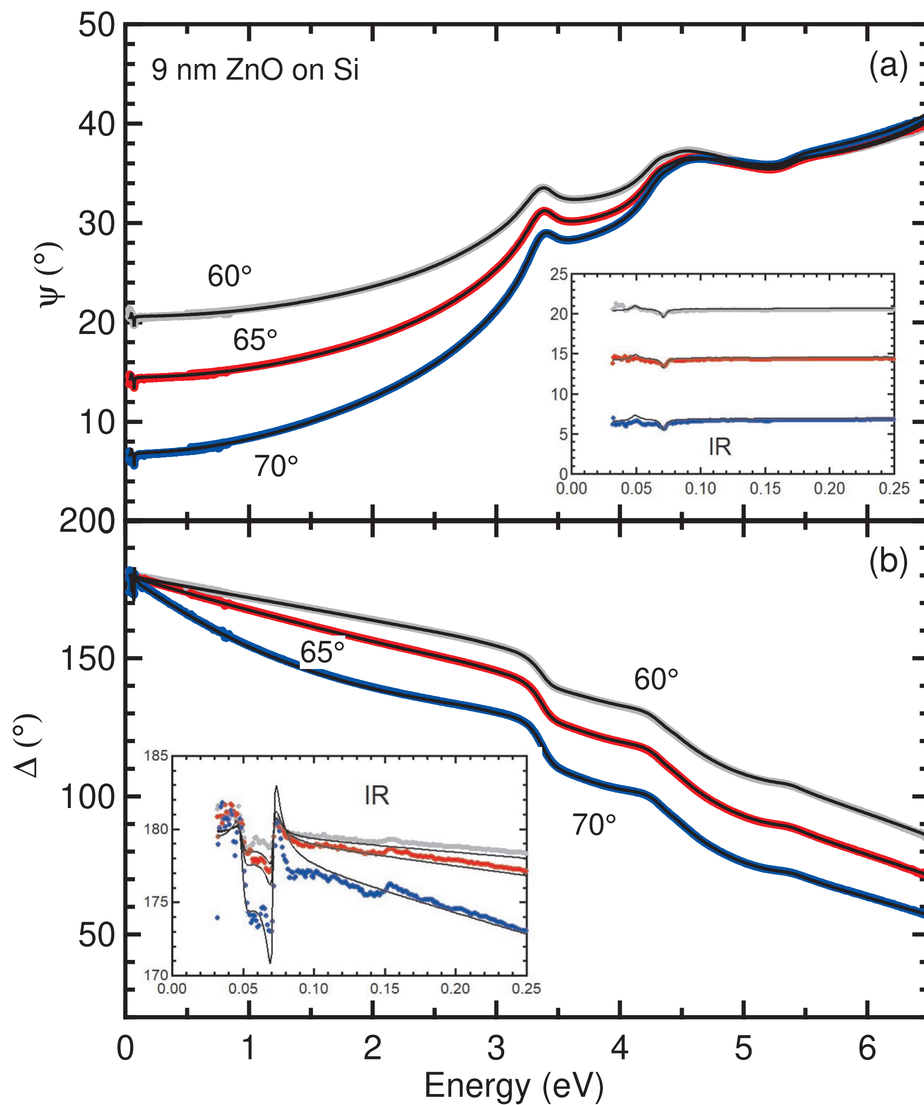

Figure 4.1: Ellipsometric angles ψ and Δ for 9 nm ZnO on Si. Symbols: experimental data; solid: best fit with an isotropic model based on Eq. (88). The inset shows a magnified view of the infrared spectral region from 0 to 0.25 eV.

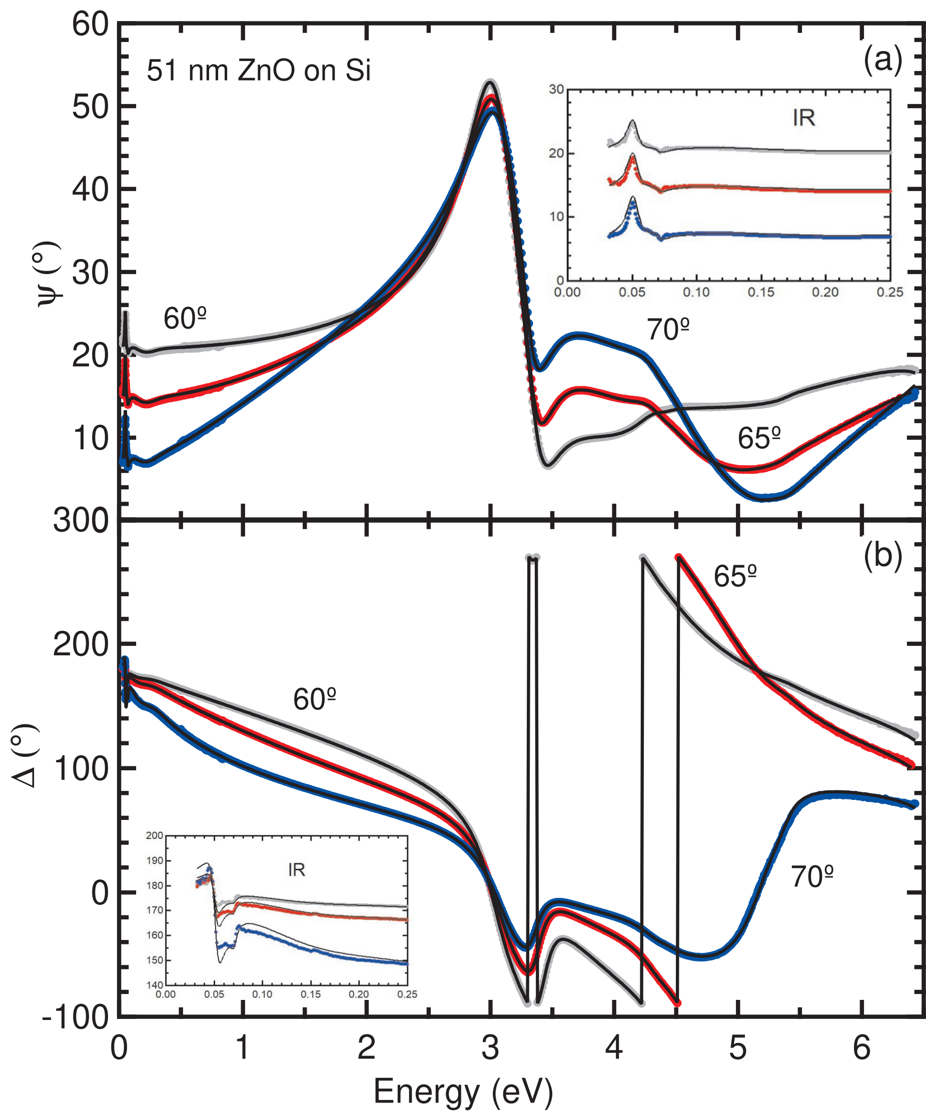

Figure 4.2: As Fig. 4.1, but for 51 nm ZnO on Si.

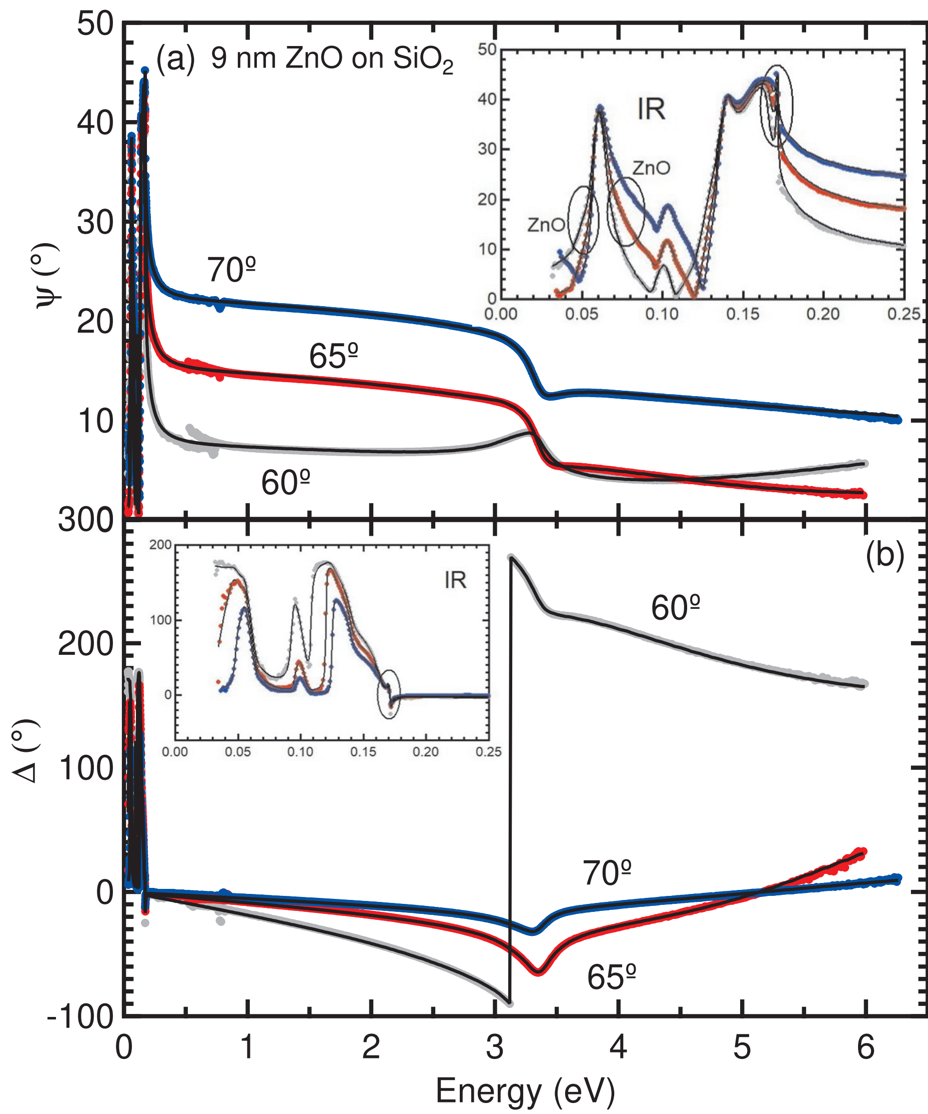

Figure 4.3: As Fig. 4.1, but for 9 nm ZnO on SiO_2. ZnO vibrational features affect the spectra mostly within the ovals.

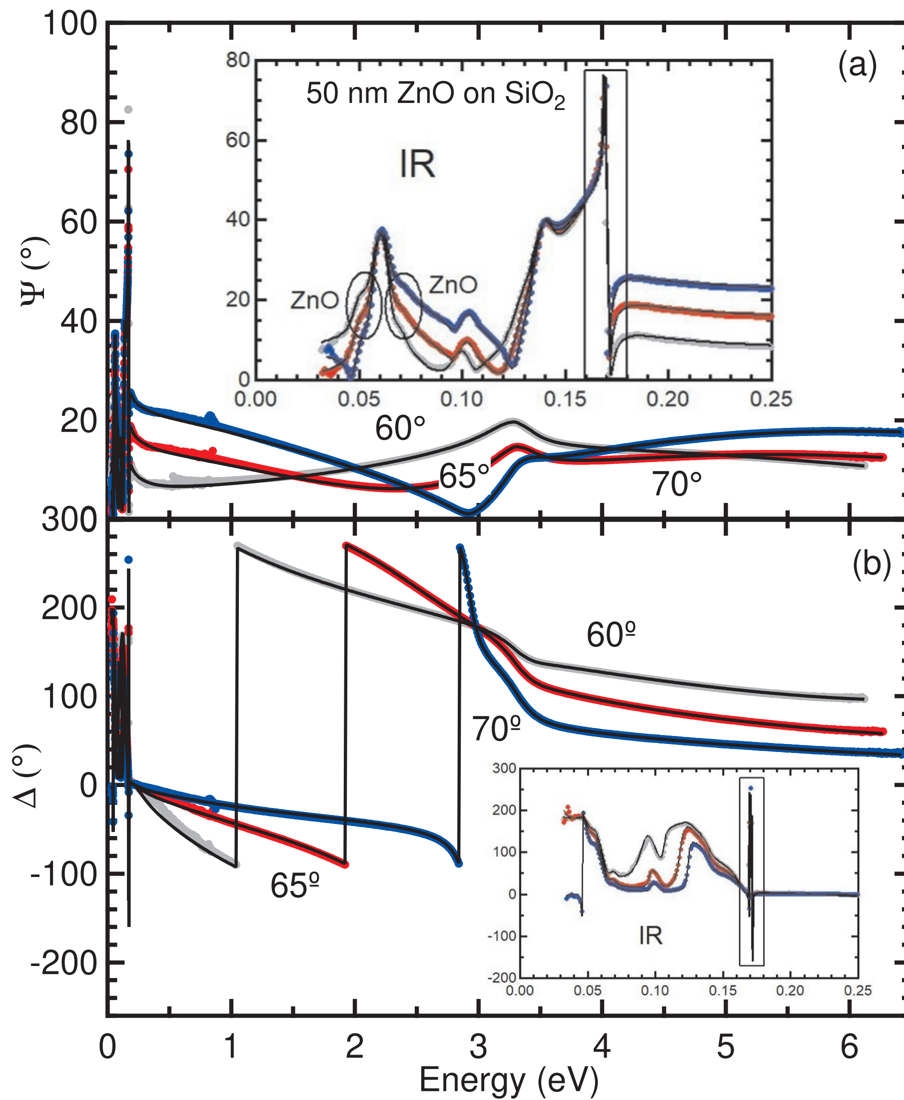

Figure 4.4: As Fig. 4.3, but for 50 nm ZnO on SiO_2 with a partially anisotropic model for ZnO. Effects of ZnO anisotropy appear within the rectangular boxes.

similar to the model (99) for bulk ZnO described in the supplemental material. This model allows us to describe the entire dielectric function from the mid-infrared to the deep ultraviolet with a single equation, while retaining the option of different broadening parameters γ for the transverse optical (TO) and longitudinal optical (LO) phonons. The first factor [14] contains the infrared lattice response, while the second factor describes the electronic response with oscillator functions $g_i(\omega)$, such as Tauc-Lorentz or Herzinger-Johs parametric oscillators [46,74]. The third factor, which is not needed for bulk ZnO, contains complex Gaussian functions $G_i(\omega)$ with an imaginary part

$$\mathrm{Im}\left[G\left(\omega\right)\right] = Ae^{-\left(\frac{\omega-E}{\sigma}\right)^2} - Ae^{-\left(\frac{\omega+E}{\sigma}\right)^2} \tag{89}$$

and a Kramers-Kronig consistent real part. It describes an anomalous broad infrared absorption, perhaps related to defects, such as oxygen vacancies [112]. These Gaussians are required to describe the optical constants for some of the thicker ZnO layers, especially on quartz. The Gaussian oscillator has three parameters, a dimensionless amplitude A, a resonance energy E, and a FWHM broadening $\Gamma = 2\sigma\sqrt{\ln 2}$. At most two Gaussians were needed to achieve a good fit to the ellipsometric angles. Gaussian parameters are listed in Tables 4.1 and 4.2, along with the TO and LO parameters.

For ZnO on Si, our model consists of the following layers: ambient, roughness, ZnO layer, interfacial SiO_2, Si substrate. The ZnO layer thickness on Si

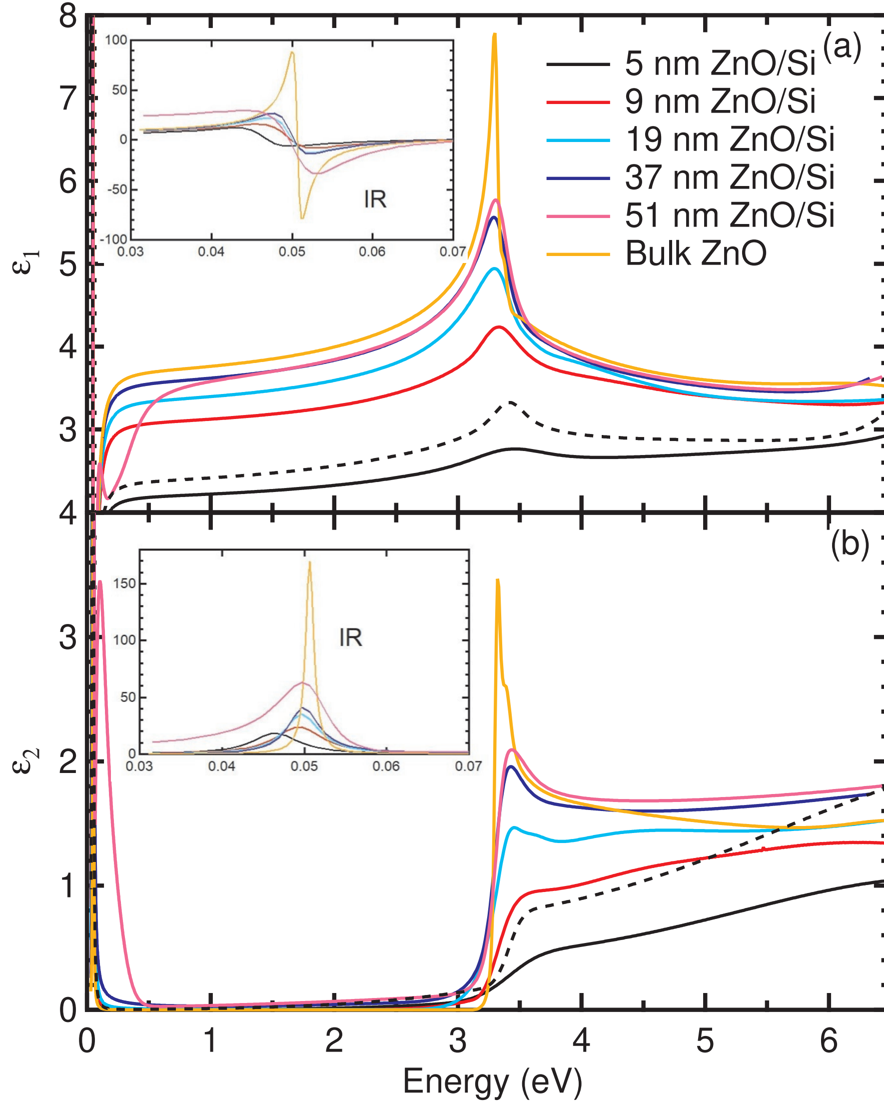

Figure 4.5: Real and imaginary parts of the complex dielectric function for ZnO films on Si versus photon energy. The inset shows a magnified view of the infrared spectral region from 30 to 70 meV. The dotted lines are explained in Sec. 4.8.11.

was treated as a parameter shown in Table 4.3. SE and XRR find very similar results for the ZnO layer thickness. The interfacial SiO_2 layer thickness was fixed at 1 nm. The roughness layer thickness was obtained from the XRR results in Table 4.3. The entire model for ZnO on Si has 25-31 free parameters, including the ZnO thickness, four TO/LO energies and broadenings, three parameters for each Gaussian, four for the Tauc-Lorentz oscillator, seven for each simplified parametric oscillator, and two for the UV pole. We started by fitting the TO/LO and Gaussian parameters to the ellipsometric angles in the infrared spectral region, taking the UV parameters from the bulk as a starting point. Then, we also adjusted the UV parameters by fitting the entire dataset. To avoid instabilities in the IR to UV fit, we had to fix some infrared parameters to the values obtained by fitting the infrared data set. These parameters are marked (f) in Tables 4.1 and 4.2. For the fit of the thinnest ZnO layers on Si, we had to enforce the condition [14] $\Gamma_{\mathrm{LO}} \geq \Gamma_{\mathrm{TO}}$.

To determine the dielectric functions for ZnO on SiO_2 (quartz), we first obtained the dielectric function of quartz from measurements of a bare substrate, see supplemental material, especially Fig. 4.16. We proceeded in a similar fashion to fit the ellipsometric angles for ZnO on quartz as on Si. However, the thickest ZnO layers on SiO_2 required a partially anisotropic model (with different phonon energies and broadenings in the ordinary and extraordinary direction and a constant birefringence offset $\epsilon_{\infty e} - \epsilon_{\infty o}$=0.08), see Sec. 4.8.4. This model contained

the following layers: ambient, roughness, ZnO layer, quartz substrate. We did not include an interfacial layer in this model, because we do not know how the substrate clean and ALD growth affected the quartz substrate surface. Our data did not require a fully anisotropic treatment of the optical constants [113].

After these oscillator fits were completed and the ZnO layer thickness determined, we also performed independent wavelength-by-wavelength (or point-by-point) fits, where the thickness was fixed and the real and imaginary parts of the dielectric function treated as free parameters at each wavelength. Both methods resulted in very similar dielectric functions (see Figs. 4.17 and 4.18), but the point-by-point dielectric function is usually noisier than the oscillator fit.

4.5 Ellipsometry Analysis

The dielectric functions for ZnO layers on Si and SiO_2 with various thicknesses between 5 and 51 nm are shown in Figs. 4.5 and 4.6. Data for bulk ZnO, determined as described in the supplementary material and in good agreement with prior ellipsometry measurements [115, 116] and theory [117], are also shown for comparison. Both ϵ_1 and ϵ_2 show significant variations with thickness over the complete spectral range, regardless of substrate.

For ZnO on Si, the absorption above the band gap (say, at 4 eV) increases monotonically with layer thickness. The exciton-phonon complexes [118–121] are not visible in the ZnO layers, only in the bulk. The excitonic enhancement of the

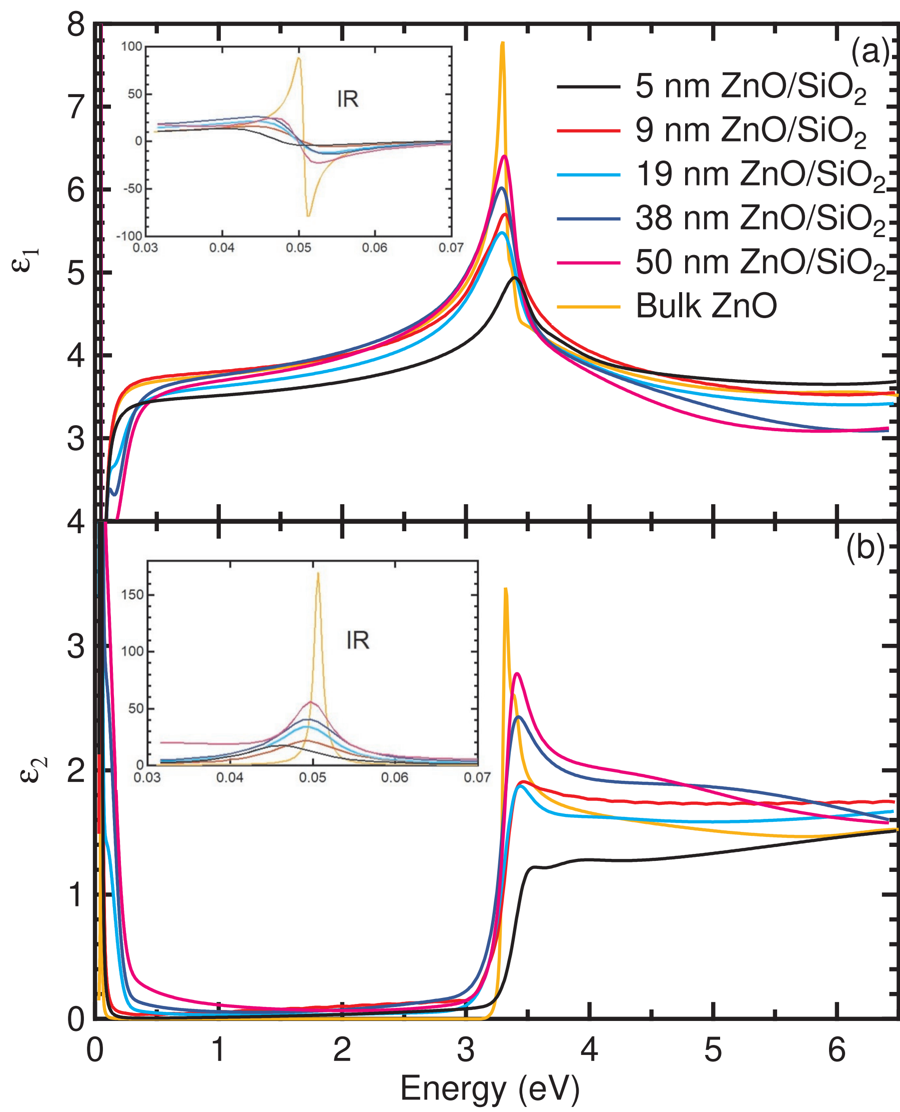

Figure 4.6: As Fig. 4.5, but for ZnO on SiO_2 (quartz).

Table 4.1: Longitudinal (LO) and transverse optical (TO) phonon energies E and broadenings Γ (errors in parentheses) of ZnO films on Si compared to the bulk for the ordinary (o) and extraordinary (eo) beam. Some films required additional Gaussian (G) oscillators with dimensionless amplitude A, energy E, and broadening Γ (both in cm^{-1}). Parameters marked (f) were adjusted to the infrared portion of the data and then fixed during the fit over the whole range.

		E_{TO} (cm^{-1})	Γ_{TO} (cm^{-1})	E_{LO} (cm^{-1})	Γ_{LO} (cm^{-1})
Bulk	o	408.75(6)	9.7(1)	589.67(5)	9.76(8)
	eo	378.9(5)	8(f)	574.3(1)	8.13(4)
Bulk[a]	o	408.2(3)		592.1(2)	
	eo	379(2)		577.1(4)	
51 nm		410(f)	61(f)	573(f)	75(f)
	G	A=3.8(f)	E=82(f)	Γ=1560(f)	
	G	A=2.4(f)	E=210(f)	Γ=2475(f)	
37 nm		402(f)	37(3)	577(f)	75(f)
19 nm		401(4)	41(f)	578(4)	50(5)
9 nm		399(f)	55(f)	575(5)	same as Γ_{TO}
5 nm		376(f)	55(f)	562(5)	same as Γ_{TO}

[a] Ref. 114.

Table 4.2: As Table 4.1, but for ZnO films on SiO_2. The fit is not sensitive to the values shown in italics, which were chosen arbitrarily.

		E_{TO} (cm^{-1})	Γ_{TO} (cm^{-1})	E_{LO} (cm^{-1})	Γ_{LO} (cm^{-1})
50 nm	o	403(f)	45(f)	591(f)	288 (f)
	eo	380(f)	*45*	580(f)	58 (f)
	G	A=1.6(f)	E=329(f)	Γ=1607(f)	
	G	A=0.9(f)	E=219(f)	Γ=231(f)	
38 nm	o	403(f)	74(f)	577(f)	180(f)
	eo	380(f)	*74*	581(f)	52(f)
	G	A=0.8(f)	E=577(f)	Γ=1376(f)	
19 nm	o	402(f)	70(f)	584(f)	118(f)
	eo	380(f)	70(f)	587(5)	41(f)
	G	A=0.47(f)	E=577(f)	Γ=1406(f)	
9 nm		399(f)	*83*	589(f)	95(f)
5 nm[a]		*376*	*90*	*558*	*90*

[a]Assuming identical parameters as for ZnO on Si.

absorption is much weaker in the ZnO layers (especially the thinner ones) than in bulk ZnO. The excitonic peak is broadened and completely disappears for the 5 and 9 nm thick ZnO layers on Si. The Tauc gap E_g determined from a Tauc plot (αE versus $\sqrt{E}$, see Sec. 4.8.7) increases for thinner layers and can be described with a confinement model [122]

$$E_g(t) = E_{g,\infty} + \frac{F}{t^2} - \Delta E, \tag{90}$$

see Fig. 4.7(a), where $E_{g,\infty}$=3.29 eV is the bulk ZnO Tauc gap, t the layer thickness, F the confinement factor (equal to $\hbar^2\pi^2/2\mu_{eh}$ for infinitely high barriers, where μ_{eh} is the electron-hole reduced effective mass), and ΔE a thickness-independent difference between the bulk and layer Tauc gap (for example due to defects, doping, etc). The bulk Tauc gap (determined by linear extrapolation of a Tauc plot as shown in Sec. 4.8.7) is about 80 meV lower than the bulk band gap of ZnO, usually given as 3.37 eV, see Ref. 116. The blueshift between our thinnest (5 nm) and thickest (51 nm) layers is no more than 80 meV, lower than what has been reported in the literature for other ZnO layers [102–104]. For the thickest ZnO layer (51 nm) on Si, there is a strong Gaussian absorption of unknown origin, with parameters given in Table 4.1. ϵ_1 drops towards the infrared spectral region due to the dispersion related to infrared lattice absorption. For the thickest (51 nm) layer, ϵ_1 drops earlier (near 1 eV) and reaches a minimum near 0.2 eV due to the unknown Gaussian absorption.

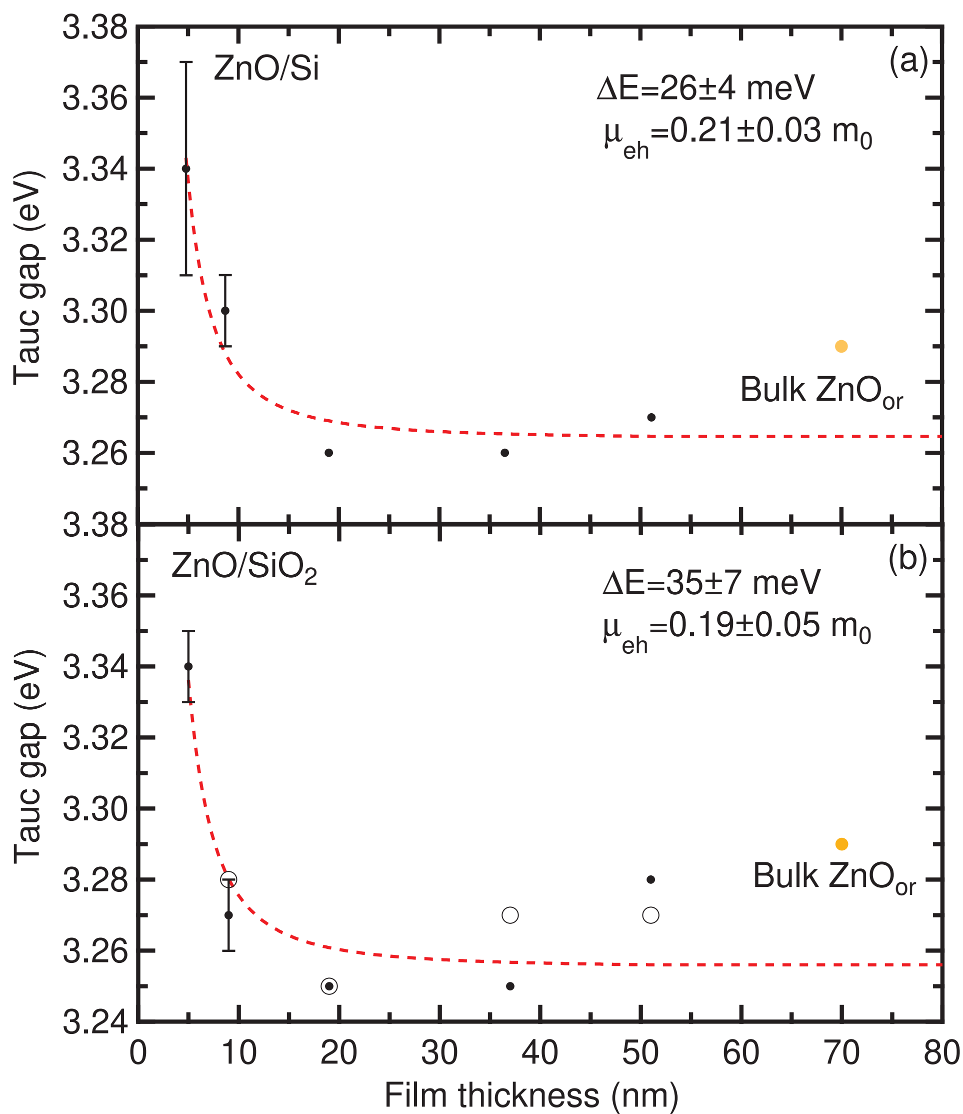

Figure 4.7: Tauc band gap of ZnO on Si (a) and SiO_2 (b) as a function of layer thickness from ellipsometry (•) and transmission measurements (∘). The dotted line shows the best fit with Eq. 90.

The dependence of ϵ_1 on thickness for ZnO on Si is Kramers-Kronig consistent with the dependence of ϵ_2. The excitonic enhancement of ϵ_1 near the band gap becomes weaker and is broadened in thinner films. In addition, there is a drastic reduction (by 40%) of ϵ_∞, determined from the second factor in Eq. (88) by setting ω=0, for thinner films, see Fig. 4.8(b). The differences of ϵ_1 between thinner and thicker films diminish towards higher energies. Unfortunately, we are not able to measure beyond 6.5 eV.

The thickness dependence of the optical constants for ZnO on quartz is qualitatively similar to the behavior on Si, but weaker. The excitonic peak at the band gap is not broadened as strongly in ZnO on SiO_2. This makes it easier to see the blueshift due to confinement, see Fig. 4.7(b). Also, the absorption does not drop off as rapidly as the thickness decreases. The unknown infrared Gaussian absorption is present in several layers on SiO_2. The high-frequency dielectric constant ϵ_∞ is nearly independent of thickness, see Fig. 4.8(b).

The phonon parameters used in these fits are given in Tables 4.1 and 4.2. The values of the TO phonon energies versus layer thickness are shown in Fig. 4.9 in comparison to the bulk [114]. From the TO and LO angular frequencies of the E_1 phonon, we can calculate the Born effective charge [123]

$$(e_t^*)^2 = V\mu\epsilon_0\epsilon_\infty\left(\omega_{LO}^2 - \omega_{TO}^2\right), \tag{91}$$

see Fig. 4.8(c), where ϵ_0 is the vacuum permittivity and ϵ_∞ the high-frequency

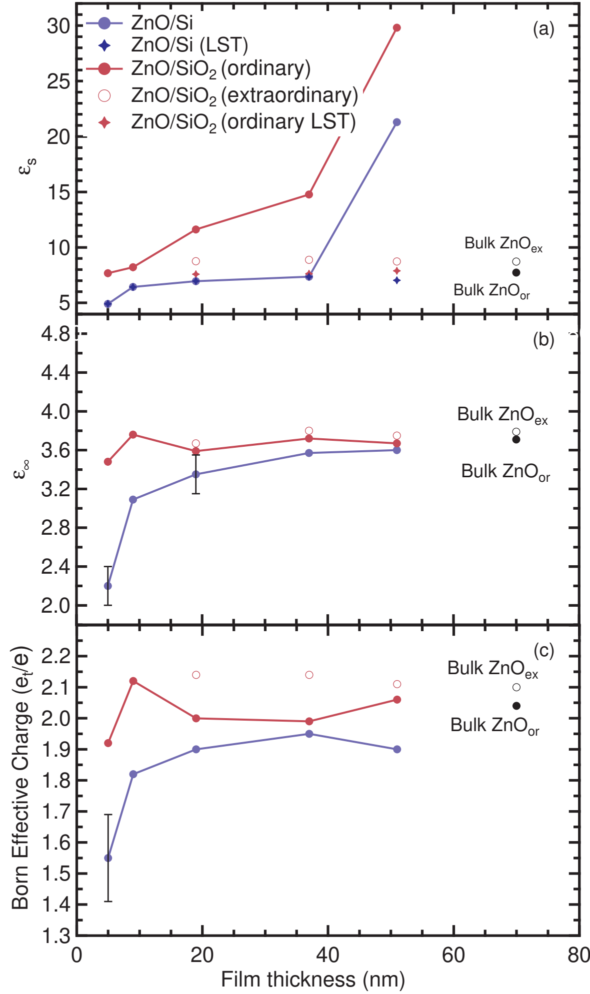

Figure 4.8: (a) Static dielectric constant ϵ_s calculated from Eq. (88) by setting ω=0 (•, ∘) and calculated from the TO and LO energies using the Lyddane-Sachs-Teller (LST) relation (119) (✦). (b) Thickness dependence of the high-frequency dielectric constant ϵ_∞, determined from the second factor in Eq. (88) by setting ω=0. (c) Born effective charge of the E_1 (•) and A_1 (∘) optical phonon calculated from Eq. (91) for ZnO on Si (blue) and on SiO_2 (red). The lines are drawn to guide the eye.

dielectric constant. μ is the reduced mass of the Zn and O atoms. V is the volume per ZnO formula unit.

4.6 Discussion

4.6.1 Quantum confinement

ZnO layers on Si and quartz show a confinement shift of about 80 meV for 5 nm thickness (for both types of substrates), see Fig. 4.7. This result is reasonable, similar to what has been found for InGaAs quantum wells with InP barriers [124]. Fitting the band gap versus thickness using Eq. (90) yields two parameters $\Delta E \approx 30$ meV and $\mu_{eh} \approx 0.2$, as shown in Fig. 4.7. These parameters are nearly the same for both substrates. The value of μ_{eh} from our confinement fit is very similar to the reduced excitonic effective mass determined from fits to optical spectra (photoreflectance and photoluminescence) [125]. The corresponding electron and hole effective masses are 0.29 and 0.66, respectively [125].

4.6.2 High-frequency dielectric constant

The second significant result is that the high-frequency dielectric constant ϵ_∞ is nearly independent of layer thickness for ZnO on SiO_2, but drops by 40% in the thinnest ZnO layers on Si, see Fig. 4.8. How do we explain this? ϵ_∞ is given by [126, 127]

$$\epsilon_\infty = 1 + \left(\frac{\omega_{\mathrm{pl}}}{\omega_{\mathrm{Penn}}} \right)^2 S_0, \tag{92}$$

where

$$\omega_{\rm pl}^2 = \frac{\rho e^2}{\epsilon_0 m_0} \tag{93}$$

is the unscreened plasma frequency, $\omega_{\rm Penn}$ the Penn gap, and S_0 a constant typically assumed to be unity [126]. The electron density ρ is the total number of electrons per unit cell divided by the unit cell volume. This number only depends on the elements in our compound (Zn and O, 8 electrons per formula unit) and the cell volume. Since the XRR density varies by less than 10% (see Sec. 4.8.3) and varies more for ZnO on SiO_2 than on Si, variations in density (or plasma frequency) cannot explain the observed changes in ϵ_∞.

On the other hand, the Penn gap $\omega_{\rm Penn}$ is the energy separation between the bonding and anti-bonding sp^3 hybrids, averaged in k-space over all bands. This Penn gap becomes smaller if the excitonic electron-hole interactions are turned on, which shifts oscillator strength to lower energies [128, 129]. Variations of the Penn gap (and thus ϵ_∞) can therefore be explained with variations of the excitonic interactions.

The dependence of S_0 on excitonic effects was recently discussed by Cirilo-Lombardo [130]. In the absence of excitonic effects, S_0=1 (Penn's [126] result). If excitonic effects are considered, then $S_0=\frac{2}{3}$. Therefore, as the excitonic peak becomes stronger, ϵ_∞ should decrease; as the excitonic peak becomes weaker, ϵ_∞ should increase (if the Penn gap remains constant). This is the opposite of what we observe and therefore the impact of the excitonic interaction on S_0 does not

explain our observations.

We pointed out previously [106] that the band alignments at ZnO interfaces with Si and SiO_2 are very different [131, 132]. ZnO/SiO_2 is a type-I interface where both electron and hole are confined in the ZnO well by the SiO_2 barrier. Therefore, strong excitonic effects are expected in ZnO/SiO_2 quantum wells. On the other hand, ZnO/Si is a type-II (staggered) interface. While electrons are confined in the ZnO layer, holes will diffuse into the Si substrate, especially if the ZnO layer is thin. (See Fig. 9 in Ref. 106.) This will break apart the exciton and thus lead to an increase of the Penn gap, which reduces ϵ_∞, as we observe.

We can also invoke the optical conductivity sum rule [70]

$$\omega_{\mathrm{pl}}^2 = \frac{2}{\pi}\int_0^\infty \epsilon_2\left(\omega\right)\omega d\omega. \tag{94}$$

Since the electron density ρ (and therefore ω_{pl}) is nearly constant, reducing $\epsilon_2\left(\omega\right)$ near the band gap (as excitonic effects are weakened) requires a shift of oscillator strength to higher energies (outside of our spectral range), to keep the integral nearly constant. To clarify this point, it would be useful to measure optical constants beyond 6.5 eV, perhaps in a nitrogen-purged ellipsometer [83], at a synchrotron,citeGoRa10, or with a high-harmonic femtosecond laser source [133]. The experimental problem with such measurements is that the importance of surface roughness increases as the photon energy gets larger.

The other sum rule [70]

$$\epsilon_\infty = 1 + \frac{2}{\pi}\int_0^\infty \frac{\epsilon_2(\omega)}{\omega} d\omega \tag{95}$$

directly relates the high-frequency dielectric constant to an integral containing the imaginary part of the dielectric function ϵ_2. As excitonic effects are reduced in ZnO layers on Si, oscillator strength is shifted to higher photon energies [128, 129], which clearly reduces ϵ_∞ from Eq. (95), because the denominator is larger for higher photon energies.

4.6.3 Decreased absorption

It can be seen clearly from Figs. 4.5 and 4.6 that the magnitude of ϵ_2 decreases in thinner films. It decreases more in ZnO on Si due to the weakening of excitonic effects (as discussed above in subsection 4.6.2), but to a lesser extent also in ZnO on SiO_2. The decreased absorption is described by the imaginary part ϵ_2 of the dielectric function, which is related to its real part ϵ_1 through Kramers-Kronig transform. [46, 70] It can be seen in Fig. 4.5 that ϵ_2 for bulk ZnO decreases towards higher photon energies, while ϵ_2 for the thinnest layers increases at higher energies. This may be a reflection of the shift of oscillator strength towards higher energies as the excitonic effects are decreased.

Excitonic contributions to the absorption and dispersion of semiconductors are described by the Elliot-Tanguy theory [134, 135]. The parameters of this theory

are the bulk band gap, its broadening, the strength of the band gap absorption (amplitude; related to the effective masses of electrons and holes, the transition matrix element, and fundamental constants), the exciton binding energy, and the excitonic screening parameter. This Tanguy oscillator is included in commercial software (WVASE32) and can be used to fit the ellipsometric angles. However, in the case of ZnO, one also needs to consider the exciton-phonon complexes. This introduces two additional parameters, the phonon energy and the exciton-phonon coupling constant [120,121]. Unfortunately, fitting the ellipsometric angles while including the excitonic effects and exciton-phonon complexes is not currently possible in commercial software. There is an explicit theory for the imaginary part [120,121], but not for the real part of the dielectric function. Therefore, a fit to our ellipsometric angles including excitonic effects and exciton-phonon complexes (to determine exciton and exciton-phonon coupling parameters) is beyond the scope of our current work. We note that it is possible to determine the imaginary part of ϵ from a point-by-point fit as shown in Figs. 4.17 and 4.18 and then fit this result with the Elliot theory for ϵ_2, including exciton-phonon complexes [120,121]. However, this approach does not properly include the experimental errors of the ellipsometric angles as a function of photon energy. It may also lead to results that are not Kramers-Kronig consistent.

Therefore, we confine our discussion to the experimental finding that the excitonic absorption peaks near the ZnO band gap are significantly reduced in am-

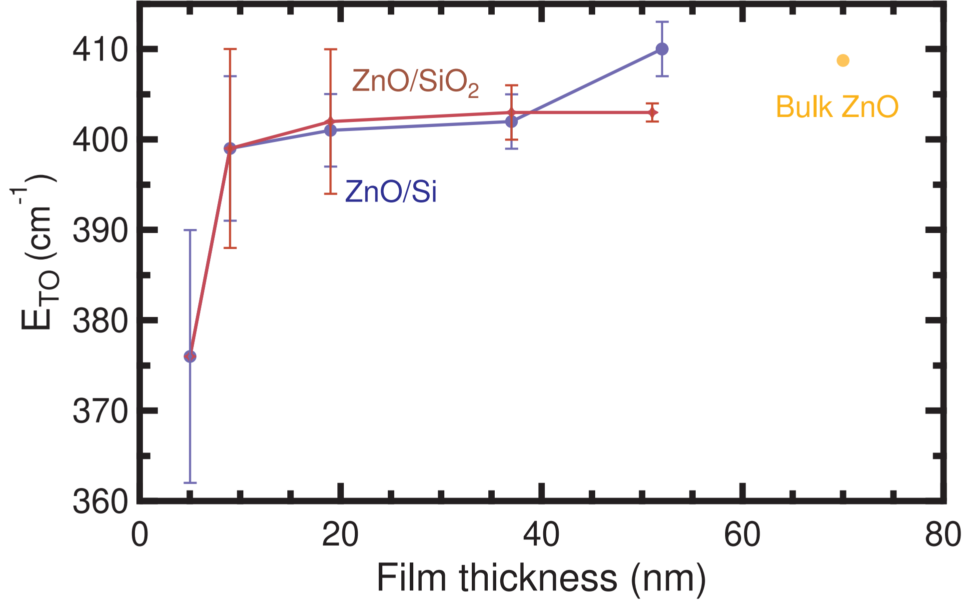

Figure 4.9: Transverse optical (E_1 TO) phonon energies versus layer thickness for ZnO on Si and SiO_2 in comparison with bulk ZnO.

plitude as well as broadened in ZnO layers on both Si and SiO_2. We qualitatively conclude that excitonic effects are weakened in thin layers, especially on Si, but defer a quantitative treatment of these effects to future work.

4.6.4 Phonon energies and Born effective charge

From our infrared ellipsometry data, it is difficult to determine if the TO and LO energies of the E_1 phonon depend on layer thickness, see Fig. 4.9. For the thinnest ZnO layers on Si, the TO absorption peaks are very weak and broad (see Figs. 4.5 and 4.6), which leads to large errors of the TO energies that do not allow a clear statement about phonon softening at small thicknesses. For ZnO on SiO_2, even

for our thickest layers, the ZnO vibrational features are just minor corrections to the strong infrared response of quartz, see Fig. 4.4.

In the bulk [114], the E_1 TO and LO energies are about 408 cm^{-1} (50.6 meV) and 590 cm^{-1} (73.2 meV), respectively, compare Table 4.1. Theory states [136–138] that a reduction of particle size (in ZnO nanoparticles) leads to a broadening in k-space, which is on the order of 20% of the Brillouin zone radius for a particle with a 5 nm diameter. This k-space uncertainty leads to a (possibly asymmetric) broadening and a redshift or blueshift (depending on the phonon dispersion curvature) of optical phonon peaks, as observed in our experiments on thin ZnO layers. The shifts and broadenings in thin layers are not very large, however, because the dispersion of the E_1 phonon near the Γ-point is rather flat [139]. A redshift and broadening of the E_1 LO phonon was indeed observed in ZnO nanoparticles with Raman spectroscopy [140]. However, it was pointed out that laser heating in resonant Raman spectroscopy with a UV laser will also cause a redshift [141], putting the results of Ref. 140 in question.

In an ellipsometry measurement of a c-axis textured layer, the electric field vector interacts with E_1 phonons, which have atomic displacements in the plane of the layer. This in-plane dimension is not confined by the thickness of a thin layer, only by the lateral extension of grains. However, the wave vector of the excited phonon is equal to the wave vector of the photon (perpendicular to the layer) and therefore confined by the layer thickness. In other words, while the

motion of the atoms is not confined by the thin layer, the uncertainty of the phonon wave vector is affected by the finite layer thickness. Therefore, the shift of the E_1 phonon energy in a thin layer should be similar to a nanoparticle, which is confined in all three directions.

The E_1 LO phonon is not observable in bulk ZnO crystals with infrared transmission or ellipsometry experiments, because this phonon does not couple with infrared light. However, in thin layers, the so-called Berreman effect [142] causes a structure in the ellipsometric angles at the LO energy, which is clearly observable even for a 9 nm thick ZnO layer on Si, compare Fig. 4.1. A softening of the E_1 LO phonon energy by 20-30 cm^{-1} is possible (similar to the softening of the E_1 TO phonon shown in Fig. 4.9), but the errors are rather large.

We therefore prefer not to make a definitive statement about the thickness dependence of the E_1 phonon energies and do not discuss this phenomenon quantitatively. Assuming a Gaussian lineshape for TO phonon absorption may not be the optical approach for ultrathin layers, but adding additional parameters to describe asymmetry is not supported by the ellipsometric angles and the low signal to noise ratio in our spectra.

From the TO and LO phonon energies, we can also calculate the Born effective charge, see Eq. (91) and Fig. 4.8(c). The Born effective charge follows the same trends as the high-frequency dielectric constant, see Fig. 4.8(b): It is nearly independent of thickness for ZnO on SiO_2, but decreases significantly (by about 20%)

for ZnO on Si. The difference of the squares of the LO and TO phonon energies changes much less, see Table 4.1.

4.6.5 Static dielectric constant

The static dielectric constant ϵ_s can be calculated in two different ways: First, we can set ω=0 in Eq. (88), which directly yields ϵ_s in our WVASE ellipsometry software. These results are shown by circles in Fig. 4.8(a). We find that thicker layers have much larger static dielectric constants than the bulk because of the strong infrared Gaussian absorption of unknown origin, which also contributes to ϵ_s by Kramers-Kronig transform.

The static dielectric constants

$$\epsilon_s = \epsilon_\infty \frac{\omega_{LO}^2}{\omega_{TO}^2} \tag{96}$$

calculated from the Lyddane-Sachs-Teller relations [70] shown by crosses in Fig. 4.8(a) are much closer to the bulk values, which gives us confidence in our results for ϵ_∞ and the optical phonon energies. We conclude that the static dielectric constant is influenced by defect absorption much more than by changes in the E_1 phonon energies. To a lesser extent, ϵ_s is also influenced by the thickness dependence of ϵ_∞, but the ratio of the E_1 LO and TO phonon energies is nearly constant.

4.7 Summary

We used broad-band spectroscopic ellipsometry from 0.03 to 6.6 eV to investigate the origin of the variability of the optical constants of ZnO thin films on two different substrates (Si and quartz). The blueshift of the band gap with decreasing layer thickness is small. It follows a simple inverse-square law due to confinement in a quantum well with infinitely high barriers. On the other hand, there is a very significant decrease of excitonic effects in thin layers, especially for ZnO on Si, leading to a reduction of the excitonic absorption, a broadening of the exciton peak, and a corresponding decrease of the high-frequency dielectric constant. Since excitonic effects shift oscillator strength from higher to lower photon energies, our results are fully consistent with the sum rules for optical constants. We speculate that the exciton is stabilized by type-I ZnO/SiO_2 heterojunctions, but breaks apart near type-II ZnO/Si interfaces. Surface electric fields in thin ZnO layers may also play a role.

Acknowledgements

This work was supported by the National Science Foundation (DMR-1505172). We are grateful to Adam Dubroka and Daniel Franta at Masaryk University (Brno, Czech Republic) for reminding us of the importance of sum rules and to Oliver Herfurth (Universität Leipzig, Germany) for sharing his insights on exciton-phonon

complexes.

4.8 Supplementary Material

4.8.1 Surface roughness

The surface roughness of our ZnO layers on Si and SiO_2 was determined by x-ray reflectance (XRR) and atomic force microscopy (AFM). Typical AFM and plan-view SEM images for similar layers are shown in Ref. 105. For the thickest ZnO layers on Si and SiO_2, the roughness was also studied with ellipsometry, by describing the surface roughness layer with the Bruggeman effective medium approximation (EMA) and a 50% void fraction [46]. Ellipsometry was not sensitive to surface roughness for thinner layers. AFM was performed on a Bruker Dimension FastScan instrument with a TESPA etched Si probe in non-contact tapping mode with a scan window size of 10×10 μm^2. The RMS surface roughness was calculated using the Bruker NanoScope analysis software and averaged over several sites. To compare the SE or XRR ellipsometry roughness with the AFM roughness, we must consider the unflattened AFM roughness, because the ellipsometry or XRR spot size is much larger than the AFM scan range.

A comparison of the roughness results for all three techniques is shown in Fig. 4.10: The surface roughness measured by XRR for the ZnO films on Si and SiO_2 substrates (see below) is in good agreement with the unflattened AFM RMS roughness.

Figures 4.10 (c) and (d) show the projections of the 3D AFM scans for the 51 nm and 5 nm ZnO/Si films, respectively, onto a plane perpendicular to the surface. The white frames, which identify the Bruggeman EMA layers, are about twice as high as the RMS surface roughness from AFM, because they extend from the lowest valley to the highest peak. We therefore show one half of the Bruggeman EMA layer thickness in Figs. 4.10(a) and (b), which compares well with the roughness determined from XRR and AFM.

4.8.2 Crystal structure

The crystal structure of ZnO layers on Si and SiO_2 was investigated using x-ray powder diffraction on a PANalytical Empyrean diffractometer operated in line focus mode with 45 kV anode voltage and a 40 mA beam current producing Cu K_α radiation with λ=1.5419 Å wavelength. The bremsstrahlung continuum was removed using a Bragg-Brentano HD (BBHD) optical module with a fixed $\frac{1}{4}^\circ$ divergence slit, a 4 mm beam mask, 0.04 rad soller slits, and a fixed 1° anti-scatter slit as the incident beam optics. As the diffracted beam optics, we used a programmable anti-scatter slit, 0.04 rad soller slits, and a 0.02 mm thick Ni filter (to block the K_β radiation). The diffracted intensity was measured with a PIXcel1D-Medipix3 array detector (PANalytical).

Typical symmetric 2θ-ω scans of ZnO on Si and SiO_2 with different film thicknesses are displayed in Fig. 4.11. The XRD peaks were labeled according to the

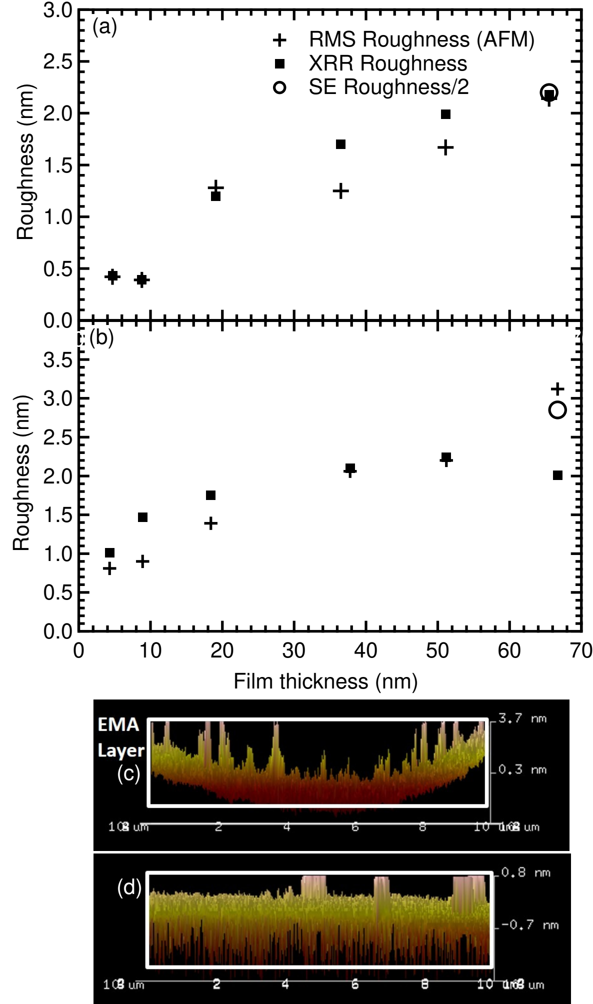

Figure 4.10: Surface roughness of ZnO films on (a) Si and (b) quartz as a function of ZnO thickness. + and ■: unflattened root mean square (RMS) roughness determined from AFM and XRR, respectively; ○: half of the roughness layer thickness obtained from an ellipsometry (SE) model with roughness. (c) Projection of the 3D AFM image for the 51 nm thick ZnO/Si film onto a plane perpendicular to the surface. The white frame shows the EMA surface roughness layer used to model SE data. (d) Same as (c), but for a 5 nm ZnO/Si layer.

Table 4.3: List of samples used in this study with nominal thickness t and results from XRR analysis, including thickness t_{XRR}, interfacial SiO_2 layer thickness $t_{\mathrm{SiO_2}}$ (for ZnO on Si), surface roughness R from XRR, and average electron density ρ_e. For comparison, the bulk ZnO electron density is 1.51 $e/\mathring{A}^3$. The layer thickness t_{SE} determined from ellipsometry is also given. The last two columns list the grain size d and the vertical strain $\epsilon_\perp$ measured with XRD.

Nominal t (nm)	Sub-strate	t_{XRR} (nm)	$t_{\mathrm{SiO_2}}$ (nm)	R (nm)	ρ_e ($e/\mathring{A}^3$)	t_{SE} (nm)	d (nm)	$\epsilon_\perp$ (%)
5	Si	4.5	1.3	0.4	1.42	7.6	12	0.10
9	Si	9.5	1.4	0.8	1.44	11.2	12	0.47
19	Si	19.4	1.0	0.8	1.46	20.7	20	0.01
38	Si	36.0	1.5	1.6	1.50	37.2	27	0.07
52	Si	50.5	1.0	1.7	1.49	50.5	26	0.01
69	Si	69.1	1.4	2.0	1.48	NA	30	0.03
5	SiO_2	4.1	NA	1.1	1.35	4.1	NA	NA
9	SiO_2	8.7	NA	1.2	1.39	7.8	12	−0.19
19	SiO_2	18.8	NA	1.4	1.47	19.6	21	0.17
38	SiO_2	36.0	NA	1.7	1.49	34.1	31	0.10
52	SiO_2	51.5	NA	1.5	1.45	48.4(f)	31	−0.10
69	SiO_2	70.8	NA	1.1	1.44	NA	31	−0.05

International Center for Diffraction Data database (PDF card number 01-079-2205). Since the ZnO (002) peak is the strongest, the layers have a preferred c-axis orientation, but other ZnO (100) and (101) peaks are also seen, especially in thicker layers. This indicates that the c-axis orientation is rather weak. For low-temperature growth of intrinsic (undoped) ZnO by ALD, both the polar (001) and the charge-neutral (100) surface are expected [99], consistent with the strongest XRD peaks in Fig. 4.11. The thinnest (5 nm) layers have barely visible x-ray diffraction peaks. They are either amorphous or there is insufficient scattering volume for diffraction using our experimental conditions. Similar XRD spectra were found for other ZnO layers produced by ALD [99, 105] or magnetron sputtering [101].

The grain height of polycrystalline thin films can be determined using the Scherrer formula (B. D. Cullity and S. R. Stock, *Elements of X-Ray Diffraction*, Prentice Hall, Upper Saddle River, NJ, 2001; P. F. Fewster, *X-Ray Scattering from Semiconductors and other Materials*, World Scientific, Singapore, 2015)

$$d = \frac{0.9\lambda}{\beta \cos\theta_B}, \tag{97}$$

where β is the full width at half maximum (FWHM) of the Bragg peak (plotted as a function of 2θ, after subtracting the instrumental broadening) and θ_B the Bragg angle of the ZnO (002) diffraction peak. This grain size is often associated with the film thickness [101, 104], but this approach does not seem to work for our layers.

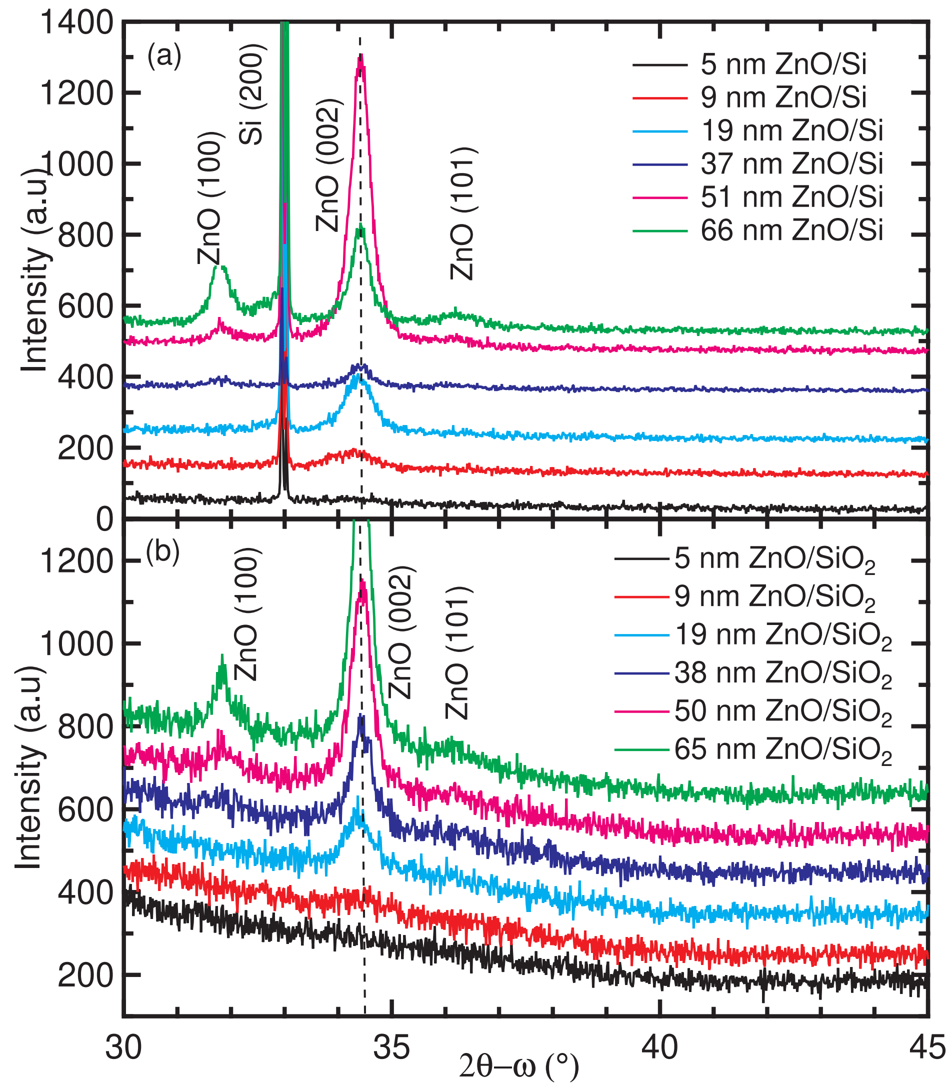

Figure 4.11: X-Ray diffraction pattern for (a) ZnO/Si and (b) ZnO/SiO_2 with different film thickness.

For our thinnest (5 nm) layers, the grain height is 12 nm (which is not physically possible), see Table 4.3. For the thicker layers (38 to 69 nm thickness from XRR), the grain height is found to be around 31 nm, much less than the thickness. This discrepancy is not caused by the resolution of the instrument, since the FWHM of the Si (111) peak at 2θ=28.42° is only 0.11°, considerably less than the FWHM of the ZnO layer peaks. We conclude that our ZnO layers are very smooth, but have rather small grains, since they were grown at low temperature (200°C) and not annealed after growth.

From the position of the ZnO (002) peak in comparison with a bulk wurtzite ZnO crystal, we can determine the vertical lattice strain $\epsilon_{\perp}$, also given in Table 4.3. For all but one layer, the strain is small and not even the sign of the strain can be determined with certainty. Therefore, the variations of the dielectric function reported in this paper are more likely to be a function of thickness rather than a function of strain, which has been reported from some piezo-electric materials, such as perovskites [86–88].

4.8.3 X-Ray Reflectivity (XRR)

X-ray reflectance was used to obtain the ZnO layer thickness, electron density, and surface and interface roughness, with results given in Table 4.3. Data were taken on a PANalytical Empyrean instrument (same as for XRD) with a Ge (220) two-bounce hybrid monochromator, a fixed 1/32° divergence slit, and a 4 mm

beam mask to produce a parallel beam. The reflected beam path consisted of a 0.27° parallel-plate collimator with a 0.1 mm XRR slit, a 0.04 rad soller slit, and a Xe proportional detector. A programmable beam attenuator with a 0.125 mm Ni foil was activated when the Xe detector count rate exceeded a preset threshold. The sample was aligned carefully to be perpendicular to the plane of incidence and to reduce the straight-through beam intensity by 50% at zero incidence angle.

XRR spectra for all samples, displayed as reflectance versus scattering vector

$$Q = \frac{4\pi}{\lambda} \sin\theta, \tag{98}$$

where λ=1.5406 Å is the Cu $K_{\alpha 1}$ wavelength and θ the angle of incidence (measured relative to the sample surface), are shown in Fig. 4.12 on a semi-logarithmic scale. The data were analyzed using the Parrat formalism (L. G. Parrat, *Surface studies of solids by total reflection of x-rays*, Phys. Rev. **95**, 359, 1954) with details in Ref. 105, resulting in the sample parameters in Table 4.3. We used the MotoFit program (http://motofit.sourceforge.net) in an Igor Pro (Wavemetrics, Inc., Lake Oswego, OR, USA) environment to fit our XRR data and determine the fit parameters. For some samples, two or three ZnO layer sections with different electron densities were required to achieve a good fit between model and data. In such cases, the thickness given in Table 4.3 is the sum of the individual thicknesses and the electron density is a weighted average over all ZnO sections.

Some trends are apparent by direct inspection of the XRR graphs. (1) The

critical angle given by the sharp drop of the reflectance is nearly the same for all but the thinnest samples, indicating a nearly constant electron density (independent of layer thickness). (2) The period of the Kiessig fringes shows significant changes with layer thickness. (3) The agreement between data and fit is excellent using our model, indicating a high level of confidence in the accuracy of our layer thicknesses and densities. (4) The amplitude of the Kiessig fringes, which depends on the contrast of the electron density of layer and substrate, is nearly the same for ZnO on Si and on SiO_2, because Si and its oxide have nearly the same electron density. (5) The drop of reflectance versus Q is relatively slow, which allows us to measure reflectance for large values of Q. This indicates that the surface roughness for our ZnO layers is rather small.

Errors of the XRR thicknesses in Table 4.3 can be estimated by manual variation of the parameters followed by visual comparison of the fit and the data ("chi-by-eye"). We found that the accuracy of the XRR thicknesses in Table 4.3 was about 1%. The genetic algorithm is usually best suited for fitting XRR and high-resolution x-ray diffraction data to a model. Unfortunately, the Motofit implementation of this algorithm does not return any errors. We also tried fitting our data with a Marquardt-Levenberg algorithm in Motofit (which is said to return errors), but this algorithm did not converge for our data.

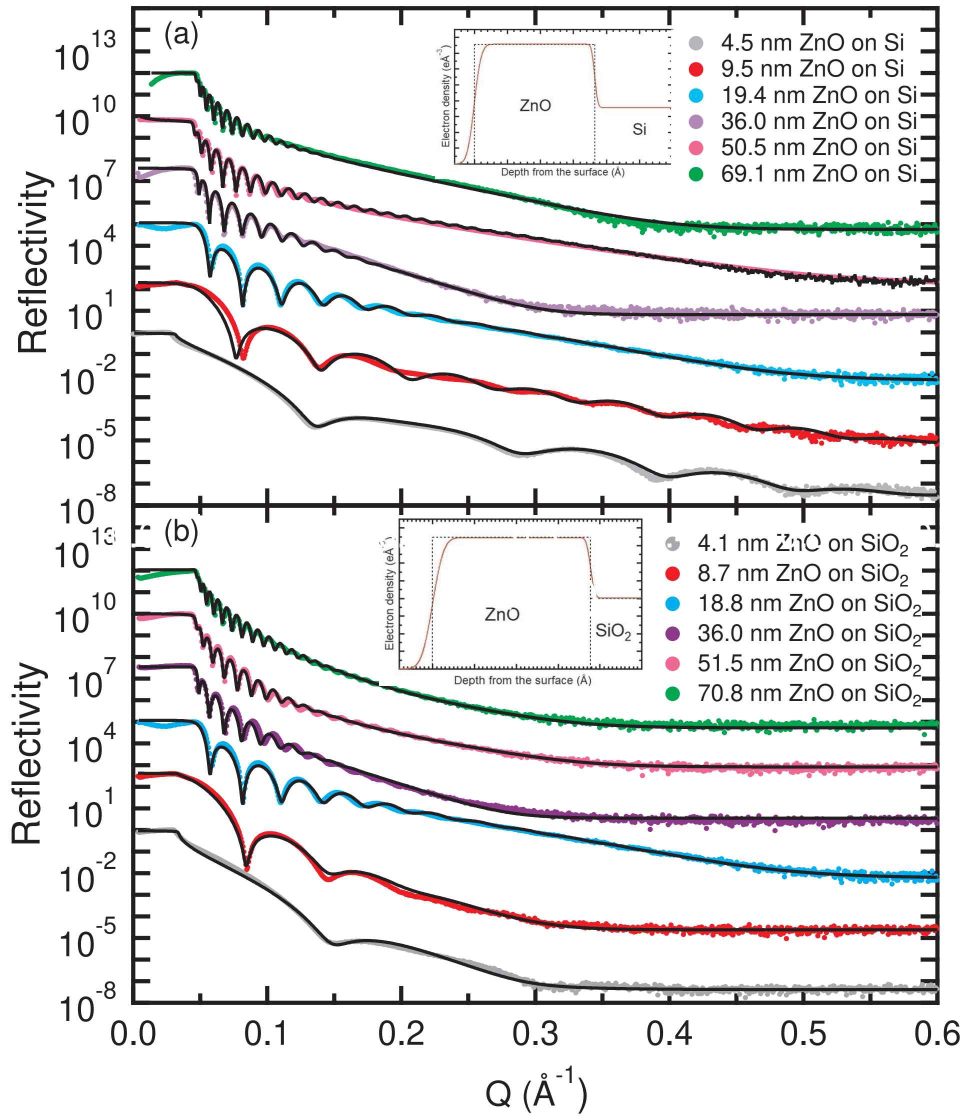

Figure 4.12: X-ray reflectivity for (a) ZnO/Si with film thickness 5 nm, 9 nm, 19 nm, 37 nm, 51 nm, and 66 nm (b) ZnO/SiO_2 with film thickness 5 nm, 9 nm, 19 nm, 38 nm, 50 nm, and 65 nm. The solid line shows the model data and circles represent the experimental data. The curves were shifted vertically for clarity. The inset shows the electron density versus depth from the x-ray reflectivity fit for one thickness (38 nm).

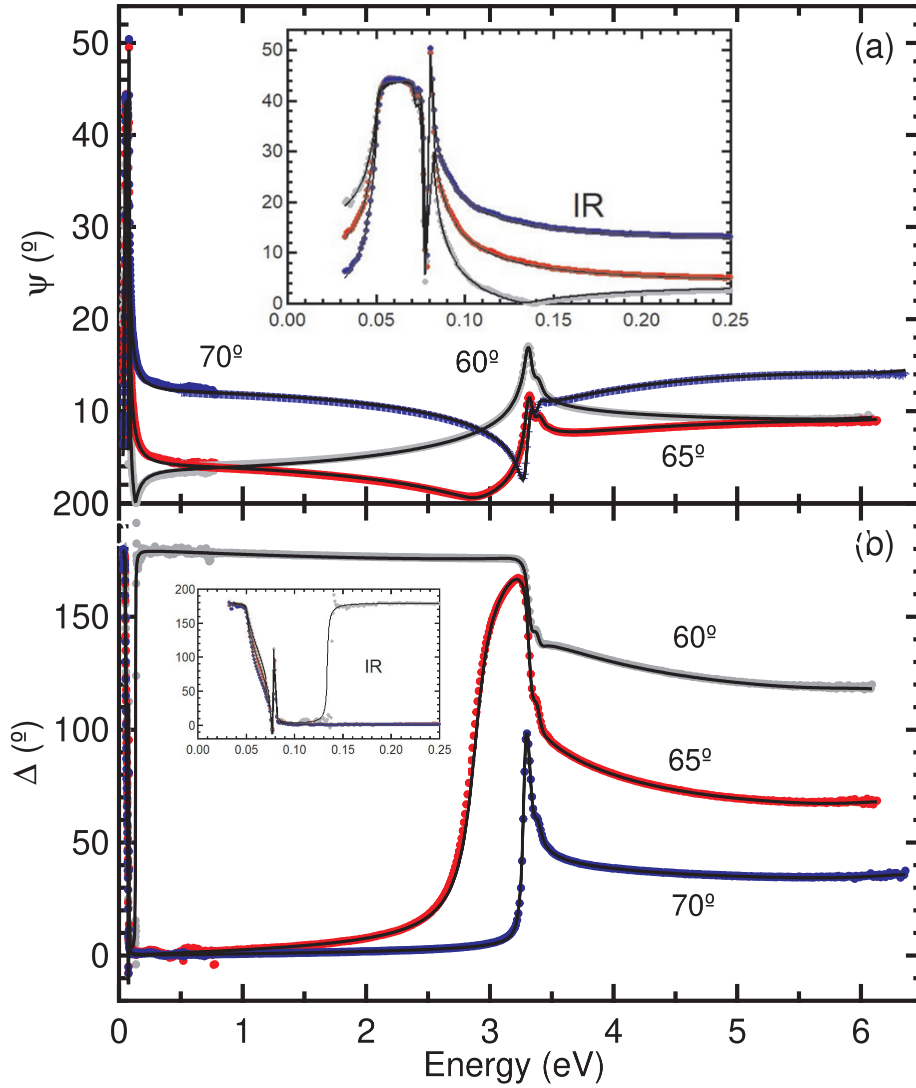

Figure 4.13: Ellipsometric angles (a) ψ and (b) Δ for bulk ZnO with 21 Å surface roughness, similar to Ref. 21. Symbols: experimental data; solid: fit using Eq. (99).

4.8.4 Optical properties of bulk ZnO

For comparison with results from thin ZnO layers on Si and SiO_2, we also performed ellipsometry measurements on a bulk c-axis oriented ZnO crystal obtained commercially. This work was described previously [21]. In summary, the ordinary and extraordinary dielectric function of wurtzite ZnO are each described as a product [21]

$$\epsilon\left(\omega\right) = \epsilon_{\mathrm{TO}}\left(\omega\right)\epsilon_{\mathrm{electronic}}\left(\omega\right), \tag{99}$$

where the first factor [21]

$$\epsilon_{\mathrm{TO}}\left(\omega\right) = \frac{\omega_{\mathrm{LO}}^2 - \omega^2 - i\gamma_{\mathrm{LO}}\omega}{\omega_{\mathrm{TO}}^2 - \omega^2 - i\gamma_{\mathrm{TO}}\omega} \tag{100}$$

describes the infrared lattice absorption and the second factor

$$\epsilon_{\mathrm{electronic}}\left(\omega\right) = 1 + \sum_i g_i\left(\omega\right) \tag{101}$$

the optical properties due to interband transitions. ω_{TO} and ω_{LO} are the angular frequencies of the transverse (TO) and longitudinal (LO) optical phonons and γ_{TO} and γ_{LO} the corresponding broadenings. The terms $g_i\left(\omega\right)$ are called *oscillators*. They describe the electronic contributions to the dielectric susceptibility due to different types of interband transitions. For bulk ZnO, we used two Tauc-Lorentz oscillators with a common band gap in the near-gap region, one for the unresolved exciton triplet and another one for exciton-phonon complexes [118–121]. (N. O. Lipari, *Exciton energy levels in wurtzite-type crystals*, Phys. Rev. B **4**, 4535, 1971;

B. Gil, *Oscillator strengths of A, B, and C excitons in ZnO films*, Phys. Rev. B **64**, 201310, 2001). At higher energies, we added two simplified Herzinger-Johs oscillators and a pole at 11 eV. In the infrared spectral range, the anisotropy is addressed by assigning different values to the phonon parameters for the ordinary and extraordinary beam. The sensitivity to the anisotropy is reduced in the visible and UV range for our experimental geometry. We therefore assume that the extraordinary part of the dielectric susceptibility is larger by 0.08 than the ordinary part throughout that spectral range. We call this a *partially anisotropic model*, because the anisotropy is included only in the infrared region and for ϵ_∞. This ignores the dichroism of ZnO. [113] Surface roughness was included within the Bruggeman effective medium approximation.

Figure 4.13 shows the ellipsometric angles ψ and Δ from 60° to 70° angle of incidence for bulk c-axis oriented ZnO from 0.03 to 6.5 eV obtained using FTIR ellipsometry and variable angle UV/VIS spectroscopic ellipsometry. The fit shows a partially anisotropic model with Eq. (99) including surface roughness. The signs of anisotropy [111] are most apparent near 80 meV. The TO and LO phonon parameters from this fit are given in Table 4.1. With this model, we extracted the ordinary and extraordinary complex dielectric functions (ϵ_o and ϵ_e) of bulk ZnO versus photon energy from 0.03 to 6.50 eV, as shown in Fig. 4.14. Because of the assumptions of our partially anisotropic fit, ϵ_{2e}=ϵ_{2o} and ϵ_{1e}=ϵ_{1o}+0.08 in the visible and UV range. The differences between the ordinary (E_1 phonon) and

extraordinary (A_1 phonon) infrared lattice absorption are clearly visible by a shift of the infrared absorption and dispersion peaks.

4.8.5 Dielectric function of quartz substrate

Fused (amorphous) quartz substrates were purchased from EL-CAT Inc., Ridgefield Park, NJ. They were specified as UV grade fused silica, 20 by 20 mm in size with 500 μm thickness, and single-side polished with an rms roughness of no more than 0.5 nm. No XRD peaks were seen, see Fig. 4.11, only a broad background typical for amorphous materials. (Compare Y. Deng, Y. L. Du, M. S. Zhang, J. H. Han, and Z. Yin, *Nonlinear optical properties in $SrTiO_3$ thin films by pulsed laser deposition*, Solid State Commun. **135**, 221, 2005, for XRD spectra of thick $SrTiO_3$ layers on fused quartz. Our amorphous quartz XRD background looks similar.)

The ellipsometric angles ψ and Δ for 50° to 80° angle of incidence from 0.03 to 6.0 eV are shown in Fig. 4.15. ψ decreases monotonically from 0.5 to 6.0 eV (for the larger incidence angles) due to the normal dispersion of quartz, whose dielectric constant increases from 2.06 to 2.49 over the same energy range. Δ is negative in this energy range (for the larger incidence angles). Its magnitude increases with photon energy. This indicates that there is a thin surface layer which has a larger dielectric constant than quartz.

In the visible and UV spectral range, we describe the optical constants of

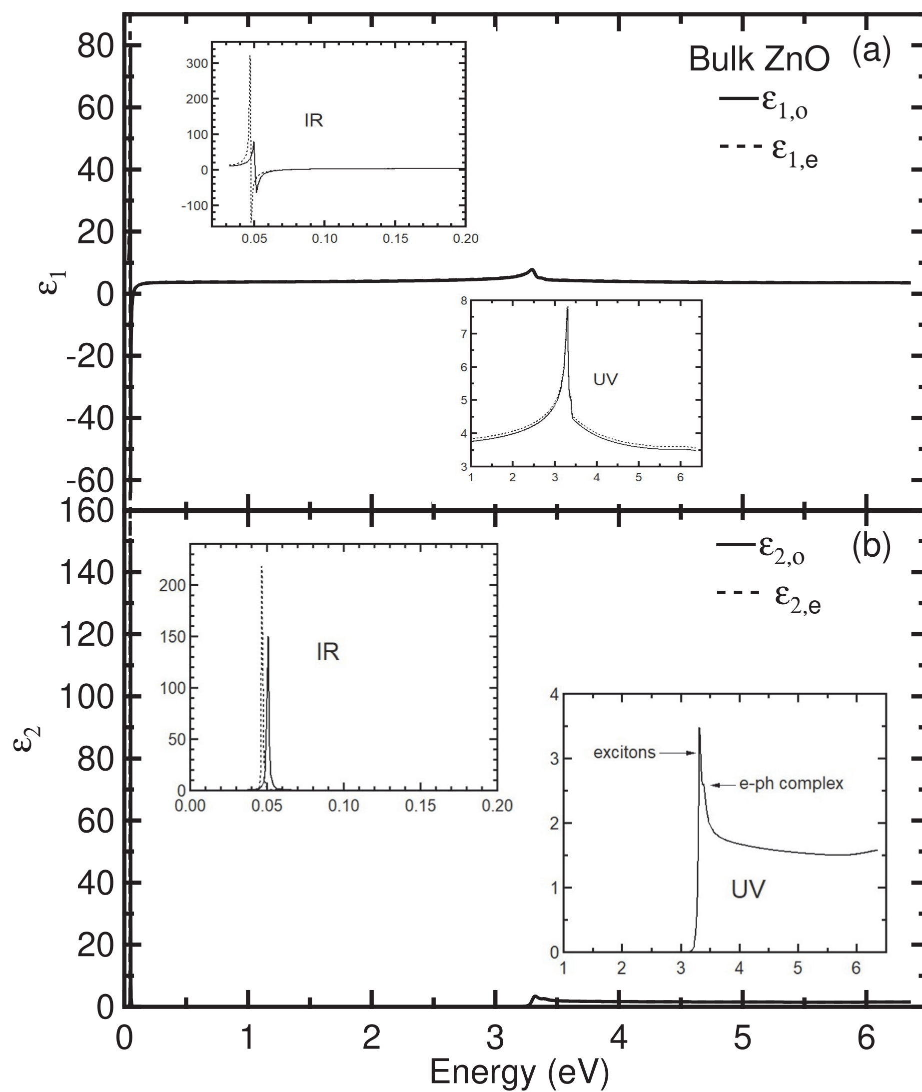

Figure 4.14: (a) Real and (b) imaginary parts of the complex dielectric function for bulk ZnO versus photon energy, determined from the ellipsometric angles in Fig. 4.13 with a partially anisotropic model. Here ϵ_o and ϵ_e are the ordinary and extraordinary dielectric function, respectively

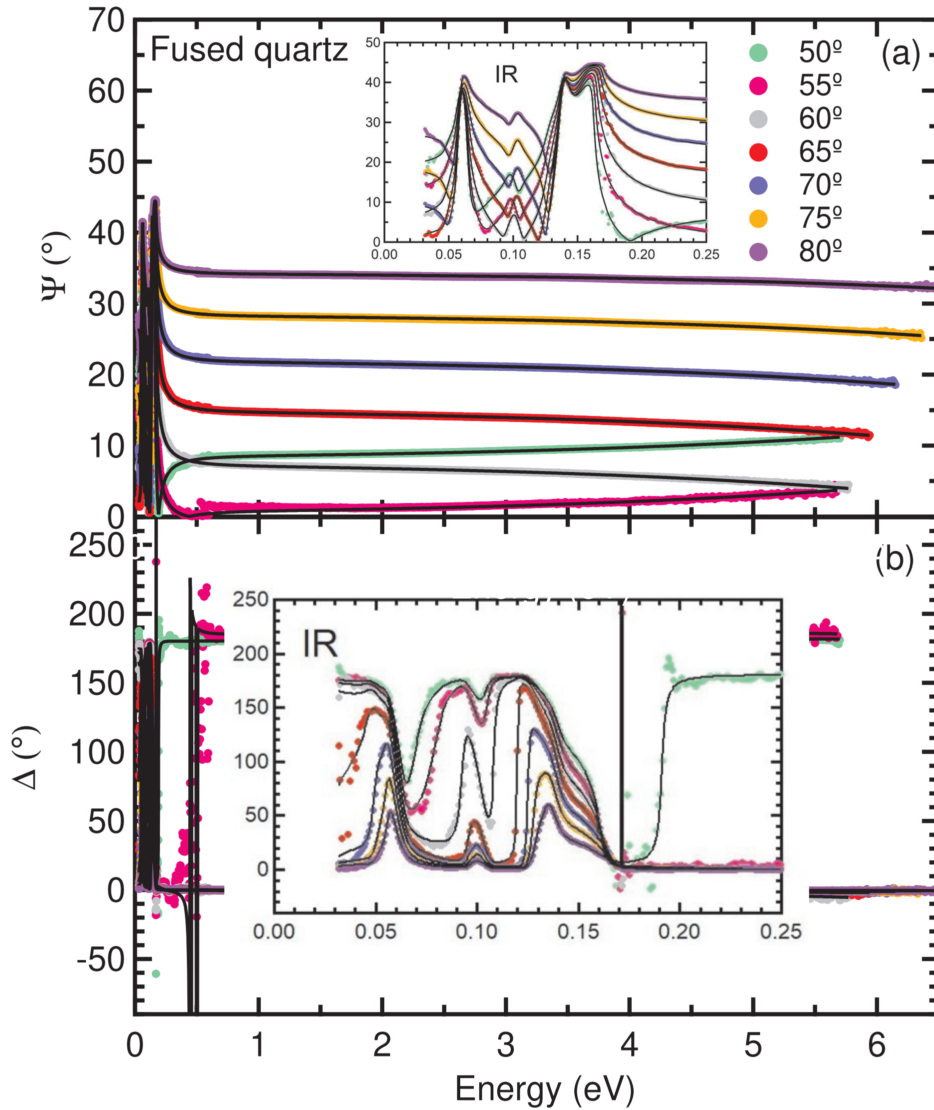

Figure 4.15: Ellipsometric angles ψ and Δ for a bare single-side polished fused quartz substrate for angles of incidence from 50° to 80° (symbols). The lines show the best fit to a model which describes the quartz optical constants with a sum of Gaussians and poles and which includes a thin surface layer, which has a slightly larger ϵ than the substrate.

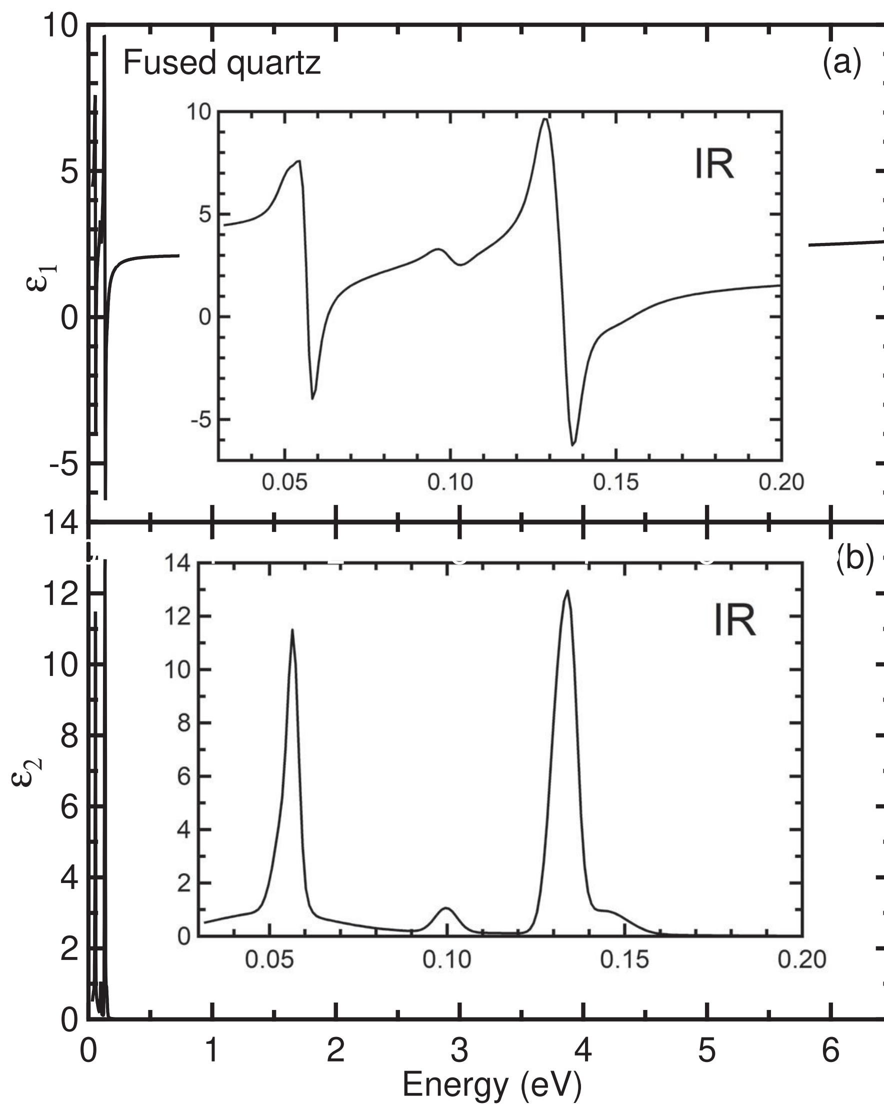

Figure 4.16: Dielectric function of fused (amorphous) quartz, obtained by fitting the ellipsometric angles shown in Fig. 4.15. The insets show the infrared spectra region.

quartz with an isotropic Sellmeier model, i.e., a constant value of ϵ_∞=1.24 and a pole at 11 eV (fixed) with a magnitude of 107 eV^2. (These parameters are strongly correlated and therefore have large errors. The pole energy is consistent with the band gap of quartz, often quoted between 9 and 10 eV.) For the surface layer, we assume the same parameters as for quartz, but with a larger value of ϵ_∞. The exact value of ϵ_∞ of the surface layer and its thickness are strongly correlated and cannot be determined separately. However, a surface layer thickness of 1 nm and ϵ_∞=1.76 for the surface layer achieve an excellent description of Δ in the UV region. (Adsorbed surface layers like water or oil usually have a smaller refractive index than glass and are not likely the reason for this surface layer. A SiO suboxide, on the other hand, has a larger refractive index than SiO_2 and might be a good candidate. There might also be polishing damage near the surface, for example residue from the slurry used for polishing, perhaps diamond or alumina, both of which have a larger refractive index than quartz. Surface characterization techniques such as Auger spectrometry or x-ray photoelectron spectroscopy were not available for our work.) In the infrared spectral region, absorption from molecular vibrations is described with a sum of eight Gaussians, taking the values established for thermal oxide as the starting point for our fit. The optical constants of the quartz substrate obtained from this model are shown in Fig. 4.16.

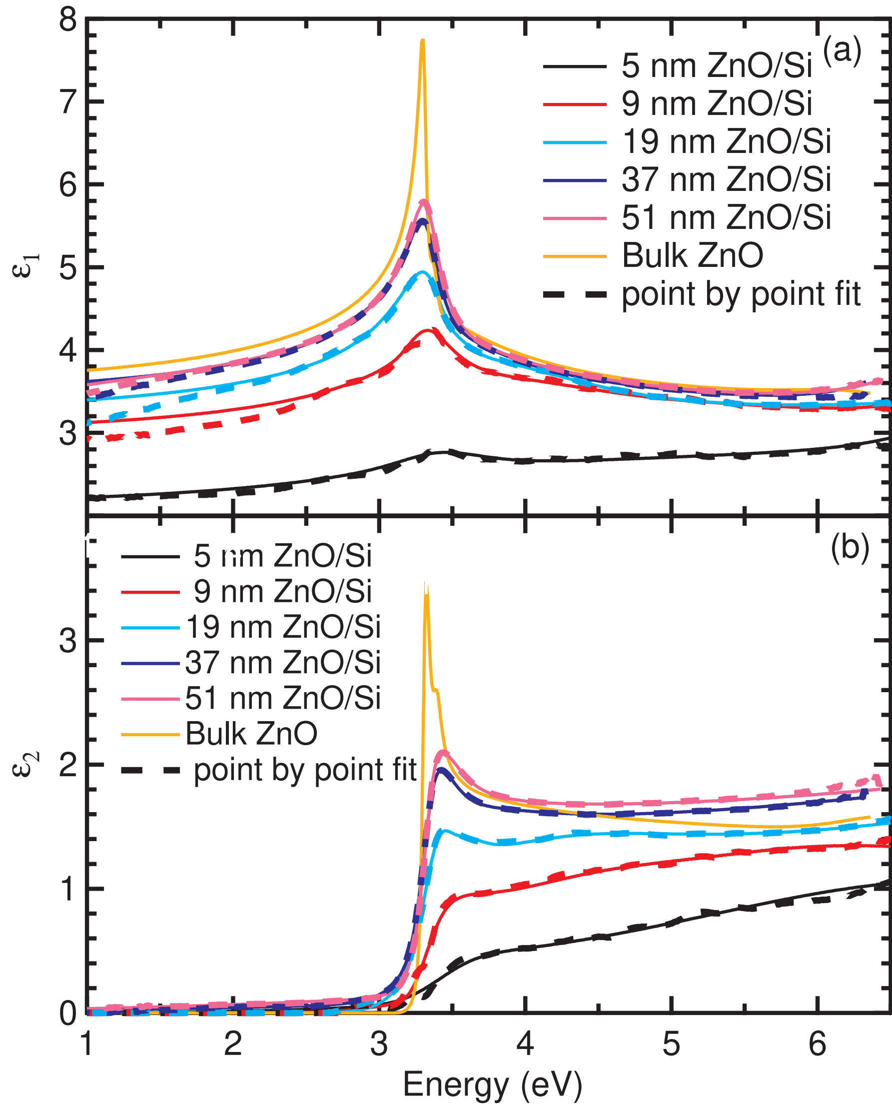

Figure 4.17: Results from point-by-point fits to determine the optical constants of ZnO on Si for various thicknesses (dashed), in comparison to oscillator fits (solid). The mid-infrared spectral region is not shown, because the data are quite noisy in that range.

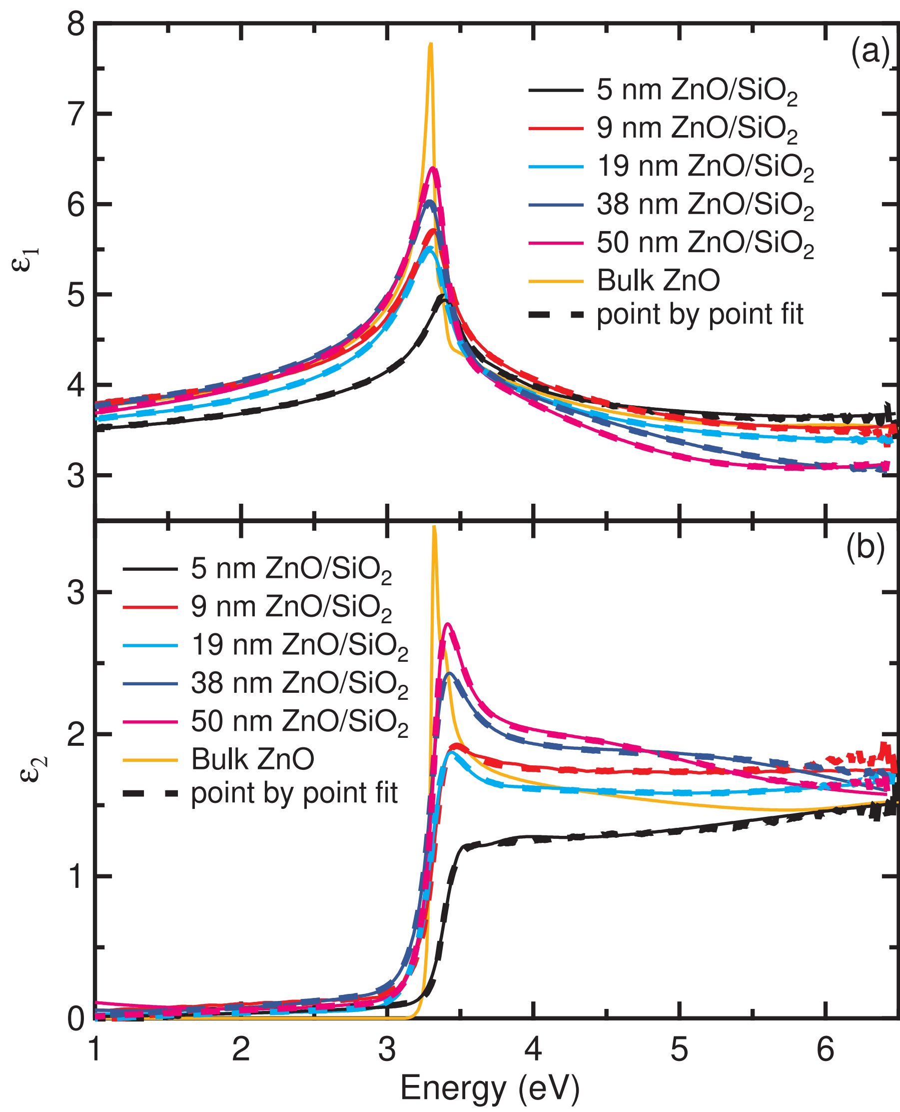

Figure 4.18: As Fig. 4.17, but for ZnO on SiO_2.

4.8.6 Comparison of oscillator and point-by-point fits

After the oscillator fits using Eq. (88) were completed and the ZnO layer thicknesses on Si and SiO_2 determined, we also performed independent wavelength-by-wavelength (or point-by-point) fits, where the ZnO thickness was fixed and the real and imaginary parts of the dielectric function were treated as free parameters at each wavelength [45, 46]. (Surface and interface layers were included in the point-by-point fit in the same manner as in the oscillator fit.) Both methods resulted in very similar dielectric functions (see Figs. 4.17 and 4.18), but the point-by-point fit is usually a little noisier than the oscillator fit. The agreement is usually better for ϵ_2 than for ϵ_1.

For ZnO on Si, we see a monotonic increase of ϵ_2 at 4 eV (above the band gap) from thinner to thicker films. The value of ϵ_2 below the band gap is very small. This indicates that our layered model is very good. Pseudo-absorption below the gap usually indicates that some of the layer thicknesses in the ellipsometry model are incorrect. For ZnO on SiO_2, ϵ_2 also increases from thinner to thicker films, but the increase is not entirely monotonic, because ϵ_2 at 4 eV is smaller for the 19 nm thick layer than for the 9 nm thick layer.

Small uncertainties in the optical constants of the quartz substrates can cause an apparent pseudo-absorption below the band gap. Therefore, it turned out to be crucial to develop accurate optical constants for our quartz substrates, see Sec.

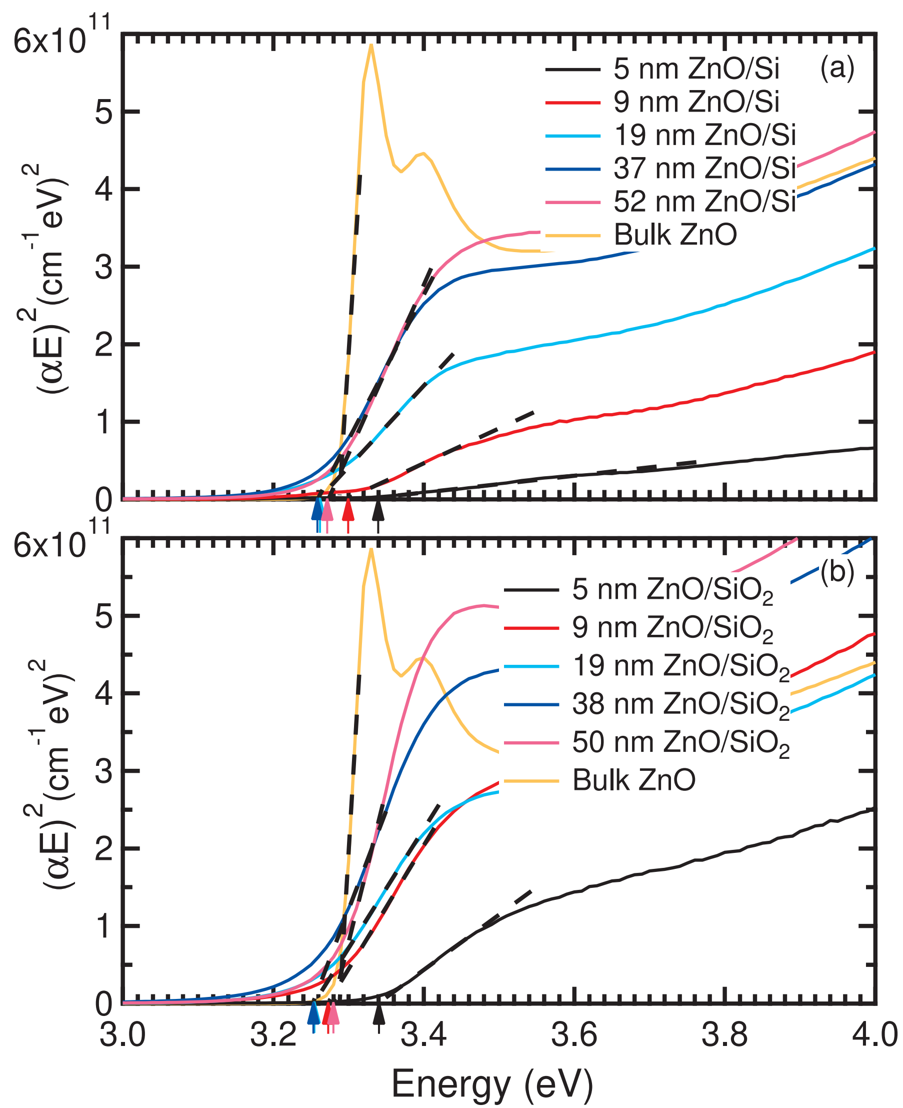

Figure 4.19: Tauc plot extrapolation for bulk ZnO and (a) ZnO on Si (b) ZnO on SiO_2 with different film thickness

4.8.5. In contrast to earlier work, there are no artifacts in the ϵ_2 optical constants near the band gap. ϵ_2 in ZnO thin layers qualitatively looks similar to the bulk, except that the exciton-phonon continuum is not resolved and the exciton peak is broader and weaker.

The agreement between the oscillator and point-by-point fit methods is also good for ϵ_1 near or above the band gap. For ZnO on Si, however, ϵ_1 from the point-by-point fit falls off faster towards the infrared than ϵ_1 from the oscillator fit. There is no physical reason for this faster dropoff, since there are no absorption processes between the TO phonon energy and the band gap. Therefore, we believe that the oscillator fit yields more accurate results for ϵ_1 than the point-by-point fit. The discrepancy for ZnO on Si might be due to inaccuracies in the treatment of the interfacial layer between the Si substrate and the ZnO layer or due to small errors in the optical constants of the Si substrate, see Sec. 4.8.10.

4.8.7 Band gap determination using Tauc plot

The direct optical band gap of a material is often found by plotting $(\alpha E)^2$ versus E, where α is the absorption coefficient and E the photon energy. This is sometimes called a Tauc plot [122]. One looks for a linear region in this graph, extrapolates to zero, and then identifies the intercept with the optical band gap. While this technique is clearly arbitrary and influenced by the choice of the linear region and the extrapolation, it is used frequently. Figure 4.19 demonstrates the use of this

technique to determine the band gap of bulk ZnO and thin ZnO layers on Si and SiO_2. When using this technique, it is very important to use the point-by-point optical constants (see Sec. 4.8.6) for the extrapolation, since the use of oscillators may bias the optical constants used for extrapolation. Results are shown and discussed in the main manuscript.

4.8.8 Comparison of ellipsometry and transmission results

Some studies [102] report the absorption coefficient for thin ZnO layers determined using transmission measurements. This procedure is dangerous, because both the real and imaginary parts of the dielectric function (and complex refractive index) change with layer thickness, see Fig. 4.6, but only one quantity (transmitted intensity) is measured. One measured quantity cannot be used to determine two unknowns. Therefore, it is our position that transmission measurements by themselves cannot be used to determine absorption coefficients of a thin layer, unless the refractive index of the layer is well known (and does not depend on the deposition conditions of the layer).

On the other hand, it can be advantageous to combine ellipsometry measurements of a layer A on a single-side polished transparent substrate B with transmission measurements of the same layer A on a double-side polished substrate of material B. Both ellipsometry and transmission results can be loaded into a multi-sample environment and fitted simultaneously. The ellipsometry results will be

more accurate for large absorption coefficients, while the transmission results will be more accurate for small absorption coefficients. Combining both datasets will lead to more accurate optical constants over the complete spectral range. A nice application of this technique to GaN on sapphire has been presented by Yu *et al.* (G. Yu, G. Wang, H. Ishikawa, M. Umeno, T. Soga, T. Egawa, J. Watanabe, and T. Jimbo, *Optical properties of wurtzite structure GaN on sapphire around fundamental absorption edge (0.78-4.77 eV) by spectroscopic ellipsometry and the optical transmission method*, Appl. Phys. Lett. **70**, 3209 (1997)).

Unfortunately, we could not use this technique, because we did not have ZnO layers on two-side polished quartz substrates. As a work-around, we performed transmission measurements of ZnO layers on our single-side polished quartz substrates (see Table 4.3) with the single-side polished bare quartz substrate taken as the transmission background. These transmission results (referenced to the single-side polished quartz substrate) should be similar to transmission results of the same ZnO layer on a double-side polished substrate (with a two-side polished quartz substrate as the reference). We therefore used these transmission results to determine the absorption coefficient (taking the refractive index from our ellipsometry measurements, see Fig. 4.6). The results are shown in Fig. 4.20 (dotted) in comparison to absorption coefficients determined from a point-by-point fit to ellipsometry results (solid). It can be seen that both datasets show the same trends (versus thickness and photon energy), but there is a constant offset, pre-

sumably due to artifacts from the scattering of the transmitted light by the rough back surface of the quartz substrate, which were not properly taken into account in our model. For this analysis, it is very important to consider the dependence of the refractive index on thickness (see Fig. 4.6). If that is neglected, then α shows the wrong trend versus thickness and pseudo-absorption artifacts appear below the band gap. We can also use the absorption coefficients determined from our transmission measurements to determine the band gap with a Tauc plot, see Sec. 4.8.7 and Fig. 4.19.

4.8.9 Lattice vibration versus total infrared optical response

As shown by Eq. (88), we write the total optical response as a product of three factors. The second factor describes the electronic contribution to the dielectric function. In the far-infrared region, this contribution is nearly constant and equal to

$$\epsilon_\infty = 1 + \sum_i g_i \left(\omega = 0\right), \tag{102}$$

the high-frequency dielectric constant. One might also ask about the relative contribution of the E_1 infrared-active phonon to the total dielectric response in the infrared region. If we wrote the dielectric function as a sum of oscillators (which is the common method of treatment), then this question would be trivial to answer. As explained in Ref. 21, however, we have good reasons for our factorized approach. Most importantly, we want to fit our data while allowing two different

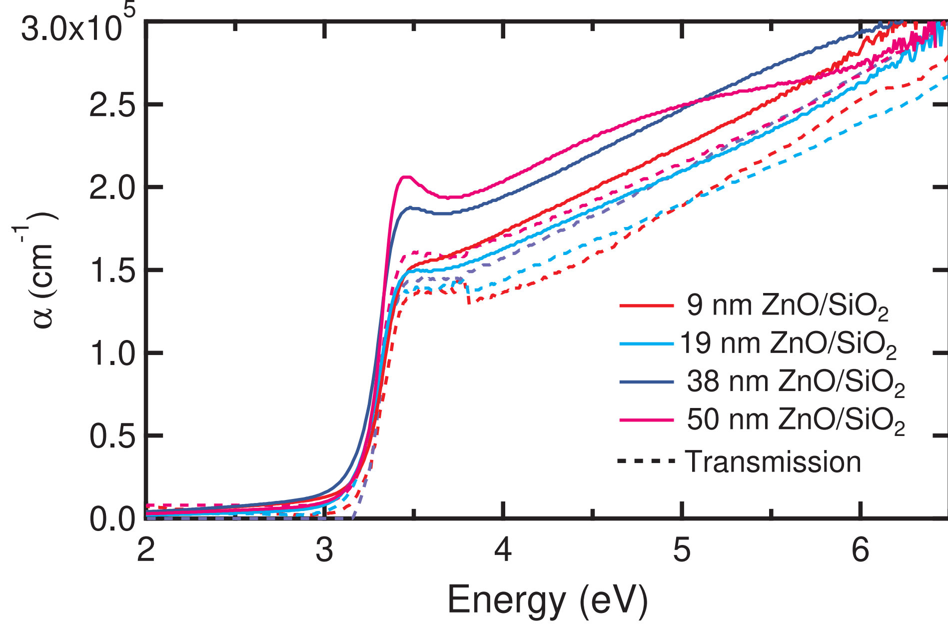

Figure 4.20: Absorption coefficient of ZnO layers with different thicknesses on SiO_2 quartz substrates determined from ellipsometry measurements (solid) and transmission measurements of the same layers with the bare single-side polished quartz substrate as a reference (dotted).

broadening parameters for the TO and LO features from the E_1 phonon, but without an arbitrary parameter ϵ_∞, which comes from the second factor in our approach. Therefore, we attribute the quantity

$$\epsilon_{\mathrm{TOLO}}\left(\omega\right) = \epsilon_\infty \frac{\omega_{\mathrm{LO}}^2 - \omega^2 - i\gamma_{\mathrm{LO}}\omega}{\omega_{\mathrm{TO}}^2 - \omega^2 - i\gamma_{\mathrm{TO}}\omega} \tag{103}$$

to the lattice contribution contained in the total infrared response. This quantity gets multiplied by the third factor (involving Gaussians) to obtain the total infrared optical response. Figure 4.21 shows the total dielectric function in the

infrared region (solid) in comparison with the contribution from the E_1 phonon given by Eq. (103) (dotted) for those layers where Gaussian oscillators where included in our model, see Tables 4.1 and 4.2.

For ZnO layers on SiO_2, this decomposition looks as expected: The TO/LO absorption is lower than the total absorption. The Gaussian oscillators add absorption at very low energies and they also magnify the TO/LO absorption. The TO/LO absorption approaches the total absorption at high energies. Similarly, ϵ_1 is larger at low energies if the Gaussian absorption is included in the dielectric function and it magnifies the maxima and minima in the region of anomalous dispersion, but the Gaussian absorption makes little difference to ϵ_1 at the higher energies. For the 51 nm layer of ZnO on Si, the Gaussian contribution is larger (no longer a small correction) and therefore distorts the entire TO/LO lineshape, making it very asymmetric.

4.8.10 Impact of Si substrate optical constants

Several sets of optical constants for Si have appeared in the literature over the past 40 years, see Fig. 4.22. The silicon optical constants determined by Herzinger *et al.* [74] (often described as "Woollam silicon") are used nearly universally at universities as well as in the semiconductor industry to describe the optical response of dielectric layers on Si (001) substrates. Therefore, this dataset for Si was also the basis for our work. It is interesting, however, to ask how other op-

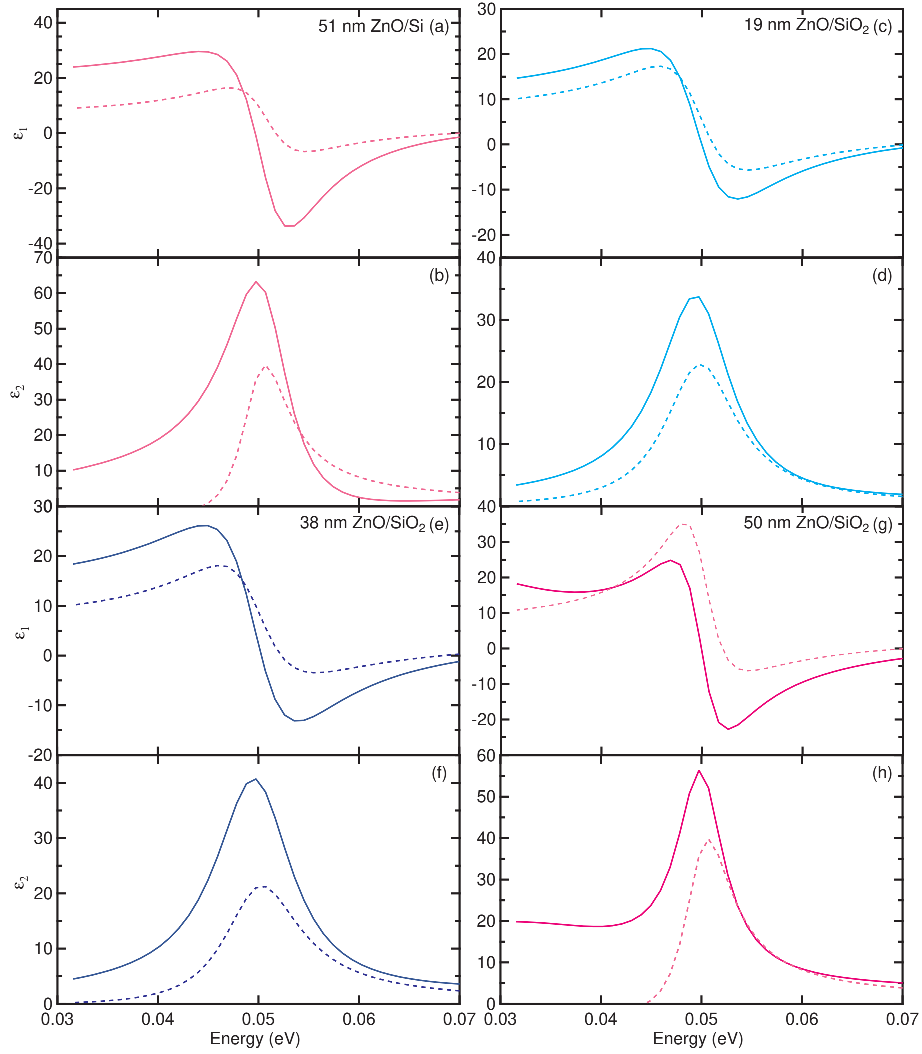

Figure 4.21: Total dielectric function in the infrared region (solid) in comparison with the contribution from the E_1 phonon given by Eq. (103) (dotted).

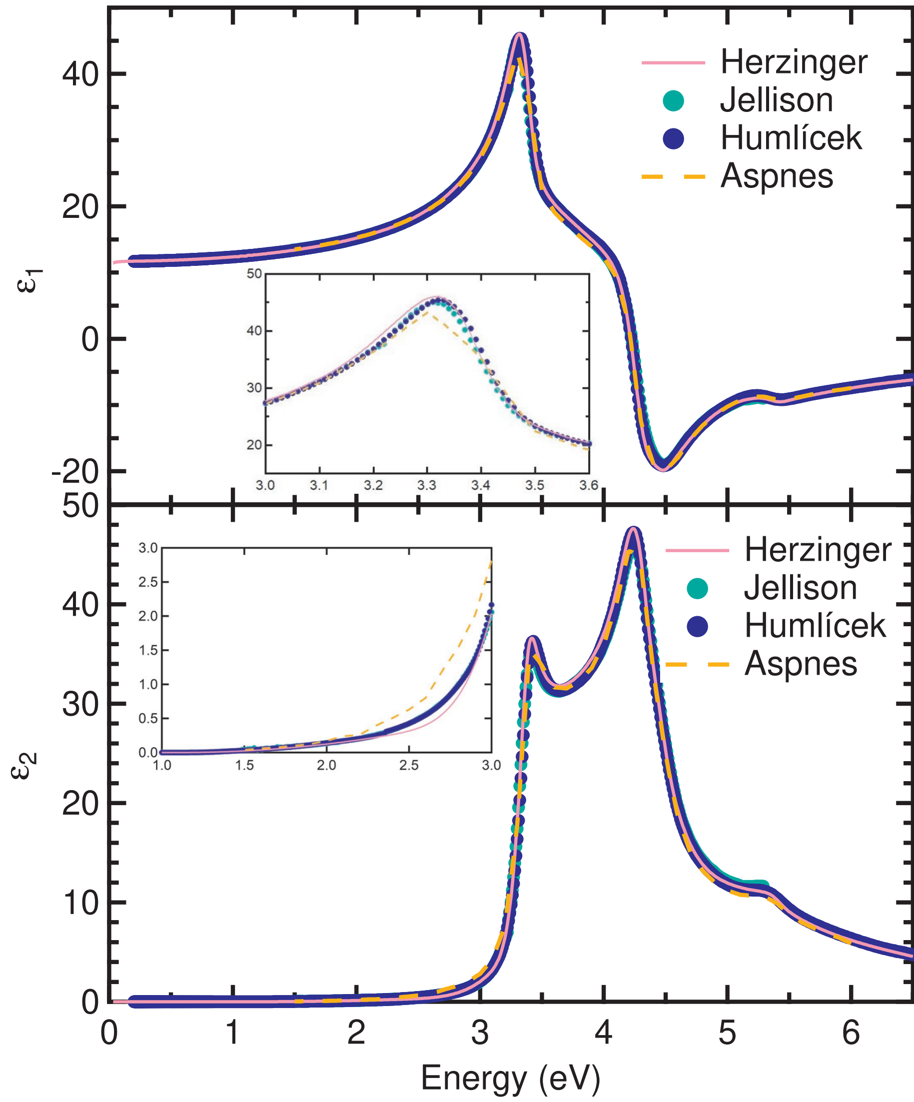

Figure 4.22: Comparison of several sets of optical constants for the Si substrate referenced in the text.

tical datasets for the Si substrate optical constants will affect our results for the thickness-dependent dielectric functions of ZnO layers on Si. (For quartz substrates, as discussed in Sec. 4.8.5, we found it very important to develop our own optical constants from a bare reference substrate rather than use optical constants from a database.)

The oldest comprehensive dataset for the dielectric function of Si is based on work by Aspnes and Studna (D. E. Aspnes and A. A. Studna, *Dielectric functions and optical parameters of Si, Ge, GaP, GaAs, GaSb, InP, InAs, and InSb from 1.5 to 6.5 eV*, Phys. Rev. B **27**, 985-1009 (1983)). This work was later revisited by Yasuda and Aspnes (T. Yasuda and D. E. Aspnes, *Optical-standard surfaces of single-crystal silicon for calibrating ellipsometers and reflectometers*, Appl. Opt. **33**, 7435-7438 (1994)). For three reasons, we did not select these datasets as Si reference constants for our work. (1) Aspnes often states that semiconductor optical constants depend on the surface orientation. These two papers cited above describe work performed on bare Si (111) surfaces, while our layers were grown on Si (001). (2) These data were taken on a rotating-analyzer ellipsometer without compensator. Therefore, the accuracy of these data for small values of ϵ_2 below 3.5 eV is limited. (3) These authors tried to minimize the thickness of surface overlayers to achieve a bare Si (111) surface. Since the dielectric function depends not only on the surface orientation, but also on surface conditions (M. K. Kelly, S. Zollner, and M. Cardona, *Modelling the optical response of surfaces measured by*

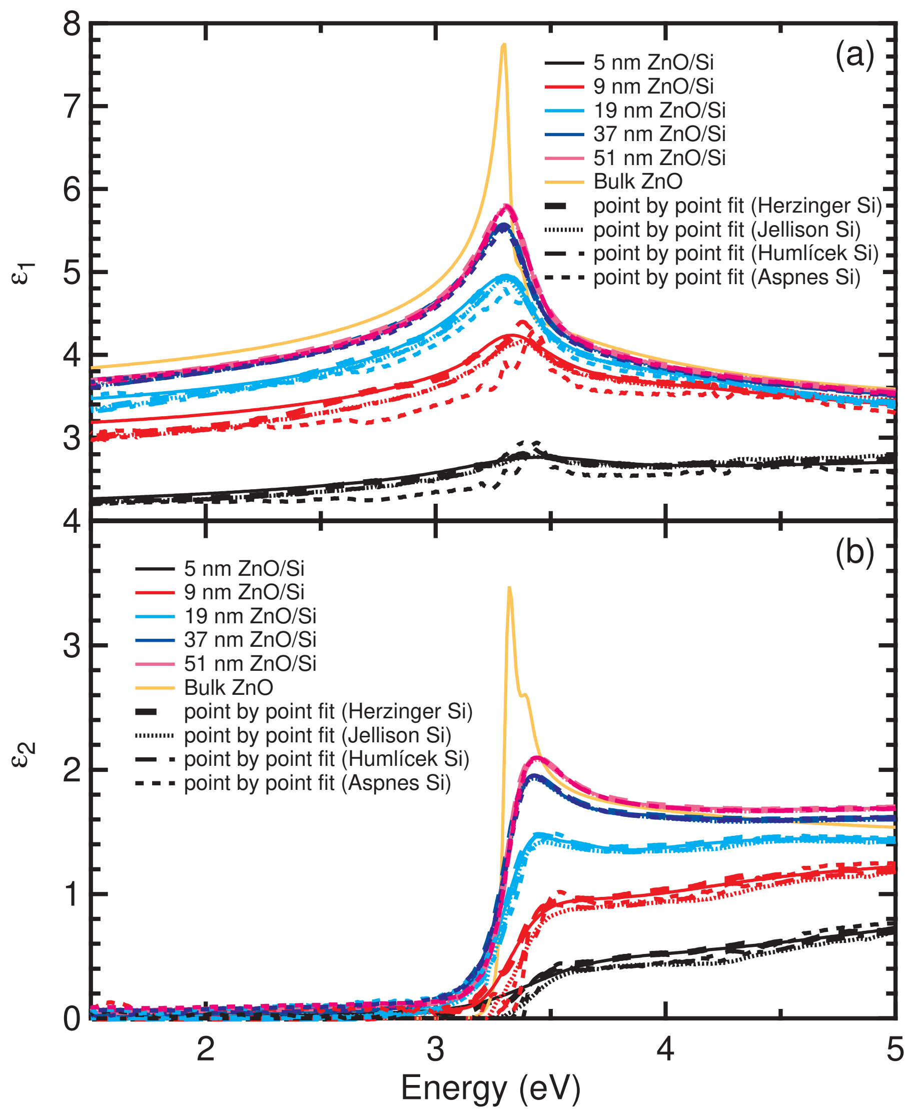

Figure 4.23: Dielectric functions for ZnO layers on Si with different thicknesses as shown in Fig. 4.17, but with different reference constants for the Si substrate.

spectroscopic ellipsometry, Surf. Sci. **285**, 282-294 (1993)), the Woollam Si data seem more appropriate to describe the dielectric function of a Si (001) substrate covered with transparent layers. The modern value of the early work by Aspnes *et al.* consists mainly in the precise description of preparing bare Si (111) surfaces.

Jellison (G. E. Jellison, *Optical functions of silicon determined by two-channel polarization modulation ellipsometry*, Opt. Mater. **1**, 41-47 (1992)) derived the silicon optical constants from a Si (001) surface with a phase-modulation ellipsometer, which provides accurate values of ϵ_2 below 3.5 eV. He also corrected his data for a thin oxide overlayer. Therefore, this data set is very accurate. Finally, Humlíček and Šik (J. Humlíček and J. Šik, *Optical functions of silicon from reflectance and ellipsometry on silicon-on-insulator and homoepitaxial samples*, J. Appl. Phys. **118**, 195706 (2015)) achieved very high accuracy of the Si (001) dielectric function below 3.5 eV with measurements of variable-thickness silicon-on-insulator substrates produced by wafer bonding and back etching of the donor wafer.

Four of these five sets of Si optical constants mentioned above are compared in Fig. 4.22. (We did not find a digitized set of the data by Yasuda and Aspnes.) More detailed comparisons were shown by Humlíček and Šik (2015). The overall agreement is excellent, but small differences exist, especially near the E_1 and E_2 critical points. The extinction coefficient also varies below 3.5 eV between datasets.

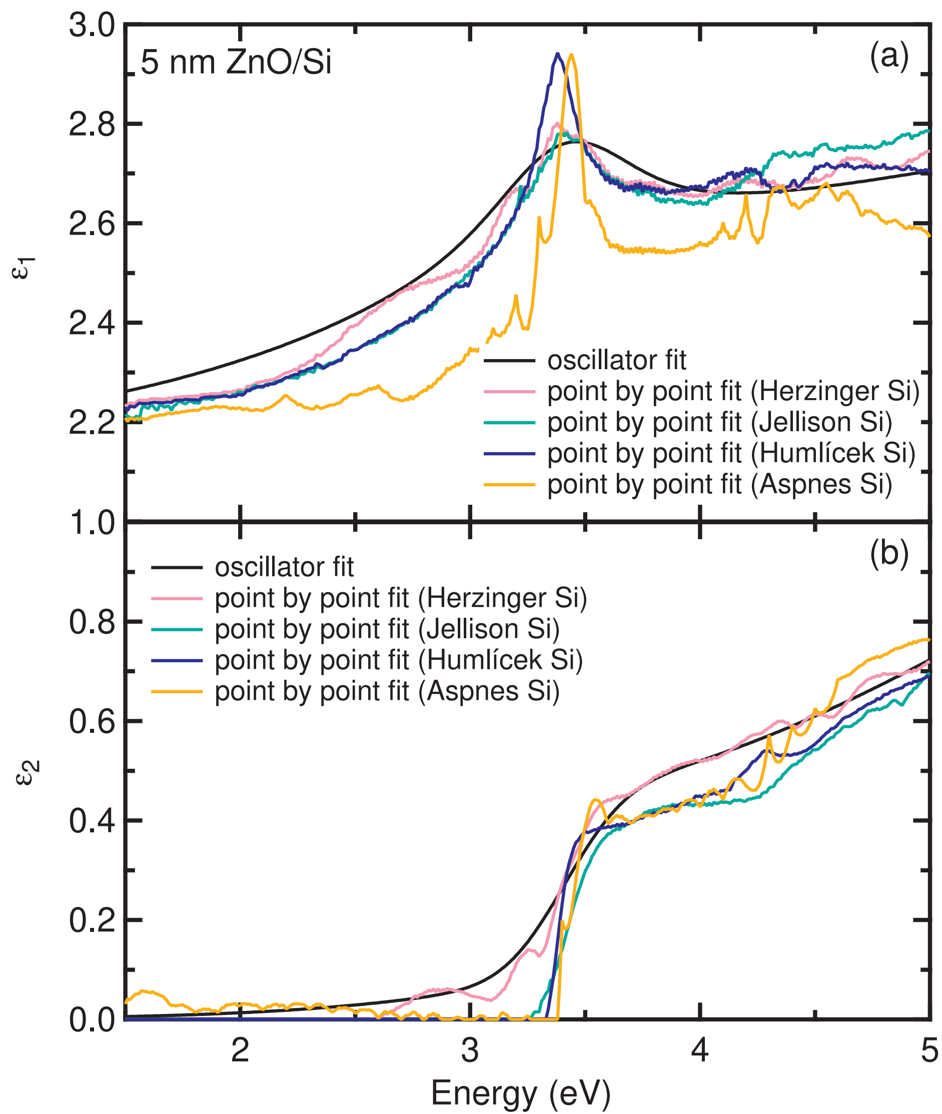

Figure 4.24: As Fig. 4.23, but for the 5 nm ZnO on Si layer.

Figure 4.23 shows the optical constants for all our ZnO layers on Si obtained with a point-by-point fit, but with different Si substrate optical constants. The choice of the dielectric function of the Si substrate does not significantly influence the resulting ZnO optical constants for thicker layers, but differences are found for thinner ZnO layers, where the optical constants of the Si substrate have more influence. The largest differences can be seen for the Si optical constants of Aspnes and Studna (1983), which are probably the least accurate. Despite all these differences, the main conclusions of our work are not affected: There are significant monotonic variations of both ϵ_1 and ϵ_2 with ZnO layer thickness, which are not affected by the choice of the Si substrate optical constants.

Figures 4.24 and 4.25 show a magnified view of these comparisons for the thinnest ZnO on Si layers with 5 nm and 9 nm thickness. There are slight variations in the band gap given by the peak of ϵ_1 or the absorption threshold of ϵ_2 for different choices of the Si substrate optical constants. We also find different broadenings of the direct band gap given by the widths of the peak of ϵ_1 and the abruptness of the rise of ϵ_2. The choice of the Si substrate optical constants will have an influence on extracting exciton parameters (like exciton binding energy and broadening) for the thinnest ZnO layers. This will influence future work, when we consider excitonic effects and exciton-phonon coupling in our analysis.

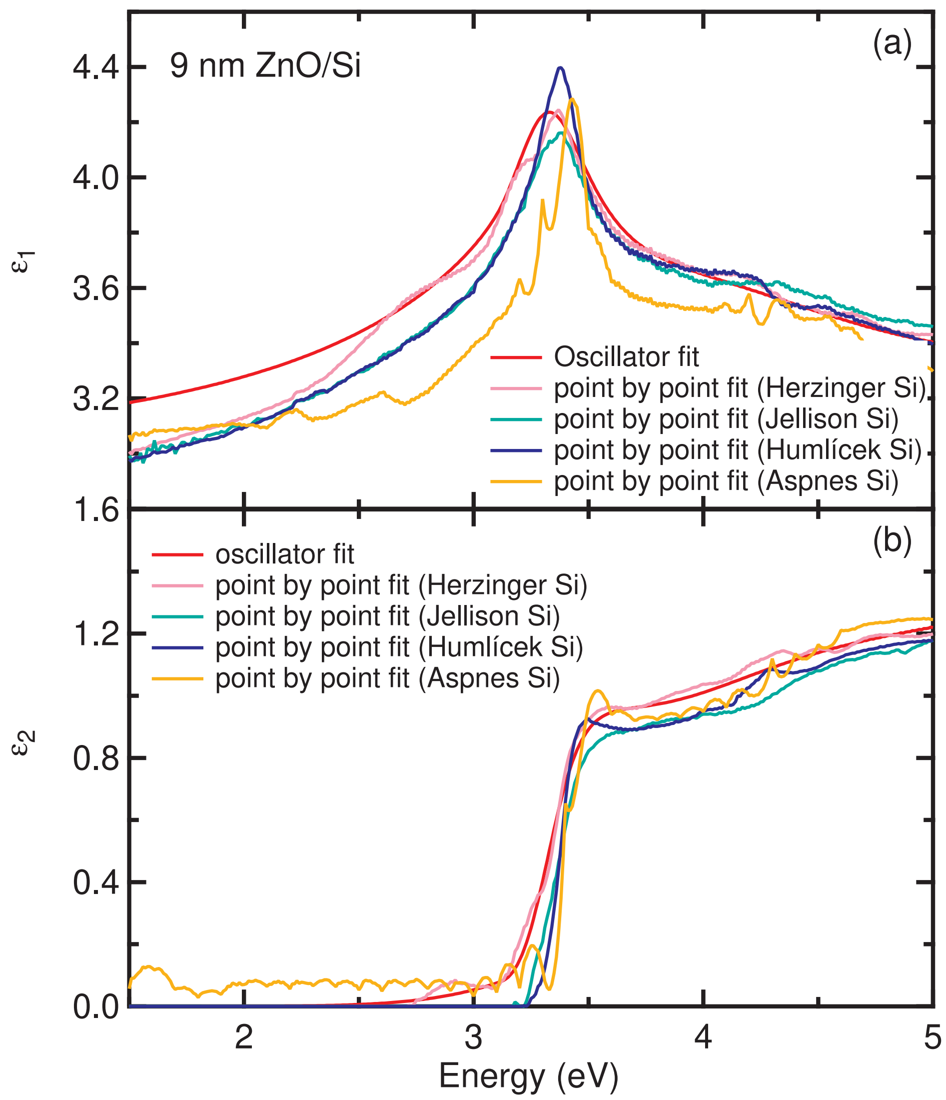

Figure 4.25: As Fig. 4.23, but for the 9 nm ZnO on Si layer.

4.8.11 Accuracy of thicknesses determined from ellipsometry

It is well known that spectroscopic ellipsometry cannot determine both thickness and refractive index for transparent layers as the thickness goes to zero [45,46,91]. For ultrathin layers, ellipsometry measures only the optical thickness, i.e., the product nt of the refractive index n and the thickness t. As the film thickness gets larger, interference fringes become visible, where the ellipsometric angle Δ jumps by 2π. The refractive index of the layer can then be determined from the amplitude of the interference fringes of the ellipsometric angle ψ, which is related to the optical contrast, i.e., the ratio of the refractive indices of layer and substrate. The spacing of the interference fringes is related to the optical thickness. The two quantities n and t can therefore be determined from the amplitude and spacing of the interference fringes. This method is implemented in commercial ellipsometry data analysis software.

In the intermediate thickness regime, one performs a uniqueness fit: [45] One fixes the thickness (over a certain range) and fits all other parameters, then plots the mean standard error from this fit versus thickness. If there is a clear minimum, then one can reasonably assume that the layer thickness is given by this minimum. We performed this procedure for our thinnest ZnO layer on Si, compare Table 4.3, where the XRR thickness (4.5 nm) deviates significantly from the ellipsometry thickness (7.6 nm). The result is shown in Fig. 4.26. We conclude from this

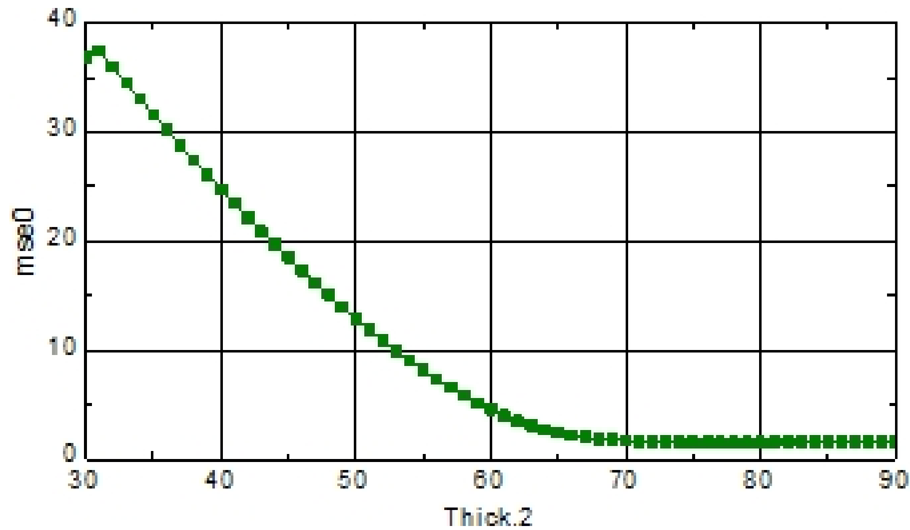

Figure 4.26: Uniqueness fit (mean standard error versus thickness in Å) for a ZnO layer on Si with a nominal thickness of 5 nm.

figure that the thickness of this layer is not at all likely to be less than 6 nm, but it might possibly be much thicker. We plot the same data in Fig. 4.27 on a narrower scale, which shows a clear minimum for t=7.6 nm. We conclude that the ellipsometry thickness of this layer is likely to be between 7.3 and 8.0 nm. (There are no generally accepted criteria in the ellipsometry community [45] on how to select a tolerance interval for a parameter from a uniqueness fit.)

We conclude that the roughly 50% difference of the thicknesses of the thinnest ZnO layer on Si determined from XRR and from ellipsometry (see Table 4.3) is much larger than the error of the XRR technique (about 1%, see Sec. 4.8.3) or the ellipsometry technique (about 5%, see above). How can we explain this? One of us has previously discussed the accuracy of several characterization techniques,

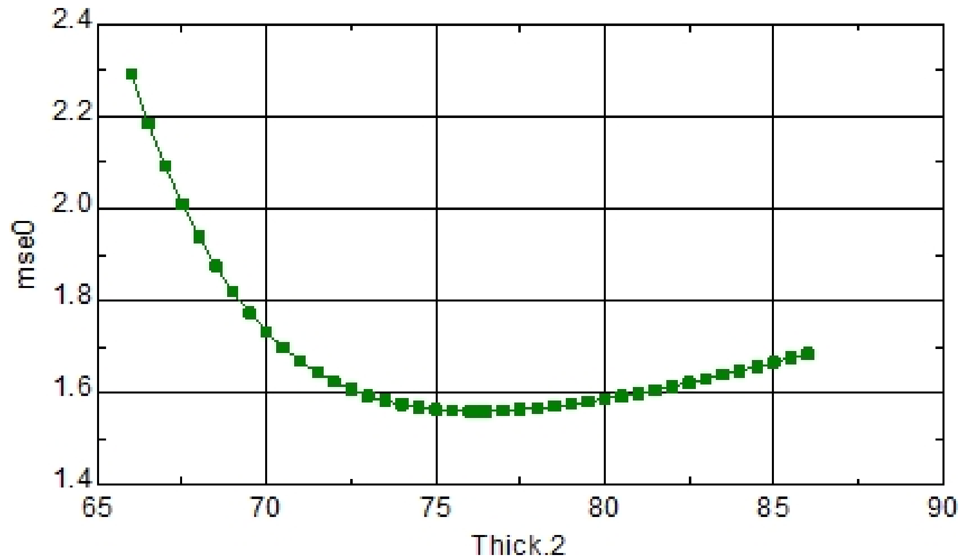

Figure 4.27: Same data as in Fig. 4.26, but shown in a narrower range of thicknesses.

especially XRR, ellipsometry, and transmission electron microscopy to determine the thickness of thin metal oxides on Si (S. Zollner, Y. Liang, R. B. Gregory, P. L. Fejes, D. Theodore, Z. Yu, D. H. Triyoso, J. Curless, and C. Tracy, *Limits of optical and x-ray metrology applied to thin gate dielectrics*, in *Characterization and Metrology for ULSI Technology 2005*, edited by D. G. Seiler, A. C. Diebold, R. McDonald, C. R. Ayre, R. P. Khosla, S. Zollner, and E. M. Secula, (American Institute of Physics, Melville, NY, 2005), AIP Conf. Proc. **788**, p. 166-171). As in this earlier work, we note that XRR considers an interfacial SiO_2 layer to be part of the Si substrate (because Si and SiO_2 have similar electron densities) while ellipsometry sees it as part of the layer (because ZnO and SiO_2 are much less polarizable than Si and have much smaller magnitudes of the dielectric function).

Figure 4.28: Transient dielectric function of Ge versus photon energy.

We assumed a 1 nm thick SiO_2 interfacial oxide layer between Si and ZnO in our ellipsometry model, but it is possible that this interfacial oxide is thicker. Unfortunately, there is no good answer for the discrepancy between the XRR and ellipsometry results for the thickness of the thinnest ZnO layer on Si. This discrepancy for ZnO layers on Si becomes smaller as the layers become thicker. It is not a big issue for ZnO layers on quartz.

One might ask: What if the XRR thickness (4.5 nm) was the correct thickness of our thinnest ZnO layer on Si? What would the ZnO dielectric function be under this assumption? Unfortunately, we are not able to answer this question, because no good fit to the ellipsometric angles can be found while assuming a 4.5 nm ZnO thickness combined with a 1 nm thick SiO_2 interfacial layer. However, we are able to obtain a good fit if we assume a thickness of 5.0 nm for the thinnest ZnO layer on Si, combined with an interfacial SiO_2 layer thickness of 3.6 nm (rather than 1.0 nm as in our standard model described in Sec. 4.4). The results from this fit are shown by the dashed lines in Fig. 4.5. Our main conclusions, a significant reduction of ϵ_1 below the band gap and a weakening of the excitonic absorption, are not affected qualitatively, but there are quantitative differences between the two models for the thinnest ZnO layer on Si.

5 TEMPERATURE DEPENDENCE OF THE OPTICAL PHONON REFLECTION BAND IN GAP

This article was published in the Journal of Vacuum Science and Technology B, volume **39**, 052201 (2021).

Nuwanjula S. Samarasingha and Stefan Zollner

Department of Physics, New Mexico State University, MSC 3D, P.O. Box 30001, Las Cruces, New Mexico 88003, USA

5.1 Abstract

We explore the effect of temperatures between 80 and 720 K on the energy and linewidth of zone-center transverse (TO) and longitudinal (LO) optical phonons in bulk gallium phosphide (GaP) using Fourier transform infrared ellipsometry from 0.03 to 0.60 eV. We extract the optical phonon parameters of GaP by fitting the ellipsometric angles with the Lowndes-Gervais model, which applies two different broadening parameters to the TO and LO phonons. In GaP, the two-phonon density of states is larger for the decay of TO phonons than for LO phonons. Therefore, we observed a larger TO phonon broadening (compared to the LO phonon) and an asymmetric reststrahlen line shape. This would lead to a negative imaginary part of the dielectric function just above the LO phonon energy, but the addition of two-phonon absorption avoids this. We find a temperature dependent

redshift and broadening of TO and LO phonons with increasing temperature due to thermal expansion and anharmonic phonon-phonon scattering, involving three and four phonon decay processes. We also investigate the temperature-dependence of the high-frequency dielectric constant. Its variation is explained by thermal expansion and the temperature dependence of the Penn gap.

5.2 Introduction

Most insulators and non-conducting polar semiconductors exhibit bands of high reflectance in the far- or mid-infrared spectral range. These so-called *reststrahlen* bands extend from the energy of transverse optical (TO) phonons to that of the corresponding longitudinal optical (LO) phonons. They have been studied extensively for many materials [14–21].

One open question regarding these restrahlen bands is the relative magnitude of the broadening parameters of the TO and LO phonons. Lowndes [14] and Schubert [15] explain that the sum of the broadenings γ_{TO} of the TO phonons must be smaller than the sum of the broadenings γ_{LO} of the LO phonons. Berreman and Unterwald [16] call this the "passivity" condition, ensuring that the imaginary part of the dielectric function $\epsilon(\omega)$ does not become negative. This condition is satisfied for alkali halides [14].

It is often violated for other materials, however, as shown by Lockwood, Yu, and Rowell [17] for six different zinc blende semiconductors using infrared re-

flectance measurements at oblique incidence combined with a derivative analysis technique, where $\gamma_{TO}>\gamma_{LO}$ is found for AlAs, GaP, InP, InAs, and InSb. For highly ordered materials, such as zinc blende semiconductors, these broadenings are lifetime broadenings, related to the decay of optical phonons into acoustic ones [22]. For GaP, the decay of TO phonons into two acoustic phonons is very fast, because a maximum of the two-phonon density of states (DOS) occurs at the TO energy [23, 24]. By contrast, the two-phonon DOS is lower at the LO energy and therefore $\gamma_{TO}>\gamma_{LO}$ for GaP. As we will show below, the resulting negative ϵ_2 above the LO energy is compensated by two-phonon absorption.

To further investigate the broadenings of the reststrahlen bands in semiconductors, we measured the temperature dependence of the dielectric function of GaP in the mid-infrared spectral region from 80 to 720 K. We selected GaP for our study, because its reststrahlen band is at rather high energies (due to the low mass of the P atom) and Fourier-transform infrared (FTIR) ellipsometry measurements can therefore be performed using commercial instrumentation. Furthermore, the reststrahlen band is not distorted by two-phonon absorption between the TO and LO energies [25]. We find a redshift and broadening of the TO and LO phonons due thermal expansion and anharmonic phonon decay.

Gallium phosphide (GaP) is an isotropic indirect III/V compound semiconductor with a band gap E_g of approximately 2.25 eV at room temperature [26,27]. It crystallizes in the zinc blende structure [26, 28] with the cubic space group T_d^2.

GaP has two atoms per primitive cell, resulting in three-fold degenerate acoustic and optical phonon modes at Γ. The polar Fröhlich interaction splits the optical modes into a TO doublet and an LO singlet [29, 30], which are both Raman- and infrared-active. Throughout this paper we refer to these infrared- and Raman-active phonons as "optical phonons". This thermally stable indirect wide band gap material is an excellent semiconductor for optoelectronic and photonic applications, especially in light-emitting diodes (LEDs) [31], detectors, solar cells, and high-temperature transistors [27]. It is therefore important to study the optical properties of this semiconductor, including the effects of cryogenic and elevated temperatures.

Since the TO and LO phonons are both infrared- and Raman-active, they can be studied with infrared reflection, transmission, or ellipsometry as well as Raman scattering, as demonstrated by Barker [20]. In reflection measurements, one observes a band of high reflection from the TO energy to just above the LO energy. The precise location of the upper end of the restrahlen band depends on the angle of incidence [15]. In infrared transmission experiments (of very thin GaP layers), one observes an absorption band at the TO energy defined by $\epsilon_2(\omega)$. At the LO energy, where $\epsilon_1(\omega)=0$, there is a similar peak in the loss function $-\mathrm{Im}[1/\epsilon(\omega)]$, but light does not couple with LO phonons to lowest order. In infrared ellipsometry measurements, the ellipsometric angle ψ forms a reststrahlen band similar to that found in reflectance measurements, while the ellipsometric

angle Δ usually transitions from 180° at low energies (due to the high value of the static dielectric constant) to 0° at high energies (due to the low value of the high-frequency dielectric constant), but this statement is not true for small or very large angles of incidence. For measurements on bulk substrates, the ellipsometric angles can directly be converted into the complex dielectric function and the loss function. No fitting is required.

TO and LO phonons also cause Raman peaks in inelastic light scattering spectra. As explained by Barker and Loudon [20, 32], $\epsilon_2(\omega)$ determines the Raman lineshape of the TO phonon, while $-\mathrm{Im}\left[1/\epsilon(\omega)\right]$ governs the LO Raman line, see Fig. 2 in Barker [20]. Therefore, it should be possible to directly compare the Raman energies and linewidths with the energies and linewidths of the peaks in $\epsilon_2(\omega)$ and $-\mathrm{Im}\left[1/\epsilon(\omega)\right]$ determined with infrared ellipsometry. This is a fundamental premise for the work described in this article.

The vibrational properties of bulk GaP have already been studied theoretically and experimentally by several authors. Using FTIR reflectance, Lockwood *et al.* [17] investigated TO and LO phonons in several III-V semiconductor materials, including bulk GaP, in the reststrahlen region at room temperature. Bairamov *et al.* [33, 34] measured the effect of temperature on the optical phonon frequency and linewidth with Raman scattering and explained their results with the anharmonic decay of optical phonons into two or three acoustic phonons. They found a redshift and increasing broadening with increasing temperature from 4.2 K to

550 K and also an increasing asymmetry of the TO phonon at high temperatures. Debernardi [22, 23] calculated the temperature and pressure dependence of the Raman linewidths and energies of the TO and LO phonons from 0 to 325 K. From the observation of first order Raman spectra, Mooradian and Wright [35] found almost no phonon frequency shift between room temperature and helium temperature. The spectral range of most of these works is around the reststrahlen band (250-550 cm^{-1}) of bulk GaP. However, several other theoretical and experimental studies of optical phonons in bulk GaP exist [36–40], including inelastic neutron scattering data and shell model calculations [28]. Some of them identified not only the long wavelength optical phonons at the Γ point of the Brillouin zone, but also zone edge phonons [20, 41, 42].

5.3 Experimental methods and models

A bulk unintentionally doped single side polished GaP wafer grown by the liquid encapsulated Czochralski method with 0.5 mm thickness, (111) surface orientation, and a (110) flat was obtained commercially (MTI Corporation, Richmond, CA). The sample had n-type conductivity with an electron concentration on the order of n=5×10^{16} cm^{-3} and a resistivity of about 0.3 Ωcm. By comparison, the electron concentrations of GaP used for similar studies in the literature range from 10^{16} to 10^{17} cm^{-3}. The electron density may influence the observed phonon line broadenings.

The ellipsometric angles Ψ and Δ of the as-received GaP wafer were acquired (without cleaning) on a J. A. Woollam FTIR Mark II ellipsometer from 0.03-0.60 eV (mid and near-infrared spectral regions) with 1 cm^{-1} resolution from 80-720 K with 25 K step size (30 measurements) inside an ultra-high vacuum cryostat (Janis ST-400) with diamond windows (Diamond Materials GmbH, Freiburg, Germany) at 70° angle of incidence [15]. At each temperature, measurements were performed with 15 positions per revolution of the rotating compensator. To increase the signal-to-noise ratio, we averaged 50 interferometer mirror scans at each compensator position. Systematic errors were reduced with $P=\pm 45°$ polarizer angles and also zone averaging the analyzer ($A=0°, 90°$). WVASE32 (J. A. Woollam Co., Lincoln, NE) and IGOR Pro (WaveMetrics, Lake Oswego, OR) scientific data analysis software were used to analyze our data.

We first measured Ψ and Δ in air at three different incidence angles of 60°, 65°, and 70° to calibrate the cryostat windows [43]. The GaP sample was then attached to a copper cold finger using metal clamps. The temperature was measured with two type-E (nickel-chromium/constantan) thermocouples. One located near the cryogen reservoir was used to control the temperature with a Lakeshore temperature controller. The second thermocouple was directly attached to the surface of the GaP sample and measured the temperature of the sample surface. The difference between both thermocouple readings was up to 60 K at the highest temperatures.

The cryostat was then sealed and pumped to a pressure below 10^{-5} Torr. In order to reduce the surface contamination, the sample was heated to 700 K for several hours with a 50 Ω resistor installed in the cryostat. This anneal may change the surface reconstruction, but no serious degradation of the sample is expected [44]. The cryostat was then allowed to cool down to room temperature while continuing to pump. Once a sufficiently low base pressure of 10^{-9}-10^{-8} Torr was reached, we started to cool the system down to 80 K using liquid nitrogen. Measurements were then taken from low to high temperatures in steps of about 25 K. Typical results at 300 K in air are shown in Fig. 5.1.

The static and high-frequency dielectric constants ϵ_s and ϵ_∞ and the optical phonon parameters (amplitude A, TO and LO phonon energies ω_{TO} and ω_{LO}, and corresponding broadenings γ_{TO} and γ_{LO}) were obtained by fitting the ellipsometric angles of GaP at each temperature either with a single Lorentzian

$$\epsilon\left(\omega\right) = \epsilon_\infty + \frac{A\omega_{\mathrm{TO}}^2}{\omega_{\mathrm{TO}}^2 - \omega^2 - i\gamma_{\mathrm{TO}}\omega}, \tag{104}$$

or with the Lowndes-Gervais model [14, 18]

$$\epsilon(\omega) = \epsilon_\infty \frac{\omega_{LO}^2 - \omega^2 - i\gamma_{LO}\omega}{\omega_{TO}^2 - \omega^2 - i\gamma_{TO}\omega}. \tag{105}$$

Details of this approach are given in Ref. 21 and in the supplementary material. A thin surface overlayer with variable thickness (about 35 Å), described as a 50/50 mixture of GaP and voids within the Bruggeman effective medium approximation, was also included in the model [45, 46].

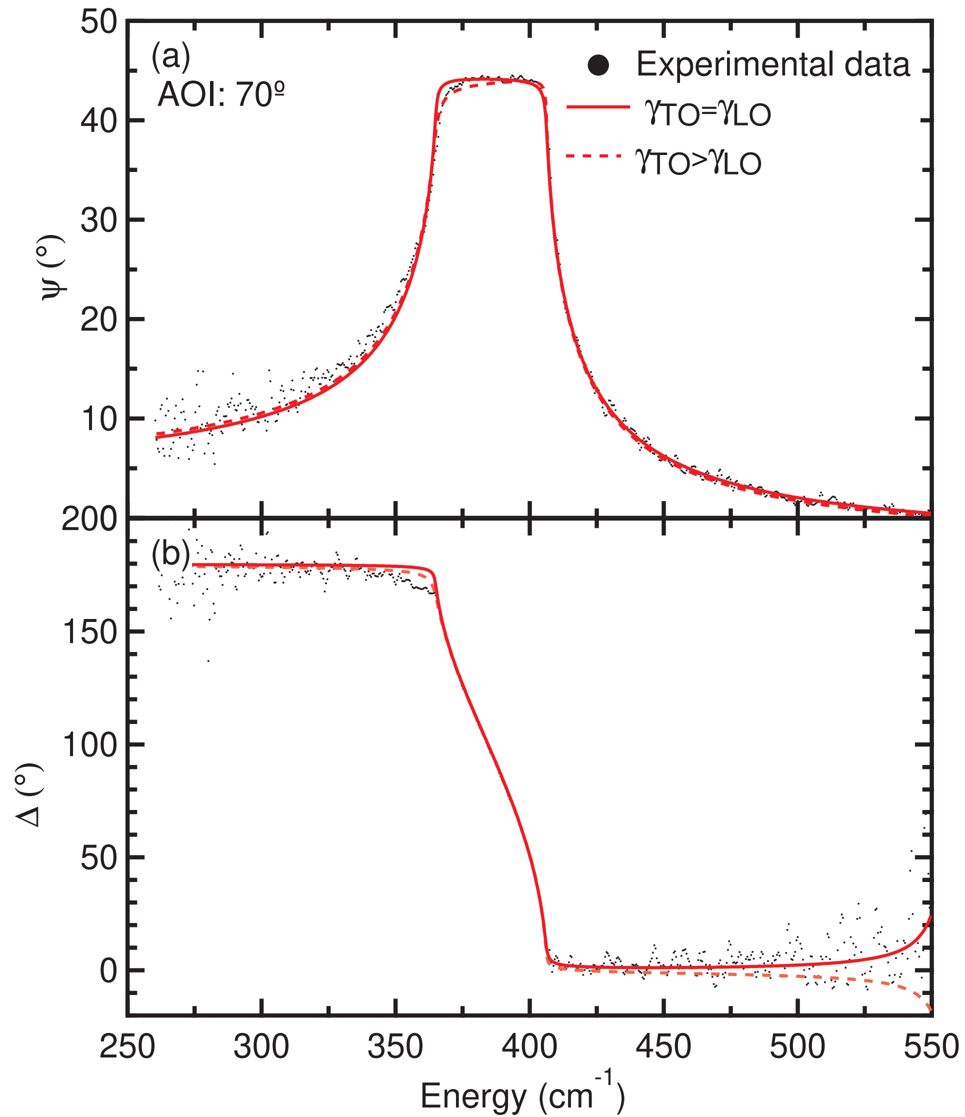

Figure 5.1: Ellipsometric angles (a) ψ and (b) Δ at 300 K in air at 70° angle of incidence (AOI) for bulk GaP with a surface layer. The symbols show experimental data. Solid and dashed lines show the result of a fit using Eq. (105).

Once the surface layer thickness and phonon parameters have been determined from this model for each temperature, it is also possible to fix the surface layer thickness and fit the ellipsometric angles with the optical constants at each photon energy as parameters. This so-called "point-by-point fit" leads to results in Fig. 5.2. It can be seen clearly that the extrema of ϵ_1 and ϵ_2 show a redshift, increasing broadening, and decreasing amplitude with increasing temperature. Tabulated optical constants [47] are shown for comparison.

5.4 Results and discussion

5.4.1 Optical phonon parameters at 300 K

We used four different models to extract the phonon parameters from the experimental data, with results shown in Table 5.1 for room temperature. Models (1) and (4) fit the ellipsometric angles ψ and Δ with consideration of the experimental errors [46] to Eqs. (104) and (105), respectively. This the most common data analysis methods for ellipsometry data. Models (2) and (3) fit $\langle \epsilon_2 (\omega) \rangle$ and $-\text{Im}\left[1/ \langle \epsilon (\omega) \rangle\right]$ with Lorentzians to determine the TO and LO phonon parameters, respectively. These results should be comparable with the Raman results of Bairamov *et al.* [33] A detailed comparison of results from the four models follows below.

The Lorentz model allowed us to find ϵ_∞, A, ω_{TO}, and γ_{TO} at room temperature, either by fitting the ellipsometric angles with the experimental errors

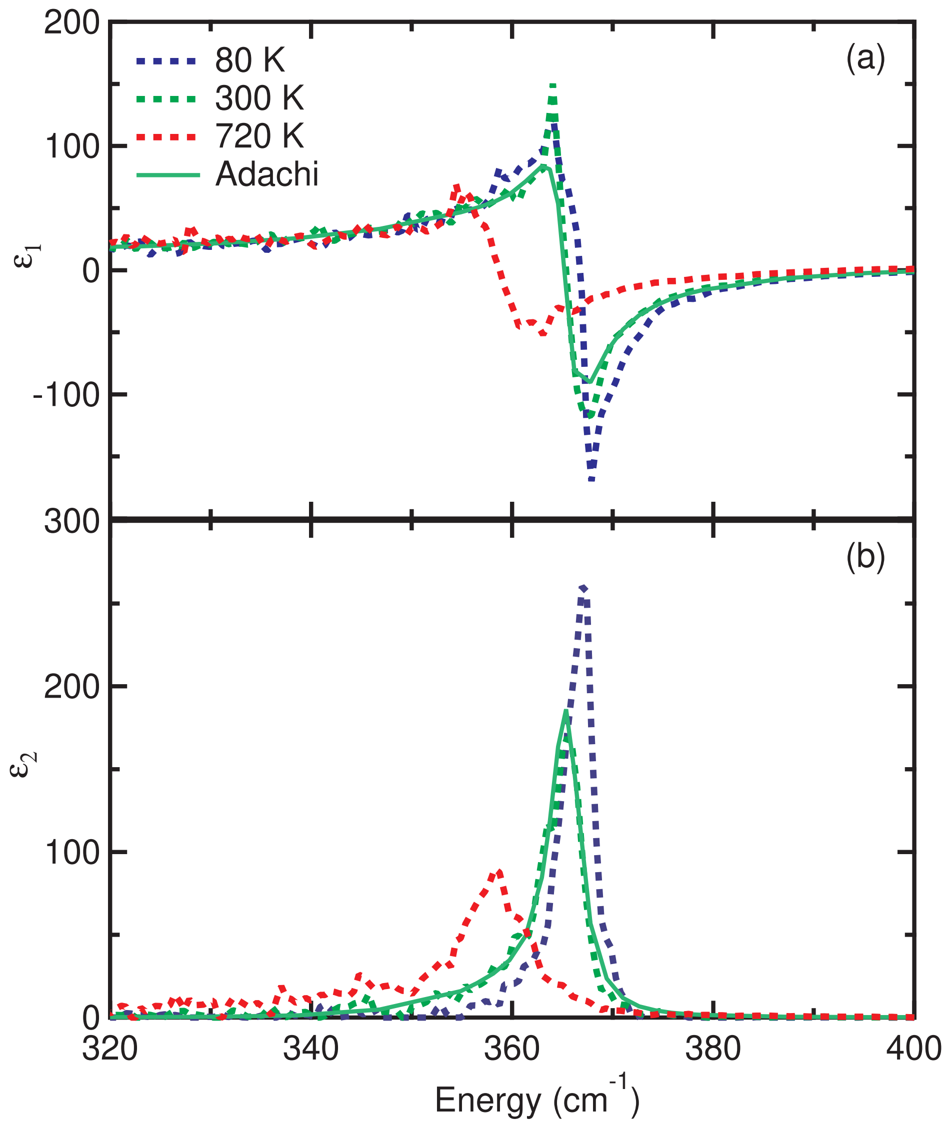

Figure 5.2: (a) Real and (b) imaginary parts of the complex dielectric function of bulk GaP at three different temperatures versus photon energy (dashed), determined from a "point-by-point" fit, in comparison with room temperature results as described in [47] (solid).

(model 1) or only the imaginary part $\langle\epsilon_2\rangle$ of the pseudo-dielectric function (model 2). Both models yield similar results, see Table 5.1, but γ_{TO} is smaller when fitting the ellipsometric angles (model 1). The Lorentzian broadening affects both the lower and upper corner of the reststrahlen band. If $\gamma_{\mathrm{TO}}>\gamma_{\mathrm{LO}}$, model (1) will find an intermediate Lorentzian broadening close to the average of γ_{TO} and γ_{LO}. On the other hand, if we only fit $\langle\epsilon_2\rangle$ in model (2), we find the larger broadening γ_{TO} of the TO phonon. This explains why models (1) and (2) report different values for γ_{TO}, see Table 5.1.

These models (1-2) assume equal broadenings for the TO and LO phonons. Results from the Lorentz model (1) are shown by the solid lines in Fig. 5.1. This model (1) fits the ellipsometric angles near the LO energy well, but not near the TO energy. The Lorentzian line shape is symmetric, while the ellipsometric angle ψ is more rounded at the TO energy (indicating a larger broadening) than at the LO energy.

Following Fig. 2 in Barker [20], we also determined the energy and broadening of the LO phonon by fitting the pseudo-loss function (122) with a Lorentzian, see Fig. 5.7. Results are shown in model (3) of Table 5.1. We find that γ_{TO} is two to four times larger than γ_{LO}. This motivates the use of the Lowndes-Gervais model (4), see Eq. (105), to fit the ellipsometric angles, because it treats γ_{TO} and γ_{LO} as two independent parameters. These results are shown by the dashed line in Fig. 5.1 and in model (4) of Table 5.1.

Table 5.1: Phonon parameters at 300 K determined with different models:(1) TO phonon parameters obtained from the Lorentz model by fitting the ellipsometric angles with the experimental errors. ω_{LO} was calculated from Eq. (121). (2) Same, but from fitting only $\langle\epsilon_2\rangle$. (3) LO phonon parameters from a Lorentzian fit to the pseudo-loss function. (4) Results from the Lowndes-Gervais model, Eq. (105). Data from the literature is also shown. Probable errors are listed in parentheses.

Model	ϵ_∞	A	ω_{TO} (cm^{-1})	γ_{TO} (cm^{-1})	ω_{LO} (cm^{-1})	γ_{LO} (cm^{-1})
(1)	9.02(1)	1.950(2)	364.81(3)	1.61(3)	402.33(6)	NA
(2)	NA	1.97(3)	365.24(3)	3.86(8)	NA	NA
(3)	NA	0.0211(1)	NA	NA	402.3(2)	0.88(1)
(4)	9.02(1)	NA	364.81(3)	2.91(4)	402.33(2)	0.90(3)
Ref. 17	9.24(2)		366.3(3)	2.6(6)	402.50(5)	1.2(1)
Ref. 20	9.09	1.92	365.3	1.1	402.2	
Ref. 33[a,b]			364.5	3.5	402.5	2
Ref. 35[a]			367.3		403.0	
Ref. 48	9.091		363.4			
Ref. 49[c]				>4		0.76

[a]Raman scattering.

[b]n=9×10^{16} cm^{-3} (increased LO broadening).

[c]Coherent anti-Stokes Raman scattering.

Our value of ϵ_∞=9.02 ±0.01 is only about 0.8% smaller than ϵ_∞=9.091 determined by Parsons and Coleman [48,50]. A better accuracy should not be expected for spectroscopic ellipsometry and can only be obtained with minimum-deviation prism measurements [51]. Using the LST relation (119), we find a static dielectric constant ϵ_s=10.97, also slightly (1.6%) smaller than ϵ_∞=11.147 found with far-infrared measurements [48, 50]. The temperature dependence of these dielectric constants will be discussed later within the context of Fig. 5.6. Our value for ω_{LO} =402.33±0.06 cm^{-1} agrees to within 0.1 cm^{-1} with Lockwood *et al.* [17] and Palik [48,50], but differences in the literature for ω_{TO} are several wave numbers. This is unexpected, since the upper end of the reststrahlen band near ω_{LO} depends on the angle of incidence and on the free electron concentration (see supplementary material), while the lower end of this band should unambiguously yield ω_{TO}.

It can be seen in Fig. 5.1 (dashed lines) that the reststrahlen band for bulk GaP is asymmetric, a clear indication that the TO and LO phonon broadenings are different. We can also see an asymmetry of ϵ_2 in Fig. 5.2. We obtained a better fit (dashed line in Fig. 5.1) to our data with larger TO broadening ($\gamma_{\mathrm{TO}}>\gamma_{\mathrm{LO}}$). The mean squared error [46] (difference between model and measured ellipsometric angles, weighted with the experimental errors) is about 10% smaller with the Lowndes-Gervais model than when fitting with a single Lorentzian. The same observation ($\gamma_{\mathrm{TO}}>\gamma_{\mathrm{LO}}$) was made by others [17] not only for GaP, but also for four other zinc blende semiconductors. Only GaAs is an exception and fulfills

the Lorentzian condition $\gamma_{\mathrm{TO}} \approx \gamma_{\mathrm{LO}}$. Raman scattering measurements of GaP at room temperature [20] also find $\gamma_{\mathrm{TO}} > \gamma_{\mathrm{LO}}$. The TO and LO Raman lineshapes closely follow the peaks of the imaginary part of the dielectric function and the loss function, respectively [20].

We interpret the GaP phonon broadenings as pure lifetime broadenings, similar to the radiative broadenings discussed by Loudon [52]. (See supplementary material for a discussion of other potential contributions to the broadenings.) The TO phonon energy at the Γ-point in the Brillouin zone is at a maximum of the two-phonon density of states. It is almost exactly the same as the sum of the longitudinal and transverse acoustic (LA+TA) phonon energies at the X-point. Therefore, the TO phonon can decay very efficiently into two acoustic phonons, while the same is not true for the LO phonon [24]. The complex self-energy $D(\omega_{\mathrm{TO}})$ has a large imaginary part. This explains $\gamma_{\mathrm{TO}} > \gamma_{\mathrm{LO}}$.

The phonon dephasing time τ is related to its broadening by [49, 53] $\gamma = 2\hbar/\tau$, where $\hbar = 0.658$ meVps is the reduced Planck's constant. The LO phonon lifetime should therefore be larger than that of the TO phonon. This was indeed observed with picosecond pump-probe coherent anti-Stokes Raman scattering (CARS) experiments [54], where Kuhl and Bron [49] found $\tau_{\mathrm{LO}} \approx 14$ ps ($\gamma_{\mathrm{LO}} \approx 0.76$ cm^{-1}) and $\tau_{\mathrm{TO}} < 2.6$ ps ($\gamma_{\mathrm{TO}} > 4$ cm^{-1}) for GaP at 300 K, see Table 5.1. An earlier CARS study [55] found a longer lifetime of 5.5 ps for a polariton near the TO phonon, resulting in a lower value of $\gamma_{\mathrm{TO}} = 2$ cm^{-1}.

5.4.2 Two-phonon absorption

Berreman and Unterwald [16] introduced the passivity condition $\gamma_{\mathrm{TO}} \leq \gamma_{\mathrm{LO}}$ to ensure that the imaginary part $\epsilon_2(\omega)$ of the dielectric function does not become negative. This condition is violated for GaP, as described in the previous section. Therefore, our model predicts a negative $\epsilon_2(\omega)$ just above the LO phonon energy, as shown by the dashed line in Fig. 5.3.

The passivity condition $\epsilon_2 \geq 0$ only applies to the total dielectric function, not to its individual contributions. So far, our Lowndes-Gervais model (105) only includes absorption of light by a single phonon. However, we must also consider multiphonon absorption [20,56–59], where one photon simultaneously creates two, three, or more phonons.

Multi-phonon absorption is too weak ($\epsilon_2 < 0.1$, $\alpha < 100$ cm^{-1}) to be observable with spectroscopic ellipsometry, which is more appropriate for measuring large absorption coefficients ($\alpha > 10^3$ cm^{-1}). Transmission measurements are better suited for the detection of small α. We were only able to gain a glimpse of multi-phonon absorption by increasing the band width of our ellipsometer to 4 cm^{-1} and the number of scans fourfold, resulting in the experimental data shown in Fig. 5.3. We clearly see that $\epsilon_2 > 0$ in the region from 400 to 600 cm^{-1}. We include multi-phonon absorption in our model with three broad Gaussians, which are added to Eq. (105), as shown by the solid line in Fig. 5.3.

These arguments show qualitatively that $\gamma_{\mathrm{TO}}>\gamma_{\mathrm{LO}}$ is not unphysical, if the resulting negative values of ϵ_2 are compensated by multi-phonon absorption. The anharmonic decay of optical phonons into acoustic phonons and multi-phonon absorption of a photon are both higher-order processes involving the interaction of several phonons. Therefore, it should not surprise that both processes are related.

5.4.3 Temperature dependence of optical phonon parameters

To accurately determine the temperature dependence of the optical phonon parameters and the (apparent) surface layer thickness, the ellipsometry angles Ψ and Δ of bulk GaP at each temperature were fitted with the Lowndes-Gervais model as described in section 5.3. All of these models consisted of a single Lowndes oscillator and the surface layer. The variation of this apparent GaP surface layer thickness with temperature is shown in Fig. 5.17 and discussed in the supplementary material. It changes from 0 to 48 Å over the whole temperature range.

The experimental phonon broadenings are determined by the instrumental resolution and defects (such as polishing damage [58]), which are independent of temperature. In addition, there is a temperature dependence of the broadenings due to the anharmonic decay of optical phonons. In analytical empirical models [33, 60], one usually considers three-phonon processes (where the optical phonon decays into two acoustic phonons of equal energy) and four-phonon processes

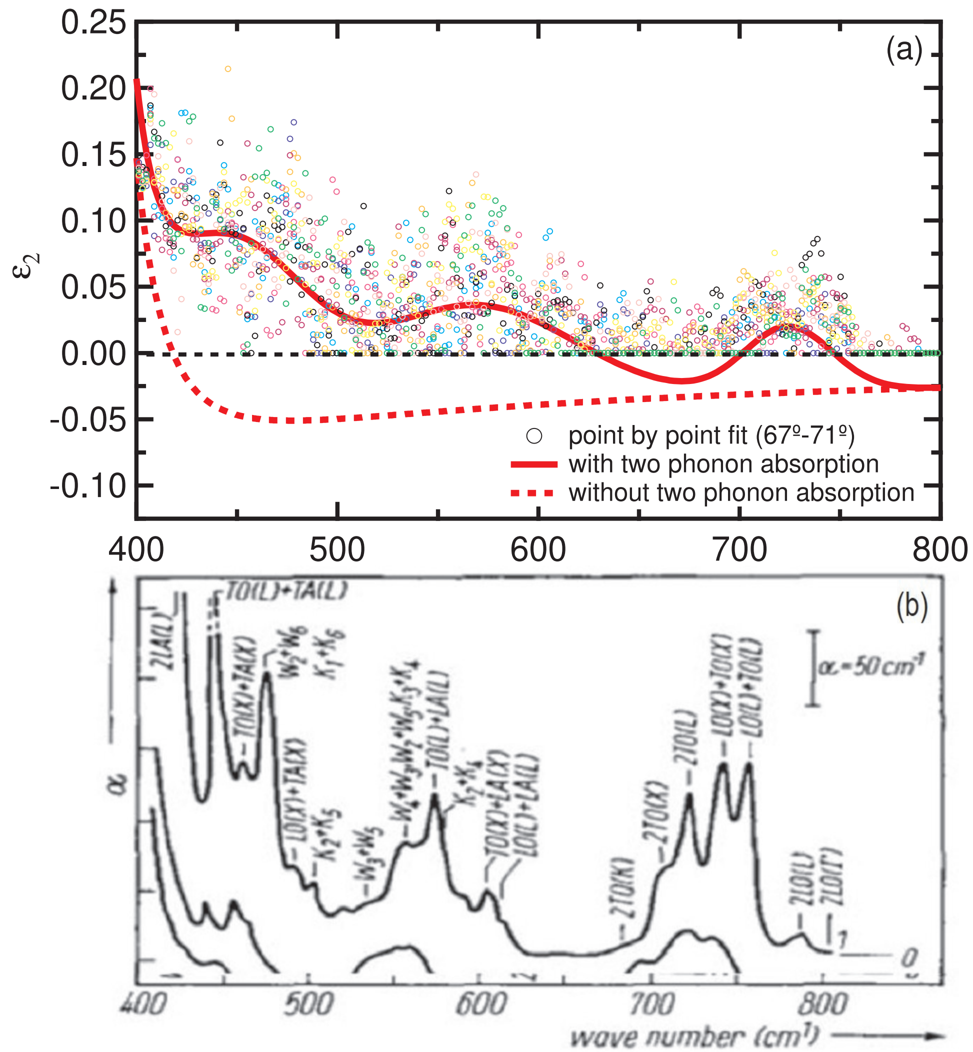

Figure 5.3: (a) Imaginary part of the complex dielectric function for GaP versus photon energy in the region of two-phonon absorption. (b) Absorption coefficient from a high-resolution transmission measurement [59]. Reprinted with permission from [B. Ulrici and E. Jahne, phys. stat. sol. (b) **86**, 517 (1978)]. Copyright [2021], [John Wiley and Sons].

(where the optical phonon decays into three acoustic phonons of equal energy). *Ab initio* calculations [22] based on realistic phonon dispersions obtained from density-functional theory relax the assumption that all decay products have the same energy, as long as the overall energy and crystal momentum are conserved. Three-phonon decay processes with a 2:1 ratio of the acoustic phonon energies seem particularly important [61]. The temperature-dependent broadenings can be calculated from the imaginary part of a complex self-energy describing the interaction between the optical phonon and its decay products [61].

The temperature dependence of the phonon energies is given by the corresponding real part of the same self energy [23]. However, there is also a contribution to the phonon energies due to thermal expansion [61]. We therefore begin with the discussion of the temperature dependence of the broadenings, followed by the temperature dependence of the phonon energies. We follow the formalism laid out by Bairamov *et al.* [33] and Menendez and Cardona [61].

1) Temperature dependence of phonon broadenings

The broadenings of the TO and LO phonon energies for GaP at each temperature are shown in Fig. 5.4. Solid circles show the results obtained by fitting the ellipsometric angles with a Lowndes model (105). Open circles show results obtained by fitting $\langle \epsilon_2 \rangle$ and the pseudo-loss function with a Lorentzian. Both methods yield the same values for the LO phonon broadenings, but the TO broadenings

found from fitting $\langle\epsilon_2\rangle$ are significantly larger than when fitting the ellipsometric angles. This discrepancy is discussed in detail in the supplementary material.

Our LO broadenings closely follow the 1979 results by Bairamov *et al.* [34], Kuhl and Bron [49], and Vallée [62] obtained from Raman linewidths or coherent anti-Stokes Raman scattering decay times of high-purity GaP samples (dotted). Earlier Raman work [33] used a GaP sample with a higher electron concentration of 9×10^{16} cm^{-3}, where the LO broadening is increased due to plasmon-phonon coupling (dashed). The Raman broadenings of the TO phonon [33] (dashed) are not affected by doping. They follow our results for fitting $\langle\epsilon_2\rangle$ with a Lorentzian (open symbols), since the Raman lineshape closely follows ϵ_2, see Ref. 20.

Debernardi [22,23] calculated the temperature and pressure dependence of the Raman linewidths and energies of the TO and LO phonons from 0 to 325 K, as shown by the dashed-dotted lines. However, his calculated linewidths for the TO phonon agree with Bairamov *et al.* [33] only at low temperatures and are much larger than the experimental results at higher temperatures. In the case of the LO phonon linewidths, the agreement with experiment [34,49,62] is much better.

Empirically, the broadenings due to anharmonic decay can be fitted with an expression [33,60,63]

$$\gamma(T) = \gamma_0 + A\left[1 + \frac{2}{e^x - 1}\right] + B\left[1 + \frac{3}{e^y - 1} + \frac{3}{(e^y - 1)^2}\right], \qquad (106)$$

where A and B are three- and four-phonon coupling constants, respectively. The

reduced phonon energies x and y are

$$x = \frac{\hbar\omega_0}{2k_B T} \quad \text{and} \quad y = \frac{\hbar\omega_0}{3k_B T}. \tag{107}$$

ω_0 is the unrenormalized phonon frequency and k_B is the Boltzmann constant. The parameter γ_0 describes temperature-independent mechanisms, such as inhomogeneous broadening due to defects or the instrumental resolution. Table 5.2 lists the best-fit parameters of Eq. (106) for TO and LO phonons. The broadenings calculated with these parameters (shown by the solid lines in Fig. 5.4) agree very well with the experimental results. Our anharmonic parameters A and B agree well with those in Ref. 33 for the TO phonon (except for a constant shift related to a different value for γ_0 due to a different fitting method), but our parameter B is much smaller for the LO phonon, since our sample had a lower doping concentration than in Ref. 33.

2) Temperature dependence of phonon energies

The temperature dependence of the optical phonon energies due to thermal expansion (TE) is given by [61,64,65]

$$\omega_{\mathrm{TE}}(T) = \omega_0 \exp\left[-3\gamma \int_0^T \alpha_l(\theta)\, d\theta\right], \tag{108}$$

where ω_0 is the phonon energy at 0 K, γ the Grüneisen parameter for the phonon mode, and α_l the linear thermal expansion coefficient. Since thermal expansion is small, it suffices [33] to keep only the linear term in the exponential in Eq. (108).

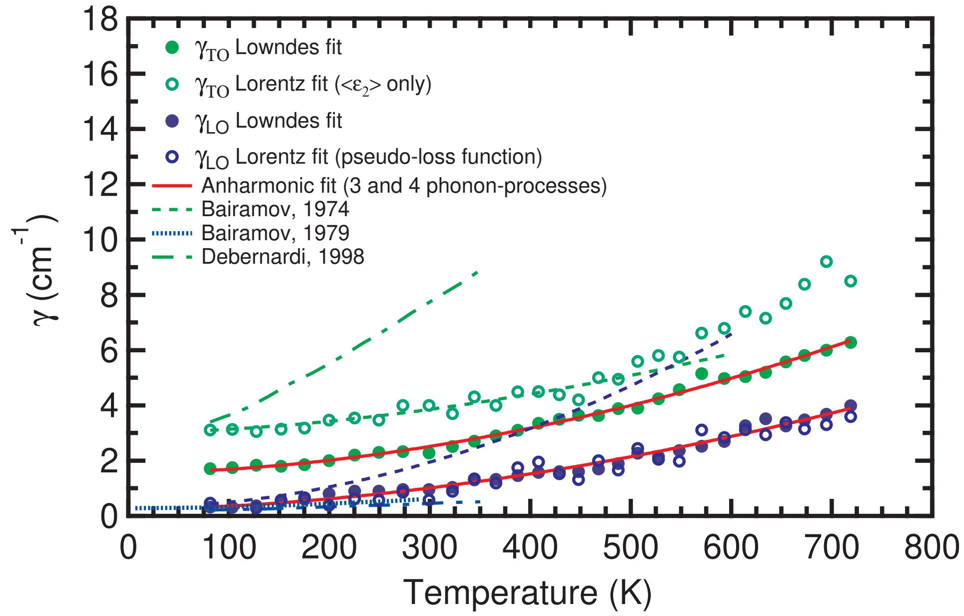

Figure 5.4: Temperature dependence of the TO and LO phonon broadenings (symbols). Solid lines show the best fit to our data using Eq. (106) with parameters in Table 5.2. Raman linewidths from Refs. 33, 34 are shown by dashed and dotted lines, respectively. The dashed-dotted lines show results from density-functional perturbation theory [22, 23]

.

Table 5.2: Anharmonic decay parameters for Eq. (106) for the temperature dependence of TO and LO phonon broadenings. Errors are shown in parentheses. Energies marked (f) were fixed during the fit, compare Table 5.3.

This work	TO	LO
A (cm^{-1})	0.2(1)	0.2(f)
B (cm^{-1})	0.08(1)	0.069(2)
γ_0 (cm^{-1})	1.4(1)	0.03(4)
ω_0 (cm^{-1})	367.3(f)	406.6(f)
Ref. 33	TO	LO
A (cm^{-1})	0.20	0.16
B (cm^{-1})	0.06	0.20
γ_0 (cm^{-1})	2.8	0
ω_0 (cm^{-1})	366	404

The thermal expansivity can be described using a Debye model for the phonons [66]

$$\alpha_l\left(T\right)=\alpha_{l\infty}D\left(\frac{\Theta_D}{T}\right), \tag{109}$$

where Θ_D=440 K is the Debye temperature, $\alpha_{l\infty}$=5.8×10^{-6} K^{-1} the thermal expansion coefficient in the high temperature limit, and [33, 66]

$$D\left(\eta\right)=\frac{3}{\eta^3}\int_0^\eta\frac{e^\xi\xi^4}{\left(e^\xi-1\right)^2}d\xi. \tag{110}$$

Instead, we can also use tabulated values [23, 67, 68] for the thermal expansion coefficient and perform the integration in Eq. (108) numerically.

The dependence of TO and LO phonon energies on temperature determined from a Lowndes fit to the ellipsometric angles is shown in Fig. 5.5 (symbols). Both show a redshift (decrease) with increasing temperature. The contribution of thermal expansion to these redshifts (dashed) is not sufficient to explain the experimental data. Therefore, Bairamov *et al.* [33] also included three- and four-phonon anharmonic decay processes.

The anharmonic contribution to the redshift can be described as [60]

$$\omega(T)=\omega_0-C\left[1+\frac{2}{e^x-1}\right]-D\left[1+\frac{3}{e^y-1}+\frac{3}{(e^y-1)^2}\right], \tag{111}$$

where and C and D are the anharmonic coupling strengths. The second and third terms in Eq. (111) relate to three- and four-phonon decay processes, respectively. Setting D=0 (i.e., ignoring four-phonon processes) does not achieve a good fit.

In principle, one should subtract the redshift due thermal expansion from the observed redshift and then fit the parameters C and D. This was done by Bairamov *et al.* [33], which resulted in the parameters shown in Table 5.3. In practice, however, one often ignores the thermal expansion contribution [60] and directly fits the experimental data with Eq. (111). These parameters are also shown in Table 5.3. The two methods result not only in different sets of coupling constants C and D, but also in differences for the unrenormalized phonon energies ω_0.

This redshift can also be fitted empirically with a Bose-Einstein expression [69]

$$\omega(T) = \omega_0 - C\left[1 + \frac{2}{e^{\frac{\theta_B}{T}} - 1}\right] \tag{112}$$

as an anharmonic three-phonon decay with an adjustable effective phonon energy $\omega_{\rm eff}{=}k_B\theta_B$, where θ_B is an effective phonon temperature related to the Debye temperature of GaP (440 K). These results are also shown in Table 5.3.

3) Temperature dependence of high-frequency and static dielectric constants

The high frequency dielectric constant ϵ_∞ for bulk GaP was also obtained from fitting the ellipsometric angles at each temperature with the Lowndes model (105). It increases with temperature, as shown in Fig. 5.6. ϵ_∞ can be expressed as [70]

$$\epsilon_\infty = 1 + \left(\frac{E_u}{E_{\rm Penn}}\right)^2, \tag{113}$$

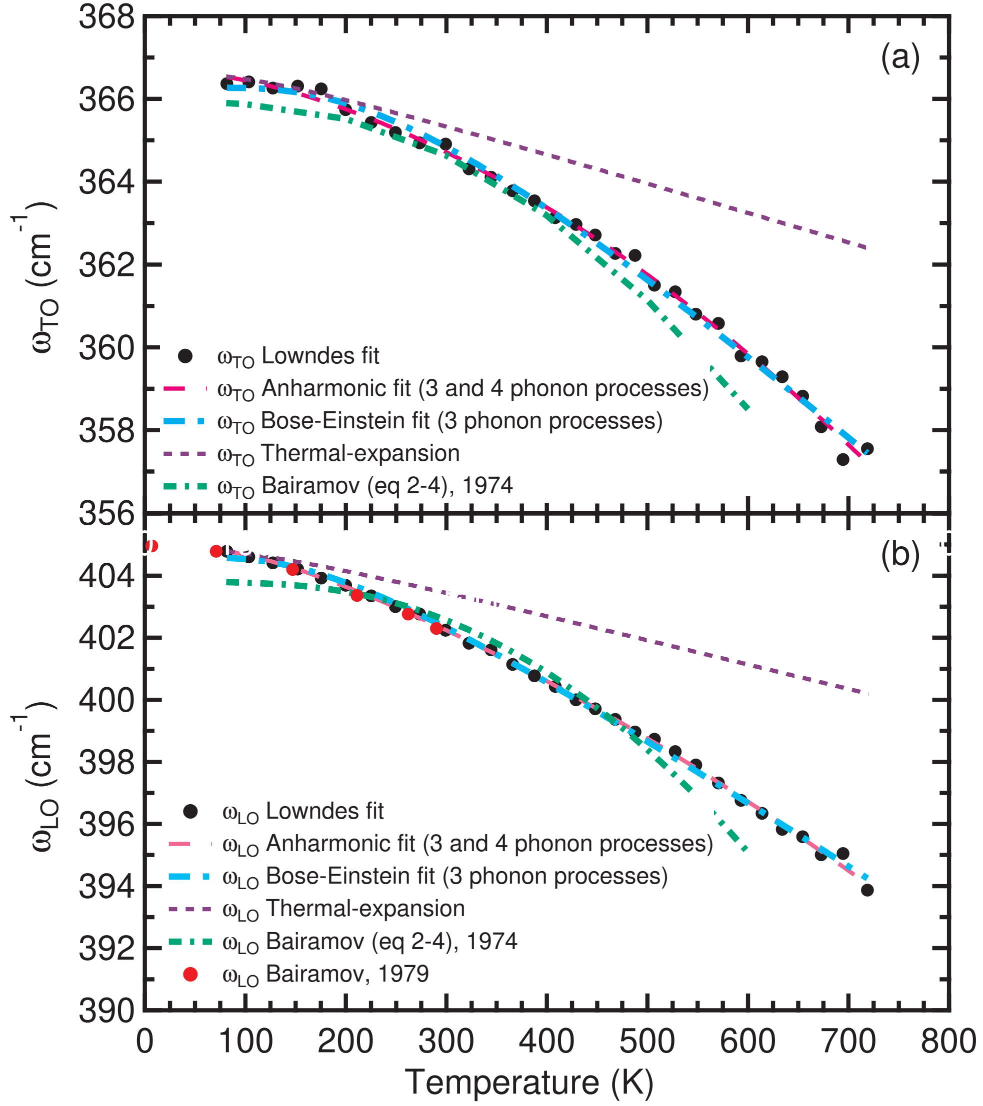

Figure 5.5: Temperature dependence of the (a) transverse (ω_{TO}) and (b) longitudinal (ω_{LO}) optical phonon energies of GaP (symbols). The dashed line shows the contribution of thermal expansion. Fits using Eqs. (111) and (112) with parameters in Table 5.3 are shown by dashed-dotted lines.

Table 5.3: Anharmonic decay parameters for the temperature dependence of TO and LO phonon energies. Errors are shown in parentheses.

Anharmonic decay parameters	TO	LO
This work, Eq. (111), ignoring thermal expansion.		
ω_0 (cm^{-1})	367.3(2)	406.6(1)
C (cm^{-1})	0.5(1)	1.6(1)
D (cm^{-1})	0.14(1)	0.11(1)
Ref. 33, Eq. (111), Raman, thermal expansion subtracted.		
ω_0 (cm^{-1})	364.5	401.4
C (cm^{-1})	−1.76	−2.98
D (cm^{-1})	0.30	0.51
This work, Eq. (112), ignoring thermal expansion.		
ω_0 (cm^{-1})	374.6(8)	410.5(4)
C (cm^{-1})	8.3(9)	5.9(4)
ω_{eff} (cm^{-1})	530(30)	380(20)

where the unscreened plasma frequency of the valence electrons is given by

$$E_u^2 = \hbar^2 \omega_u^2 = \frac{\hbar^2 N e^2}{m_0 \epsilon_0} = (16.5 \text{ eV})^2 . \tag{114}$$

N is the density of valence electrons per unit volume (8 electrons per formula unit), e the charge of the electron, m_0 the free electron mass, and ϵ_0 the vacuum permittivity. The resulting Penn gap E_{Penn}=5.83 eV, calculated from ϵ_∞ at 300 K, is the average separation between the valence and conduction band across the Brillouin zone, usually located near the E_2 gap (5.28 eV for GaP, see Refs. 70,71). We assume that E_2 and E_{Penn} have the same temperature dependence.

Taking the derivative of Eq. (113) with respect to temperature yields [72, 73]

$$\frac{d\epsilon_\infty}{dT} = -3\alpha_l (\epsilon_\infty - 1) - 2(\epsilon_\infty - 1)\frac{d \ln E_2}{dT}. \tag{115}$$

The first term considers the decrease of the electron density due to thermal expansion, which results in a decrease of ϵ_∞. The second term describes the increase of ϵ_∞ due to the decrease of the Penn gap with increasing temperature. This is the dominant term.

We calculated the temperature dependence of ϵ_∞ at room temperature, resulting in

$$\left.\frac{d\epsilon_\infty}{dT}\right|_{300 \text{ K}} = (-1.2 + 7.6) \times 10^{-4} \text{ K}^{-1} = 6.4 \times 10^{-4} \text{ K}^{-1}. \tag{116}$$

This value compares favorably with the experimental variation of ϵ_∞ between 200 and 400 K, which is 4.5×10^{-4} K^{-1}. Therefore, we conclude that the model (115) for the temperature dependence of ϵ_∞ is reasonable.

The temperature dependence of ϵ_s was calculated from the Lyddane-Sachs-Teller (LST) relation (119) and is also shown in Fig. 5.6. Since the ratio of the TO and LO phonon energies does not strongly depend on temperature, the variations of ϵ_s with temperature are very similar to those of ϵ_∞. We find that ϵ_s changes by about 1% between 0 and 300 K, which is three times larger than the change calculated by Debernardi [23].

5.5 Summary

We used FTIR spectroscopic ellipsometry from 0.03-0.60 eV to determine the effects of temperature on the properties of long-wavelength optical phonons of GaP at temperatures ranging from 80 to 720 K. With different experimental conditions, we also observed two-phonon absorption. GaP shows an asymmetric reststrahlen line shape, because the linewidth of the TO phonon is larger than that of the LO phonon at all temperatures. This violates the Lowndes passivity condition and the imaginary part ϵ_2 of the dielectric function becomes slightly negative just above the LO energy. To achieve a physically meaningful non-negative total dielectric function, we must also add multi-phonon absorption to the single phonon absorption. We also observed that the energies of the TO and LO optical phonons show a redshift and increasing broadening with increasing temperature due to thermal expansion and anharmonic phonon-phonon decay. The static and high-frequency dielectric constant increased with increasing temperature because of

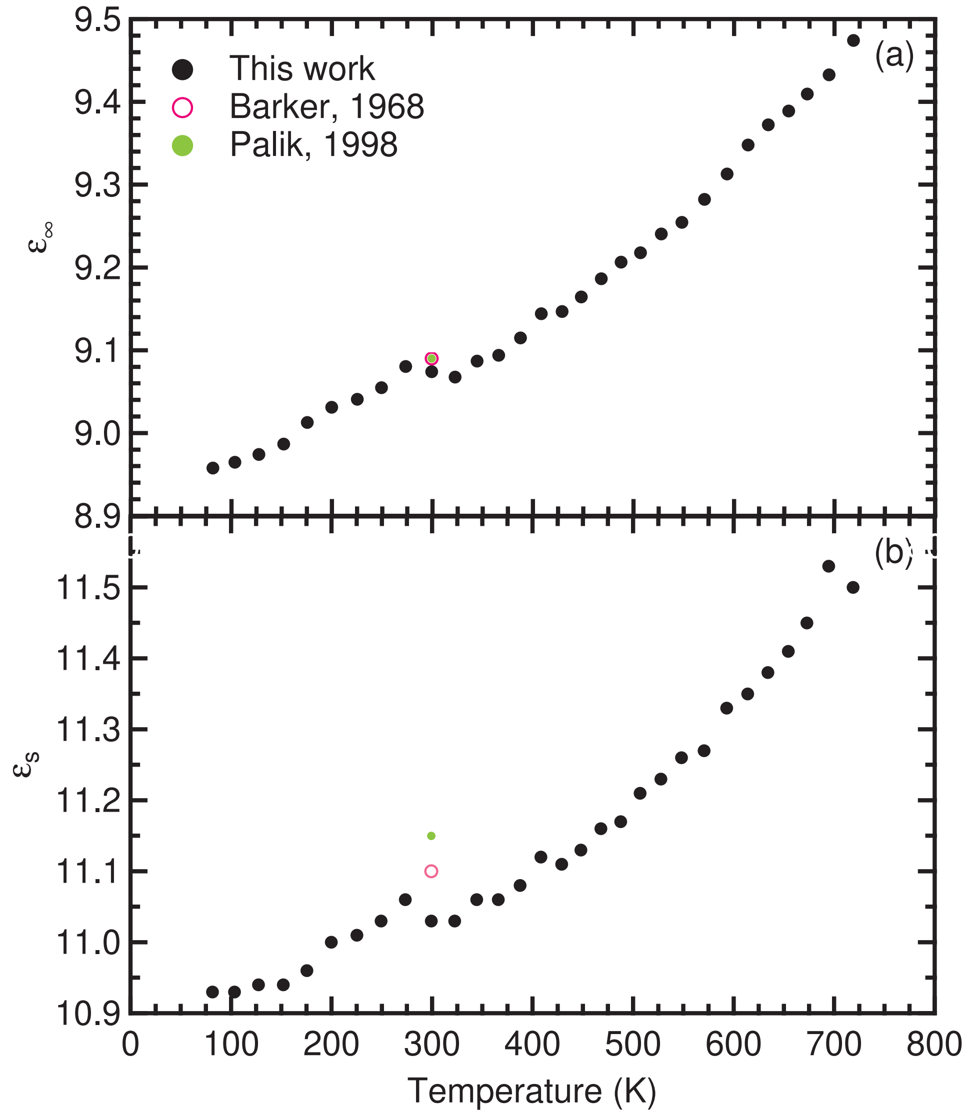

Figure 5.6: Temperature dependence of the (a) high-frequency (ϵ_∞) and (b) static (ϵ_s) dielectric constants. ϵ_∞ was found by fitting the experimental data with Eq. (105). ϵ_s was calculated from the Lyddane-Sachs-Teller relation (119). Data from the literature [20, 48, 50] are also shown.

the thermal expansion of the crystal and the temperature dependence of the Penn gap.

Acknowledgements

This work was supported by the National Science Foundation (DMR-1505172) and by the US Army (W911NF-16-1-0492). We wish to thank Professor David J. Lockwood (National Research Council of Canada) and Professor Sotirios Ves (Aristotle University of Thessaloniki, Greece) for helpful discussions regarding this research topic.

Data availability

The data that support the findings of this study are available from the corresponding author upon reasonable request.

5.6 Supplementary Material

5.6.1 Lorentz model for a single phonon

The static and high-frequency dielectric constants ϵ_s and ϵ_∞ and the optical phonon parameters (amplitude A, TO and LO phonon energies ω_{TO} and ω_{LO}, and corresponding broadenings γ_{TO} and γ_{LO}) were obtained by fitting the ellipsometric angles of GaP at each temperature either with a single Lorentzian or with the Lowndes-Gervais model [14, 18]. The difference between these two models is

that the Lowndes-Gervais model assigns two different broadening parameters γ_{TO} and γ_{LO} to the two phonons, while the Lorentz model has only one broadening parameter γ_{TO}.

Following Helmholtz (Ann. Phys. **230**, 582, 1875) or Wooten (*Optical Properties of Solids*, Academic, New York, 1972), the dispersion due to damped vibrations of molecules in a solid under the influence of an electromagnetic wave can be described by a Lorentz oscillator [20]

$$\epsilon(\omega) = \epsilon_\infty + \frac{A\omega_{\mathrm{TO}}^2}{\omega_{\mathrm{TO}}^2 - \omega^2 - i\gamma_{\mathrm{TO}}\omega}. \tag{117}$$

TO phonons therefore appear as a strong symmetric peak with linewidth γ_{TO} (FWHM) just below ω_{TO} (due to damping) in the imaginary part ϵ_2 of the complex dielectric function [25]. The maximum height of this peak is

$$\epsilon_2(\omega_{\mathrm{TO}}) \approx A\frac{\omega_{\mathrm{TO}}}{\gamma_{\mathrm{TO}}} \tag{118}$$

for $\gamma_{\mathrm{TO}} \ll \omega_{\mathrm{TO}}$. The peak position ω_{TO} can usually be determined very precisely from the position of the ϵ_2 peak. However, the peak amplitude is influenced by both A and γ_{TO}. In practice, this leads to parameter correlations when fitting data, especially if the peak shape is not precisely Lorentzian (e.g., due to asymmetry).

The minimum and maximum of the real part ϵ_1 of the dielectric function are separated by γ_{TO}. In this region, ϵ_1 shows anomalous dispersion. The LO phonon energy is defined by $\epsilon_1(\omega_{\mathrm{LO}})=0$. It can be found from the Lyddane-Sachs-Teller

(LST) relation [17]

$$\epsilon_s = \epsilon_\infty \frac{\omega_{\mathrm{LO}}^2}{\omega_{\mathrm{TO}}^2}. \tag{119}$$

The real part $\epsilon_1(\omega)$ is negative between ω_{TO} and ω_{LO}. This leads to a region of high reflectivity called reststrahlen band. Representative graphs of the dielectric function, the complex refractive index, and the reflectivity at normal incidence for a Lorentz oscillator are shown by Wooten (1972). The ellipsometric angles at 70° angle of incidence calculated from the Lorentz model are shown by solid lines in Fig. 5.1. It is important to note that the Lorentz model shows strong symmetry in the dielectric function, the reflectivity at normal incidence, and in the ellipsometric angles (but not in the complex refractive index or the absorption coefficient). For γ_{TO}=0, the reflectance R equals unity and the ellipsometric angle ψ=45° within the reststrahlen band. The corners of R and ψ are very sharp. The rise of ψ or R occurs precisely at the TO frequency, but the drop is pushed beyond the LO frequency at higher angles of incidence [15]. These corners are rounded symmetrically once γ_{TO} increases and R and ψ are lower than their ideal undamped values. The most precise determination of the broadening parameter γ_{TO} can therefore be made from the ellipsometric angle ψ within the reststrahlen region and its deviation from 45°. This is independent of the value of the amplitude A. Within the reststrahlen band, there is enhanced sensitivity to the low absorption caused by two-phonon processes (J. Humlíček, Thin Solid

Films **313-314**, 687, 1998). Setting ω=0 in Eq. (117), we find the relationship

$$\epsilon_s = \epsilon_\infty + A \tag{120}$$

between the static (ω=0) and high-frequency ($\omega \rightarrow \infty$) dielectric constants. Combining Eqs. (119) and (120), we find

$$\omega_{\mathrm{LO}} = \omega_{\mathrm{TO}} \sqrt{1 + \frac{A}{\epsilon_\infty}}. \tag{121}$$

As shown in Fig. 5.7, the pseudo-loss function

$$\mathrm{Im}\left(-\frac{1}{\langle\epsilon\rangle}\right) = -\langle\eta_2\rangle = \frac{\langle\epsilon_2\rangle}{\langle\epsilon_1\rangle^2 + \langle\epsilon_2\rangle^2} \tag{122}$$

shows a strong peak at the LO phonon energy (Wooten, 1972). To obtain the amplitude B, energy ω_{LO}, and broadening γ_{LO} of the LO phonon, the experimental data points in the pseudo-loss function (122) were fitted in IGOR Pro with the imaginary part of a Lorentzian

$$-\langle\eta_2\rangle = \frac{B\omega_{\mathrm{LO}}^2 \gamma_{\mathrm{LO}} \omega}{(\omega_{\mathrm{LO}}^2 - \omega^2)^2 + \gamma_{\mathrm{LO}}^2 \omega^2}. \tag{123}$$

The parameters from this fit are shown in model (3) of Table 5.1. The LO phonon energy of 402.3 cm^{-1} obtained from this pseudo-loss function fit matched perfectly with the calculated value 402.33 cm^{-1} from Eq. (121).

5.6.2 Frequency-dependent broadening

The Lorentz oscillator function (117) can be solved for the broadening parameter

$$i\gamma\omega = \omega_{\mathrm{TO}}^2 \frac{\epsilon - \epsilon_s}{\epsilon - \epsilon_\infty} - \omega^2. \tag{124}$$

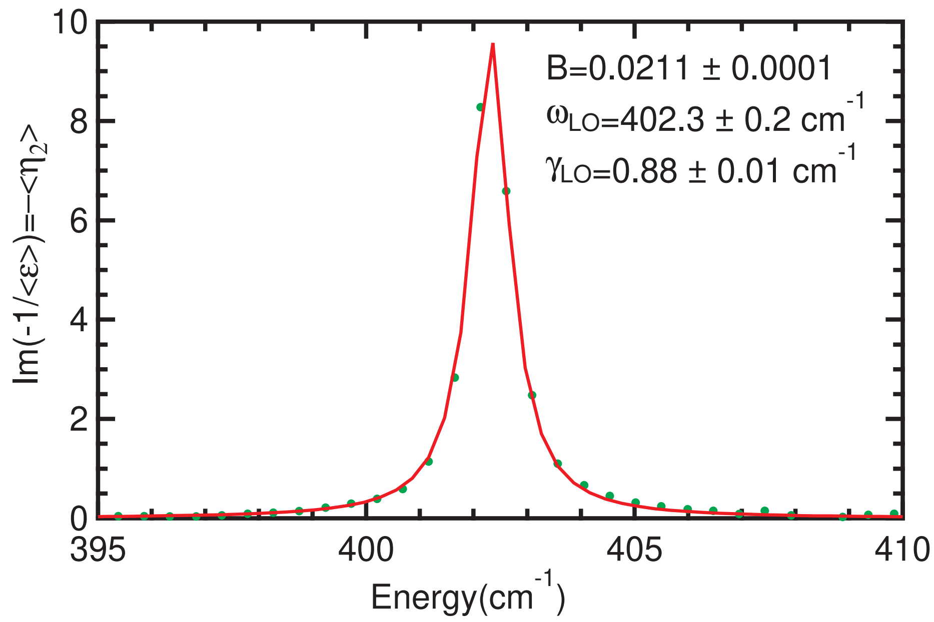

Figure 5.7: Pseudo-loss function for GaP in the reststrahlen region at room temperature (in air) fitted with a Lorentzian as in Eq. (123).

If ϵ follows a Lorentzian lineshape, then of course this expression (124) yields a constant γ_{TO}. However, we can also evaluate this expression for other types of lineshapes or from experimental data $\epsilon(\omega) = \epsilon_1 + i\epsilon_2$, if the static and high-frequency dielectric constants ϵ_s and ϵ_∞ are found from extrapolation.

We can break up Eq. (124) into real and imaginary components [39] (see also A. Rastogi, K. F. Pai, T. J. Parker, and R. P. Lowndes, in *Proceedings of the International Conference on Lattice Dynamics, Paris, September 5-9, 1977*, edited by M. Balkanski (Flammarion, Paris, 1978), p. 142)

$$\begin{aligned} i\gamma\omega &= \omega_{\mathrm{TO}}^2 \frac{(\epsilon_1 - \epsilon_s)(\epsilon_1 - \epsilon_\infty) + \epsilon_2^2}{(\epsilon_1 - \epsilon_\infty)^2 + \epsilon_2^2} - \omega^2 + \\ +i &\ \omega_{\mathrm{TO}}^2 \frac{(\epsilon_s - \epsilon_\infty)\epsilon_2}{(\epsilon_1 - \epsilon_\infty)^2 + \epsilon_2^2}. \end{aligned} \tag{125}$$

In the anharmonic literature [39], the broadening term

$$i\gamma\omega = 2\omega_{\mathrm{TO}}\left[\Delta(\omega) + i\Gamma(\omega)\right] \tag{126}$$

in the denominator of the Lorentzian lineshape (117) is typically associated with a complex self-energy $\Delta(\omega) + i\Gamma(\omega)$. In this view, ω_{TO} is the unrenormalized (truly harmonic) resonance frequency of the oscillator. The real part $\Delta(\omega)$ of this self energy has two contributions due to thermal expansion and due to the anharmonic decay of optical phonons into acoustic ones. It usually leads to a redshift of the phonon frequency. The imaginary part $\Gamma(\omega)$ causes a broadening of the phonon resonance, leading to a FWHM of $\gamma_{\mathrm{TO}} \approx 2\Gamma(\omega_{\mathrm{TO}})$.

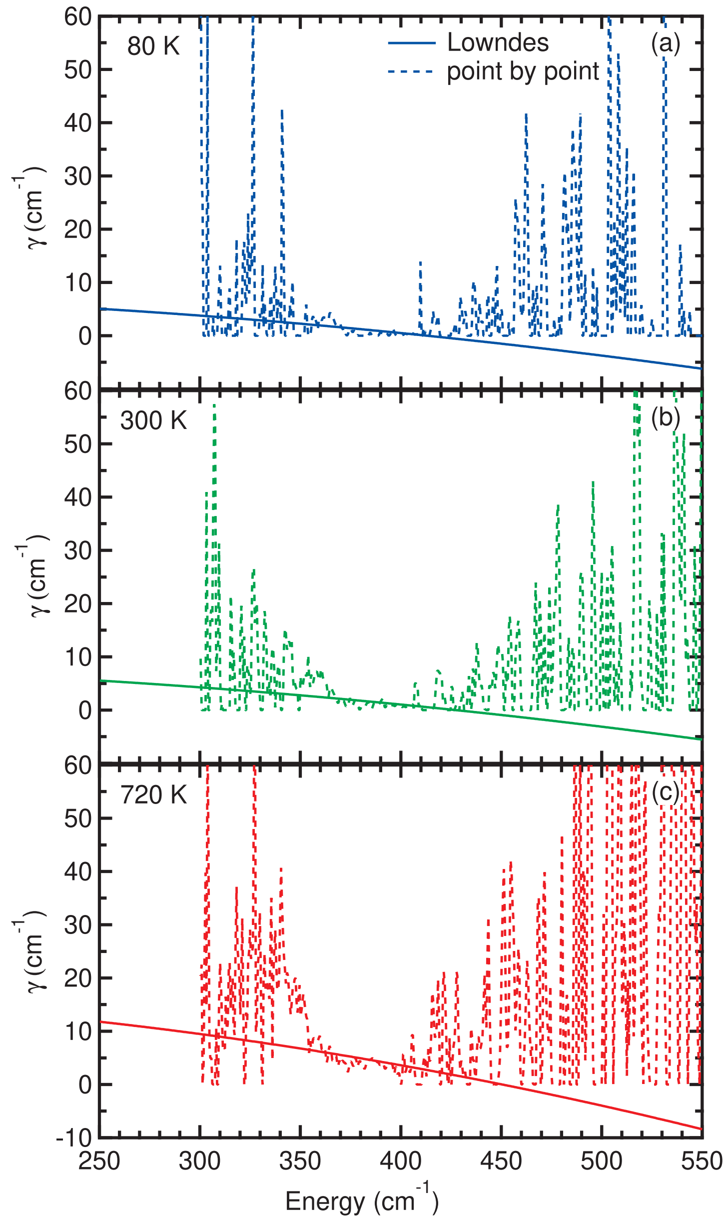

Figure 5.8: Frequency-dependent scattering rate of GaP at (a) 80 K, (b) 300 K, and (c) 720 K calculated from the Lowndes lineshape in Eq. (105) (solid) and from our experimental (point-by-point fit) data (dashed) in Fig. 5.2.

We first evaluate the broadening γ in Eq. (125) for a Lowndes lineshape (105), shown by the solid lines in Fig. 5.8. The Lowndes parameters were taken from fits to our ellipsometric angles at three different temperatures. The broadening parameter decreases steadily with increasing photon energy, since $\gamma_{\mathrm{TO}}>\gamma_{\mathrm{LO}}$, and eventually becomes negative above the LO frequency where $\epsilon_2<0$ for our Lowndes parameters. A negative broadening parameter leads to a pole in the dielectric function below the real axis. This is forbidden, because it violates both the causality and the passivity conditions [16]. In practice, this is offset by higher-order phonon absorption processes which lead to a positive ϵ_2 as discussed in Sec. 5.4.2.

The application of Eq. (125) to our experimental data is somewhat disappointing, see the dashed lines in Fig. 5.8. First, we note that γ is always positive, because our ellipsometry fitting software enforces $\epsilon_2>0$. The noise is very high above the LO phonon energy, where the reflected light intensity is very low. We have excellent signal-to-noise ratio in the reststrahlen region between ω_{TO} and ω_{LO}, which allows a very accurate determination of the broadening parameter in this region. The data is also noisy below the TO phonon energy, because this spectral region is at the very edge or even below the specified energy range of our instrument. A better signal-to-noise ratio in FTIR ellipsometry would be needed to study the frequency dependent scattering rate.

The broadening parameter γ increases with increasing temperature and therefore one expects that this technique should yield better results at higher temper-

atures, where the broadenings are larger. With a bit of imagination, we might indeed locate a peak in the broadening at 720 K below the TO energy, see Fig. 5.8, where it is expected [20]. See also Ushioda *et al.*, Phys. Rev. B **8**, 4634 (1973), and Ushioda and McMullen, Solid State Commun. **11**, 299 (1972). Similar results are shown in Ref. 39 for ZnSe and by Ratogi *et al.* (1978) for RbBr and $KTaO_3$.

5.6.3 Accurate determination of the broadening parameter

In Fig. 5.4, we show the TO and LO broadenings versus temperature fitted to our experimental data using two different methods: (1) We fitted the ellipsometric angles weighted with the experimental errors with the Lowndes model in Eq. (105). (2) We fitted the imaginary part of the pseudodielectric function $\langle\epsilon_2\rangle$ and the pseudo-loss function $\langle\eta_2\rangle$, see Eq. (122), with a Lorentzian to obtain the TO and LO broadenings, respectively. Both methods yield the same broadenings for the LO phonon, but not for the TO phonon. We therefore discuss how the choice of the TO broadenings in the models affects the agreement with the experimental data. Since the Raman lineshapes of the TO and LO phonons closely follow the peaks of ϵ_2 and the loss function [20], it is not surprising that the second method provides better agreement with the Raman broadenings determined by Bairamov *et al.* [33]

To investigate this question, we show the ellipsometric angles ψ and Δ, the imaginary part $\langle\epsilon_2\rangle$ of the pseudo-dielectric function, and the pseudo-loss function

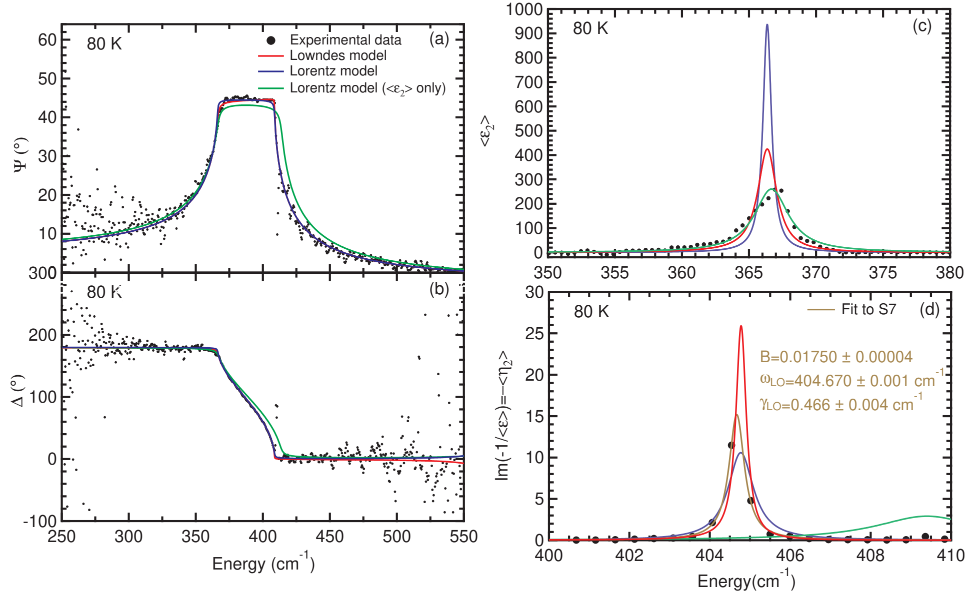

Figure 5.9: Ellipsometric angles (a) ψ and (b) Δ, (c) imaginary part $\langle\epsilon_2\rangle$ of the pseudo-dielectric function, and (d) pseudo-loss function $-\langle\eta_2\rangle$ versus photon energy for GaP at 80 K (symbols) fitted with two different Lorentz models (blue, green) with different broadening parameters. A Lowndes fit (red) is also shown. The pseudo-loss function is also fitted with a Lorentzian, compare Eq. (123), shown by the brown line.

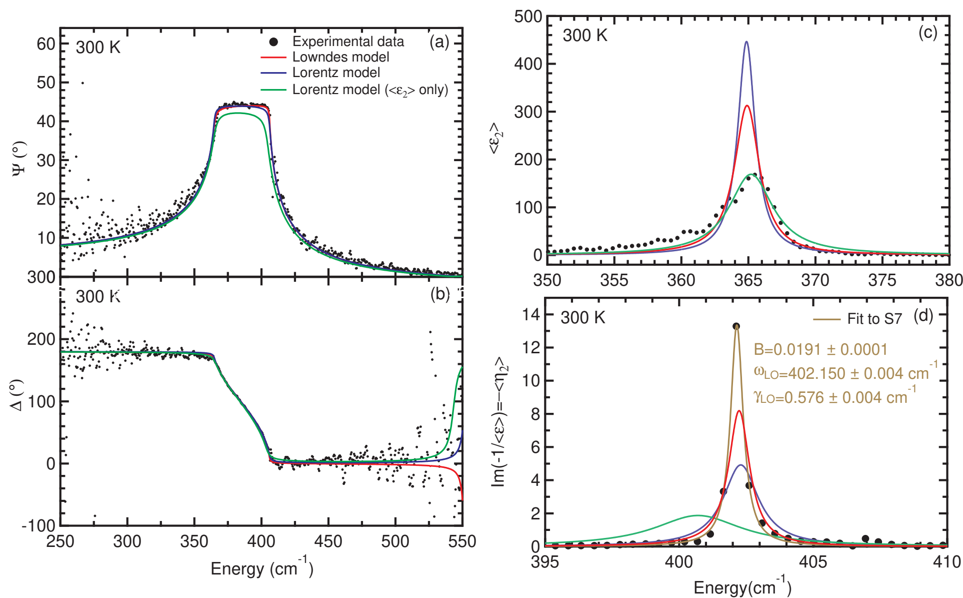

Figure 5.10: Same as Fig. 5.9, but at 300 K (inside the cryostat). The parameters are slightly different from Fig. 5.7.

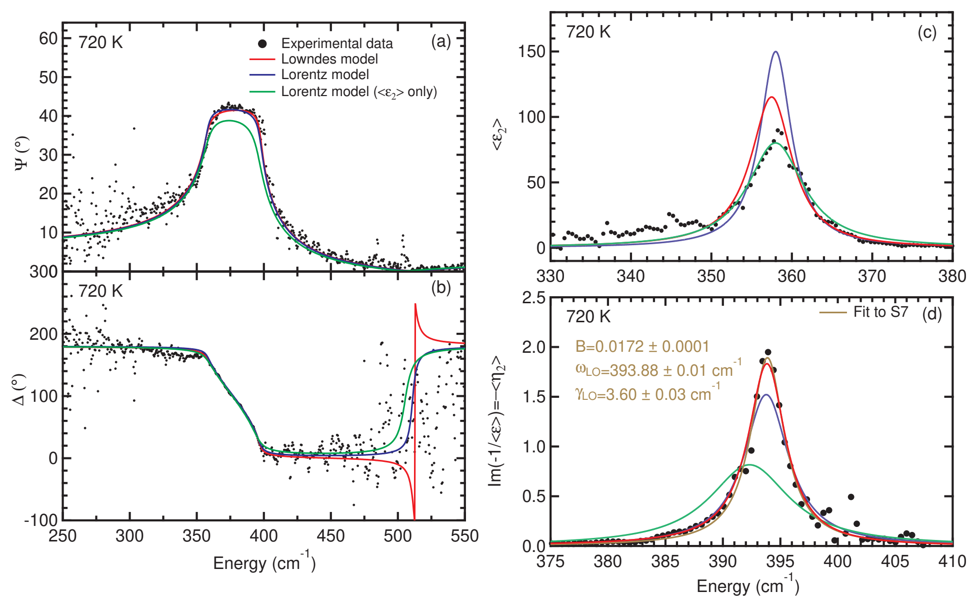

Figure 5.11: Same as Fig. 5.9, but at 720 K.

$-\langle\eta_2\rangle$ versus photon energy for GaP at three different temperatures in Figs. 5.9, 5.10, and 5.11 (symbols). The Lowndes model (shown by red lines), fitted to the ellipsometric angles, describes the ellipsometric angles and the pseudo-loss function very well, but it significantly overshoots the magnitude of the peak in $\langle\epsilon_2\rangle$. Since the resolution of the ellipsometer was set to 1 cm^{-1} and the peak width at room temperature is γ_{TO}=2.9 cm^{-1}, we do not believe that this is an issue with the instrumental resolution. The asymmetry of the $\langle\epsilon_2\rangle$ peak also does not explain this discrepancy. Perhaps small systematic errors in the ellipsometric angles lead to large errors in $\langle\epsilon_2\rangle$, especially for very large values of $\langle\epsilon_2\rangle$.

Fitting the ellipsometric angles with a Lorentzian (shown in blue in Figs. 5.9, 5.10, and 5.11) overshoots the $\langle\epsilon_2\rangle$ peak even more. In this case, the fit arrives at a low value of γ, because the same broadening is used for the TO and LO phonons. The LO phonon broadening is very small and therefore the Lorentz fit takes an average value of the TO and LO broadenings as the Lorentzian broadening γ, which is too small. Therefore, we understand why the Lorentzian fit to the ellipsometric angles overshoots the $\langle\epsilon_2\rangle$ peak.

Finally, we determine γ_{TO} by fitting the $\langle\epsilon_2\rangle$ peak with a Lorentzian (green line). We obtain a good fit to the data and the amplitude of the $\langle\epsilon_2\rangle$ peak is reproduced well. However, the large broadening leads to a poor fit of the ellipsometric angles and the pseudo-loss function peak. The peak value of the ψ-reststrahlen band is much lower in the model than in the data. Also, the falling slope near the

LO energy is pushed too far towards larger energies. For completeness, we also show a Lorentzian fit to the pseudo-loss function peak (brown).

We noted earlier that the peak of the ψ-reststrahlen band strongly depends on the broadening. For γ=0, the maximum of ψ equals 45° and decreases with increasing γ between the TO and LO energies. Therefore, accurate measurements of ψ using spectroscopic ellipsometry allow accurate measurements of γ, even when the instrumental resolution is larger than γ. While absolute reflectance measurements are very difficult experimentally, the accuracy of ψ is usually better than 0.3° in the mid-infrared spectral range around 30 μm wavelength.

It is well known that the magnitude of the reststrahlen bands in GaP reflection measurements is influenced by polishing and etching, presumable due to changes in surface roughness [58]. A poorly prepared surface will reduce the measured reflectance or the ellipsometric angle ψ. Since our value of ψ is above 44° at room temperature, our surface is quality is excellent and does not explain the broad $\langle \epsilon_2 \rangle$ peak.

5.6.4 Relationship between Phonon Lifetimes and Broadenings

According to Laubereau and Kaiser [53] and Kuhl and Bron [49], the relationship between the broadening of the Raman phonon in wave numbers $\Delta\bar{\nu}$ and the phonon dephasing time (coherence time, or simply lifetime) τ=T_2 is

$$\Delta\bar{\nu} = \frac{1}{\pi c \tau}, \tag{127}$$

where c is the speed of light. The phonon wave number $\bar{\nu}$ is related to its wavelength λ and its energy E through

$$hc\bar{\nu} = \frac{hc}{\lambda} = hf = E, \tag{128}$$

where h is Plack's constant. Therefore,

$$\gamma = \Delta E = hc\Delta\bar{\nu} = \frac{hc}{\pi c\tau} = \frac{h/2\pi}{\pi\tau/2\pi} = \frac{\hbar}{\tau/2} = \frac{2\hbar}{\tau}. \tag{129}$$

Kuhl and Bron [49] found a dephasing time T_2 for GaP at room temperature of 14 ps. The coherent anti-Stokes Raman decay constant $T_2/2$ is therefore 7 ps. The corresponding Raman broadening γ equals 0.094 meV or 0.76 cm^{-1}, as shown in Fig. 2 of Kuhl and Bron [49].

A different perspective is given by von der Linde, Kuhl, and Klingenberg [54]. For GaAs at 77 K, they list a phonon lifetime of τ=6.3 ps and a broadening $\Delta\bar{\nu}$=0.85 cm^{-1} or γ=0.10 meV. This suggests a relationship similar to the radiative broadening of Loudon [52]

$$\gamma = \frac{\hbar}{\tau}. \tag{130}$$

Laubereau, von der Linde, and Kaiser [55] also emply Eq. (130). Equations (129) and (130) differ by a factor of two.

In some publications [39,52] (R. F. Wallis, I. P. Ipatova, and A. A. Maradudin, Fiz. Tverd. Tela **8**, 1064, 1966; Sov. Phys. Solid State **8**, 850, 1966), the full width at half maximum (FWHM) of a Lorentzian is taken to be γ=$2\gamma'$. In that case

$$2\gamma' = \frac{\hbar}{\tau} \quad \text{or} \quad \gamma' = \frac{\hbar}{2\tau}. \tag{131}$$

This convention is related to the identity

$$\begin{aligned}\epsilon(\omega) &= \epsilon_\infty + A\left(\frac{1}{\omega_0-\omega-i\gamma'}+\frac{1}{\omega_0+\omega+i\gamma'}\right) = \\ &= \epsilon_\infty + \frac{2A\omega_0}{(\omega_0^2+\gamma'^2)-\omega^2-2i\gamma'\omega}.\end{aligned} \tag{132}$$

In other words, Eq. (132) indicates that the sum of two complex-conjugate harmonic terms with broadening γ' equals a Lorentzian with a full width at half maximum (FWHM) of $2\gamma'$. Note also the shift of the resonance frequency due to broadening. Compare Loudon [52] and the WVASE32 software guide published by the J. A. Woollam Co.

For our work described in this manuscript, we follow Eq. (129) from Laubereau and Kaiser [53].

5.6.5 Origin of the TO and LO Phonon Broadenings

In the main manuscript we interpreted the TO and LO broadenings as pure lifetime broadenings, but we should also discuss other potential contributions to the phonon broadenings. To this end, we first calculate the optical penetration depth d_{opt} (the inverse of the absorption coefficient α) from our model, see Fig. 5.12.

We find that the penetration depth is 200 nm at the TO energy and even larger at different photon energies. Therefore, the width of our phonon peaks is not likely influenced by polishing damage near the surface. Of course, we are not able to rule out other inhomogeneous broadening mechanics, such as crystal

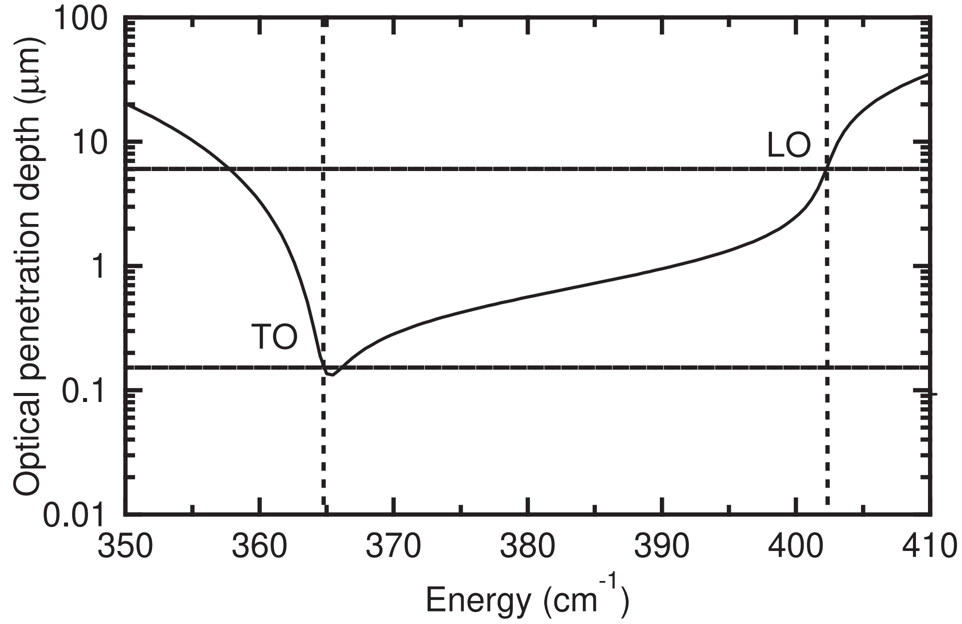

Figure 5.12: Optical penetration depth for GaP in the reststrahlen region as a function of photon energy.

defects or impurities.

The finite penetration depth also leads to an uncertainty

$$\Delta q = \frac{2\pi}{d_{opt}} \sim 0.005\frac{2\pi}{a} \tag{133}$$

of the phonon wave vector, where a is the lattice constant of GaP. We find the corresponding uncertainty ΔE by calculating the phonon dispersion of GaP from a ten-parameter shell model [28] using the programs of Kunc and Nielsen (Comput. Phys. Commun. **17**, 413, 1979) as shown in Fig. 5.13. For our (111) oriented sample, the uncertainty is along the Λ-direction. We find that the finite penetration depth causes an energy broadening of no more than 0.002 cm^{-1}, much smaller

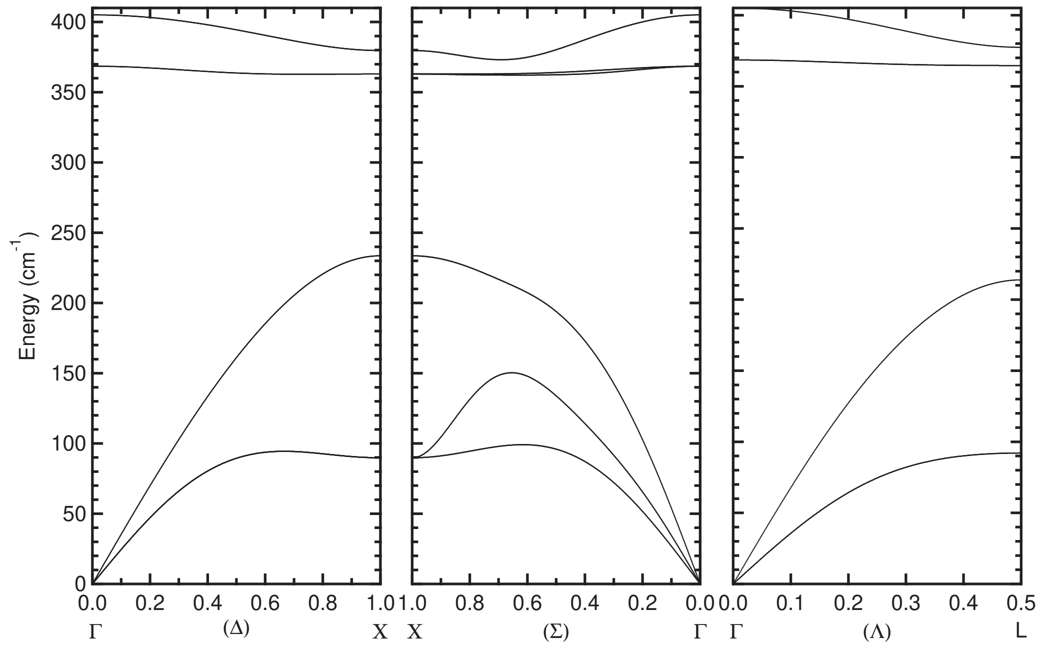

Figure 5.13: Phonon dispersion curves for GaP, calculated using a ten-parameter shell model [28]

.

than our spectrometer resolution (1 cm^{-1}). Therefore, we conclude that the finite penetration depth does not have a significant impact on the phonon broadenings of GaP. By contrast, the finite penetration depth of x-rays determines the widths of Bragg reflections in C, Si, and Ge (Pietsch, Holy, Baumbach, *High-Resolution X-Ray Scattering*, Springer, New York, 2004, Fig. 1.5).

Finally, we discuss the impact of doping on the optical phonon broadenings. For an effective electron Drude (or conductivity) mass of (P. Kühne, T. Hofmann,

C. M. Herzinger, and M. Schubert, Thin Solid Films **519**, 2613, 2011)

$$m_{\rm cc} = \frac{3m_l m_t}{2m_l + m_t} = 0.35m_0 \tag{134}$$

for GaP in the X-valley (where m_l=1.12m_0 and m_t=0.22m_0 are the longitudinal and transverse masses, respectively, and m_0 is the free electron mass) and an electron concentration near 5×10^{16} cm^{-3}, the screened plasma frequency [21] ω_P is about 5 meV or 40 cm^{-1}. The lower (LP) and upper phonon-plasmon (UP) resonances are therefore given by (Varga, Phys. Rev. **137**, A1896, 1965; Mooradian and Wright, Phys. Rev. Lett. **16**, 999, 1966; Kukharskii, Solid State Commun. **13**, 1761, 1973)

$$\omega_{\rm LP,UP}^2 = \frac{1}{2}\left(\omega_P^2 + \omega_{\rm LO}^2\right) \pm \sqrt{\frac{1}{4}\left(\omega_P^2 + \omega_{\rm LO}^2\right)^2 - \omega_P^2 \omega_{\rm TO}^2}. \tag{135}$$

The UP energy is the experimentally measured LO energy modified by doping.

Using ω_P=40 cm^{-1}, $\omega_{\rm TO}$=364.8 cm^{-1}, and $\omega_{\rm LO}$=401.9 cm^{-1}, we find $\omega_{\rm LP}$=36.3 cm^{-1} (below our spectral range) and $\omega_{\rm UP}$=402.3 cm^{-1}. This means that the "true" LO energy for an undoped sample is about 0.4 cm^{-1} below our measured value of 402.3 cm^{-1} for our electron concentration of 5×10^{16} cm^{-3}. This might explain small variations of the reported values of $\omega_{\rm LO}$ in the literature, if no doping correction was performed.

With increasing doping concentration, the UP broadening (i.e., the observed LO broadening due to the interaction between the LO phonon and free carriers) increases considerably, while the TO phonon broadening remains about the same

(Kukharskii 1973). This was observed in two different studies by Bairamov *et al.,* [33, 34] where the sample with the higher resistivity of 10^{10}-10^{12} Ωcm had an LO broadening of 0.6 cm^{-1}, while a less pure sample with a carrier concentration of 9×10^{16} cm^{-3} had an LO broadening of 2 cm^{-1}, see Table 5.1. Therefore, free-carrier effects cannot explain why the TO broadening is larger than the LO broadening. We also verified this by adding the effects of free carriers in our ellipsometry model with a Drude term. As shown in Fig. 5.14, the ellipsometric angle ψ for a 70° angle of incidence depends on the doping level for carrier concentrations exceeding 5×10^{17} cm^{-3}, one order of magnitude higher than for our sample. For this simulation we assumed a mobility of 375 cm^2/Vs (independent of carrier concentration), calculated from the resistivity of 0.3 Ωcm specified by the supplier of this sample.

Since we perform measurements at elevated temperatures, one might also ask if the density of thermally excited carriers can contribute to the broadenings of LO phonons. We therefore calculated the intrinsic carrier density (N. W. Ashcroft and N. D. Mermin, *Solid State Physics*, Saunders, Fort Worth, 1976, p. 575)

$$n_i\left(T\right)=\tfrac{1}{4}\left(\tfrac{2k_BT}{\pi\hbar^2}\right)^{3/2}\left(m_cm_v\right)^{3/4}e^{-\frac{E_g}{2k_BT}}= \tag{136}$$
$$=\ 2.5\left(\frac{m_cm_v}{m_0^2}\right)^{3/4}\left(\tfrac{T}{300\ K}\right)^{3/2}e^{-\frac{E_g}{2k_BT}}\times10^{19}\ \mathrm{cm}^{-3}.$$

Here we need to use the density of states mass for electrons

$$m_c=N_v^{2/3}\sqrt[3]{m_lm_t^2}=0.79m_0, \tag{137}$$

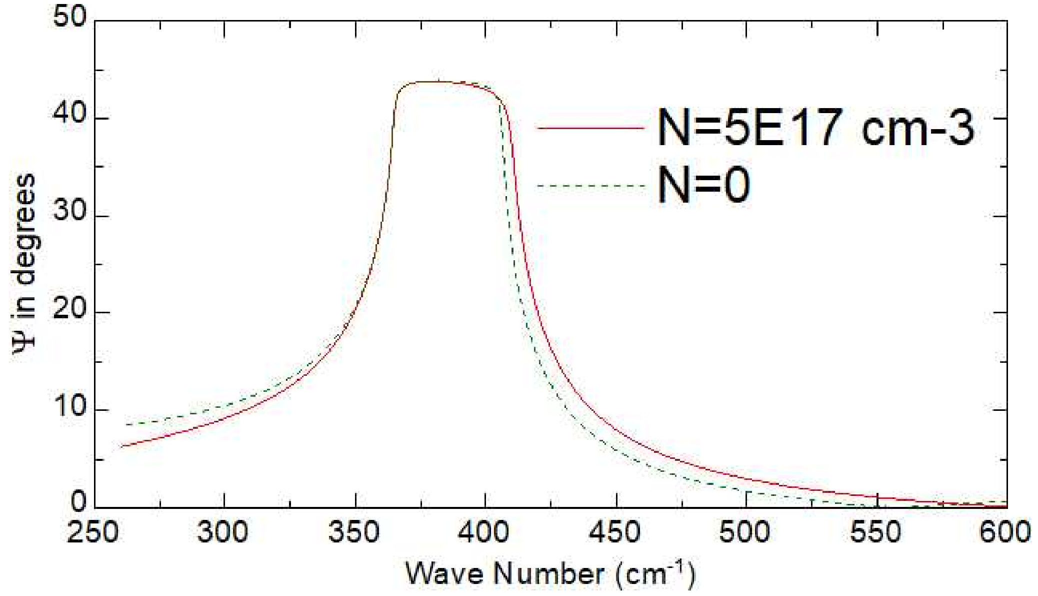

Figure 5.14: Doping dependence of the ellipsometric angle ψ for bulk GaP at room temperature and 70° angle of incidence.

where N_v=3 is the number of X-valleys. The other parameters are m_v=0.83m_0 and E_g=2.25 eV. The results of calculating the intrinsic carrier density (136) are shown in Fig. 5.15. Even at our highest temperatures, the intrinsic density of thermally excited carriers is many orders of magnitude lower than the doping concentration of 5×10^{16} cm^{-3} and therefore can be ignored.

5.6.6 GaP born effective charge

In a polar crystal, there is a charge transfer between the atoms involved in the chemical bond. This is known as the Born effective charge e_t^*. It does not have a large influence on the energies of long-wavelength TO phonons, but it adds

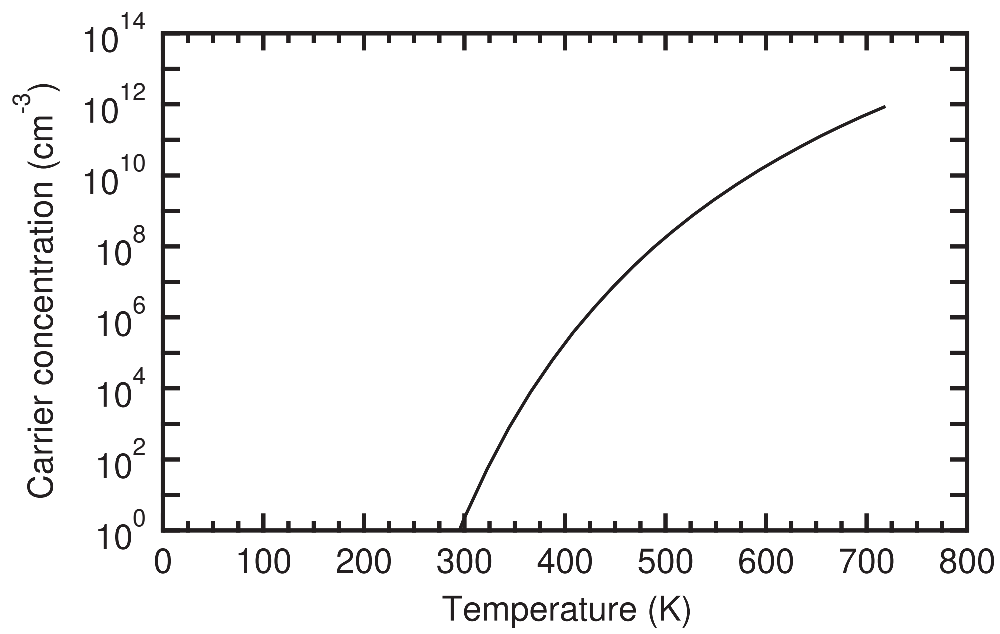

Figure 5.15: Intrinsic carrier concentration of GaP as a function of temperature calculated from Eq. (136).

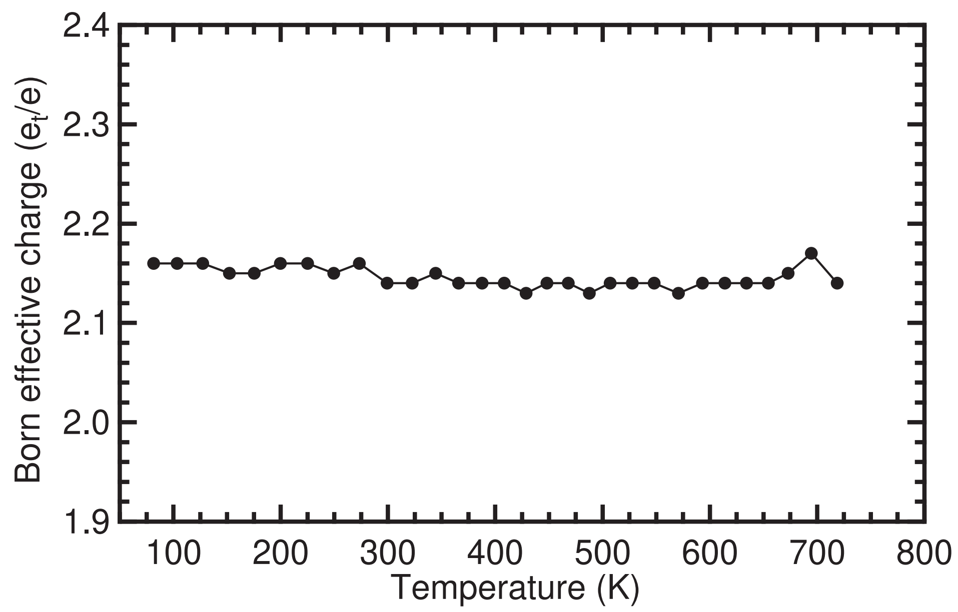

Figure 5.16: Temperature dependence of the Born effective charge calculated from Eq. (138) for bulk GaP.

an additional Coulombic restoring force to the long-wavelength LO vibrations (Fröhlich interaction). This leads to a splitting of the TO and LO phonons at the Γ-point. From this Fröhlich splitting, the Born effective charge

$$e_t^* = \sqrt{V\mu\epsilon_0\epsilon_\infty(\omega_{LO}^2 - \omega_{TO}^2)} \tag{138}$$

can be calculated at each temperature, see Reparaz *et al.*, Appl. Phys. Lett. **96**, 231906 (2010). V is the volume per GaP formula unit (volume of the primitive unit cell), μ the reduced mass of the Ga and P atoms, ϵ_0 the vacuum permittivity, and ϵ_∞ the high-frequency dielectric constant. As shown in Fig. 5.16, the Born effective charge does not depend on temperature, as one would expect. The average Born effective charge is 2.15(1) over the whole temperature range. We did not observe the small increase in the Born effective charge with temperature due to thermal expansion predicted by Debernardi [23].

5.6.7 Variation of the apparent GaP surface layer thickness

Insulators are mostly transparent in the mid-infrared spectral region, above the phonon absorption energies and below the band gap. In this region, the ellipsometric angle Δ must be 0 or π for a bare substrate, depending on the relative magnitude of the angle of incidence and the Brewster angle. Experimentally, one observes deviations of Δ from the ideal values for two reasons: (1) Surface overlayers, such as surface roughness, native oxides, or adsorbed overlayers such as water,

ice, or other airborne molecular contamination. See G. E. Jellison and B. C. Sales, Appl. Opt. **30**, 4310 (1991). (2) Systematic errors affecting the measurement of Δ, especially those caused by the diamond windows of our UHV cryostat [43].

In Fig. 5.17, we report the surface layer thickness in our experiments, modeled as a 50/50 mixture of GaP and voids within the Bruggeman effective medium approximation. We call this the *apparent* surface layer thickness, because it might be affected by systematic errors from the cryostat windows.

An initial measurement of the GaP sample in air (without windows) finds a surface layer thickness of 38 Å, shown by the green data point. The sample is then mounted in the cryostat followed by pumping to UHV conditions. This reduces the surface layer thickness to 29 Å, as shown by the blue data point. This reduction might be due evaporation of some of the overlayer, but it could also be due to errors caused by our windows. We then heat the sample to 800 K for several hours and let it cool down to room temperature overnight. This reduces the surface layer thickness to 9 Å, as shown by the red data point. Most likely, this value of 9 Å represents the residual surface roughness, after all adsorbed contaminants have evaporated.

We now start our temperature series at 80 K, where the surface layer thickness is 19 Å. We gradually increase the temperature to 275 K and measure the pseudo-dielectric function at each step for several hours. This increases the surface layer thickness to 48 Å, as ice forms on the sample. At the next temperature (300 K),

the surface layer thickness is only 18 Å, because most of the ice has evaporated. As we heat the sample to 325 K, the surface layer thickness is 8 Å and it gradually is reduced to zero as we heat towards 700 K. It is not likely that the surface layer thickness will actually vanish at 700 K. It is more likely that our data are affected by experimental errors due to the diamond windows. These windows are not getting warm, even at the highest sample temperatures. Therefore, the errors due to the windows are likely independent of temperature. It is likely that we underestimate the surface layer thickness in the cryostat by about 10 Å, due to the retardance of the diamond windows.

This discussion emphasizes that one must be careful when interpreting changes of optical constants with temperature. A careful preparation of the sample is required to minimize surface overlayers. It can be very helpful to heat the sample for several hours to reduce airborne molecular contamination, if this does not change the properties of the sample. It is inevitable for ice to form on the sample below room temperature, even under the best (10^{-8} Torr) vacuum conditions achievable in our setup.

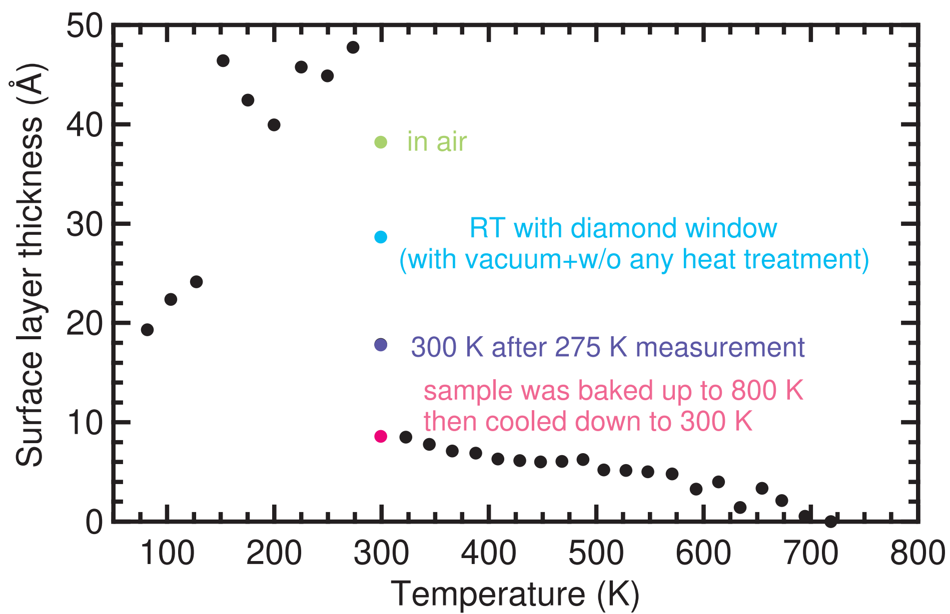

Figure 5.17: Variation of the apparent GaP surface layer thickness with temperature.

6 CONCLUSION

In this work, we introduced a convenient way to describe the dielectric function ϵ over a broad range. This new comprehensive formalism can be used to describe the entire dielectric function from the midinfrared to the deep ultraviolet of insulators, semiconductors, and metals. Here we defined ϵ as a product of Drude, TO/LO phonon, and electronic interband transition factors. We applied this factorized broadband description to bulk wurtzite ZnO and ZnO thin films. With this approach, we investigate the thickness dependence optical properties of ZnO thin films on Si and quartz (SiO_2) substrates. Regardless of the substrate both ϵ_1 and ϵ_2 show significant variations with thickness over the complete spectral range. The bandgap of thin ZnO layers shows a small blue shift ($\approx$ 80 meV) with decreasing film thickness due to quantum confinement. Near the band gap, the excitonic absorption shows a drastic reduction with decreasing film thickness. This behavior is more apparent in ZnO on Si than on SiO_2. The reduction of excitonic effects leads to a reduction of the static and high-frequency dielectric constant with deceasing film thickness.

We also studied the temperature dependence of transverse (TO) and longitudinal (LO) optical phonon energies and the linewidths of bulk GaP. Due to thermal expansion and anharmonic phonon-phonon decay, we observed a redshift and increasing broadening of TO and LO phonons with increasing temperature. The

static and high-frequency dielectric constant increases with increasing temperature. This variation can be explained by the thermal expansion of the crystal and the temperature dependence of the average band gap (Penn gap).

7 FUTURE WORK

In order to explain the behavior of excitonic absorption near the ZnO bandgap with film thickness, our ellipsometric spectra need to be fit with the Elliot–Tanguy theory model [134, 135]. This theory describes the excitonic contributions to the absorption and dispersion of semiconductors. As explained in chapter 4, we would like to model our ellipsometric spectra including excitonic effects and exciton-phonon complexes. This will allow us to fully understand the dielectric function and dependence of the excitonic Tanguy parameters on film thickness and substrate material. Since ZnO is an excellent semiconductor for high temperature electronics, the temperature dependent optical properties of ZnO thin films can be the next experimental step.

In case of GaP, we would like to extend our measurement range to cover the far-infrared regions and study the frequency dependent scattering rate with a better signal-to-noise ratio.

REFERENCES

[1] H. Morkoç and Ü. Özgür. *Zinc oxide: fundamentals, materials and device technology* (John Wiley Sons, 2008).

[2] J. A. Woollam Co. , Inc. , Lincoln, NE. Model V-VASE.

[3] H. Fujiwara, R. W. Collins, *Spectroscopic ellipsometry for photovoltaics* (Springer, Switzerland, 2018).

[4] http://academic.brooklyn.cuny.edu/physics/holden/ellips.jpg

[5] T. Guo, M. Li, Y. Zhou, L. Ni, X. Fu, X. Hu, Optik **145**, 188-201 (2017).

[6] J. A. Woolam Co. , Inc. , Guide to Using WVASE32R, (J. A. Woollam Co. , Inc. , Lincoln, NE, 2009)

[7] http://hyperphysics.phy-astr.gsu.edu/hbase/quantum/bragg.html

[8] B. D. Cullity and S. R. Stock, *Elements of X-Ray Diffraction*, (Prentice Hall,Upper Saddle River, NJ, 2001).

[9] M. Ermrich, and O. Detlef, *XRD for the analyst: Getting acquainted with the principles*, (PANalytical, 2013).

[10] U. Pietsch,V. Holy, and T. Baumbach, *High-resolution X-ray scattering: from thin films to lateral nanostructures*, (Springer Science Business Media, 2004).

[11] D. S. Sivia, *Elementary scattering theory: for X-ray and neutron users*. (Oxford University Press, 2011).

[12] R. R. L. De Oliveira, D. A. C. Albuquerque, T. G. S. Cruz, F. M. Yamaji, and F. L. Leite, *Measurement of the nanoscale roughness by atomic force microscopy: basic principles and applications*, (Atomic force microscopy-imaging, measuring and manipulating surfaces at the atomic scale 3 2012).

[13] P. Eaton, and P. West, *Atomic force microscopy*, (Oxford university press, 2010).

[14] R. P. Lowndes, Phys. Rev. B **1**, 2754 (1970).

[15] M. Schubert, *Infrared Ellipsometry on Semiconductor Layer Structures: Phonons, Plasmons, and Polaritons* (Springer, Berlin, 2004).

[16] D. W. Berreman and F. C. Unterwald, Phys. Rev. **174**, 791 (1968).

[17] D. J. Lockwood, G. Yu, and N. L. Rowell, Solid State Commun. **136**, 404 (2005).

[18] F. Gervais and B. Piriou, J. Phys. C: Solid State Phys. **7**, 2374 (1974).

[19] A. S. Barker, Phys. Rev. **136**, A1290 (1964).

[20] A. S. Barker, Phys. Rev. **165**, 917 (1968).

[21] S. Zollner, P. Paradis, F. Abadizaman, and N. S. Samarasingha, J. Vac. Sci. Technol. B **37**, 012904 (2019).

[22] A. Debernardi, Phys. Rev. B **57**, 12847 (1998).

[23] A. Debernardi, Solid State Commun. **113**, 1 (2000).

[24] S. Ves, I. Loa, K. Syassen, F. Widulle, and M. Cardona, phys. stat. sol. (b) **223**, 241 (2001).

[25] T. I. Willett-Gies, C. M. Nelson, L. S. Abdallah, and S. Zollner, J. Vac. Sci. Technol. A **33**, 061202 (2015).

[26] C. I. Ribeiro-Silva, A. Picinin, J. P. Rino, M. G. Menezes, and R. B. Capaz, Comp. Mater. Sci. **161**, 265 (2019).

[27] A. R. Aparna, V. Brahmajirao, and T. V. Karthikeyan, Procedia Materials Science **6**, 1650 (2014).

[28] P. H. Borcherds, K. Kunc, G. F. Alfrey, and R. L. Hall, J. Phys. C: Solid State Phys. **12**, 4699 (1979).

[29] D. Snoke, *Solid State Physics* (Addison-Wesley, San Francisco, 2000).

[30] J. L. Birman, Phys. Rev. **127**, 1093 (1962).

[31] M. M. Sobolev and V. G. Nikitin, Tech. Phys. Lett. **24**, 329 (1998).

[32] A. S. Barker and R. Loudon, Rev. Mod. Phys. **44**, 18 (1972).

[33] B. Kh. Bairamov, Yu. E. Kitaev, V. K. Negoduiko, and Z. M. Khashkhozhev, Fiz. Tverd. Tela **16**, 2036 (1974) [Sov. Phys. Solid State **16**, 1323 (1975)]. There is a missing exponential in the Debye integral just below Eq. (5) of this paper, compare Ref. 66.

[34] B. Kh. Bairamov, D. A. Parshin, V. V. Toporov, and Sh. B. Ubaidullaev, Pis'ma Zh. Tekh. Fiz. **5**, 1116 (1979) [Sov. Tech. Phys. Lett. **5**, 466 (1979)].

[35] A. Mooradian and G. B. Wright, Solid State Commun. **4**, 431 (1966).

[36] A. H. Kachare, J. M. Cherlow, T. T. Yang, and W. G. Spitzer, J. Appl. Phys. **47**, 161 (1976).

[37] A. K. W. Abdullah, G. A. Gledhill, C. Patel, and T. J. Parker, **29**, 719 (1989).

[38] M. Hass, Semiconductors and Semimetals **3**, 3 (1967).

[39] K. A. Maslin, C. Patel, and T. J. Parker, Infrared Phys. **32**, 303 (1991).

[40] M. Giehler and E. Jahne, phys. stat. sol. (b) **73**, 503 (1976).

[41] B. Pödör, phys. stat. sol. (b) **120**, 207 (1983).

[42] B. Pödör and V. P. Izvekov, Rev. Phys. Appl. (Paris) **18**, 737 (1983).

[43] F. Abadizaman, *Optical characterization of Ni using spectroscopic ellipsometry at temperatures from 80 K to 780 K*, Ph.D. thesis, New Mexico State University (2020).

[44] Y. Sun, D. C. Law, and R. F. Hicks, Surf. Sci. **540**, 12 (2003).

[45] H. G. Tompkins and J. N. Hilifiker, *Spectroscopic Ellipsometry: Practical Application to Thin-Film Characterization* (Momentum, New York, 2016).

[46] H. Fujiwara, *Spectroscopic Ellipsometry* (Wiley, Chichester, 2007).

[47] S. Adachi, *Optical Constants of Crystalline and Amorphous Semiconductors* (Springer, New York, 1999).

[48] D. F. Parsons and P. D. Coleman, Appl. Opt. **10**, 1683 (1971).

[49] J. Kuhl and W. E. Bron, Solid State Commun. **49**, 935 (1984).

[50] A. Borghesi and G. Guizetti, in *Handbook of Optical Constants of Solids*, edited by E. D. Palik (Academic, New York, 1998).

[51] W. L. Bond, J. Appl. Phys. **36**, 1674 (1965).

[52] R. Loudon, *The Quantum Theory of Light* (Oxford, New York, 1984).

[53] A. Laubereau and W. Kaiser, Rev. Mod. Phys. **50**, 607 (1978).

[54] D. von der Linde, J. Kuhl, and H. Klingenberg, Phys. Rev. Lett. **44**, 1505 (1980).

[55] A. Laubereau, D. von der Linde, and W. Kaiser, Opt. Commun. **7**, 173 (1973).

[56] E. S. Koteles and W. R. Datars, Solid State Commun. **19**, 221 (1976).

[57] M. V. Hobden and J. P. Russell, Physics Letters **13**, 39 (1964).

[58] D. A. Kleinman and W. G. Spitzer, Phys. Rev. **118**, 110 (1960).

[59] B. Ulrici and E. Jahne, phys. stat. sol. (b) **86**, 517 (1978).

[60] M. Balkanski, R. F. Wallis, and E. Haro, Phys. Rev. B **28**, 1928 (1983).

[61] J. Menéndez and M. Cardona, Phys. Rev. B **29**, 2051 (1984).

[62] F. Vallée, Phys. Rev. B **49**, 2460 (1994).

[63] T. Sakurai and T. Sato, Phys. Rev. B **4**, 583 (1971).

[64] W. J. Borer, S. S. Mitra, and K. V. Namjoshi, Solid State Commun. **9**, 1377 (1971).

[65] C. Postmus, J. R. Ferraro, and S. S. Mitra, Phys. Rev. **174**, 983 (1968).

[66] R. Roucka, Y.-Y. Fang, J. Kouvetakis, A. V. G. Chizmeshya, and J. Menéndez, Phys. Rev. B **81**, 245214 (2010).

[67] P. Deus, U. Voland, and H. A. Schneider, phys. stat. sol. (a) **80**, K29 (1983).

[68] O. Madelung, W. von der Osten, and U. Rössler, in *Landolt-Börnstein Numerical Data and Functional Relationships in Science and Technology*, vol. III/22a (Springer, Berlin, 1987); D. Bimberg *et al.*, in *Landolt-Börnstein Numerical Data and Functional Relationships in Science and Technology*, vol. III/17a (Springer, Berlin, 1982).

[69] L. Viña, S. Logothetidis, and M. Cardona, Phys. Rev. B **30**, 1979 (1984).

[70] P. Y. Yu and M. Cardona, *Fundamentals of Semiconductors* (Springer, Berlin, 2010).

[71] S. Zollner, M. Garriga, J. Kircher, J. Humlìček, M. Cardona, and G. Neuhold, Phys. Rev. B **48**, 7915 (1993).

[72] K. Vedam, J. L. Kirk, and B. N. N. Achar, J. Solid State Chem. **12**, 213 (1975).

[73] C. M. Nelson, M. Spies, L. S. Abdallah, and S. Zollner, J. Vac. Sci. Technol. A **30**, 061404 (2012).

[74] C. M. Herzinger, B. Johs, W. A. McGahan, J. A. Woollam, and W. Paulson, J. Appl. Phys. **83**, 3323 (1998).

[75] S. Zollner, R. Liu, J. Christiansen, W. Chen, K. Monarch, T.-C. Lee, R. Singh, J. Yater, W. M. Paulson, and C. Feng, in *Amorphous and Microcrystalline Silicon Technology-1998*, ed. by R. Schropp, H. M. Branz, M. Hack, I. Shimizu, and S. Wagner (Materials Research Society, Pittsburgh, 1998), p. 957.

[76] S. Zollner, T.-C. Lee, K. Noehring, A. Konkar, N. D. Theodore, W. M. Huang, D. Monk, T. Wetteroth, S. R. Wilson, and J. N. Hilfiker, Appl. Phys. Lett. **76**, 46 (2000).

[77] J. Price and A. C. Diebold, J. Vac. Sci. Technol. B **24**, 2156 (2006).

[78] V. Darakchieva, B. Monemar, A. Usui, M. Saenger, and M. Schubert, J. Crystal Growth **310**, 959 (2008).

[79] S. Shokhovets, M. Himmerlich, L. Kirste, J. H. Leach, and S. Krischok, Appl. Phys. Lett. **107**, 092104 (2015).

[80] G. Yu, G. Wang, H. Ishikawa, M. Umeno, T. Soga, T. Egawa, J. Watanabe, and T. Jimbo, Appl. Phys. Lett. **70**, 3209 (1997).

[81] A. Kasic, M. Schubert, S. Einfeldt, D. Hommel, and T. E. Tiwald, Phys. Rev. B **62**, 7365 (2000).

[82] R. Goldhahn, Acta Phys. Polon. **104**, 123 (2003).

[83] S. Zollner, A. A. Demkov, R. Liu, P. L. Fejes, R. B. Gregory, J. A. Curless, Z. Yu, J. Ramdani, R. Droopad, T. E. Tiwald, J. N. Hilfiker, and J. A. Woollam, J. Vac. Sci. Technol. B **18**, 2242 (2000).

[84] C. V. Weiss, J. Zhang, M. Spies, L. S. Abdallah, S. Zollner, M. W. Cole, and S. P. Alpay, J. Appl. Phys. **111**, 054108 (2012).

[85] S. Zollner, A. A. Demkov, R. Liu, J. A. Curless, Z. Yu, J. Ramdani, and R. Droopad, in *Recent Developments in Oxide and Metal Epitaxy - Theory and Experiment*, ed. by M. Yeadon, S. Chiang, R. F. C. Farrow, J. W. Evans, and O. Aucielo (Materials Research Society, Pittsburgh, 2000), p. 167.

[86] E. Chernova, O. Pacherova, D. Chvostova, A. Dejneka, T. Kocourek, M. Jelinek, and M. Tyunina, Appl. Phys. Lett. **106**, 192903 (2015).

[87] A. Dejneka, D. Chvostova, O. Pacherova, T. Kocourek, M. Jelinek, and M. Tyunina, Appl. Phys. Lett. **112**, 031111 (2018).

[88] A. Dejneka and M. Tyunina, Adv. Appl. Cer. **117**, 62 (2018).

[89] S. Zollner, C. M. Herzinger, J. A. Woollam, S. S. Iyer, A. P. Powell, and K. Eberl, Solid State Commun. **96**, 305 (1995).

[90] S. Zollner, J. P. Liu, P. Zaumseil, H. J. Osten, and A. A. Demkov, Semicond. Sci. Technol. **22**, S13 (2007).

[91] J. N. Hilfiker, J. Sun, and N. Hong, in *Spectroscopic Ellipsometry for Photovoltaics*, Vol. 1, ed. by H. Fujiwara and R. W. Collins (Springer, Cham, 2018).

[92] G. K. Pribil, B. Johs, and N. J. Ianno, Thin Solid Films **455-456**, 443 (2004).

[93] N. Leick, J. W. Weber, A. J. M. Mackus, M. J. Weber, M. C. M. van de Sanden, and W. M. M. Kessels, J. Phys. D: Appl. Phys. **49**, 115504 (2016); **49**, 269601 (2016) (E).

[94] V. K. Kamineni, M. Raymond, E. J. Bersch, B. B. Doris, and A. C. Diebold, J. Appl. Phys. **107**, 093525 (2010).

[95] V. Longo, N. Leick, F. Roozeboom, and W. M. M. Kessels, ECS J. Solid State Sci. Technol. **2**, N15 (2013).

[96] Ü. Özgür, Ya. I. Alivov, C. Liu, A. Teke, M. A. Reshchikov, S. Doğan, V. Avrutin, S.-J. Cho, and H. Morkoç, J. Appl. Phys. **98**, 041301 (2005).

[97] B. Hussain, A. Aslam, T. M. Khan, M. Creighton, and B. Zohuri, Electronics **8**, 238 (2019).

[98] S. Logothetidis, A. Laskarakis, S. Kassavetis, S. Lousinian, C. Gravalidis, and G. Kiriakidis, Thin Solid Films **516**, 1345 (2008).

[99] Z. Gao and P. Banerjee, J. Vac. Sci. Technol. A **37**, 050802 (2019).

[100] H. Fujiwara and M. Kondo, Phys. Rev. B **71**, 075109 (2005).

[101] E. Pereira da Silva, M. Chaves, S. F. Durrant, P. N. Lisboa-Filho, J. R. R. Bortoleto, Mat. Res. **17**, 1384 (2014).

[102] J. C. Nie, J. Y. Yang, Y. Piao, H. Li, Y. Sun, Q. M. Xue, C. M. Xiong, R. F. Dou, and Q. Y. Tu, Appl. Phys. Lett. **93**, 173104 (2008).

[103] A. A. Mosquera, D. Horwat, A. Rashkovskiy, A. Kovalev, P. Miska, D. Wainstein, J. M. Abella, and J. L. Endrino, Sci. Rep. **3**, 1714 (2013).

[104] X. D. Li, T. P. Chen, P. Liu, Y. Liu, Z. Liu, and K. C. Leong, J. Appl. Phys. **115**, 103512 (2014).

[105] D. Pal, A. Mathur, A. Singh, J. Singhal, A. Sengupta, S. Dutta, S. Zollner, and S. Chattopadhyay, J. Vac. Sci. Technol. A **35**, 01B108 (2017).

[106] D. Pal, J. Singhal, A. Mathur, A. Singh, S. Dutta, S. Zollner, and S. Chattopadhyay, Appl. Surf. Sci. **421**, 341 (2016).

[107] H. Zaka, B. Parditka, Z. Erdélyi, H. E. Atyia, P. Sharma, and S. S. Fouad, Optik **203**, 163933 (2020).

[108] N. Ehrmann and R. Reineke-Koch, Thin Solid Films **519**, 1475 (2010).

[109] M. Mirzaee, A. Zendehnam, and S. Miri, Scientia Iranica F **20**, 1071 (2013).

[110] P. Wang, H. Du, S. Shen, M. Zhang, and B. Liu, Nanoscale Res. Lett. **7**, 176 (2012).

[111] T. E. Tiwald, J. A. Woollam, S. Zollner, J. Christiansen, R. B. Gregory, T. Wetteroth, S. R. Wilson, and A. R. Powell, Phys. Rev. B **60**, 11464 (1999).

[112] A. Janotti and C. G. Van de Walle, Appl. Phys. Lett. **87**, 122102 (2005).

[113] S. Shokhovets, L. Spieß, and G. Gobsch, J. Appl. Phys. **107**, 023509 (2010).

[114] N. Ashkenov, B. N. Mbenkum, C. Bundesmann, V. Riede, M. Lorenz, D. Spemann, E. M. Kaidashev, A. Kasic, M. Schubert, M. Grundmann, G. Wagner, H. Neumann, V. Darakchieva, H. Arwin, and B. Monemar, J. Appl. Phys. **93**, 126 (2003).

[115] H. Yoshikawa and S. Adachi, Jpn. J. Appl. Phys. **36**, 6237 (1997).

[116] G. E. Jellison and L. A. Boatner, Phys. Rev. B **58**, 3586 (1998).

[117] A. Schleife, C. Rödl, F. Fuchs, J. Furthmüller, and F. Bechstedt, Phys. Rev. B **80**, 035112 (2009).

[118] W. Y. Liang and A. D. Yoffe, Phys. Rev. Lett. **20**, 59 (1968).

[119] S. Shokhovets, G. Gobsch, and O. Ambacher, Superlattice Microst. **39**, 299 (2006).

[120] S. Shokhovets, O. Ambacher, B. K. Meyer, and G. Gobsch, Phys. Rev. B **78**, 035207 (2008).

[121] M. D. Neumann, C. Cobet, N. Esser, B. Laumer, T. A. Wassner, M. Eickhoff, M. Feneberg, and R. Goldhahn, J. Appl. Phys. **110**, 013520 (2011).

[122] M. Fox, *Optical Properties of Solids* (Oxford University Press, 2010, Oxford, UK) 2nd edition.

[123] J. S. Reparaz, L. R. Muniz, M. R. Wagner, A. R. Goñi, M. I. Alonso, A. Hoffman, and B. K. Meyer, Appl. Phys. Lett. **96**, 231906 (2010).

[124] W. T. Tsang and E. F. Schubert, Appl. Phys. Lett. **49**, 220 (1986).

[125] N. N. Syrbu, I. M. Tiginyanu, V. V. Zalamai, V. V. Ursaki, and E. V. Rusu, Physica B **353**, 111 (2004).

[126] D. R. Penn, Phys. Rev. **128**, 2093 (1962).

[127] N. M. Ravindra, S. Auluck, and V. K. Srivastava, phys. status solidi (b) **93**, K155 (1979).

[128] S. Albrecht, L. Reining, R. Del Sole, and G. Onida, Phys. Rev. Lett. **80**, 4510 (1998).

[129] P. Gori, M. Rakel, C. Cobet, W. Richter, N. Esser, A. Hofmann, R. Del Sole, A. Cricenti, and O. Pulci, Phys. Rev. B **81**, 125207 (2010).

[130] D. J. Cirilo-Lombardo, Phil. Mag. **95**, 1007 (2015).

[131] J. B. You, X. W. Zhang, H. P. Song, J. Ying, Y. Guo, A. L. Yang, Z. G. Yin, N. F. Chen, and Q. S. Zhu, J. Appl. Phys. **106**, 043709 (2009).

[132] J. B. You, X. W. Zhang, S. G. Zhang, H. R. Tan, J. Ying, Z. G. Yin, Q. S. Zhu, and P. K. Chu, J. Appl. Phys. **107**, 083701 (2010).

[133] S. Espinoza, F. Samparisi, F. Frassetto, S. Richter, M. Rebarz, O. Finke, M. Albrecht, M. Jurkovic, O. Hort, N. Fabris, A. Zymakova, D. D. Mai, R. Antipenkov, J. Nejdi, L. Poletto, and J. Andreasson, J. Vac. Sci. Technol. B **38**, 024005 (2020).

[134] C. Tanguy, Phys. Rev. Lett. **75**, 4090 (1995); **76**, 716 (1996).

[135] C. Tanguy, Phys. Rev. B **60**, 10660 (1999).

[136] H. Richter, Z. P. Wang, and L. Ley, Solid State Commun. **39**, 625 (1981).

[137] I. H. Campbell and P. M. Fauchet, Solid State Commun. **58**, 739 (1986).

[138] V. I. Korepanov, J. Raman Spectrosc. **2020**, 1 (2020).

[139] J. Serrano, F. J. Manjón, A. H. Romero, A. Ivanov, M. Cardona, R. Lauck, A. Besak, and M. Krisch, Phys. Rev. B **81**, 174304 (2010).

[140] M. Rajalakshmi, A. K. Arora, B. S. Bendre, and S. Mahamuni, J. Appl. Phys. **87**, 2445 (2000).

[141] K. A. Alim, V. A. Fonoberov, and A. A. Balandin, Appl. Phys. Lett. **86**, 053103 (2005).

[142] J. Humlíček, phys. status sol. **215**, 155 (1999).

[143] H. Helmholtz, Ann. Phys. **230**, 582 (1875).

[144] E. Kettler, Ann. Phys. **266**, 299 (1887).

[145] P. Drude, Physik. Z. **1**, 161 (1900).

[146] P. Drude, *The Theory of Optics* (Longmans, Green, and Company, New York, 1902), p. 398.

[147] S. Roberts, Phys. Rev. **100**, 1667 (1955); **114**, 104 (1959).

[148] M. Schubert, T. Hofmann, and C. M. Herzinger, J. Opt. Soc. Am. A **20**, 347 (2003).

[149] S. Zollner, S. Gopalan, M. Garriga, J. Humlíček, L. Viña, and M. Cardona, Appl. Phys. Lett. **57**, 2838 (1990).

[150] T. N. Nunley, N. S. Fernando, N. Samarasingha, J. M. Moya, C. M. Nelson, A. A. Medina, and S. Zollner, J. Vac. Sci. Technol. B **34**, 061205 (2016).

[151] R. T. Holm, J. W. Gibson, and E. D. Palik, J. Appl. Phys. **48**, 212 (1977).

[152] J. Humlíček, R. Henn, and M Cardona, Appl. Phys. Lett. **69**, 2581 (1996).

[153] R. H. Lyddane, R. G. Sachs, and E. Teller, Phys. Rev. **59**, 673 (1941).

[154] T. Kurosawa, J. Phys. Soc. Jpn. **16**, 1298 (1961).

[155] M. Schubert, Phys. Rev. Lett. **117**, 215502 (2015).

[156] T. Willett-Gies, E. DeLong, and S. Zollner, Thin Solid Films **571**, 620 (2014).

[157] C. J. Zollner, T. Willett-Gies, S. Zollner, and S. Choi, Thin Solid Films **571**, 689 (2014).

[158] A. A. Kukharskii, Fiz. Tverd. Tela **14**, 1744 (1972) [Sov. Phys.-Solid State **14**, 1501 (1972)].

[159] A. A. Kukharskii, Solid-State Commun. **13**, 1761 (1973).

[160] A. Mooradian and G. B. Wright, Phys. Rev. Lett. **16**, 999 (1966).

[161] A. Mooradian and A. L. McWhorter, Phys. Rev. Lett. **19**, 849 (1967).

[162] S. Zollner and D. Zarr, in *2000 IEEE International Symposium on Compound Semiconductors*, edited by M. Melloch and M.A. Reed (IEEE, Piscataway, NJ, 2000), p. 251.

[163] S. Zollner, J. Appl. Phys. **90**, 515 (2001).

[164] S. Zollner, Appl. Phys. Lett. **63**, 2523 (1993).

[165] D. L. Rode and S. Knight, Phys. Rev. B **3**, 2534 (1971).

[166] M. D. Neumann, N. Esser, J.-M. Chauveau, R. Goldhahn, and M. Feneberg, Appl. Phys. Lett. **108**, 221105 (2016).

[167] M. Cardona, *Modulation Spectroscopy* (Academic Press, New York, 1969).

[168] M. Cardona, *Light Scattering in Solids I* (Springer, Berlin, 1983).